PhD-FSTC-2017-51
The Faculty of Sciences, Technology and Communication

DISSERTATION

Defence held on 22/09/2017 in Luxembourg

to obtain the degree of

DOCTEUR DE L'UNIVERSITÉ DU LUXEMBOURG

EN PHYSIQUE

by

Henrique Pereira Coutada Miranda
Born on 20 December 1989 in Barcelos, Portugal

AB INITIO APPROACHES TO RESONANT RAMAN SPECTROSCOPY OF TRANSITION METAL DICHALCOGENIDES

Dissertation defence committee

Dr. Ludger Wirtz, dissertation supervisor
Professor, Université du Luxembourg

Dr. Xavier Gonze
Professor, Université Catholique de Louvain

Prof. Dr. Feliciano Giustino
Professor, University of Oxford

Dr. Susanne Siebentritt, Chairman
Professor, Université du Luxembourg

Dr. Tanja Schilling, Vice Chairman
Professor, Albert-Ludwigs-Universität Freiburg

to Sara

Acknowledgements

I would firstly like to thank my supervisor Ludger Wirtz for very important scientific advices during the course of my PhD. I am grateful to him for presenting and allowing me to present my work to many different audiences and his help in making me keep a broad view of the field of Materials Science. I also would like to thank him for suggesting me to develop the `phononwebsite` and `excitonwebsite` tools which are a very important outcome of my thesis. Additionally I am grateful for his support during the preparation of the manuscript and expert advices on how to present the ideas in a more clear and attractive way. I am very grateful to my co-supervisor Alejandro Molina-Sánchez for helping me countless times from the start to the end of my PhD. He introduced me to many codes, has always shown availability to discuss scientific questions, helped me to focus on the most important matters, and for reading and contributing with many comments to the present document since the earliest draft to the final version. I am also very grateful to Sven Reichardt whose PhD work also concerns the simulation of Raman spectra from first principles and with whom I discussed extensively many of the topics presented in this thesis. I would also like to thank him for his very attentive revision of this thesis, and for suggesting innumerous corrections and improvements.

I am very grateful to have had the opportunity to work directly with Stéphane Berciaud and Guillaume Froehlicher in preparing one of the manuscripts we review in this thesis. Their work on the experimental characterization of the Raman spectra os 2D materials served as a fundamental inspiration to this work.

I would like to thank Andrea Marini for integrating me in the `yambo` developers group, for always showing availability to discuss scientific matters. I am also very grateful to Davide Sangalli for having helped many times with technical and scientific questions. I would like to thank my friend Pedro Melo for his constant support, his critical reading of this thesis and very valuable corrections and advices on how to improve it.

I am also very grateful to Yannick Gillet, Matteo Giantomassi and Xavier Gonze for having started the work on calculation of resonant Raman intensities from first-principles which served as an inspiration and guide to the work presented here.

I would like to thank the `yambopy` developers: Alejandro Molina-Sánchez, Alexandre Morlet, Fulvio Paleari and Mike Atambo for their contributions and support on this project that belongs to the community.

I would also like to thank Atsushi Togo for very important feedback during the development of the `phononwebsite` and collaboration during the development of its the interface with `phonondb` and `phonopy`. I am also grateful to José Pedro Silva for with helpful advices on technical issues and the best web technologies to use to develop the website.

I am also very grateful to my colleagues and friends: Efterpi Kalesaki, Fulvio Paleari, Thomas Galvani and Francesco Nacarato for all the scientific discussions and all the fun times in between work.

I would like to thank all the intern students in our group with whom I had to opportunity to work with: Raoul Weber whose work lay the foundations to the `phononwebsite` as is today, to Chaitanya Nuthalapati, Alexandre Morlet, Amal Vats and Anuj Shetty.

I would also like to thank the Fonds National de la Recherche

(FNR), Luxembourg for funding this work through the project OTPMD. The simulations were done using the HPC facilities of the University of Luxembourg.

Apart from the scientific support, and more importantly I would like to thank all the people that were personally close to me during my PhD. To Sara for being very supportive during all this time for without this support, this work would have not been possible. To my mother, father and brother that, although many times physically distant were and are always close to me.

Abstract

This thesis deals with the theory and simulation of resonant Raman spectroscopy in two-dimensional transition metal dichalcogenides. We present two different *ab initio* approaches. In the first, we calculate the Raman susceptibility tensor as a function of laser energy from the change of the dielectric susceptibility with atomic displacements. In the second, we formulate the Raman tensor in terms of time-dependent perturbation theory and calculate it using electron-light and electron-phonon coupling matrix elements obtained from density functional theory. We investigate the role of resonance, quantum interference and excitonic effects in the Raman spectra of single and triple-layer $MoTe_2$. We compare our simulations with experimental results, explaining the dependence of the Raman intensities on the excitation energy. We demonstrate that the two approaches are formally and numerically equivalent in the adiabatic limit. In addition, the second approach allows to include the dynamical effects and captures a shift of the intensities with respect to the adiabatic case. This method is also more computationally efficient and is extended to include temperature effects using many-body perturbation theory. We have implemented both of these methods in a software package with interfaces to open source *ab initio* codes. Furthermore, we have developed web based tools to visualize excitonic states and phonon modes.

List of Publications

Journal Articles

- Michael Endlich, Henrique P. C. Miranda, Alejandro Molina-Sánchez, Ludger Wirtz, and Jörg Kröger 2014 *"Moiré-Induced Replica of Graphene Phonons on Ir(111)"* Annalen der Physik 526(9–10): 372–380.
- Jing Li, Henrique P. C. Miranda, Yann-Michel Niquet, Luigi Genovese, Ivan Duchemin, Ludger Wirtz, Christophe Delerue 2015 *"Phonon-Limited Carrier Mobility and Resistivity from Carbon Nanotubes to Graphene"* Physical Review B 92(7): 75414.
- Thomas Galvani, Fulvio Paleari, Henrique P. C. Miranda, Alejandro Molina-Sánchez, Ludger Wirtz, Sylvain Latil, Hakim Amara, François Ducastelle 2016 *"Excitons in Boron Nitride Single Layer"* Physical Review B 94(12): 125303.
- Henrique P. C. Miranda, Sven Reichardt, Guillaume Froehlicher, Alejandro Molina-Sánchez, Stéphane Berciaud, Ludger Wirtz 2017 *"Quantum Interference Effects in Resonant Raman Spectroscopy of Single- and Triple-Layer MoTe2 from First-Principles"* Nano Letters 17(4): 2381–2388.
- Henrique P. C. Miranda, Sven Reichardt, Alejandro Molina-Sánchez, Ludger Wirtz *"First-principles calculation of Raman in MoS2 from a perturbative approach"*, in preparation
- Henrique P. C. Miranda, Ludger, Wirtz *"Phonon visualization website"*, in preparation

Developed tools

- YamboPy:
  `https://github.com/henriquemiranda/yambopy`
- Phonon visualization website:
  `http://henriquemiranda.github.io/phononwebsite/`
- Exciton visualization website:
  `http://henriquemiranda.github.io/excitonwebsite/`
- SLEPC to diagonalize the BSE Hamiltonian in the Yambo Code
  `https://github.com/yambo-code`

Oral presentations at conferences

- TMCS IV, *"Semi-empirical phonon calculations for graphene on Ir(111)"*, 22nd - 24th Jan 2014
- APS March Meeting 2016, *"Resonant-Raman Intensities of N-layer Transition Metal Dichalcogenides from First Principles"*, 14-18th March, 2016 Baltimore, MD
- APS March Meeting 2017, *"Ab initio calculation of resonant Raman intensities of Transition Metal Dichalcogenides"*, 13-17th March, 2017 New Orleans, LA

Posters presentations at conferences

- DPG Meeting 2014, *"Semi-empirical phonon calculations for graphene on different substrates"*, 30th March - 4th April at the University of Dresden, Germany
- Euro-TMCS I - Theory, Modelling and Computational Methods for Semiconductors, *"A force-constant model of graphene for conductivity calculations"*, 28 - 30th Jan 2015 at the University of Granada, Spain

- PSI-K - 2015 Conference, *"Electronic and Vibrational proprieties of graphene on Ir(111) and SiC(100)"*, 6 - 10th September 2015 in Donostia, San Sebastian, Spain

- Total Energy and Force Methods Workshop 2016, *"Raman Intensities of N-layer Transition Metal Dichalcogenides from First Principles"*, 11-13th January 2016, Luxembourg, Luxembourg

Contents

0

Introduction

0.1 Raman spectroscopy of 2D materials

The ability to build smaller and smaller devices stimulates the search for new materials at the nanoscale with optimal electronic and optical properties. Low-dimensional materials are a strong focus of this quest.

Layered materials are extended crystalline solids held together by strong in-plane covalent bonds and weaker out-of-plane forces. The latter are mostly van der Waals forces and can be broken by exfoliation as was demonstrated by extracting single graphene layers from graphite [1, 2]. For this finding as well as the demonstration of the potential of graphene for use in various applications, A. Geim and K. Novoselov were awarded the Nobel prize in physics in 2010. Although 2D materials have been known and used since a long time mostly as dry lubricants [3], only more recently, with this discovery, the investigation for possible nanotechnological applications has started. Graphene, however, is not the most suitable material for all types of applications. For example, its zero band gap limits its use as a semiconductor. Fortunately the family of 2D materials is wide and varied as shown in Fig. 1. One can find insulators like hexagonal boron nitride (hBN) with a band gap exceeding 6 eV and typical semiconductors such as the transition-metal dichalcogenides (TMDs). The later show great potential for semiconductor applications due to

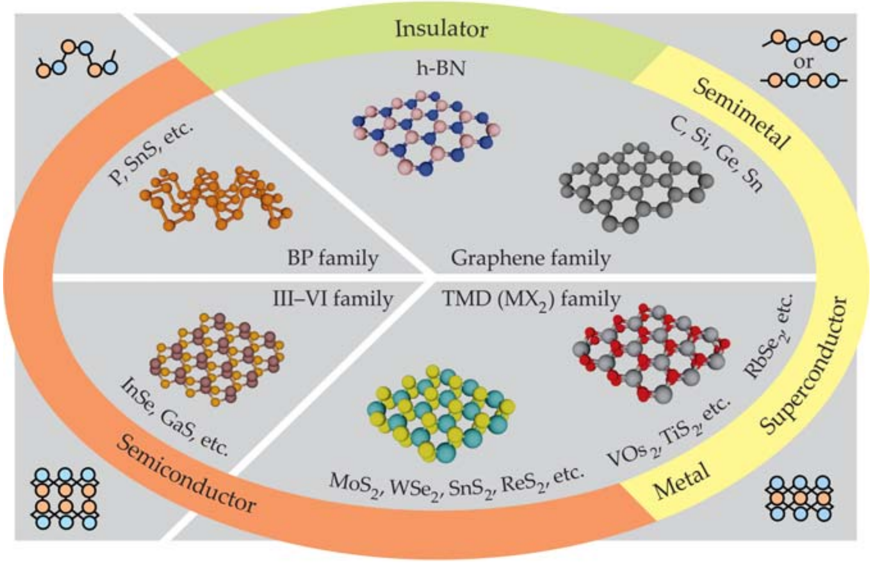

Figure 1: The world of 2D materials includes graphene and its analogues, such as hexagonal boron nitride; black phosphorus (BP) and its analogues; the III–VI family of semiconductors; and the transition-metal dichalcogenides (TMDs). Together they span the full range of electronic properties. The four corner diagrams show the materials' cross-sectional structures most of which are not strictly planar. Figure taken from [4]

their good intrinsic properties like high electronic mobility and optical gaps in the visible range (from 0.5 to 3 eV) [4]. A few applications demonstrated so far include the fabrication of transistors [5], solar cells [6], memories, and optoelectronic devices [7].

To develop these new devices it is fundamental to choose the best material possible. This requires the characterization of its properties or how those can be tuned. One can finely tune the properties by stacking different layers together [8, 9], applying strain [10] or an electric field. When modifying the material, it is essential to monitor how its properties change with the applied modification using non-invasive and precise characterization techniques.

One of the most widely known of such techniques is Raman spectroscopy. It has been extensively used in the search and optimization of 2D materials [11]. The technique was first demonstrated in 1928 by C. V. Raman and his

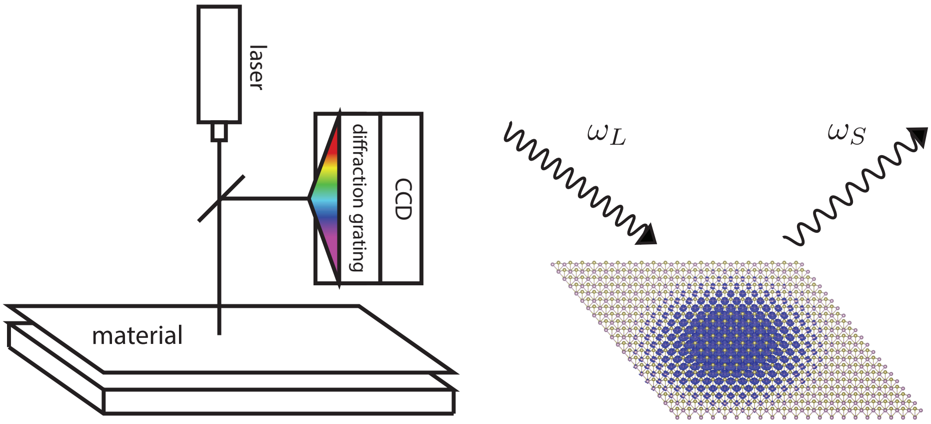

Figure 2: Schematic representation of a Raman experiment. The light scattered in the material is diffracted and detected by the CCD (left). The light scattered by the material loses energy to excitations in the material (right).

student K. S. Krishnan on liquids [12], for which they received the Nobel Prize in Physics in 1930, although the effect was previously theoretically predicted by Adolf Smekal [13]. A modern Raman experiment consists of shining a laser on the material and detect the inelastically scattered light using a diffraction grating and a charge-coupled device (CCD), as schematically shown in Fig. 2.

When the incident light interacts with the material, part of it is elastically scattered, leading to a peak in the scattered light spectra at the energy of the incident laser. Another part loses energy in the material and the spectra shows peaks shifted by the energies of the excitations with respect to the elastic peak. These excitations can be phonons [14, 15], excitons [16] or magnons [17], among others. The intensities of the corresponding peaks are related to the strength of the coupling with the laser light. The change of the Raman intensities as a function of incident laser light energy contains information about the optical properties, like the optical gap, the exciton-photon and exciton-phonon coupling [18]. Raman spectroscopy is thus a very complete technique, providing information about electronic, vibrational and optical properties in a single experiment. Raman is frequently used to investigate 2D materials. In the case of graphene, it gives information on the number of layers, the underlying substrate, the quality of sample (defects), on the doping and strain [19].

For TMDs it has also been used to determine the number of layers via the difference between the A_1' (A_{1g}) and E' (E_g) modes for odd (even) number of layers [20, 21, 22]. It has been used to investigate excitonic effects in up to three layers and bulk MoS_2 [18]. More recently, the Davydov splitting of diverse phonon modes was experimentally measured using Raman spectroscopy [23, 24, 25, 26]. In this case a strong dependance of the Raman intensities with laser energy is reported but not understood from experimental data alone.

An essential complement to experiments is their simulation from a theoretical point of view. With the improvement of computational power and algorithms in the last decades, it has become possible to calculate (to a good approximation) many experimental quantities like lattice parameters, phonon modes, optical response or electronic conductivity. The description of these has been the motivation of a big effort in the community of solid-state physics and theoretical spectroscopy over the last 50 years. In particular, the theory of Raman scattering has been described in previous works using perturbation theory [15, 27, 28, 29, 30]. In these approaches, the Raman intensities are calculated in terms of the electron and phonon dispersions as well as electron-phonon and electron-light coupling matrix elements. This accounts for many effects observed in the experiments like the laser energy dependence of the intensities and Stokes shift due to the phonon excitation. In practical calculations, however, these works mostly relied on semi-empirical models like tight-binding or **k**.**p** to obtain the necessary quantities. These methods have the drawback that they require *a priori* knowledge about the material.

Ab initio methods, can be directly applied to a wide variety of materials without the need of parametrization. However, most standard *ab initio* implementations to calculate Raman intensities available today are limited to the non-resonant regime and the adiabatic phonon limit [31, 32]. Recently, a method based on finite differences of the dynamic dielectric susceptibility with respect to the atomic positions was demonstrated in silicon [33] and TMDs [34]. This method relies entirely on first-principles methods and correctly describes the laser energy dependence of the intensities. We will apply this method to study the evolution of the Raman intensities with laser energy for single- and triple-layer $MoTe_2$. The interest in this particular system stems from the experimental observation of a strong dependence of the Raman intensities of the A_1' modes with number of layers and laser energy as we will show in Chapter 5. We compare our calculation results with experimental data, with good agreement and most importantly we explain it in terms of quantum interference effects. Using this approach we unravel the role of excitonic effects and selection rules in the Raman intensities. This constitutes the main outcome of our previous publication (Ref. [35]) and of the present thesis. The main advantage of this approach is that excitonic effects are easily included in the Raman spectra using the implementations available to calculate excitonic effects on the level of many-body perturbation theory (Bethe-Salpeter equation). Its drawback is that many electronic band structure and exciton calculations are required to obtain the Raman intensities for the different phonon modes. Furthermore, relying on static finite differences, it does not capture dynamical effects of phonons.

To overcome these problems, we propose an approach using perturbation theory and matrix elements calculated from first-principles. We show that this method correctly reduces to the static finite differences in the adiabatic phonon limit but allows to go beyond it incorporating the dynamical effects of phonons. Moreover, temperature effects can also be included in the calculations. This method constitutes the second main outcome of the present work. It allows us to calculate in a computationally very efficient manner the one-phonon resonant Raman response. While we have tested this approach for layered materials, its applicability is much more general. We also outline an approach to express the derivative of the susceptibility including excitonic effects in terms of electron-phonon matrix elements. This will allow to calculate the Raman tensor at a much lower computational cost avoiding to use finite differences.

To run the calculations and interpret the results, we have developed in the course of this thesis a series of tools that have a broad range of applicability. To visualize phonons and excitons we developed two web-based visualization tools. We also improved the work-flow for running the calculations by creating a set of automatization scripts in a new `Python` project called `yambopy`. Since this work required diagonalization of large excitonic Hamiltonians, we implemented in the `yambo` code an interface using the SLEPC library that allows us to obtain excitonic eigenvalues and eigenvectors using an iterative procedure. This enables us to obtain selected excitonic states in large systems at a much smaller computational cost.

0.2 Outline of the thesis

The calculation of Raman spectra from first-principles requires to combine many state of the art computational electronic structure methods. This thesis is organized according to the different ingredients needed for the calculations as shown in Fig. 3.

In the first Chapter we write the Hamiltonian describing the system at the microscopic level. To solve this Hamiltonian as a whole is a daunting task and in practice many approximations have to be employed. The first one is the Born-Oppenheimer approximation that allows us to treat the movement of the electrons and nuclei separately. We describe this approximation, along with the density functional theory and the GW methods used to calculate the electronic energies and wave functions in Chapter 1. In Chapter 2 we describe the vibration of the ions in the lattice in terms of phonon modes. For that we write the equations of motion using force constants which we calculate from first-principles using density functional perturbation theory. In Chapter 3 we incorporate perturbatively the effects of the lattice vibrations on the electronic structure leading to two important effects: the band gap renormalization and a finite lifetime for the electrons and holes in a given state. We show how the material interacts with light in Chapter 4 and how excitons are formed. In Chapter 5 we combine the methods described in Chapters 1, 2, and 4 to obtain the Raman intensities for $MoTe_2$ using the static finite differences approach. Finally in Chapter 6 we combine the ingredients obtained in all the previous chapters to calculate the resonant Raman intensities of MoS_2 using a perturba-

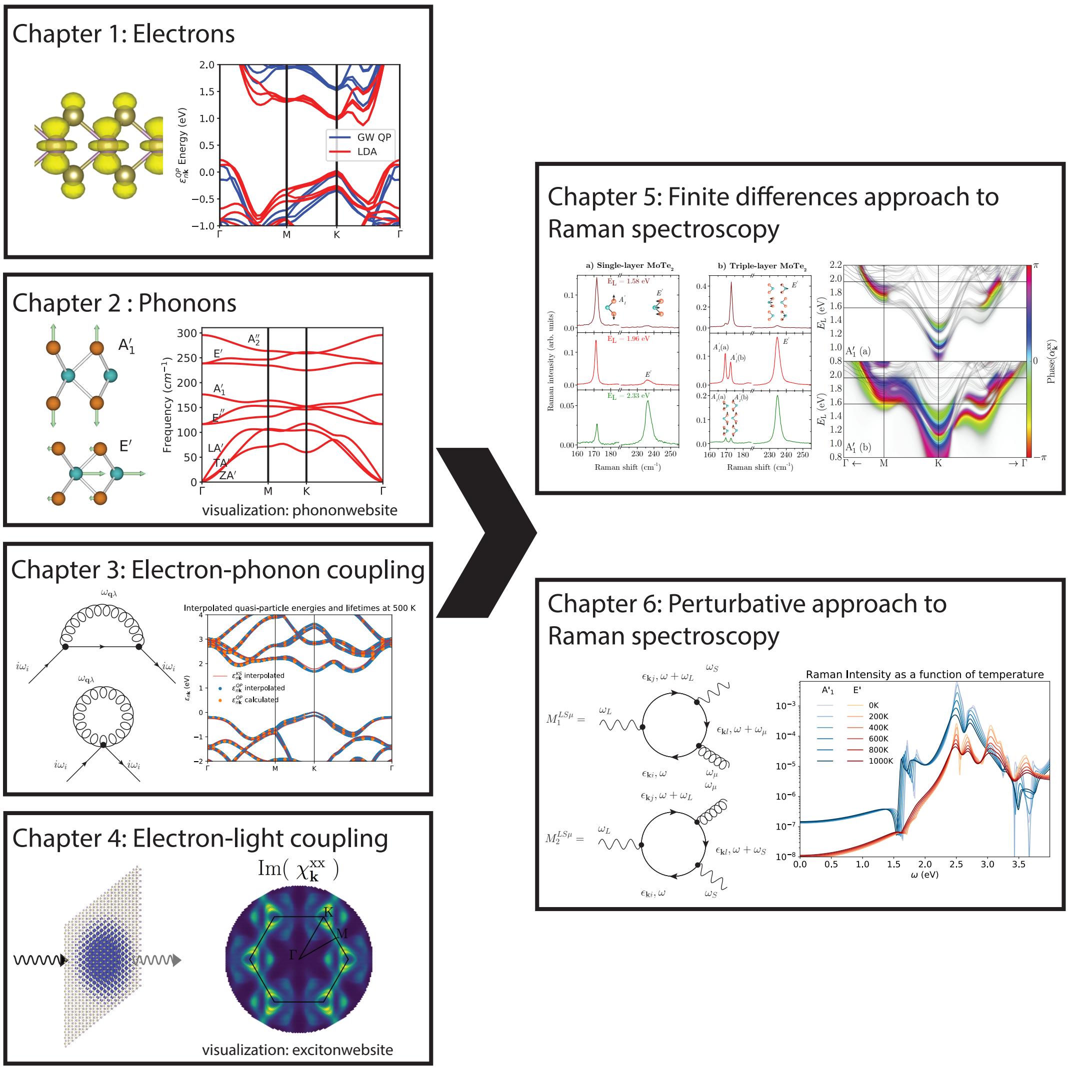

Figure 3: Outline of the thesis in figures. We start by individually describing all the ingredients needed for the calculation of the Raman susceptibilities in the finite differences and perturbative approaches.

tive approach.

In Appendix A we describe the newly developed tools for automatization of the calculations. We then describe the web-based tools to visualize phonons and excitons in Appendix B. In Appendix C we analytically show the equivalence between the finite differences and and the diagrammatic calculations.

1

Electrons: Screening effects in 2D materials

The starting point to predict the properties of a material is the description of the movement of the electrons in the potential created by the nuclei. The Hamiltonian of the system of electrons and nuclei interacting through the Coulomb force is [36]

$$
\begin{aligned}
\hat{H} =& \hat{H}_e + \hat{H}_n + \hat{H}_{\mathrm{e-n}} \\
\hat{H} =& -\sum_i \frac{\hbar^2}{2m_e}\nabla_i^2 + \frac{1}{2}\sum_{i\neq j}\frac{e^2}{\mathbf{r}_i - \mathbf{r}_j} \\
& -\sum_I \frac{\hbar^2}{2M_I}\nabla_I^2 + \frac{1}{2}\sum_{I\neq J}\frac{Z_I Z_J e^2}{|\mathbf{R}_I - \mathbf{R}_J|} \\
& -\sum_{i,I}\frac{Z_I e^2}{|\mathbf{r}_i - \mathbf{R}_I|}
\end{aligned}
\tag{1.1}
$$

where m_e is the mass of the electron, M_I the mass of the nuclei, Z_I the charges of the nuclei and $\mathbf{r}$ is the position of the electrons $\mathbf{R}$ of the nuclei. The lower case indices refer to electrons and upper case to the nuclei.

This Hamiltonian is exact in the non-relativistic case, and its eigenvalues and eigenfunction yield all the information about the many-body (MB) system.

The issue is that, although we can formulate the problem and implement it on a computer, it cannot be solved for systems of more than a few electrons and nuclei. In order to describe the interacting wave function of the system we have to store all the possible Slater determinants [37, Section 1.2]. This requires huge amounts of memory and computational power. To overcome this difficulty, we have to do approximations and simplify the problem to a more manageable one.

A first approximation is done by verifying that the kinetic terms involving the inverse masses of the atomic nuclei M_I^{-1} are much smaller than the ones involving the inverse of the electron mass m_e^{-1}. This approximation allows us to decouple the electronic and nuclear part of the Hamiltonian. We speak of the so-called *Born-Oppenheimer approximation* (BOA) which is widely used in Quantum Chemistry and Condensed Matter Physics.

Even though it relies on expanding the motion of the nuclei around their equilibrium positions, this simplification allows to obtain the vibrational modes ($\hat{H}_n$ term) of the nuclei and their coupling with the electronic states ($\hat{H}_{\mathrm{e-n}}$ term) in the adiabatic phonon limit.

Within the BOA we can focus on the Hamiltonian describing the electronic states

$$\hat{H}_e = -\frac{\hbar}{2m_e}\sum_i \nabla_i^2 - \sum_{i,I}\frac{Z_I e^2}{|\mathbf{r}_i - \mathbf{R}_I|} + \frac{1}{2}\sum_{i\neq j}\frac{e^2}{\mathbf{r}_i - \mathbf{r}_j} \tag{1.2}$$

Although simpler, this Hamiltonian still cannot be solved exactly for systems with more than a few electrons. There are, however, multiple approaches to solve it approximately and gradually increase the accuracy of the results by doing more complex computations. Here we will introduce an approach that combines density functional theory (DFT) as a starting point for a many-body perturbation theory calculation (MBPT). In density functional theory, the many-body system is mapped onto a system of independent particles that is solved self-consistently. The resulting wave functions serve as the basis for the MBPT calculation that recovers the many-body character of the system. This approach has the advantage of never having to deal with the full many-body wave function, yet recovering the physical observables with high accuracy. The treatment of the many-body perturbation theory can indeed be made exact as long as the system is treated self-consistently at the MBPT level using Hedin's equations [1].

1.1 Density functional theory

DFT is one of the most widely used approaches for computational simulation of Condensed Matter systems. Here we will outline the basic principles and refer to the literature when appropriate [36, 39].

The advantage of using DFT stems from its ability to make accurate first-principles ground-state calculations computationally efficient. It does so by re-casting the problem of solving the complicated many-body problem into one of solving a group of independent particles self-consistently [40, 41]. Most of the many-body effects are accounted for in a term which is unknown in principle but for which approximate expressions exist.

The different aspects of the description of the material (electrons, phonons, etc) and their interaction with light is described within the DFT framework. In DFT we describe the system of electrons based on their charge density $n(\mathbf{r})$. The total energy is written as a functional of $n(\mathbf{r})$ [42]

$$E(\{\mathbf{R}_0\}) = T[n(\mathbf{r})] + E_{\mathrm{Hartree}}[n(\mathbf{r})] + E_{xc}[n(\mathbf{r})] + E_{\mathrm{en}}[n(\mathbf{r})] + E_n(\{\mathbf{R}_0\}), \quad (1.3)$$

where $T[n(\mathbf{r})]$ is the kinetic energy of the system with ground-state defined by the charge density $n(\mathbf{r})$, and $E_{xc}[n(\mathbf{r})]$ is the *exchange-correlation* energy which for now is only a term that captures all the interactions not captured by the other terms. $E_{en}(\mathbf{r})$ is energy of the interaction between electrons and nuclei, $\{\mathbf{R}_0\}$ represents the positions of all the nuclei in the system frozen at given coordinates (as prescribed by the BOA) and $E_n(\{\mathbf{R}_0\})$ is the Coulomb repulsion between the nuclei.

---

[1] The derivation of Hedin's equations is found in the original paper [38]. It is also extensively discussed in the literature [37]

The $E_{\text{Hartree}}[n(\mathbf{r})]$ and $E_{\text{en}}[n(\mathbf{r})]$ terms are

$$\begin{aligned} E_{\text{Hartree}}[n(\mathbf{r})] =& \frac{e^2}{2}\int \frac{n(\mathbf{r})n(\mathbf{r}')}{|\mathbf{r}-\mathbf{r}'|}d^3\mathbf{r}d^3\mathbf{r}', && (1.4)\\ E_{\text{en}}[n(\mathbf{r})] =& \int V_{en}(\mathbf{r})n(\mathbf{r})d^3\mathbf{r}, && (1.5) \end{aligned}$$

with $V_{en}(\mathbf{r})$ given by

$$V_{en}(\mathbf{r}) = -\sum_I \frac{Z_I e^2}{|\mathbf{r}-\mathbf{R}_I|}, \tag{1.6}$$

where Z_I is the nuclear charge and $\mathbf{R}_I$ the position of the nuclei (consistent with Eq. (1.1)). Note that $V_{en}(\mathbf{r})$ parametrically depends on all the positions of the ions in the system.

With functionals for the kinetic $T[n(\mathbf{r})]$ and *exchange-correlation* $E_{xc}[n(\mathbf{r})]$ energies we can minimize Eq. (1.3) to obtain the charge density $n(\mathbf{r})$. One possibility for the parametrization of $T[n(\mathbf{r})]$ functional is the Thomas-Fermi model. This, however, is not very accurate for most physical systems of interest as it is based on the homogeneous electron gas. A solution to this problem was proposed by Kohn and Sham and consists of introducing an *ansatz* [36] of independent electronic wave functions. In this basis, the kinetic energy $T[n(\mathbf{r})]$ is calculated using the Laplace operator

$$\begin{aligned} T[n(\mathbf{r})] =& -\frac{\hbar^2}{2m_e}\sum_{n=1}^{N}\langle\psi_n|\nabla^2|\psi_n\rangle\,, \\ \langle\psi_n|\nabla^2|\psi_n\rangle =& \int \psi_n^*(\mathbf{r})\nabla_{\mathbf{r}}^2\psi_n(\mathbf{r})d^3\mathbf{r}, \end{aligned}\quad, \tag{1.7}$$

and the charge density as the sum of the modulus square of the wave functions

$$n(\mathbf{r}) = \sum_{n=1}^{N}|\psi_n(\mathbf{r})|^2, \tag{1.8}$$

where N is the number of electrons. This approach requires that the wave functions $\psi_n(\mathbf{r})$ (Eq. (1.7)) and the charge density $n(\mathbf{r})$ (Eq. (1.8)) are calculated

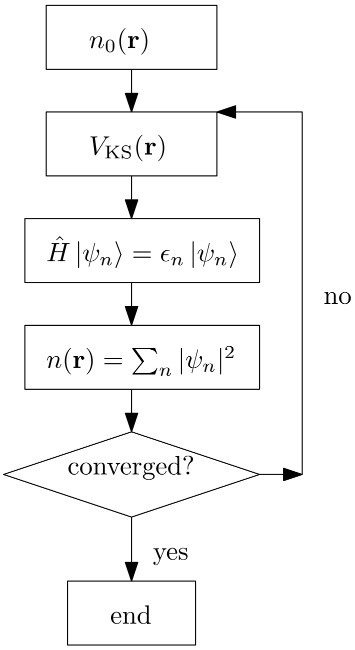

Figure 1.1: Flow of a self-consistent DFT calculation in the Kohn-Sham scheme. Figure adapted from [39, Chapter 6]

self-consistently as shown in Fig. 1.1. This in turn, implies the determination of the wave functions at each step by solving the eigenvalue problem

$$\hat{H}_{\mathrm{KS}}\left|\psi_n\right\rangle = \epsilon_n \left|\psi_n\right\rangle, \tag{1.9}$$

where n is an index to distinguish the independent particle states, $\psi_n(\mathbf{r})$, and ϵ_n their energies. The Hamiltonian is

$$\hat{H}_{\mathrm{KS}} = -\frac{\hbar}{2m_e}\nabla_{\mathbf{r}}^2 + V_{\mathrm{KS}}(\mathbf{r}), \tag{1.10}$$

with the Kohn-Sham potential given by

$$V_{\mathrm{KS}}(\mathbf{r}) = V_{en}(\mathbf{r}) + V_{\mathrm{Hartree}}(\mathbf{r}) + V_{\mathrm{xc}}(\mathbf{r}), \tag{1.11}$$

$$V_{\mathrm{Hartree}}(\mathbf{r}) = \frac{\delta E_{\mathrm{Hartree}}}{\delta n(\mathbf{r})}, \tag{1.12}$$

$$V_{\mathrm{xc}}(\mathbf{r}) = \frac{\delta E_{\mathrm{xc}}}{\delta n(\mathbf{r})}. \tag{1.13}$$

were $\frac{\delta E}{\delta n(\mathbf{r})}$ is the functional derivative with respect to the density. H_{KS} is a functional of the density, hence to obtain the independent-particle states, an initial guess for the density $n_0(\mathbf{r})$ is required.

The *exchange-correlation* term captures the difference in energy between the exact kinetic energy and the independent particle kinetic energy plus the difference between the exact interaction energy and the Hartree approximation and is a functional of the charge density [37]. The first approximation to the *exchange-correlation* functional was the local-density approximation (LDA) where the effects of exchange and correlation are assumed to be the same as in a system of a homogeneous electron gas. This assumption allows one to write the exchange term with a simple analytic form and to calculate the correlation energy with great accuracy using Monte-Carlo methods [43]. This approach has turned out to be accurate for solids and is still widely used due to its efficiency and simplicity and good performance. This approximation, however was not so successful in molecules where the charge density is in general more localized than in the case of solids. To overcome this issue, the generalized gradient approximations (GGAs) were introduced [44]. In these type of functionals, the *exchange-correlation* terms depend not only on the charge density but also on its gradients.

The “true” form of the exchange-correlation functional depends on the solution of the full many-body problem. This formulation is however not practical, as we want to avoid to calculate the full many-body system. Different approximations for the determination of this functional exist [45], some based on physical principles (like the LDA), others are built to reproduce experimental results for certain systems. As calculations with more accurate and exact methods become feasible, it will become possible to converge closer and closer to the “true” *exchange-correlation* functional with different methods and approaches, for example using machine learning [46].

From the auxiliary system in Eq. (1.9) we define a self-consistent set of equations to obtain the charge density $n(\mathbf{r})$ and wave functions $\psi_n(\mathbf{r})$ of the ground state. These are the so-called Kohn-Sham equations [36]. It is important to remark that DFT describes the ground state only and as such, to calculate electronic and optical gaps, we need to go beyond it in the theoretical description as we will show in Sec. 1.2.

So far we have not specified the basis we will use to expand the wave functions. The most commonly used for solids is the plane-wave basis set. Plane-waves are particularly useful for allowing us to systematically increase the size of the basis and consequently the accuracy of the calculation. Additionally it offers the advantage of having simple Fourier transformations that are particularly useful to evaluate certain integrals. This choice is also appropriate to describe delocalized electrons[1] as the plane-waves are inherently delocalized. Another possible basis set is the one of atomic orbitals localized around the atoms [47, 48]. A hybrid between localized orbitals and plane-waves are the wavelets basis set [49]. Many other choices of basis set exist [36], but we will not discuss them here.

In periodic systems we can define Bloch states (**k**-dependent). The wave functions of the system are determined by diagonalizing the Hamiltonian in reciprocal space

$$\hat{H} \left| \psi_{n\mathbf{k}} \right\rangle = \epsilon_{n\mathbf{k}} \left| \psi_{n\mathbf{k}} \right\rangle , \tag{1.14}$$

where $\left| \psi_{n\mathbf{k}} \right\rangle$ are the eigenstates of the electrons and $\epsilon_{n\mathbf{k}}$ the eigenvalues. These eigenvalues and eigenstates describe the system as a first approximation and provide a convenient basis set to be used in perturbative methods. These methods allow us to recover the many-body character of the system and will be described in the next section.

---

[1] In general the electrons in the valence bands are localized near the ionic positions, and are responsible for the chemical bonding of the system. The conduction electrons are, however, more delocalized. It might seem contradictory to use a ground-state theory to describe delocalized conduction electrons. However, as we will show in Sec. 1.2, we are not looking for exact solutions at this point.

1.2 Many-body perturbation theory

In this section we will present the basic topics of many-body perturbation theory (MBPT). MBPT consists in treating the complicated many-body interactions in a perturbative way starting from an approximate solution[1]. The advantage is that we can avoid calculating the complicated MB wave function and instead calculate only the quantities of interest. The topics introduced here are extensively discussed in the literature [50, 51, 52], and we will show only a brief introduction from a practical perspective. These methods will be applied to improve the description of the MB system and its optical response. The first correction, the Hartree-Fock and GW methods which we describe in Section 1.2.3 allows us to overcome some of the issues of using approximate functionals for the *exchange-correlation* $E_{xc}[n(\mathbf{r})]$ in Eq. (1.3).

1.2.1 Second quantization

We start by introducing the concept of second quantization[2] which we will use throughout different chapters of this manuscript. In second quantization, we define *creation* and *annihilation* operators for the particles in the system. These operators “create” or “annihilate” electrons in the system (we start with a zero-particle state $|0\rangle$)

$$\hat{c}_n |0\rangle = 0, \qquad\qquad \hat{c}_n^\dagger |0\rangle = |n\rangle . \tag{1.15}$$

Since we will be dealing with a system in the ground-state, we can define the vacuum as a state made with all the electrons in the valence bands. In this formalism we distinguish two different types of operators acting on the electrons

---

[1] A typical starting point are the Kohn-Sham wave functions obtained from DFT.

[2] The topic of second quantization is treated in more detail in references [50, Chapter 7], [51, Chapter 1] and [52, Section 1.2]

($\hat{c}_c$ and $\hat{c}_c^\dagger$) and holes ($\hat{c}_v$ and $\hat{c}_v^\dagger$):

$$\hat{c}_c \left|0\right\rangle = 0, \qquad \hat{c}_c^\dagger \left|0\right\rangle = \left|c\right\rangle, \tag{1.16}$$

$$\hat{c}_v \left|0\right\rangle = 0, \qquad \hat{c}_v^\dagger \left|0\right\rangle = \left|v\right\rangle. \tag{1.17}$$

These operators for electrons and holes obey certain commutation relations that ensure that the MB wave function retains the correct symmetry properties

$$\{\hat{c}_c, \hat{c}_v\} = 0, \qquad \left\{\hat{c}_c^\dagger, \hat{c}_v^\dagger\right\} = 0, \qquad \left\{\hat{c}_c, \hat{c}_v^\dagger\right\} = \delta_{cv} \tag{1.18}$$

where $\{\hat{a}, \hat{b}\} = \hat{a}\hat{b} + \hat{b}\hat{a}$ is the anti-commutator for fermions. An advantage of these definitions is that all the operators acting on the MB system are expressed in terms of "creation" and "annihilation" operators and the matrix elements of the interaction terms.

1.2.2 Green's functions

1.2.2.1 Zero temperature

Another important tool in the language of many-body perturbation theory are the Green's functions. These functions describe the propagation of single particles governed by the full many-body Hamiltonian.[1] This will allow us to perturbatively include interaction terms using the Feynman diagrammatic techniques. We will outline here the main concepts that will be needed in the next chapters. Mathematically, (at zero temperature) the *time-ordered* or *causal* one-particle Green's function is given by [50, Chapter 9]

$$G_{\mathbf{k}}(t_2 - t_1) = -i \left\langle \Psi_0 \middle| T\{\hat{c}_{\mathbf{k}}(t_2)\hat{c}_{\mathbf{k}}^\dagger(t_1)\} \middle| \Psi_0 \right\rangle, \tag{1.19}$$

where Ψ_0 is the exact normalized wave function of the interacting N-particle system. The operators $\hat{c}_{\mathbf{k}}(t)$ and $\hat{c}_{\mathbf{k}}^\dagger(t)$ destroy and create a particle in state with momentum $\mathbf{k}$ (the band index is omitted for simplicity) at time t respectively.

---

[1] A pictorial representation of the interpretation of what is a Green's function is given in [50, Chapters 1,2 and 3]. A more formal description is done in [50, Chapters 9]

Their time evolution is given in the Heisenberg picture

$$\hat{c}^{\dagger}_{\mathbf{k}}(t_1) = e^{i\hat{H}t_1}\hat{c}^{\dagger}_{\mathbf{k}}e^{-i\hat{H}t_1}, \tag{1.20}$$

$$\hat{c}_{\mathbf{k}}(t_2) = e^{i\hat{H}t_2}\hat{c}_{\mathbf{k}}e^{-i\hat{H}t_2}, \tag{1.21}$$

where $\hat{H}$ is the Hamiltonian of the fully interacting system. The T operator is the Wick time-ordering operator and when acting on the time-dependent operators permutes them so that the time in which they act is decreasing from left to right. In the case of fermions, it multiplies them by a factor $(-1)^P$ where P is the number of permutations needed to make the operators time-ordered. Wick's theorem allows us to evaluate matrix elements of the interacting system by permuting the operators acting at different times and generating the different terms. A detailed explanation of Wick's theorem can be found in Ref. [50, Appendix F]. These different terms are them added up in a perturbative series. An alternative way to find these different terms is by the Feynman diagrammatic technique.

The Green's function of the system can be written as two separate branches as in Ref. [50, Eq. 9.5])

$$G_{\mathbf{k}}(t_1 - t_2) = \begin{cases} -i\left\langle \Psi_0 | \hat{c}_{\mathbf{k}}(t_2)\hat{c}^{\dagger}_{\mathbf{k}}(t_1) | \Psi_0 \right\rangle, & t_2 > t_1, \\ +i\left\langle \Psi_0 | \hat{c}^{\dagger}_{\mathbf{k}}(t_1)\hat{c}_{\mathbf{k}}(t_2) | \Psi_0 \right\rangle, & t_2 < t_1. \end{cases} \tag{1.22}$$

The *independent particle* Green's function is given by

$$G^{(0)}_{\mathbf{k}}(t_1 - t_2) = \begin{cases} -i\theta(\epsilon_{\mathbf{k}} - \epsilon_F)e^{-i\epsilon_{\mathbf{k}}(t_2 - t_1)/\hbar}, & t_2 > t_1, \\ +i\theta(\epsilon_F - \epsilon_{\mathbf{k}})e^{-i\epsilon_{\mathbf{k}}(t_2 - t_1)/\hbar}, & t_2 < t_1, \end{cases} \tag{1.23}$$

where ϵ_F is the Fermi level and $\theta(t)$ is the Heaviside step-function, defined as

$$\theta(t) = \begin{cases} 1, & t > 0, \\ 0, & t < 0. \end{cases} \tag{1.24}$$

The Fourier representation of the independent particle Green's function becomes

$$G^{(0)}_{\mathbf{k}}(\omega) = \frac{\theta(\epsilon_F - \epsilon_{\mathbf{k}})}{\omega - \epsilon_{\mathbf{k}} - i\delta} + \frac{\theta(\epsilon_{\mathbf{k}} - \epsilon_F)}{\omega - \epsilon_{\mathbf{k}} + i\delta}. \tag{1.25}$$

were $idelta$ is an infinitesimal quantity [50, Appendix I].

1.2.2.2 Finite temperature

In the finite temperature case the expectation value of any operator is defined as [50, Chapter 14]

$$\rho = e^{-\beta(\hat{H}-\mu N)}, \tag{1.26}$$

$$\langle \hat{O} \rangle = \frac{Tr\{\hat{O}\rho\}}{Tr\{\rho\}}, \tag{1.27}$$

where ρ is the "grand distribution function" and Z is the "grand partition function". The finite temperature Green's functions is then given by

$$G^T_{\mathbf{k}}(t_1 - t_2) = -i \left\langle T\{\hat{c}_{\mathbf{k}}(t_2)\hat{c}^\dagger_{\mathbf{k}}(t_1)\}\right\rangle, \tag{1.28}$$

$$= -i\frac{Tr[T\{\hat{c}_{\mathbf{k}}(t_2)\hat{c}^\dagger_{\mathbf{k}}(t_1)\}\rho]}{Tr\{\rho\}}. \tag{1.29}$$

The *independent particle* Green's function at finite temperature is given by

$$G^T_{\mathbf{k}}(t_1 - t_2) = \begin{cases} -ie^{-i\epsilon_{\mathbf{k}}(t_2-t_1)/\hbar}[f(\epsilon_{\mathbf{k}})], & t_2 > t_1, \\ +ie^{-i\epsilon_{\mathbf{k}}(t_2-t_1)/\hbar}[1 - f(\epsilon_{\mathbf{k}})], & t_2 < t_1. \end{cases} \tag{1.30}$$

where f is the Fermi-Dirac distribution $f(\epsilon_{\mathbf{k}}) = (1 + e^{\epsilon_{n\mathbf{k}}/k_bT})^{-1}$

The Fourier representation of the Green's function is then given by [53, Eq. 4.5]

$$G_{\mathbf{k}}(\omega) = \frac{f(\epsilon_{\mathbf{k}})}{\omega - \epsilon_{\mathbf{k}} - i\delta} + \frac{1 - f(\epsilon_{\mathbf{k}})}{\omega - \epsilon_{\mathbf{k}} + i\delta} \quad , \tag{1.31}$$

where we have omitted the band index.

To expand G^T in terms of Feynman diagrams one has to use the imaginary time Green's function [50, Chapter 14]. In these, the time variable is replaced by an imaginary time $it \to \tau$ in what is known as the Matsubara formalism. This allows us to use the Feynman diagrammatic expansions, including temperature in the electrons and Bosons. The Green's function for the electrons in this case is written as

$$\mathcal{G}^0_{\mathbf{k}}(i\omega) = \frac{1}{i\omega - \epsilon_{\mathbf{k}}}. \tag{1.32}$$

We will use this to obtain the temperature dependent electron self-energy in Chapter 3 and the temperature-dependent independent-particle dielectric polarizability in Chapter 4.

1.2.3 From Hartree-Fock to GW

Here we outline the idea of the MBPT approach with DFT as a starting point. To do so we consider two examples: the Hartree-Fock (HF) and the GW approximations[1]. The idea of applying MBPT with DFT as a starting point is that DFT yields results very close to the full solution, and hence the MB interactions can be treated perturbatively. These perturbations also change the purely independent particle character of the electrons in the system to what is normally known as *quasi-particles* (QP). A QP is, simply put, a particle moving in the many-body system while interacting with it. We can think of it as a ship moving in the sea feeling the effect of the waves while producing its own waves.[2] This description has the advantage that we never deal with all the ships and all the waves at the same time (the MB wave function). This picture is of course only valid in case the many-body effects are weak and the behav-

---

[1] More information about the HF method can be found in [37, Section 4.1] and [50, Section 4.7]. The GW method is discussed in [37, Section 11] and [54]

[2] A precedent analogy is made in Ref. [50, Chapter 0] where a particle is compared to a horse and the *quasi-particle* to the horse plus the "dust cloud kicked up by a galloping horse in a western".

ior with respect to the independent particle picture does not change much. It offers the advantage that the different interactions can be treated separately according to how strong they are. This idea has been used in the past 40 years with remarkable success in accurately describing complex systems at a affordable computational cost [54].

The Hamiltonian for the *free* electrons moving in the system is given in second quantization by

$$\hat{H}_e = \sum_i \epsilon_i \hat{c}_i^\dagger \hat{c}_i \quad , \tag{1.33}$$

where $\hat{c}_i^\dagger$ and $\hat{c}_i$ are the electron *creation* and *annihilation* operators defined in the previous section and ϵ_i are the single particle energies. The index i denotes a single particle state that in the case of using DFT calculations of an infinitely periodic crystal means $\mathbf{k}$ for the k-point and n for the band index.

The relation between the KS Green's function and the Green's function of the many-body system is obtained by replacing the approximate *exchange-correlation* energy and adding the MB self-energy $\Sigma_i(\omega)$ [55]

$$G_i(\omega) = G_i^0(\omega) + G_i^0(\omega)[\Sigma_i(\omega) - V_i^{xc}]G_i(\omega). \tag{1.34}$$

In the next sections we will outline some of the approximations for this self-energy.

1.2.3.1 Hartree-Fock

We introduce now the many-body Hamiltonian, including pair-wise interactions between the electron

$$\hat{H} = \sum_i \epsilon_i \hat{c}_i^\dagger \hat{c}_i + \frac{1}{2} \sum_{ij,nm} V_{ijnm} \hat{c}_i^\dagger \hat{c}_j^\dagger \hat{c}_n \hat{c}_m \tag{1.35}$$

where V_{ijnm} are the Coulomb interaction matrix elements [37, Appendix A]

$$V_{ijnm} = \int d^3\mathbf{r} d^3\mathbf{r}' \psi_i^*(\mathbf{r}) \psi_j(\mathbf{r}') v_c(\mathbf{r}, \mathbf{r}') \psi_n(\mathbf{r}') \psi_m^*(\mathbf{r}) \qquad (1.36)$$

Those are calculated using the *bare* Coulomb potential $v_c(\mathbf{r}) = 1/|\mathbf{r}|$ with the Fourier transform $v_c(\mathbf{q}) = 4\pi/|\mathbf{q}|^2$.

The two leading order terms from this interaction are represented in Fig. 1.2 in terms of Feynman diagrams[1]. One takes into account the forward scattering amplitude which corresponds to the tadpole diagram a). The second term accounts for the *exchange* interaction and is represented by diagram b). Diagram a) is already included self-consistently at the DFT level (see Eq. (1.4)) and Diagram b) has the form [55]

$$\Sigma^x_{n\mathbf{k}} = -\sum_{\mathbf{q}} \sum_m v_c(\mathbf{q} + \mathbf{G}) |\rho_{nm}(\mathbf{k}, \mathbf{q}, \mathbf{G})|^2 f(\epsilon_{m\mathbf{k}-\mathbf{q}}) \qquad (1.37)$$

where $\rho_{nm}(\mathbf{k}, \mathbf{q}, \mathbf{G}) = \langle \psi_{n\mathbf{k}} | e^{i(\mathbf{q}+\mathbf{G})\cdot\mathbf{r}} | \psi_{m\mathbf{k}-\mathbf{q}} \rangle$. This correction improves in the description of the many-body system and stems from the condition that the fermions must be anti-symmetric and indistinguishable. These conditions are imposed by a single Slater determinant construction of the Many-Body wave function. In extended systems, the HF correction greatly overestimates the quasi-particle corrections to the DFT eigenvalues.

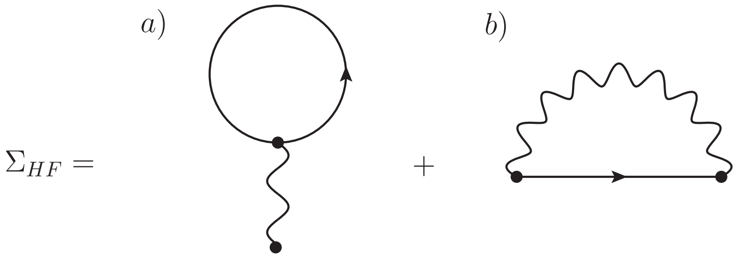

Figure 1.2: Feynman diagrams for the HF self-energy

---

[1] For a good introduction to the meaning and interpretation of a Feynman diagram see Ref. [50, Chapters 1, 2 and 3].

1.2.3.2 GW approximation

The reason for the failure of HF is the lack of screening of the Coulomb interaction in the exchange diagram of Fig. 1.2 b). The screening leads to an effective weakening of the Coulomb interaction due to the presence of the other electrons in the system. This means that one electron does not interact so strongly with another because other electrons are “in the way”. The screening of the Coulomb interaction accounts for some effects of correlation, meaning that the interaction between every two electrons depends on the others in the system. This has the effect of reducing the HF QP corrections closer to the experimentally observed value compared to the DFT values [1].

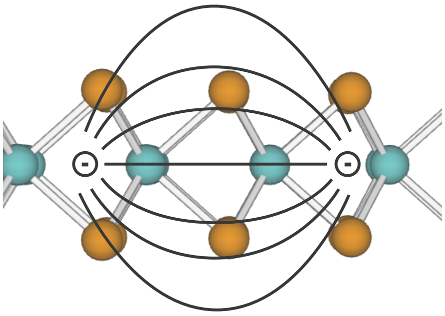

Figure 1.3: Weaker coulomb interaction screening due to the low dimensionality of the material ($MoTe_2$ in this case). The interaction lines between two point charges are not screened in all space.

The screening of the Coulomb interaction is smaller in lower dimensional compounds (2D, 1D or point-like). The reason is that since the electrons are not distributed uniformly in all space, the Coulomb interaction is not completely screened, leading to a bigger QP correction. This correction is smaller than in the HF case, as there is still some screening. A pictorial representation of the non-uniform distribution of electrons and how this affects the screening is shown in Fig. 1.3. The inclusion of the screened Coulomb interaction in the exchange term of Fig. 1.2 is what is known as the GW approximation which is diagrammatically represented in Fig. 1.4.

---

[1] A good discussion about the meaning of correlation is found in Ref. [37, Chapter 2.1]

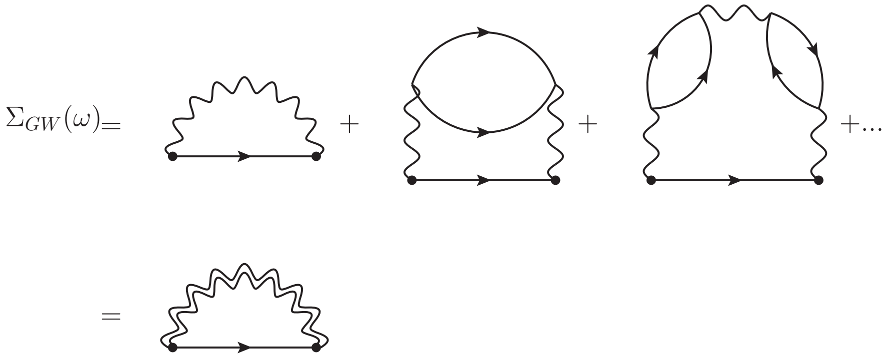

Figure 1.4: Feynamn diagrams for the GW self-energy.

The difference between the GW diagrams of Fig.1.4 and HF of Fig.1.2 is that the interaction line in the exchange term (second diagram) can be mediated by electron-hole pairs. We can focus on the term in Fig.1.2 b) and replace the bare Coulomb interaction with one that is screened. The screening is evaluated using the random-phase approximation (RPA). The diagrammatic representation of RPA is shown in Fig. 1.5.

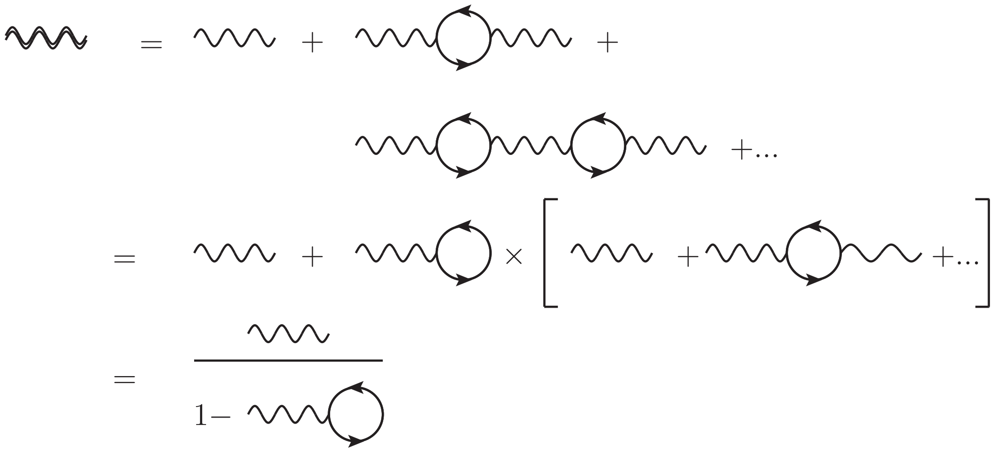

Figure 1.5: Diagrammatic representation of the screened Coulomb interaction calculated in the *random phase approximation* (RPA).

The diagrams of Fig. 1.5 can then be translated into mathematical expressions [50]

$$W^{RPA}_{\mathbf{G}\mathbf{G}'}(\mathbf{q},\omega) = \frac{v_c(\mathbf{q}+\mathbf{G})}{1 + v_c(\mathbf{q}+\mathbf{G})\Pi^0_{\mathbf{G}\mathbf{G}'}(\mathbf{q},\omega)} = \frac{v_c(\mathbf{q}+\mathbf{G})}{\epsilon^{RPA}_{\mathbf{G}\mathbf{G}'}(\mathbf{q},\omega)} \tag{1.38}$$

where $\Pi^0(\mathbf{q},\omega)$ is the irreducible polarization bubble which we will show how to calculate in detail in Chapter 4. $W_{RPA}(\mathbf{q},\omega)$ is simply the RPA-screened Coulomb interaction.

Using Eq. (1.38), the diagrams from Fig. 1.4 can also be translated into mathematical expressions as [55]

$$\Sigma^{GW}_{n\mathbf{k}}(\omega) = \Sigma^{x}_{n\mathbf{k}} + \Sigma^{c}_{n\mathbf{k}}(\omega) \tag{1.39}$$

giving us the expressions to calculate the GW self-energy. The first term is the exchange self-energy from HF in Eq. (1.37) and is added to the correlation term

$$\begin{aligned}\Sigma^{GW}_{n\mathbf{k}}(\omega) =& i\sum_{m\mathbf{q}}\sum_{\mathbf{G}\mathbf{G}'} v_c(\mathbf{q}+\mathbf{G})\rho_{nm}(\mathbf{k},\mathbf{q},\mathbf{G})\rho^*_{nm}(\mathbf{k},\mathbf{q},\mathbf{G}') \\ &\times \int \frac{d\omega'}{2\pi} G^0_m(\mathbf{k}-\mathbf{q},\omega-\omega')[\epsilon^{RPA}]^{-1}_{\mathbf{G}\mathbf{G}'}(\mathbf{q},\omega')\end{aligned} \tag{1.40}$$

In a practical calculation of the GW quasiparticles one starts by computing the screened Coulomb interaction in Eq. (1.38) which requires the calculation of the irreducible polarizability $\Pi^0(\mathbf{q},\omega)$. This is commonly done at the independent particle level using the DFT states. The bottleneck at this stage is the sum over many empty bands required to obtain a well converged real part of the polarizability $\Pi^0_{\mathbf{G}\mathbf{G}'}(\mathbf{q},\omega)$. Since the evaluation of the polarizability is **q**-independent, the computations for the different points can be done in parallel. The second step is the evaluation of Eq. (1.37) which is not very computationally demanding. The last step is the calculation of Eq. (1.40) which also requires a large part of the overall computational time and also requires a sum over empty states. In this case the evaluation of each QP correction is independent of the others and their computation can be parallelized.

1.2.4 GW band-structure of MoTe$_2$

The expressions described in the previous section are implemented in various open-source and proprietary codes available to the community. As an illustrative example of the many-body effects in the electronic band-structure, we report here the results of GW calculations for single-layer (1L) and triple-layer (3L) MoTe$_2$ performed using the `yambo` code [55]. In these calculations

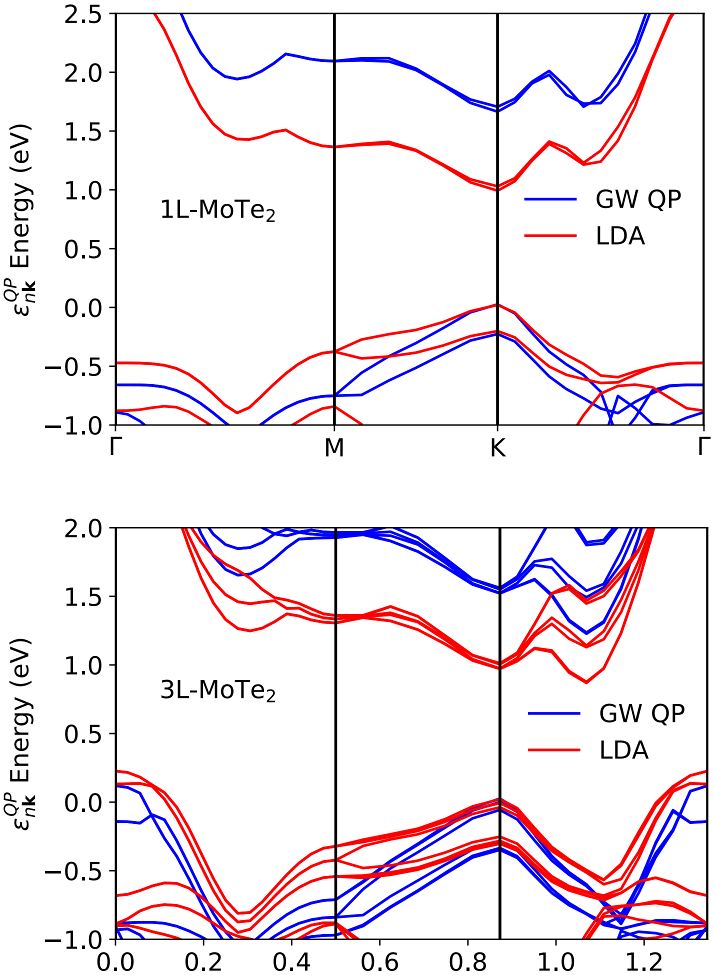

Figure 1.6: GW corrections for single- and triple-layer MoTe$_2$ in the upper and lower panel respectively.

we are interested in obtaining a scissor operator for the subsequent calculations of the optical absorption (Chapter 4) and Raman susceptibility (Chapter 5). The scissor operator [56] consists of assuming that the QP corrections to the DFT eigenvalues can be reproduced by a constant shift of the conduction bands. The values obtained from the GW calculations in single- and triple-layer $MoTe_2$ are reproduced in Table 1.1. A more elaborate approximation is to consider that the correction consists of both a shift of the conduction bands plus a different stretching for the valence and conduction bands. For simplicity, we consider only a rigid scissor shift due to the GW correction.

	scissor shift (eV)
Single-layer	0.667
Triple-layer	0.548

Table 1.1: Scissor operator for single- and triple-layer $MoTe_2$.

2

Phonons: Vibrating nuclei

In this chapter, we study the vibrational degrees of freedom of the nuclei in crystals. We expand the total energy in terms of displacements of the atoms around their equilibrium positions using the Born-Oppenheimer approximation (BOA). We then write the equations of motion for the nuclei in the harmonic approximation. These equations are solved to obtain vibrational eigenmodes of the nuclei. In Section 2.2 we will make the connection with the quantum case using *creation* and *annihilation* operators in the second quantization formalism. The interactions of the electrons with the nuclei are calculated using different *ab initio* approaches which we will describe in Section 2.3. Second quantization will then be used throughout the rest of the thesis for the description of the electron-phonon self-energy in Chapter 3 and Raman scattering in Chapter 5.

2.1 Equations of motion for the nuclei

In this section we define phonons as the collective motion of the nuclei in an extended periodic system. We highlight the main points of the derivations given in Ref. [57]. For that we start by expanding in a Taylor series the total energy of the system around the equilibrium positions of the nuclei

$$
\begin{aligned}
E(\{\mathbf{R}\}) =& E(\{\mathbf{R}^0\})+ \\
& \sum_{I\alpha} \frac{\partial E(\{\mathbf{R}^0\})}{\partial R_{I\alpha}} (R_{I\alpha} - R^0_{I\alpha})+ \\
& \frac{1}{2} \sum_{I\alpha J\beta} \frac{\partial E(\{\mathbf{R}^0\})}{\partial R_{I\alpha} \partial R_{J\beta}} (R_{I\alpha} - R^0_{I\alpha})(R_{J\beta} - R^0_{J\beta}) + \mathcal{O}(\mathbf{R}^3),
\end{aligned} \tag{2.1}
$$

where $\{\mathbf{R}\}$ and $\{\mathbf{R}^0\}$ are the set of positions and equilibrium positions of all the nuclei in the system respectively, I is a combined index that denotes the index of the atom in the unit cell and the index of the unit cell in the system (in the case of periodic crystals), $\mathbf{R}_I$ is the position [1] of the atom and α and β are cartesian directions. The first term corresponds to the total energy of the system in equilibrium. The second term contains the forces felt by an atom upon displacement around its own equilibrium position

$$
F_{I\alpha}(\{\mathbf{R}^0\}) = - \left. \frac{\partial E(\{\mathbf{R}\})}{\partial R_{I\alpha}} \right|_{\mathbf{R}=\mathbf{R}^0} . \tag{2.2}
$$

The last term contains the force constants that correspond to the induced force on an atom when another atom is displaced

$$
C_{I\alpha,J\beta} = \left. \frac{\partial^2 E(\{\mathbf{R}\})}{\partial R_{I\alpha} \partial R_{J\beta}} \right|_{\mathbf{R}=\mathbf{R}^0} = - \left. \frac{\partial F_{I\alpha}(\{\mathbf{R}\})}{\partial R_{J\beta}} \right|_{\mathbf{R}=\mathbf{R}^0} . \tag{2.3}
$$

The truncation of the expansion at the second order corresponds to the harmonic approximation. The additional terms that appear beyond second-order are *anharmonic* terms. These are important to determine phonon lifetimes as well as the structure's lattice constants at different temperatures. Different approaches are currently being developed to determine and study anharmonic effects in materials [58, 59]. These topics are beyond the scope of the present work and we will be using the harmonic approximation throughout the rest of

---

[1] At this point it is convenient to note that $\mathbf{R}_I = \mathbf{r}_I + \mathbf{r}_{\tilde{I}}$ where $\mathbf{r}_I$ is the position of the unit cell that contains the atom and $\mathbf{r}_{\tilde{I}}$ is the position of the atom in the unit cell. For the most part we will use only $\mathbf{R}_I$ for the position.

the manuscript.

Equation (2.1) can be re-written by defining a variable that corresponds to the displacement of the atoms around their equilibrium positions, $R_{I\alpha} = R^0_{I\alpha} + u_{I\alpha}$ leading to

$$\begin{aligned} E(\{\mathbf{R}\}) =& E(\{\mathbf{R}^0\})+ \\ & -\sum_i F_{I\alpha} u_{I\alpha}+ \\ & \frac{1}{2}\sum_{I\alpha,J\beta} C_{I\alpha,J\beta} u_{I\alpha} u_{J\beta} + \mathcal{O}(u^3). \end{aligned} \tag{2.4}$$

If we take the system to be in equilibrium, all the forces acting on the atoms must vanish ($F_{I\alpha} = 0$). The Hamiltonian of the system in the harmonic approximation is then [57, Chapter 3]

$$H = \frac{1}{2}\sum_{I\alpha} m\dot{u}^2_{I\alpha} + \frac{1}{2}\sum_{I\alpha,J\beta} C_{I\alpha,J\beta} u_{I\alpha} u_{J\beta}, \tag{2.5}$$

and the equation of motion is

$$M_I \ddot{u}_{I\alpha} = -\sum_{J\beta} C_{I\alpha,J\beta} u_{J\beta}. \tag{2.6}$$

We introduce here the type of solutions that we seek for the vibrational problem

$$u^{\mu}_{I\alpha}(\mathbf{q},t) = \frac{1}{2}\frac{1}{\sqrt{M_I}}\left\{A^{\mu}(\mathbf{q})\widetilde{\xi}^{\mu}_{I\alpha}(\mathbf{q})e^{i[\mathbf{q}\cdot\mathbf{R}_I-\omega_\mu(\mathbf{q})t]} + A^{\mu *}(\mathbf{q})\widetilde{\xi}^{\mu *}_{I\alpha}(\mathbf{q})e^{-i[\mathbf{q}\cdot\mathbf{R}_I-\omega_\mu(\mathbf{q})t]}\right\}, \tag{2.7}$$

where $\widetilde{\xi}^{\mu}$ are the phonon mode eigenvectors [1]. Recall that $\mathbf{R}_I$ is the sum of the position of the atom in the unit cell and the position of the unit cell in the

---

[1] To seek solutions for the problem in this form corresponds to a canonical transformation of the coordinates to a new set of coordinates that allows to decouple the vibrations of the set of $3N$ harmonic oscillators.

crystal. Replacing $\mathbf{R}_I = \mathbf{r}_I + \mathbf{r}_{\tilde{I}}$ we obtain

$$u^{\mu}_{I\alpha}(\mathbf{q},t) = \frac{1}{2}\frac{1}{\sqrt{M_I}}\left\{A^{\mu}(\mathbf{q})\xi^{\mu}_{I\alpha}(\mathbf{q})e^{i[\mathbf{q}\cdot\mathbf{r}_I-\omega_{\mu}(\mathbf{q})t]} + A^{\mu *}(\mathbf{q})\xi^{\mu *}_{I\alpha}(\mathbf{q})e^{-i[\mathbf{q}\cdot\mathbf{r}_I-\omega_{\mu}(\mathbf{q})t]},\right\} \tag{2.8}$$

where $\xi^{\mu}_{I\alpha} = \tilde{\xi}^{\mu}_{I\alpha}e^{-i\mathbf{q}\cdot\mathbf{r}_{\tilde{I}}}$. Both definitions are valid, but lead to different dynamical matrices. This becomes evident when replacing the solutions in Eq. (2.6)

$$\omega^2_{\mu}(\mathbf{q})\tilde{\xi}^{\mu}_{I\alpha}(\mathbf{q}) = \sum_{J\beta}\frac{1}{\sqrt{M_I M_J}}C_{I\alpha,J\beta}e^{i\mathbf{q}\cdot(\mathbf{R}_I-\mathbf{R}_J)}\tilde{\xi}^{\mu}_{J\beta}(\mathbf{q}), \tag{2.9}$$

$$\omega^2_{\mu}(\mathbf{q})\xi^{\mu}_{I\alpha}(\mathbf{q}) = \sum_{J\beta}\frac{1}{\sqrt{M_I M_J}}C_{I\alpha,J\beta}e^{i\mathbf{q}\cdot(\mathbf{r}_I-\mathbf{r}_J)}\xi^{\mu}_{J\beta}(\mathbf{q}). \tag{2.10}$$

Which leads to two different definitions of the dynamical matrix:

$$\tilde{D}_{I\alpha,J\beta}(\mathbf{q}) = \frac{1}{\sqrt{M_I M_J}}C_{I\alpha,J\beta}e^{i\mathbf{q}\cdot(\mathbf{R}_I-\mathbf{R}_J)}, \tag{2.11}$$

$$D_{I\alpha,J\beta}(\mathbf{q}) = \frac{1}{\sqrt{M_I M_J}}C_{I\alpha,J\beta}e^{i\mathbf{q}\cdot(\mathbf{r}_I-\mathbf{r}_J)}. \tag{2.12}$$

We will consider in the rest of the thesis the definition of Eq. (2.12). Special care should be taken when comparing phonon eigenvectors obtained with different conventions as they may or may not include this additional phase factor. This aspect was taken into consideration in the implementation of the `phononwebsite` which we described in Appendix. B. The solution to Eq. (2.6) is an eigenvalue problem

$$\sum_{J\beta}D_{I\alpha,J\beta}(\mathbf{q})\xi^{\mu}_{J\beta}(\mathbf{q}) = \omega^2_{\mu}(\mathbf{q})\xi^{\mu}_{I\alpha}(\mathbf{q}). \tag{2.13}$$

With the definitions above we have a way to calculate the atomic displacements according to the different phonon modes of the system. What is left to know now is with which amplitude the phonon modes vibrate. In the classical limit, from the principle of equipartition of energy, we have [57, Chapter 2]

$$\langle E\rangle = \sum_{\mathbf{q}\mu} \frac{1}{2}\omega_\mu^2(\mathbf{q})|A_\mu(\mathbf{q})|^2 = \sum_{\mathbf{q}\mu} \langle E_\mu(\mathbf{q})\rangle\,, \tag{2.14}$$

$$\langle E_\mu(\mathbf{q})\rangle = \frac{1}{2}\omega_\mu^2(\mathbf{q})|A_\mu(\mathbf{q})|^2 = k_B T, \tag{2.15}$$

$$|A_\mu(\mathbf{q})|^2 = \frac{2k_B T}{\omega_\mu^2(\mathbf{q})}, \tag{2.16}$$

where k_B is the Boltzmann constant.

2.2 Quantization of the phonons

In a similar fashion as to what was done in Chapter 1 for electrons we will introduce here the *creation* and *annihilation* operators for phonons[1].

Equation (2.8) is a particular solution for the problem and represents a wave with momentum $\mathbf{q}$ (this defines the direction and wavelength of the vibration). In the most general possible solution, the wave can travel in all different possible directions and wavelengths where the momentum $\mathbf{q}$ lies in the first Brillouin zone. These are the so called *normal coordinates*. In simple terms, these coordinates are a transformation from the coordinates of the individual particles to coordinates of the system that describe the positions of these individual particles. These states and the respective energies are themselves “quasi-particles”. The name stems from the fact that they behave like particles inside the system (as they have an eigenstate and eigenenergy) even though they do not correspond to a real particle in the sense of an electron or an atomic nucleous but instead the collective motion of multiple particles. The

---

[1] For a full derivation of the form of the operators the reader is refered to Ref. [57] and for a modern treatment in Ref. [60]. We will outline here just the main concepts.

normal coordinates are defined as [57, Eq. 3.59 and Eq. 3.60]

$$Q_\mu(\mathbf{q}) = \frac{1}{2}\sum_{I\alpha}\sqrt{M_I}\xi^{\mu *}_{I\alpha}(\mathbf{q})u_{I\alpha}, \tag{2.17}$$

$$P_\mu(\mathbf{q}) = \frac{1}{2}\sum_{I\alpha}\frac{1}{\sqrt{M_I}}\xi^{\mu *}_{I\alpha}(\mathbf{q})p_{I\alpha}, \tag{2.18}$$

where $p_{I\alpha} = M_I\dot{u}_{I\alpha}$ Using these coordinates, the Hamiltonian in Eq. (2.5) is written as

$$H = \frac{1}{2}\sum_{\mathbf{q}\mu}\left[|P_\mu(\mathbf{q})|^2 + \omega^2_\mu(\mathbf{q})|Q_\mu(\mathbf{q})|^2\right]. \tag{2.19}$$

If we use the Schrödinger equation to find the energy levels of a particle in a harmonic potential, we will find that the particle occupies discrete levels of energy. The Hamiltonian for the phonons can be written in second quantization as [57, Eq. 3.71]

$$\hat{H} = \sum_{\mathbf{q}\mu}\hbar\omega_\mu(\mathbf{q})\left[\hat{a}^\dagger_\mu(\mathbf{q})\hat{a}_\mu(\mathbf{q}) + \frac{1}{2}\right], \tag{2.20}$$

where

$$\hat{Q}_\mu(\mathbf{q}) = \sqrt{\frac{\hbar}{2\omega_\mu(\mathbf{q})}}[\hat{a}^\dagger_\mu(-\mathbf{q}) + \hat{a}_\mu(\mathbf{q})], \tag{2.21}$$

$$\hat{P}_\mu(\mathbf{q}) = i\sqrt{\frac{\hbar\omega_\mu(\mathbf{q})}{2}}[\hat{a}^\dagger_\mu(-\mathbf{q}) + \hat{a}_\mu(\mathbf{q})]. \tag{2.22}$$

The displacements and momenta can be written in terms of the *creation* and *annihilation* operators as

$$\hat{u}_{I\alpha} = \sum_{\mu\mathbf{q}} \sqrt{\frac{\hbar}{2M_I\omega_\mu(\mathbf{q})}} \xi^\mu_{I\alpha}(\mathbf{q}) \left[\hat{a}^\dagger_\mu(-\mathbf{q}) + \hat{a}_\mu(\mathbf{q})\right], \tag{2.23}$$

$$\hat{p}_{I\alpha} = \sum_{\mu\mathbf{q}} \sqrt{\frac{\hbar}{2M_I\omega_\mu(\mathbf{q})}} \xi^\mu_{I\alpha}(\mathbf{q}) \left[\hat{a}^\dagger_\mu(-\mathbf{q}) - \hat{a}_\mu(\mathbf{q})\right], \tag{2.24}$$

respectively. These *creation* and *annihilation* operators have a similar effect as the corresponding operators for fermions in Sec. 1.2.1

$$\hat{a}_\mu(\mathbf{q})\,|0\rangle = 0, \qquad \hat{a}^\dagger_\mu(\mathbf{q})\,|0\rangle = |\mu(\mathbf{q})\rangle\,. \tag{2.25}$$

The commutation relations for bosonic operators are:

$$\left[\hat{a}_\mu, \hat{a}_\nu\right] = 0, \qquad \left[\hat{a}^\dagger_\mu, \hat{a}^\dagger_\nu\right] = 0, \qquad \left[\hat{a}_\mu, \hat{a}^\dagger_\nu\right] = \delta_{\mu\nu}, \tag{2.26}$$

and the phonon propagator in the Matsubara formalism is given by [52, Section 3.2]

$$D^0_\mu(\mathbf{q}\mu, i\omega_i) = \left(\frac{1}{i\omega_i - \omega_\mu(\mathbf{q})} - \frac{1}{i\omega_i + \omega_\mu(\mathbf{q})}\right). \tag{2.27}$$

We will use the phonon propagator in Chapter 3 to calculate the electron self-energy due to electron-phonon interaction in the Matsubara formalism.

2.3 Calculation of forces and force constants

Now that we have defined all the important quantities related to the vibration of the atoms, we will describe how they are computed. From a first-principles approach, we described in Chapter 1 a method to calculate the total energy of the system with the atoms *clamped* in their equilibrium positions. The most straight forward way to obtain the forces is then to evaluate the derivatives of the total energy of the system. This can be done using finite differences to calculate the derivative in Eq. (2.2). To evaluate the forces on N atoms requires $3N$ evaluations of the total energy. To obtain the force constants in Eq. (2.3) which correspond to derivatives of the forces, we need to calculate the total energy for at least $(3N)^2$ displacements. This can be reduced to half since the force-constants matrix are symmetric. Note, that N is not the number of atoms in the unit cell but the number of atoms in a supercell large enough for the periodic copies to be outside the interaction range. How long the interaction range is, depends on the particular system under study, and in practical calculations this has to be carefully checked.

This method rapidly becomes prohibitive even for a system of a couple of atoms as the force constants decay only after a fair amount of nearest neighbors shells are included. For example 3-4 for semiconductors [30], 10-20 for metals and around 30 for graphene [61]. The number of nearest neighbors in each shell increases depending on the dimensionality of the system: 1D increases with N, 2D with N^2 and 3D with N^3. This makes it clear that the direct application of this approach is impractical for many cases of interest.

2.3.1 Direct calculation of the forces

A way to reduce the number of calculations required is to apply the Hellman-Feynman theorem for the forces to the electronic structure Hamiltonian

$$\mathbf{F}_I = -\left.\frac{\partial E(\{\mathbf{R}\})}{\partial \mathbf{R}_I}\right|_{\mathbf{R}=\mathbf{R}^0} \tag{2.28}$$

$$= -\left\langle \Psi_0(\{\mathbf{R}^0\}) \left| \frac{\partial \hat{H}}{\partial \mathbf{R}_I} \right| \Psi_0(\{\mathbf{R}^0\}) \right\rangle \tag{2.29}$$

which in the case of a DFT calculation (Sec.1.1) becomes

$$\mathbf{F}_I = -\int n_{\mathbf{R}_0}(\mathbf{r}) \frac{\partial V_{\mathbf{R}_0}(\mathbf{r})}{\partial \mathbf{R}_I} d^3r - \frac{\partial E_n(\{\mathbf{R}\})}{\partial \mathbf{R}_I}, \tag{2.30}$$

where we write $n_{\mathbf{R}_0}(\mathbf{r})$ explicitly to show that the charge depends on the equilibrium positions of the ions. Using this we obtain directly the forces acting on the atoms, as long as the derivative of the Hamiltonian with the atomic positions is known. The scaling of the calculation of force constants drops from $(3N)^2$ total energy to $3N$ force calculations. Since the calculation of the forces, in general, does not add much computation overhead in comparison to the total energy calculation, this method allows one to obtain the force constants in a much easier way.

A way to reduce the number of calculations is to use the symmetry operations of the crystal. These are transformations that can be applied to all the atoms to map the system onto itself. Knowing these, one can show that the forces acting on some atoms upon displacement of another atom have to be equivalent or in some cases identically vanish [62]. This is used to greatly reduce the number of total energy or force calculations needed to obtain the force constants of the system.

The main advantage of this method is that it can be directly applied to any electronic structure method that can calculate forces. The main disadvantage is that one is constrained in the sampling of the Brillouin zone to fractional divisions commensurate with the supercell.

2.3.2 Density functional perturbation theory

It is possible to calculate directly the force constants in Eq. (2.3) in a DFT framework as shown in Refs. [56] and [63]. Consider the derivative of Eq. (2.29)

$$C_{I,J} = \left.\frac{\partial^2 E(\{\mathbf{R}\})}{\partial \mathbf{R}_I \partial \mathbf{R}_J}\right|_{\mathbf{R}=\mathbf{R}_0} = -\left.\frac{\partial \mathbf{F}_I(\mathbf{R})}{\partial \mathbf{R}_J}\right|_{\mathbf{R}=\mathbf{R}_0} \tag{2.31}$$

$$= \int \frac{\partial n(\mathbf{r})}{\partial \mathbf{R}_I} \frac{\partial V_{en}(\mathbf{r})}{\partial \mathbf{R}_I} d^3r + \int n(\mathbf{r}) \frac{\partial V_{en}(\mathbf{r})}{\partial \mathbf{R}_I \partial \mathbf{R}_J} d^3r + \frac{\partial^2 E_n(\mathbf{R_0})}{\partial \mathbf{R}_I \partial \mathbf{R}_J}. \tag{2.32}$$

Linearization of Eq. (1.8) yields

$$\frac{\partial n(\mathbf{r})}{\partial \mathbf{R}_I} = 4\mathrm{Re}\sum_n \langle \psi_n | \frac{\partial}{\partial \mathbf{R}_I} | \psi_n \rangle . \tag{2.33}$$

The change of the orbitals is obtained using standard perturbation theory and summing over all the eigenstates of $\hat{H}_{\mathrm{KS}}$

$$\frac{\partial | \psi_n \rangle}{\partial \mathbf{R}_I} = \sum_{m \neq n} | \psi_m \rangle \frac{\langle \psi_m | \frac{\partial \hat{V}_{\mathrm{KS}}}{\partial \mathbf{R}_I} | \psi_n \rangle}{\epsilon_n - \epsilon_m} \tag{2.34}$$

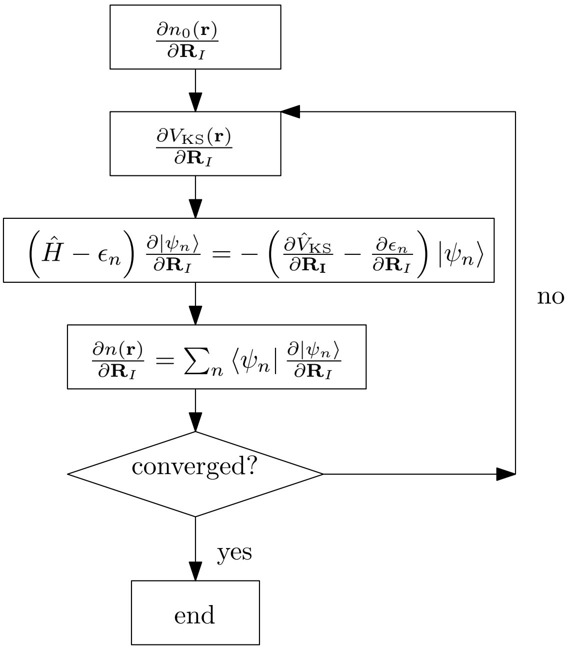

Figure 2.1: Self-consistent calculation of the derivatives of the wave functions and charge density.

This problem was reformulated in a way that no empty states are needed by taking derivatives of Eq. (1.9) with respect to the positions of the ions

$$\left(\hat{H} - \epsilon_n\right) \frac{\partial | \psi_n \rangle}{\partial \mathbf{R}_I} = -\left(\frac{\partial \hat{V}_{\mathrm{KS}}}{\partial \mathbf{R_I}} - \frac{\partial \epsilon_n}{\partial \mathbf{R}_I} \right) | \psi_n \rangle , \tag{2.35}$$

where,

$$\frac{\partial V_{\mathrm{KS}}(\mathbf{r})}{\partial \mathbf{R}_{\mathbf{I}}} = \frac{\partial V_{en}(\mathbf{r})}{\partial \mathbf{R}_{\mathbf{I}}} + e^2 \int \frac{\partial n(\mathbf{r}')}{\partial \mathbf{R}_I} \frac{1}{|\mathbf{r}-\mathbf{r}'|} d\mathbf{r}' + \left.\frac{dV_{xc}(n)}{dn}\right|_{n=n(\mathbf{r})} \frac{\partial n(\mathbf{r})}{\partial \mathbf{R}_I}. \tag{2.36}$$

This again prescribes a self-consistent solution as shown in Fig. 2.1 similarly to what is used to find the Kohn-Sham states in Fig. 1.1

2.3.3 Dielectric formulation

An alternative approach for the calculation of the change of the charge density upon an ionic displacement consists of writing it in terms of the dielectric response function [60, Section III B. 4]. In this approach the change of the charge density upon an atomic displacement is written as

$$\frac{\partial n(\mathbf{r})}{\partial \mathbf{R}_I} = \int \chi(\mathbf{r}, \mathbf{r}') \frac{\partial V_{en}(\mathbf{r}')}{\partial \mathbf{R}_I} d^3\mathbf{r}' \tag{2.37}$$

where $\chi(\mathbf{r}, \mathbf{r}')$ is the dielectric function which we will discuss in Chapter 4. This approach might prove to be advantageous with respect to the standard DFPT for calculations where the dielectric response is required (GW calculations discussed as in Chapter 1 or BSE calculations as we will discuss in Chapter 4) as it allows to reuse the results and avoid spurious computations. In these calculations the dielectric response and empty states are required and there might be no advantage in reformulating the problem in terms of occupied states as is done in DFPT to evaluate the derivative of the potential uppon atomic displacement.

2.3.4 Molecular dynamics

Another method to calculate the force constants is to perform a molecular dynamics run [64] where the positions of the nuclei are evolved in time. First the ions are *nudged* from their equilibrium position in random directions according to a certain amplitude related to the temperature of the system by

Eq. (2.16). At each time step, the forces are calculated using the Hellman-Feynman theorem (Eq. (2.29)). The positions of the atoms are then changed in time according to the equation of motion:

$$F_{I\alpha}(t) = M_I \frac{\partial^2 \mathbf{r}_{I\alpha}(t)}{\partial^2 t}. \tag{2.38}$$

Once the positions of the atoms as a function of time $\mathbf{r}_i(t)$ are known, it is possible to obtain the vibration of eigenmodes by Fourier transforming in space $\mathbf{r} \to \mathbf{q}$ and time $t \to \omega_\mu$. This approach directly incorporates anharmonic effects [65]. The main drawback is that to properly capture the long-wavelength phonon modes, large supercells are required, which quickly becomes prohibitive.

In the present work we will not use this method to obtain the vibrational spectra and instead will use a perturbative description of the vibrational spectra and Raman spectroscopy. This approach, however, might prove more feasible than the perturbative approach when going beyond the harmonic approximation. We will also point out in Section 5.2.1 that a molecular dynamics based approach might be used to obtain Raman intensities and frequencies at different temperatures.

2.3.5 Fitting to existing data

Another method to obtain the force constants is to fit them to existing data in a similar way as what is done in the case of tight-binding for the electronic structure. Force constants are defined for the different pairs of atoms interacting in the system and then are fitted to reproduce for example the phonon dispersion. We will show this for the example of graphene where we used such a model to reproduce both the phonon modes and frequencies calculated with *ab initio* methods. The advantage of this method is to provide an effective model that captures the essential physical aspects of the system at a lower computational cost.

2.4 Phonon modes of Graphene

In this section we introduce a new force constant model fitted to *ab initio* data to describe the phonon eigenmodes of graphene. Although this section is not essential to the main topic of this thesis, the results shown here are an important contribution to the calculation of electron-phonon matrix elements in graphene using empirical models. These are one of the essential quantities to calculate the Raman spectrum using the perturbative approach we will describe in Section 6. A new fit of the force constants of graphene was required as the previously available models [66, 67] did not correctly reproduce the phonon eigenvectors in the long-wavelength limit. This feature was required to correctly compute the electron-phonon coupling matrix elements using a tight-binding approach. These were in turn used to evaluate the electronic lifetimes and phonon-limited mobility of graphene and carbon nanotubes using the Boltzmann transport equation [68]. Using the models previously published, the mobility was over-estimated with respect to previously published data on graphene [69]. The advantage of fitting the force constants to *ab initio* data is that we incorporate part of the effect of long-range force constants in a smaller set of parameters. This simplifies the calculation of the phonon modes of larger structures. In our study [68] we were interested in evaluating how the mobility of carbon nanotubes approaches that of graphene by increasing the diameter. We will additionally study the effect of the long-range force constants and their importance in describing the *Kohn anomaly* [70, 71]. The *Kohn anomalies* are sharp features in the phonon dispersion due to the abrupt change of the screening of lattice vibrations in $\mathbf{q}$ vectors that connect two points of the electronic Fermi surface.

To obtain a better description of the phonon modes of graphene we have refitted the force constants model of Ref. [67] to an *ab initio* calculation of the phonon dispersion. The calculation of the dispersion was done using the `abinit` code [72]. The electronic structure is calculated in the local density approximation (LDA) using a regular 60×60 $\mathbf{k}$-mesh in the first Brillouin zone and an energy cutoff of 35 Ha. The electrons follow a Fermi-Dirac distribution

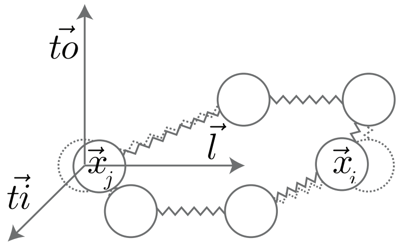

Figure 2.2: Relation between the local and cartesian coordinates. See main text for explanation.

with a thermal smearing of 0.002 Ha. We found the optimized cell parameter to be 4.631 Å. The dynamical matrices were calculated using DFPT on a 30×30 **q**-mesh. Since LDA overbinds, i.e., phonon frequencies have the tendency to be slightly too high, a scaling factor is used such that the phonon frequencies of the LO/TO mode at Gamma match the experimental value [67]. To ensure transferability to new structures, these force constants are defined in local coordinates. The transformation of the local coordinates to Cartesian is represented in Fig 2.2 and is defined as follows: the l direction is along the line connecting the two interacting atoms, ti is perpendicular to this line in the plane of the graphene sheet, and to is the out-of-plane direction.

In the local reference frame we define the longitudinal forces (ϕ_l), transverse in-plane (ϕ_{ti}), and transverse-out-of-plane (ϕ_{to}) forces that act on a particular atom when its nth nearest neighbor is displaced. In the conventional four nearest neighbors (4NN) force constant model, only these "diagonal" terms are fitted. In our model, we include also the "off-diagonal" coupling between the longitudinal direction and the transverse-in-plane direction ($\phi_{l/ti}$ and $\phi_{ti/l}$). The force constant matrix for the interaction between two atoms in the local reference frame thus reads

$$\overline{\overline{\mathbf{C}}}_n = \begin{pmatrix} \phi_n^l & \phi_n^{l/ti} & 0 \\ \phi_n^{ti/l} & \phi_n^{ti} & 0 \\ 0 & 0 & \phi_n^{to} \end{pmatrix} \tag{2.39}$$

The off-diagonal force constants $\phi^{ti/l}$ and $\phi^{l/ti}$ obey the following relations [61]

$$\phi_1^{l/ti} = \phi_3^{l/ti} = 0, \qquad \phi_2^{l/ti} = -\phi_2^{ti/l}, \tag{2.40}$$

$$\phi_1^{ti/l} = \phi_3^{ti/l} = 0, \qquad \phi_4^{l/ti} = \phi_4^{ti/l}. \tag{2.41}$$

By our fitting procedure we obtained the parameters reproduced in Table 2.1. During the fitting we have noticed that the off-diagonal terms of the second and the fourth nearest neighbor ($\phi_2^{l/ti}$ and $\phi_4^{l/ti}$ respectively) are essential to reproduce correctly the phonon modes obtained from first-principles. A good fit of the phonon frequencies alone can be achieved even without the off-diagonal terms as shown in the models in Fig. 2.3. When we are interested in calculating the electron-phonon coupling, it is essential to correctly describe the long-wavelength phonon modes. To compare the quality of the different fits available in the literature and our new fit, we analyze the analytical form of the phonon eigenvectors near Γ [73]. The canonical phonon modes (the

n	1	2	3	4
ϕ_n^l (10^4 dyn/cm)	40.905	7.402	-1.643	-0.609
ϕ_n^{ti} (10^4 dyn/cm)	16.685	-4.051	3.267	0.424
ϕ_n^{t0} (10^4 dyn/cm)	9.616	-0.841	0.603	-0.501
$\phi_n^{l/ti}$ (10^4 dyn/cm)	0.000	0.632	0.000	-1.092
$\phi_n^{ti/l}$ (10^4 dyn/cm)	0.000	-0.632	0.000	-1.092

Table 2.1: Parameters of the 4NN force constant model with off-diagonal couplings. The corresponding dispersion relation is shown in Fig. 2.3. Table originally published in Ref. [68].

phonon modes in the limit $q = 0$) have the following form [74]

$$\xi^{\tilde{LA}}_{I\alpha}(\mathbf{q}) = \frac{1}{\sqrt{2}} e^{i\mathbf{q}\cdot(\mathbf{R}+\mathbf{r_I})} \frac{\mathbf{q}}{|\mathbf{q}|}, \tag{2.42}$$

$$\xi^{\tilde{TA}}_{I\alpha}(\mathbf{q}) = \frac{1}{\sqrt{2}} e^{i\mathbf{q}\cdot(\mathbf{R}+\mathbf{r_I})} \frac{\mathbf{q}\perp}{|\mathbf{q}\perp|}, \tag{2.43}$$

$$\xi^{\tilde{LO}}_{I\alpha}(\mathbf{q}) = \gamma_I \frac{1}{\sqrt{2}} e^{i\mathbf{q}\cdot(\mathbf{R}+\mathbf{r_I})} \frac{\mathbf{q}}{|\mathbf{q}|}, \tag{2.44}$$

$$\xi^{\tilde{TO}}_{I\alpha}(\mathbf{q}) = \gamma_I \frac{1}{\sqrt{2}} e^{i\mathbf{q}\cdot(\mathbf{R}+\mathbf{r_I})} \frac{\mathbf{q}\perp}{|\mathbf{q}\perp|}. \tag{2.45}$$

As we move slightly away from $q = 0$, the phonon modes start to mix up and obey the following relations [73]

$$\xi^{LA}_{I\alpha}(\mathbf{q}) = \sqrt{1-\alpha^2|\mathbf{q}|^2}\xi^{\tilde{LA}}_{I\alpha}(\mathbf{q}) - \delta|\mathbf{q}|[\sin(3\theta_\mathbf{q})\xi^{\tilde{LO}}_{I\alpha}(\mathbf{q}) + \cos(3\theta_\mathbf{q})\xi^{\tilde{TO}}_{I\alpha}(\mathbf{q})], \tag{2.46}$$

$$\xi^{TA}_{I\alpha}(\mathbf{q}) = \sqrt{1-\alpha^2|\mathbf{q}|^2}\xi^{\tilde{TA}}_{I\alpha}(\mathbf{q}) - \delta|\mathbf{q}|[\cos(3\theta_\mathbf{q})\xi^{\tilde{LO}}_{I\alpha}(\mathbf{q}) - \sin(3\theta_\mathbf{q})\xi^{\tilde{TO}}_{I\alpha}(\mathbf{q})], \tag{2.47}$$

$$\xi^{LO}_{I\alpha}(\mathbf{q}) = \sqrt{1-\alpha^2|\mathbf{q}|^2}\xi^{\tilde{LO}}_{I\alpha}(\mathbf{q}) - \delta|\mathbf{q}|[\sin(3\theta_\mathbf{q})\xi^{\tilde{LA}}_{I\alpha}(\mathbf{q}) + \cos(3\theta_\mathbf{q})\xi^{\tilde{TA}}_{I\alpha}(\mathbf{q})], \tag{2.48}$$

$$\xi^{TO}_{I\alpha}(\mathbf{q}) = \sqrt{1-\alpha^2|\mathbf{q}|^2}\xi^{\tilde{TO}}_{I\alpha}(\mathbf{q}) - \delta|\mathbf{q}|[\cos(3\theta_\mathbf{q})\xi^{\tilde{LA}}_{I\alpha}(\mathbf{q}) - \sin(3\theta_\mathbf{q})\xi^{\tilde{TA}}_{I\alpha}(\mathbf{q})], \tag{2.49}$$

where δ is the mixing of acoustic and optical components of the phonon modes at small $\mathbf{q}$. The correct ratio δ in the transverse and longitudinal acoustic branches at $\mathbf{q} \neq 0$ can only be achieved with the inclusion of the off-diagonal force constants.

We used the δ parameter of the different models to determine their fitness in reproducing the phonon modes. By using our new fit with the parameters in Table 2.1, the *ab initio* δ ratio was reproduced to a very good degree in contrast with previously published models as shown in Fig. 2.4. The comparison of the phonon dispersions obtained from first-principles calculations and the force constant models is shown in Fig. 2.3. The model of Jishi et al. [66] that is commonly used in the literature was fitted to experimental data. With recent experiments and *ab initio* calculations, it was found that this model does not correctly capture all the phonon frequencies [67]. A new model was then proposed by Wirtz et al. [67] fitted to *ab initio* data, which correctly reproduces the phonon frequencies. This model however does not include all the off-diagonal force constants and as such it does not reproduce the *ab initio* δ parameter. The correct reproduction of the δ parameter may seem a technical detail, however, it turned out essential for a quantitatively correct calculation of the electron-phonon coupling involving these modes. Thus, the calculated mobility of graphene sensitively depends on this value as well [68].

We note that although the agreement between our new 4NN model and the *ab initio* calculation is good, the later cannot reproduce the *Kohn anomalies* in the two highest optical branches. This would require the inclusion of many more distant neighbor interactions in the model, even infinitely many, if one wants to reproduce the kink [61]. This would defeat the objective of using a simple model. However, for the calculation of the phonon-limited resistivity of graphene and carbon-nanotubes it is not needed to reproduce this feature as we have shown in Ref. [68]. The reason is that for moderate currents and not to high temperatures ($0 - 500$ K) it is mainly the low-frequency phonon modes that play a role in the electronic mobility. Our new 4NN force constants model allows one to calculate the electron-phonon scattering rates and carrier mobilities, in good agreement with *ab initio* calculations for graphene [69].

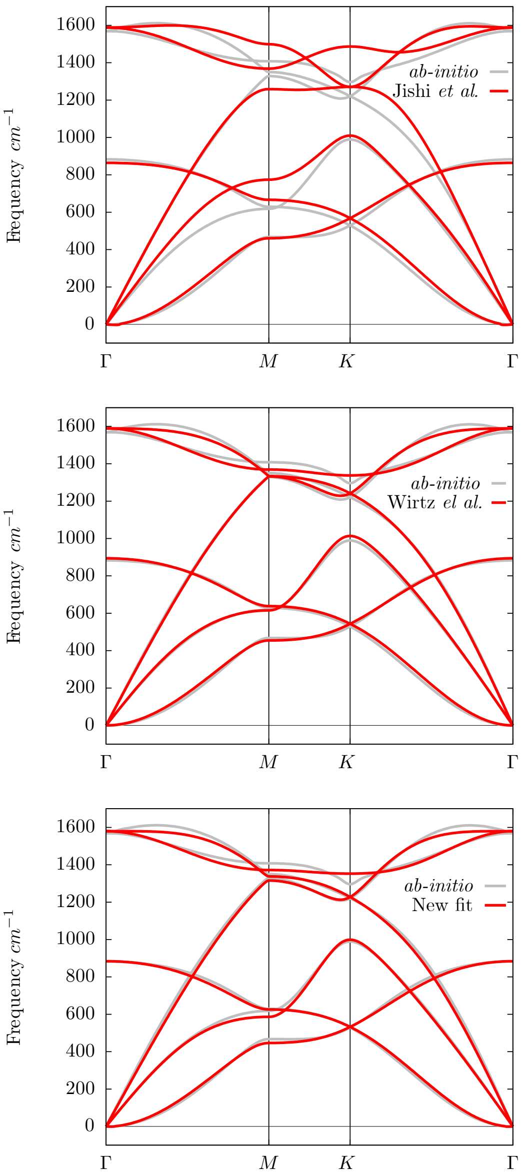

Figure 2.3: Phonon dispersion of graphene. The red lines are the frequencies calculated using the 4NN force constant model, and gray lines are DFT-LDA calculations using `abinit`. Figure taken from Ref. [68]. An interactive version of the *ab initio* data is available on the `phononwebsite` [75].

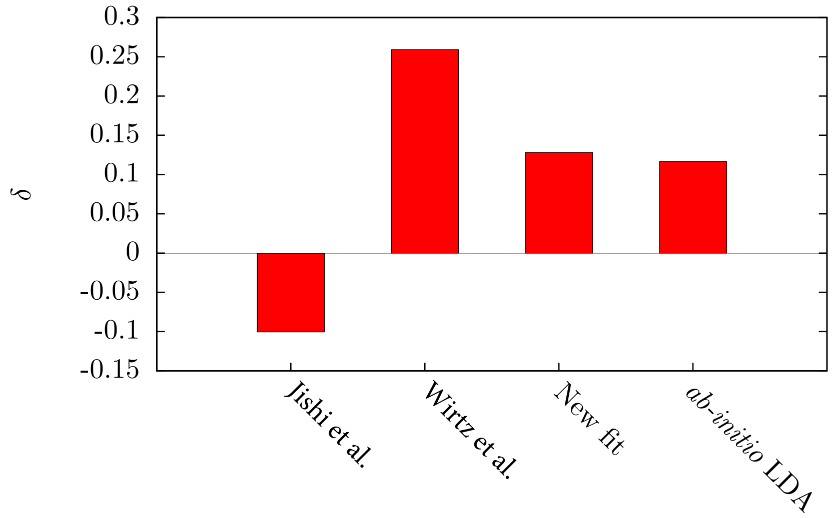

Figure 2.4: Comparison of the mixture of acoustic and optical modes of graphene for different force constant models existing in the literature.

2.5 Phonon modes of TMDs

In this section we will briefly show and describe the phonon modes of the TMDs which we will study in the present manuscript, $MoTe_2$ and MoS_2.[1] The phonon frequencies are directly related to the positions of the Raman shifted peaks in the experiments. We will show in Chapter 5 calculations of the Raman intensities for $MoTe_2$ using the finite differences method and in Chapter 6 for MoS_2 using a perturbative approach and comparing with the finite differences approach. Here we will describe the Raman-active phonon modes for single- and triple-layer $MoTe_2$ as well as the phonon modes of MoS_2.

Single layer TMDs in the hexagonal phase (we will only deal with this phase as it is the one found at room temperature for both MoS_2 and $MoTe_2$) have three atoms in the unit cell and nine distinct phonon branches. The phonon modes are characterized according to their representation in the point group within the space group of the crystal. To denote the different representa-

---

[1] Some example phonon dispersions are available in the phonon website described in Section B.1.

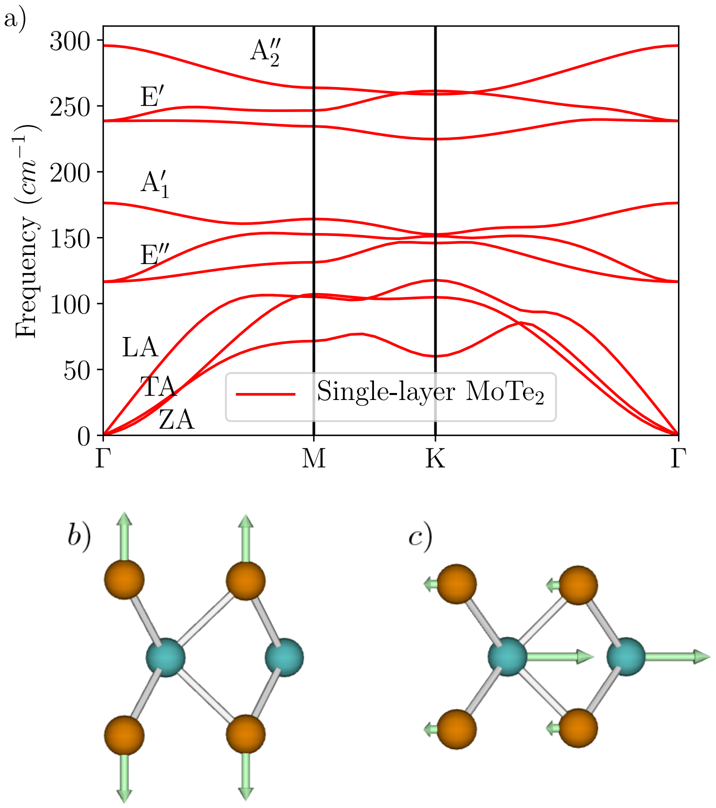

Figure 2.5: Phonon modes of single-layer $MoTe_2$. a) Phonon dispersion. b) and c) Representation of the vibrational patterns of the A_1' and E' modes of $MoTe_2$ respectively. The images of the phonon modes were generated with the `phononwebsite` [75] where an interactive version is available.

tions it is common to use the Mulliken notation [76]. Phonons of TMDs have a dispersion similar to that of graphene for the out-of-plane modes ZA and A'_1[1]. The main difference between the phonon dispersions of MoS_2 and of $MoTe_2$ is related to the masses. S is much lighter than Te (32.065 and 127.6 atomic mass units respectively). This causes the phonon modes where the Te atoms are moving to have lower frequencies than the ones of MoS_2. In structures where more layers are stacked together, more phonon modes exist. If these layers were not interacting with each other, all the phonon frequencies would have the same frequency. In reality the different layers notice each others' presence

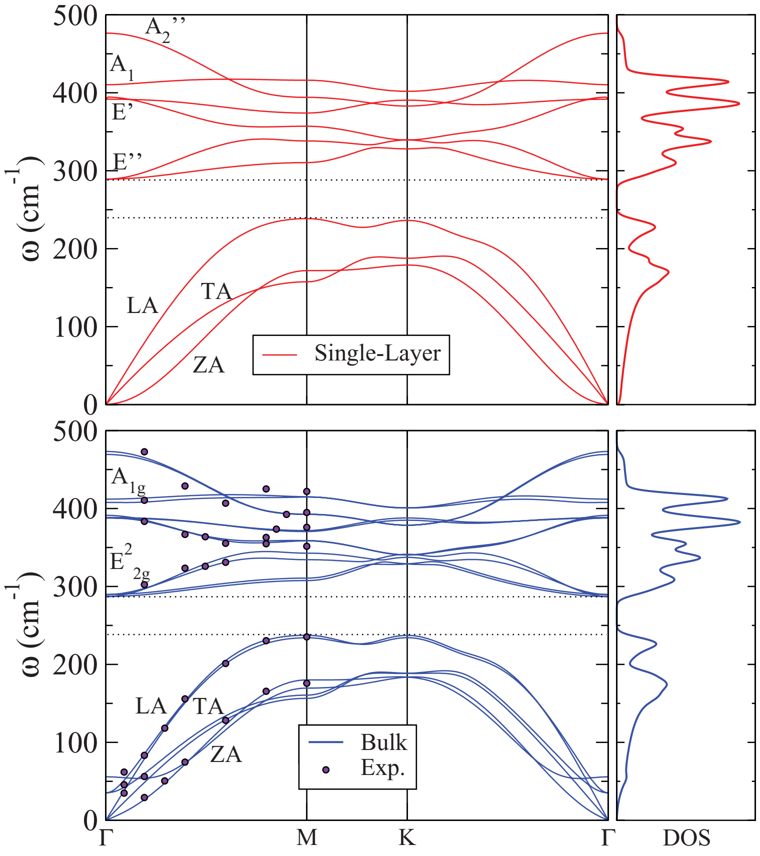

Figure 2.6: Phonon modes of single-layer and bulk MoS_2. Figure taken from Ref. [77]. Interactive version of similar calculations available on the `phononwebsite` [75].

---

[1] For a detailed analysis of the phonon modes of TMDs see Refs. [77, 22].

via van der Waals interaction. This leads to a splitting of the phonon frequencies similar to what occurs in the electronic levels of molecules. This same phenomena was first investigated by Alexander Davydov in the case of optical excitations and is referred to as Davydov splitting [78].

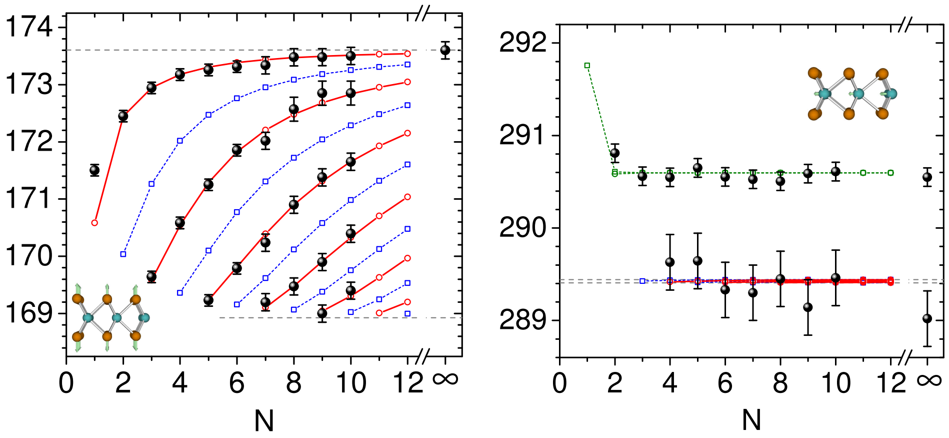

Figure 2.7: Experimental phonon frequencies for the phonon modes of $MoTe_2$ as a function of the number of layers (dots). The continuous line is a fit to a linear chain model. The modes belonging to the A_1' and A_{1g} representations are shown in panel a) and the ones to the E' and E_g representations in panel b). The blue lines correspond to phonon modes that are not Raman active. Figure taken from Ref. [24].

Accurate experimental measurements of the phonon mode frequencies as a function of the number of layers were reported [24] using Raman spectroscopy. We reproduce the results relevant to the present document in Fig. 2.7. A more detailed discussion of the phonon modes of $MoTe_2$ along with their representations is available in Ref. [24]. The modes belonging to the A_1' and A_{1g} representations have a much stronger interlayer coupling, which leads to a larger splitting of the phonon frequencies for increasing number of layers. In the case of triple-layer, we distinguish the phonon modes with the labels $A_1'(a)$ and $A_1'(b)$ for the one of lower and higher phonon frequency respectively. The Raman intensities of these will be extensively discussed in Chapter 5. The modes of the E' and E_g representations do not show such strong dependence and their frequencies remains mostly unchanged with increasing number of layers.

3

Electron-phonon coupling: Band gap renormalization and lifetimes

In this section we incorporate the effect of the ionic vibrations on the electronic structure, i.e., we investigate the electron-phonon interaction. Because the ions are vibrating around their equilibrium positions, the potential that the electrons feel is also oscillating. We can conceive the band structure as a time-dependent quantity assuming that the electrons move much faster than the ions. In the Born-Oppenheimer treatment of the electronic structure, this effect is not accounted for. However, it can be included perturbatively *a posteriori* in the same way that the Coulomb interaction was included in the GW approximation outlined in Section 1.

The vibrations of the nuclei change the energies of the electronic levels of the system, hence the band gap of semi-conductors depends on the temperature. This effect is important in technological applications where the operating temperature can vary on a large range, for example in transistors.

The amplitude of the oscillations of the ions is related to the temperature of the system (Eq. (2.16)) and the electron-phonon correction to the eigenvalues depends on it. At T=0 K the ions are oscillating due the quantum mechanical zero-point motion as shown in Section 2.2.

Apart from the zero-point motion, temperature affects the material in other ways, the most immediate being the thermal lattice expansion. This is related to long-wavelength vibrations of the atoms. It is common to say that DFT calculations are performed at zero temperature, although this is not strictly true. In the same way that temperature affects the material in different ways, the temperature also enters the theory in different ways. The electronic density of the system can be treated at the level of DFT using the canonical ensemble. Hence the temperature is considered at the level of the electrons. This effect is only relevant for metals or small gap semiconductors with $E_g < k_B T$ where there is the possibility of thermal excitations. Additionally, temperature is related to the energy of the vibrations of the ions and the thermal expansion which in turn affect the electronic properties. These effects are in general left out in standard DFT calculations. This is what is often meant by saying that temperature is neglected altogether.

To incorporate the effect of lattice vibrations of the system we first calculate the coupling between electrons and phonons. We will use it then to calculate the electron-phonon contribution to the electron self-energy thus encoding the effect the phonons have on the electrons using the language of many-body perturbation theory (MBPT).

3.1 Electron-phonon coupling Hamiltonian

The contribution to the total Hamiltonian due to electron-phonon coupling can be written in second quantization as

$$H_{\mathrm{e-n}} = \sum_{nn'\mu\mathbf{q}\mathbf{k}} g^{n,n',\mu}_{\mathbf{k},\mathbf{k}-\mathbf{q}} (\hat{c}^{\dagger}_{n,\mathbf{k}} \hat{c}_{n',\mathbf{k}-\mathbf{q}})(\hat{a}_{\mu,\mathbf{q}} + \hat{a}^{\dagger}_{\mu,-\mathbf{q}}), \tag{3.1}$$

where $\hat{a}^{\dagger}$ and $\hat{a}$ are the bosonic creation and annihilation operators, $\mathbf{q}$ is the phonon momentum, μ the phonon mode, $\mathbf{k}$ the electron momentum, n and n' the band indices and, $g^{n,n',\mu}_{\mathbf{k},\mathbf{k}-\mathbf{q}}$ the electron-phonon coupling matrix elements.

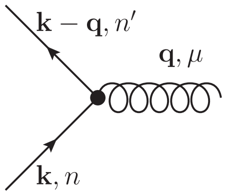

Figure 3.1: Graphical representation of the electron-phonon coupling vertex.

The electron-phonon coupling matrix elements are calculated from

$$g^{n,n',\mu}_{\mathbf{k},\mathbf{k}-\mathbf{q}} = \sum_{I\alpha} \sqrt{\frac{\hbar}{M_I \omega_{\mu\mathbf{q}}}} \tilde{\xi}^{\mu}_{I\alpha\mathbf{q}} \langle n\mathbf{k}| \frac{\partial V_{KS}(\mathbf{r})}{\partial R_{I\alpha}} |n'\mathbf{k}-\mathbf{q}\rangle \,, \tag{3.2}$$

where $|n\mathbf{k}\rangle$ has the same meaning as $|\psi_{n\mathbf{k}}\rangle$. The evaluation of these matrix elements can be done using the same DFPT methods as described in Section 2.3.2 to obtain the phonon modes. We use the $\frac{\partial V_{KS}(\mathbf{r})}{\partial \mathbf{R}_I}$ term obtained from Eq. (2.36) and the wave functions from Eq. (1.14). In this thesis we will use the implementations in the `ph.x` code from the `QE` suite [79] to obtain the electron-phonon matrix elements.

3.2 Electron-phonon self energy

We will review here the calculation of the electron-phonon self-energy in the language of MBPT [80, 60]. Like in the GW case, the self-energy of the electrons due to electron-phonon interaction will affect their energies and lifetimes [80, 60].

To be consistent in the truncation of the order of perturbation theory, there are two different Feynman diagrams contributing to the irreducible self-energy. The temperature dependent self-energy is given by the sum of the two

$$\Sigma^{ep}_{n\mathbf{k}}(\omega, T) = \Sigma^{\text{Fan}}_{n\mathbf{k}}(\omega, T) + \Sigma^{\text{DW}}_{n\mathbf{k}}(T). \tag{3.3}$$

In this section we will outline how these diagrams can be evaluated using the finite-temperature formalism introduced in Section 1.2.2.

The first term in Eq. (3.3) is called the Fan term [81] and can be represented diagrammatically as shown in Fig. 3.2. We follow the Feynman rules and translate the diagrams to mathematical expressions

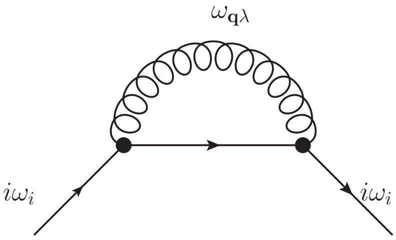

Figure 3.2: The Feynman diagrams for the Fan self-energy.

$$\Sigma^{\mathrm{Fan}}_{n\mathbf{k}}(i\omega_i) = \frac{1}{\beta}\sum_{\mathbf{q}\mu n'} |g^{n,n',\mu}_{\mathbf{k}-\mathbf{q},\mathbf{k}}|^2 \sum_{j=-\infty}^{\infty} D_\mu(\mathbf{q}\mu, i\omega_j)\mathcal{G}_{n'}(\mathbf{k}-\mathbf{q}, i\omega_i - i\omega_j) \tag{3.4}$$

Upon replacing the electronic (Eq. (1.32)) and phononic expressions (Eq. (2.27)) for the Green's function, the expressions becomes

$$\begin{aligned}\Sigma^{\mathrm{Fan}}_{n\mathbf{k}}(i\omega_i) = \frac{1}{\beta}\sum_{\mathbf{q}\mu n'} |g^{n,n',\mu}_{\mathbf{k}-\mathbf{q},\mathbf{k}}|^2 \times \\ \sum_{j=-\infty}^{\infty}\left(\frac{1}{i\omega_j - \omega_{\mathbf{q}\mu}} + \frac{1}{i\omega_j + \omega_{\mathbf{q}\mu}}\right)\left(\frac{1}{i\omega_i - i\omega_j - \epsilon_{n',\mathbf{k}-\mathbf{q}}}\right).\end{aligned} \tag{3.5}$$

Evaluation of the sum over the Matsubara frequencies yields

$$\Sigma^{\mathrm{Fan}}_{n\mathbf{k}}(i\omega_i) = \sum_{\mathbf{q}\mu n'} |g^{n,n',\mu}_{\mathbf{k}-\mathbf{q},\mathbf{k}}|^2 \left(\frac{n(\omega_{\mathbf{q}\mu}) + 1 - f(\epsilon_{n',\mathbf{k}-\mathbf{q}})}{i\omega_i - \epsilon_{n',\mathbf{k}-\mathbf{q}} - \omega_{\mathbf{q}\mu}} + \frac{n(\omega_{\mathbf{q}\mu}) + f(\epsilon_{n',\mathbf{k}-\mathbf{q}})}{i\omega_i - \epsilon_{n',\mathbf{k}-\mathbf{q}} + \omega_{\mathbf{q}\mu}}\right), \tag{3.6}$$

where $n(T,\omega) = (e^{\hbar\omega/k_bT} - 1)^{-1}$ is the Bose-Einstein distribution and k_B is the Boltzmann constant. This expression still depends on an imaginary frequency. To relate it to quantities that can be experimentally measured we analytically continue it to the real axis [50] by replacing $i\omega_i \rightarrow \omega - i\gamma$

$$\Sigma^{\mathrm{Fan}}_{n\mathbf{k}}(\omega, T) = \sum_{\mathbf{q}\mu n'} |g^{n,n',\mu}_{\mathbf{k}-\mathbf{q},\mathbf{k}}|^2 \Big(\frac{n(\omega_{\mathbf{q}\mu}, T) + 1 - f(\epsilon_{n',\mathbf{k}-\mathbf{q}}, T)}{\omega - \epsilon_{n',\mathbf{k}-\mathbf{q}} - \omega_{\mathbf{q}\mu} - i\gamma} + \tag{3.7}$$

$$\frac{n(\omega_{\mathbf{q}\mu}, T) + f(\epsilon_{n',\mathbf{k}-\mathbf{q}}, T)}{\omega - \epsilon_{n',\mathbf{k}-\mathbf{q}} + \omega_{\mathbf{q}\mu} - i\gamma} \Big), \tag{3.8}$$

where we also made the temperature dependence of the occupation factors explicit.

The second term in Eq. (3.3) is the Debye-Waller term as shown in Fig. 3.3. The loop integration yields a real quantity, hence this term does not contribute to the lifetime of the electron.

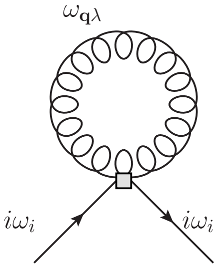

Figure 3.3: The Feynman diagram of the Debye-Weller term.

$$\Sigma^{\mathrm{DW}}_{n\mathbf{k}}(T) = \sum_{\mathbf{q}\mu n'} \Lambda^{nn'\mu}_{\mathbf{q},-\mathbf{q},\mathbf{k}} \left[2n(\omega_{\mathbf{q}\mu}, T) + 1\right] \tag{3.9}$$

where $\Lambda^{nn'\mu}_{\mathbf{q},-\mathbf{q},\mathbf{k}}$ is the second-order electron-phonon coupling matrix element. This term is calculated in terms of the first order electron-phonon coupling matrix elements using the translation invariance of the system [80, 82].

The determination of the quasiparticle energies is done using the quasiparticle equation:

$$\epsilon^{QP}_{n\mathbf{k}} = \epsilon^{KS}_{n\mathbf{k}} + \Sigma^{ep}_{n\mathbf{k}}(\omega, T)|_{\omega=\epsilon^{QP}_{n\mathbf{k}}}. \tag{3.10}$$

The zeros of this equation correspond to the energies of the new quasiparticles.

The evaluation of $\Sigma^{ep}_{n\mathbf{k}}(\omega)$ at each frequency is however a rather expensive calculation as it implies the sum over empty states. It is convenient to find a method to solve Eq. (3.10) evaluating $\Sigma^{ep}_{n\mathbf{k}}(\omega)$ the least number of times possible. This has been done using two distinct approaches. One of them is based on linearizing $\Sigma^{ep}_{n\mathbf{k}}(\omega)$ around the $\epsilon^{KS}_{n\mathbf{k}}$ energies and finding the intersection with zero. This corresponds to using Newton's method with one iteration. In the second approach, the self-energy is evaluated at different energies near the Kohn-Sham energy $\epsilon^{QP}_{n\mathbf{k}}$. The function is interpolated and the zero of Eq. (3.10) is found iteratively until the self-energy is evaluated at the energy of the quasi-particle.

The real part of the self-energy gives a correction to the energy of the state:

$$\epsilon^{QP}_{n\mathbf{k}}(T) = \epsilon^{KS}_{n\mathbf{k}} + \mathrm{Re}\{\Sigma^{ep}_{n\mathbf{k}}(\omega, T)|_{\omega=\epsilon^{QP}_{n\mathbf{k}}}\}, \tag{3.11}$$

where $\epsilon_{n\mathbf{k}}$ is the DFT eigenvalue calculated at zero temperature.

The imaginary part of the self-energy corresponds to the line width of the state and its inverse is the lifetime

$$\frac{1}{\tau_{n\mathbf{k}}(T)} = \mathrm{Im}\{\Sigma^{ep}_{n\mathbf{k}}(\omega, T)|_{\omega=\epsilon^{QP}_{n\mathbf{k}}}\}. \tag{3.12}$$

The lifetimes due to the GW self-energy are large near the gap for semiconductors. In contrast, the lifetimes due to electron-phonon interaction lead to a broadening of the electronic states near the gap. This broadening is responsible for the temperature dependance of the optical spectra as we will show in Section 4.5.5 for the case of MoS_2 and for the Raman spectra in Section 6.8. It also enters in the Boltzmann transport equation limiting the electronic conductivity as we have shown in the case of graphene and nanotubes [68].

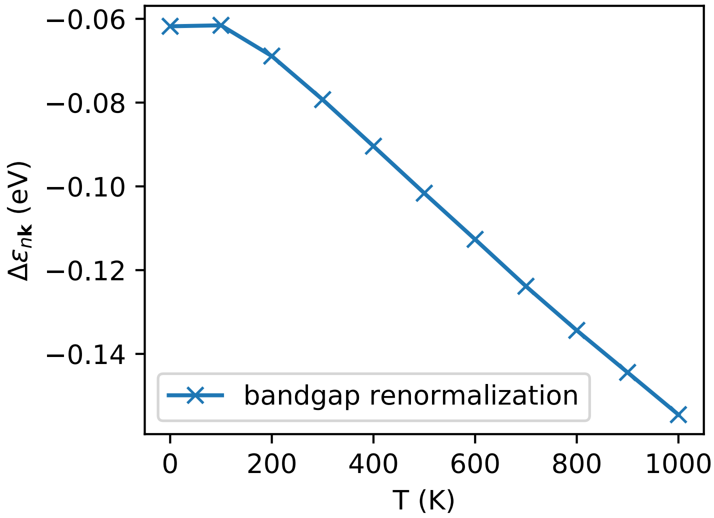

Figure 3.4: Bandgap renormalization $\Delta\epsilon_{n\mathbf{k}}$ as a function of temperature for MoS_2. $\Delta\epsilon_{n\mathbf{k}}$ corresponds to $\Sigma^{ep}_{n\mathbf{k}}(\omega, T)|_{\omega=\epsilon^{QP}_{n\mathbf{k}}}$ from Eq. (3.10).

3.3 Temperature dependent band structure of MoS_2

We show here some results for the temperature dependent band structure of MoS_2. These results will be used in Chapters 4 and 6 in the calculation of the temperature dependence of the Raman spectra of MoS_2.

Using the formulas described above as implemented in the `yambo` code, we calculated the electron-phonon self-energy from Eq. (3.3). The electron-phonon matrix elements are obtained from the `ph.x` code [79]. We described the ground state using DFT with an LDA functional. The ionic positions were relaxed with the experimental lattice parameter of 5.97 Bohr [83] and 50 Bohr of vacuum separation. We used a 24x24 **k**-mesh for both the electronic structure and the phonons. We included electron-phonon matrix elements up to 40 bands in the self-energy.

The band gap renormalization is obtained from the self-energy using Eq. (3.10). The renormalization at 0 K is 61.8 meV and the evolution with temperature is shown in Fig. 3.4. The results for the lifetimes are obtained from the self-energy using Eq. (3.12) and are represented in Fig. 3.5 along with the electronic density of states (DOS). From Fig. 3.5 we can verify that the lifetimes are roughly proportional to the electronic DOS times a constant depending on the temperature

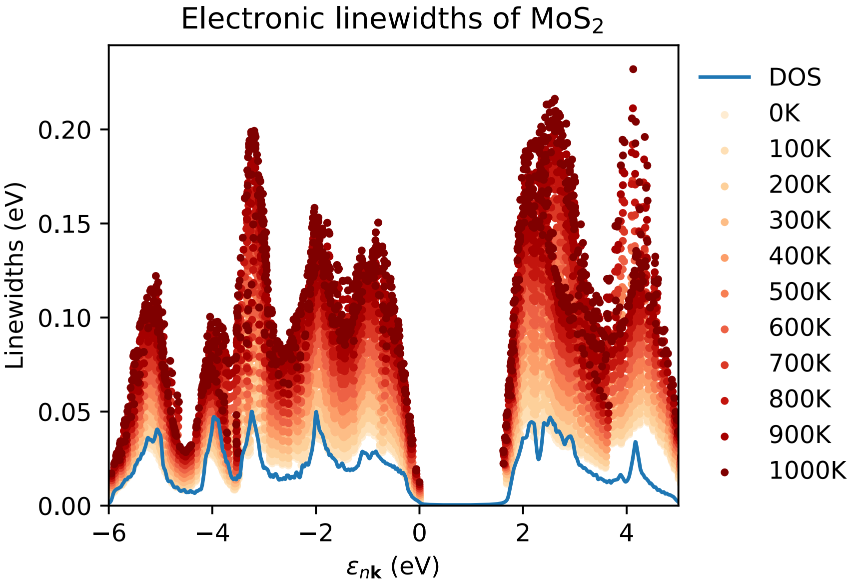

Figure 3.5: Lifetimes of the electronic states of MoS$_2$ as a function of temperature. It can be seen that the lifetimes roughly follow the electronic density of states.

$$\frac{1}{\tau_{n\mathbf{k}}(T)} \propto \alpha \cdot \{n(\omega_\mu, T) + 1\} \cdot DOS(\epsilon_{n\mathbf{k}}) \tag{3.13}$$

where $\tau_{n\mathbf{k}}(T)$ is the lifetime of the electronic state $\epsilon_{n\mathbf{k}}$ and $n(\omega_\mu, T)$ is the Bose-Einstein distribution. We remark that the definition of α in Eq. (3.13) depends on the broadening factor (0.1 eV) used to calculate the DOS. The ω_μ is an effective vibrational frequency on the order of magnitude of the phonon modes of the system. We fitted the function of Eq. (3.13) to the data from Fig. 3.5 and obtained the data in Fig. 3.6. This result indicates that if we are interested in the phonon lifetimes alone, we can estimate them from a calculation of a small set of data and extrapolate it for different temperatures. This estimative can be a good starting guess for calculations where only qualitative results are neces-

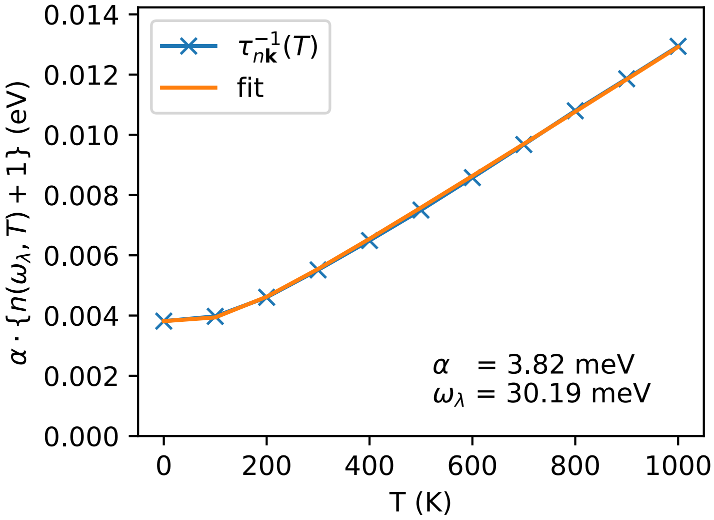

Figure 3.6: Fit of the dependence of the lifetimes on temperature. The crosses represent *ab initio* data and the fit is done using Eq. (3.13).

sary. The explicit calculation of the lifetimes in the full Brillouin zone is still desired for high accuracy and comparison with experiments.

3.3.1 Band structure and lifetimes interpolation using a Wannier basis

We interpolated the lifetimes using a newly developed technique based on the interpolation of the eigenvalues using Wannier functions [84]. In the same way that the Wannier basis proves to be efficient in interpolating band structures we decided to use this approach to interpolate other quantities related to the band-structure. The method is quite general, and in principle any quantity that depends on the band structure and the electronic states can be interpolated using this technique (orbital decomposition, electronic lifetimes, quasi-particle energies, spectral function, excitonic weights).

In a Wannier basis the $\mathbf{k}$ dependent electronic Hamiltonian is obtained by

Fourier transforming it into

$$H^{\epsilon}_{ij\mathbf{k}} = \sum_{i} \frac{1}{N_{\mathbf{r}}} H^{\epsilon}_{ij}(\mathbf{r}) e^{i\mathbf{r}\cdot\mathbf{k}}, \tag{3.14}$$

where H^{ϵ}_{ij} is the Hamiltonian projected in Wannier basis, $\mathbf{r}$ is the position of the unit cell copy of the atomic orbital in real space and $N_{\mathbf{r}}$ is the number of equivalent copies (degeneracy). Diagonalizing $H^{\epsilon}_{ij\mathbf{k}}$ we obtain pairs of eigenvalues $\epsilon_{n\mathbf{k}}$ and states $\psi^{\epsilon}_{in\mathbf{k}}$. The idea is to use the Fourier interpolation determined by the states to expand the quantities on arbitrarily fine $\mathbf{k}$-grids. This can be done by rebuilding a different Hamiltonian (on a regular $\mathbf{k}$-mesh) with the quantities we want to interpolate in a similar way as we would rebuild the $H^{\epsilon}_{ij\mathbf{k}}$ Hamiltonian

$$H^{\epsilon}_{ij\mathbf{k}} = \sum_{l} (\psi^{\epsilon}_{il\mathbf{k}}) \epsilon_{l\mathbf{k}} (\psi^{\epsilon}_{lj\mathbf{k}})^{*}, \tag{3.15}$$

$$H^{a}_{ij\mathbf{k}} = \sum_{l} (\psi^{\epsilon}_{il\mathbf{k}}) a_{l\mathbf{k}} (\psi^{\epsilon}_{lj\mathbf{k}})^{*}. \tag{3.16}$$

Then we transform this Hamiltonian to real space again

$$H^{a}_{ij}(\mathbf{r}) = \sum_{\mathbf{k}} H^{a}_{ij\mathbf{k}} e^{i\mathbf{r}\cdot\mathbf{k}}. \tag{3.17}$$

Using this Hamiltonian we can now recover $H^{a}_{ij\mathbf{k}}$ at any arbitrary $\mathbf{k}$-point mesh using Equation (3.14). In a practical implementation, it is desired to keep the order of the eigenstates and the quantity being interpolated to assign the correct quantity to the correct state. One way to accomplish that is to use the eigenstates from $H^{\epsilon}_{ij\mathbf{k}}$ to obtain the eigenvalues of $H^{a}_{ij\mathbf{k}}$ by writing

$$a_{l\mathbf{k}} = (\psi^{\epsilon}_{il\mathbf{k}}) H^{a}_{ij\mathbf{k}} (\psi^{\epsilon}_{il\mathbf{k}}). \tag{3.18}$$

In Fig. 3.7 we show the application of this method to interpolate the quasiparticle eigenvalues and lifetimes due to electron-phonon interaction at different temperatures for MoS_2.

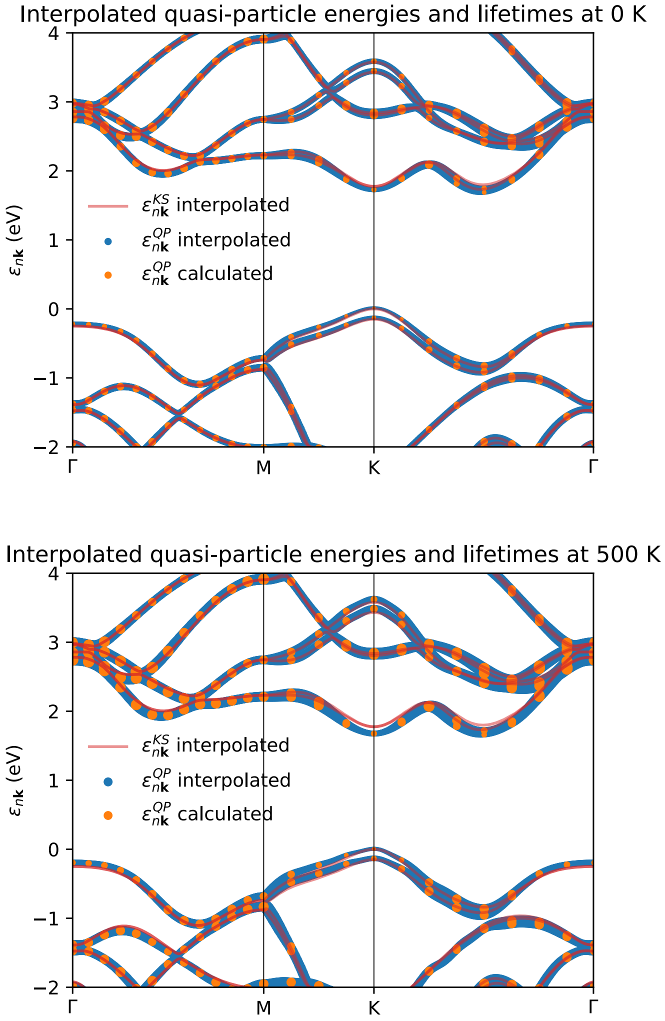

Figure 3.7: Band structure of MoS_2 and linewidths due to electron-phonon coupling calculated using the `yambo` code [55]. The linewidths are interpolated using the technique described above. The size of the calculated states and the width of the interpolated ones represents the linewidth of the state.

3.4 Conclusions

In this chapter we described how the electron-phonon matrix elements are calculated in the `ph.x` code. These quantities are then used in the expressions of the electron self-energy due to electron-phonon interaction (Eq. (3.8) and Eq. (3.9)) to calculate the temperature dependent band-structure of MoS_2. This includes mainly two effects: the band gap renormalization and lifetime dependence on temperature.

The approaches outlined here will be used to calculate the electronic lifetimes and band gap renormalization of MoS_2 to be used in Chapter 4 to calculate the temperature dependent optical spectra and in Chapter 6 to calculate the temperature dependent Raman spectra.

It should be noted that in the cases where there is a strong electron-phonon coupling, the nuclei should be treated explicitly as moving particles with their own density, beyond the BOA [85]. This approach however is more computationally costly as it requires the electronic and ionic density to be treated simultaneously. In the systems we consider, these effects are small and can be included perturbatively using the approaches outlined here.

4

Electron-light coupling: Optical absorption

4.1 Optical properties

When light shines on a medium, different processes can occur as schematically shown in Fig. 4.1. Part of the light is directly reflected, another part is scattered (elastically or inelastically) and the rest is either transmitted or absorbed. Some of the light that was absorbed will create excitations in the material which after some time will decay and recombine emitting light again in a process known as photoluminescence.[1] In this chapter we will study optical absorption, leaving the case of light scattering in particular Raman scattering to be treated in the next chapters. We will first show that the different components of the light after interaction with the material can be written in terms of the dielectric susceptibility tensor calculated from linear response theory. Next we will outline how to calculate the dielectric susceptibility tensor on the independent-particle level, and on the many-body level combining the GW approximation and Bethe-Salpeter equation (BSE). The results of the BSE yield information about the correlated movement of electrons and holes in the system.

---

[1] Good introductions to the topic of light-matter interaction are found in [14, Chapter 1], [30, Chapters 6 and 7] and [86, Chapter A].

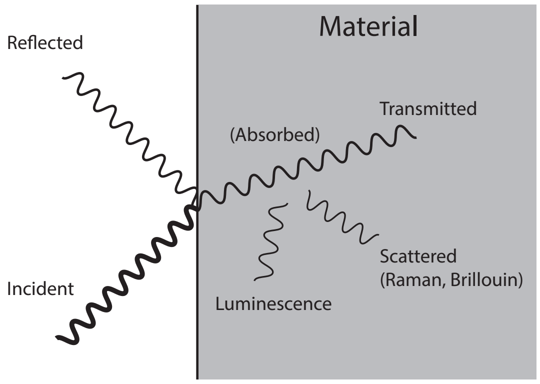

Figure 4.1: Different light-matter interaction processes as shown in Ref [30]. Both the absorption and Raman scattering are dissipative processes.

To better understand this, we will analyze and represent the wave functions of electrons and holes in the system.

4.2 Macroscopic electrodynamics

Applying an electromagnetic field to a dielectric medium will induce a polarization, $\mathbf{P}(\mathbf{r}, t)$, given by [87]

$$\mathbf{P}(\mathbf{r}, t) = \epsilon_0 \int \overline{\overline{\chi}}(\mathbf{r}, \mathbf{r}', t, t') \cdot \mathbf{E}(\mathbf{r}', t') d^3\mathbf{r}' dt', \tag{4.1}$$

where $\overline{\overline{\chi}}(\mathbf{r}, \mathbf{r}', t, t')$ is the most general form of the dielectric susceptibility tensor which relates the incident electric field to the polarization created in the material as a response and ϵ_0 is the vacuum permittivity. Time is homogeneous in the absence of time-dependent perturbations. For the discussion in this section we consider that space is also homogeneous $\overline{\overline{\chi}}(\mathbf{r}, t)$ [30]. The susceptibility is also called response function of the material. A response function is a general concept that relates a perturbation to an effect, i.e. how the material responds to an external force. In this case, the force is caused by the electric field, and the response is the creation of a polarization. The total field inside the material is given by the electric displacement vector $\mathbf{D}(\mathbf{r}, t)$. It is the sum of the external field and the induced polarization field inside the material

$$\mathbf{D}(\mathbf{r},t) = \epsilon_0 \mathbf{E}(\mathbf{r},t) + 4\pi \mathbf{P}(\mathbf{r},t) = \epsilon_0 \bar{\bar{\epsilon}} \mathbf{E}(\mathbf{r},t), \tag{4.2}$$

where $\bar{\bar{\epsilon}}$ is the dielectric tensor that relates the field inside the material to an external electric field

$$\bar{\bar{\epsilon}}(\mathbf{r},t) = \bar{\bar{\mathbb{1}}} + 4\pi \bar{\bar{\chi}}(\mathbf{r},t). \tag{4.3}$$

The real part of the susceptibility can be related to the refractive index while the imaginary part is related to absorption [87, 88]. Consider Maxwell's equations in the absence of charges and currents with a time-dependent electric field $\mathbf{E}(r,t)$

$$\nabla \times \mathbf{H} = -i\omega\epsilon_0 \bar{\bar{\epsilon}} \cdot \mathbf{E}, \tag{4.4}$$

$$\nabla \times \mathbf{E} = i\omega\mu_0 \mathbf{H}, \tag{4.5}$$

$$\nabla \cdot \mathbf{E} = 0. \tag{4.6}$$

with the electric field represented by a damped plane wave traveling in the z direction in the cartesian plane oscillating with frequency ω

$$\mathbf{E} = E_0 e^{-i(\omega t + n k_0 \cdot z)} e^{-\alpha z} \hat{k}. \tag{4.7}$$

In this case, the damping constant α is related to absorption of the electromagnetic wave because the amplitude of the electric field is diminishing exponentially as a function of the distance traveled in the material. Combining Eqs. 4.4 and 4.5 we obtain

$$\nabla \cdot (\nabla \cdot \mathbf{E}) - \nabla^2 \mathbf{E} = \omega^2 \epsilon_0 \mu_0 \bar{\bar{\epsilon}} \mathbf{E}. \tag{4.8}$$

using $c = (\epsilon_0 \mu_0)^{-1/2}$ and Eq. 4.6. Separating $\bar{\bar{\epsilon}}$ into its real and imaginary parts we obtain

$$\bar{\bar{\epsilon}} = \bar{\bar{\epsilon}}_1 + i\bar{\bar{\epsilon}}_2 = (n + i\alpha/k_0)^2, \tag{4.9}$$

$$\bar{\bar{\epsilon}}_1 = n^2 - \frac{\alpha^2}{2k_0}, \tag{4.10}$$

$$\bar{\bar{\epsilon}}_2 = in\frac{\alpha}{k_0}, \tag{4.11}$$

which indicates that the imaginary part of the dielectric tensor is related to the extinction ($\alpha > 0$) or creation ($\alpha < 0$) of the oscillating electric field inside the material. In the case $\alpha > 0$ part of the energy of the field is absorbed in the material. It is a general statement, known as the *fluctuation-dissipation theorem* [86, 89] where the imaginary part of a linear response function is related to the dissipation of energy. The theorem relates a fluctuation of the internal coordinates to a quantity characteristic of energy loss. The case of optical absorption (the energy loss part) is related to the fluctuation of the polarization in the material due to the incident electromagnetic field.

4.3 Microscopic electrodynamics

4.3.1 Electron-light interaction Hamiltonian

We want to describe the interaction of an electromagnetic field with the sample. Let us consider the same situation in the previous section of a system with electrons interacting with an external electromagnetic field. We want to obtain a Hamiltonian of the form

$$\hat{H} = \hat{H}_0 + \hat{H}_L + \hat{H}_{\mathrm{e-L}}, \tag{4.12}$$

where the first term is the Hamiltonian describing electrons, the second one the photons and the third term describes the coupling with the electromagnetic field defined by the electromagnetic potential $\hat{\mathbf{A}}(\mathbf{r})$.

The Hamiltonian from Eq. (4.12) comes by modifying a term in our electronic structure Hamiltonian in Eq. (1.2) that yields the coupling of the electrons with an electromagnetic field [86]. This replacement is called *minimal coupling* and consists of substituting $\hat{\mathbf{p}} \rightarrow \hat{\mathbf{p}} - e\hat{\mathbf{A}}(\mathbf{r})$ leading to

$$\begin{aligned} \hat{H} &= \frac{1}{2m_e}\sum_j \left(\hat{\mathbf{p}}_j - e\hat{\mathbf{A}}(\mathbf{r})\right)^2 + \hat{V}(\mathbf{r}) \\ &= \frac{1}{2m_e}\sum_j \hat{\mathbf{p}}_j^2 - \frac{e}{m_e}\hat{\mathbf{p}}_j \cdot \hat{\mathbf{A}}(\mathbf{r}) + \frac{e^2}{2m_e}\hat{\mathbf{A}}^2(\mathbf{r}) + \hat{V}(\mathbf{r}), \end{aligned} \tag{4.13}$$

where $\hat{\mathbf{p}}_j = -i\hbar\nabla_j$ is the momentum operator of the electrons and $\hat{\mathbf{A}}(\mathbf{r})$ is the electromagnetic vector potential. As is common practice in the literature, we ignore the term in e^2 that should only play a role in strong electromagnetic fields [90].

To make the connection between the electromagnetic fields and the potentials $(\hat{\mathbf{A}}, \phi)$ we choose the transverse gauge $\nabla \cdot \hat{\mathbf{A}} = 0$ and $\phi = 0$. In this gauge we have to use the transverse response formalism introducing a $\hat{\mathbf{p}} \cdot \hat{\mathbf{A}}(\mathbf{r})$ type coupling (velocity gauge) [91]. However, since the electromagnetic wave vector $\mathbf{q}$ is small when compared to the crystal momentum[1] the electromagnetic field can also be treated as a longitudinal perturbation using $\hat{\mathbf{r}} \cdot \hat{\mathbf{E}}(\mathbf{r})$ type coupling (length gauge). Indeed it can be shown that in the dipole approximation, which corresponds to taking the $\mathbf{q} \rightarrow 0$ limit, both approaches are equivalent as long as the charge conservation equation is fulfilled [91]. In the following we will use the $\hat{\mathbf{r}} \cdot \hat{\mathbf{E}}(\mathbf{r})$ type coupling. To ensure charge conservation the velocity matrix elements are obtained from the commutator

$$\hbar\hat{\mathbf{v}}_j = i[\hat{H}, \hat{\mathbf{r}}_j] \tag{4.14}$$

where $\hat{\mathbf{r}}_j$ is the position of the electron. This leads to an additional contribution in the computation of the electron-light matrix elements that is related to the commutator of the $\hat{\mathbf{r}}_j$ position operator and the non-local part of the Hamiltonian. This part has its origins in the pseudo-potentials we use to describe

---

[1] Experiments are typically made with lasers in the visible range with a wavelength of 380 nm - 750 nm while the crystal lattices are in the 0.2 nm - 0.6 nm range.

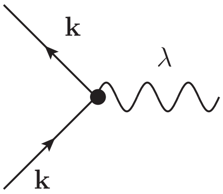

Figure 4.2: Graphical representation of the electron-light coupling vertex.

the electrons close to the atomic core. The pseudo-potentials are non-local and hence do not commute with $\hat{\mathbf{r}}_j$ (position of the electron). Thus an additional term must be considered explicitly [91]

$$\hat{\mathbf{v}}_j = \sum_j \left(\frac{\hat{\mathbf{p}}_j}{m_e} + \frac{i}{\hbar}[\hat{V}_{NL}, \hat{\mathbf{r}}_j] \right), \tag{4.15}$$

where $\hat{V}_{NL}$ denotes the non-local part of the pseudo-potential. The matrix elements of this operator are related to the position matrix elements in the dipole approximation using the commutator in Eq. (4.14). The $\hat{\mathbf{r}}$ matrix elements are the dipole or electron-light coupling matrix elements that we will use throughout this manuscript to describe the interaction of the system with the electromagnetic field

$$\Lambda^{\lambda}_{nn'\mathbf{k}} = \langle n\mathbf{k}|\hat{\mathbf{r}}^{\lambda}|n'\mathbf{k}\rangle, \tag{4.16}$$

where λ is the quantum number of the photon denoting its polarization and frequency, n and n' are the bands of the system. In this work we will use implementations openly available in the community [55, 79, 92, 72] to calculate these matrix elements. It should be noted that in the current implementation in EPW the electron-photon coupling matrix elements are calculated in the local approximation [92], i.e. not including the commutator in Eq. (4.15). This fact is important in the calculation of the Raman intensities as we will discuss in Chapter 6.

The electromagnetic fields can be quantized and described in terms of their normal coordinates

$$\hat{\mathbf{A}}(\mathbf{r}) = \sum_{\lambda\mathbf{q},} \sqrt{\frac{2\pi}{\omega_{\lambda,\mathbf{q}} V}} [\hat{b}_{\lambda,\mathbf{q}} e^{i\mathbf{q}\cdot\mathbf{r}} + \hat{b}^{\dagger}_{\lambda,\mathbf{q}} e^{-i\mathbf{q}\cdot\mathbf{r}}] \mathbf{e}_{\lambda}(\mathbf{q}), \tag{4.17}$$

where $\hat{b}^{\dagger}_{\mathbf{q}\lambda}$ and $\hat{b}_{\mathbf{q}\lambda}$ are the photon creation and annihilation operators, $e_{\lambda}(\mathbf{q})$ denotes the polarization of the electric field, and V is the quantization volume. The Hamiltonian for light is given by

$$H_L = \sum_{\lambda,\mathbf{q}} \hbar\omega_{\lambda,\mathbf{q}} \left(\hat{b}_{\lambda,\mathbf{q}} \hat{b}^{\dagger}_{\lambda,\mathbf{q}} + \frac{1}{2} \right) \tag{4.18}$$

where ω_{λ} is the frequency of the photons. The electron-light coupling Hamiltonian in the long-wavelength limit ($\mathbf{q} = 0$) is given by

$$\hat{H}_{\mathrm{e-L}} = \sum_{\lambda n n' \mathbf{k}} \Lambda^{\lambda}_{nn'\mathbf{k}} \hat{c}^{\dagger}_{n\mathbf{k}} \hat{c}_{n'\mathbf{k}} (\hat{b}_{\lambda} + \hat{b}^{\dagger}_{\lambda}). \tag{4.19}$$

4.4 Optical absorption in the independent-particle picture

Let us now calculate the optical response of the material to an external electric field from a purely perturbative approach. Here we will use the framework of many-body perturbation theory to expand the Green's function of the dielectric susceptibility in terms of the electronic states. The advantage of this formulation is that we can obtain a perturbative series expansion of the Green's function and gradually include more interactions. We will start from the simplest case where the incident laser field excites the electron from its ground state leaving a hole behind and then both recombine. This process can be represented diagrammatically as shown in Fig. 4.4. This diagram can also be thought of as the first order contribution to the self-energy of the photon in the dielectric medium, which in this case is the material under study.

The first-order polarizability of the electrons at finite temperature is shown

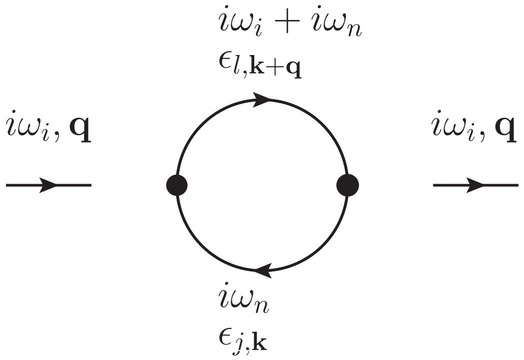

Figure 4.3: Polarization bubble in the independent-particle formalism.

diagrammatically in Fig. 4.3 and is mathematically given by

$$\begin{aligned}\Pi^0(\mathbf{q}, i\omega_i) &= \frac{1}{\beta}\sum_{jl\mathbf{k}}\sum_{n=-\infty}^{+\infty} \mathcal{G}^0_{j,\mathbf{k}}(\omega_n)\mathcal{G}^0_{l,\mathbf{k}+\mathbf{q}}(i\omega_i + \omega_n) \\ &= \frac{1}{\beta}\sum_{jl\mathbf{k}}\sum_{n=-\infty}^{+\infty} \frac{1}{i\omega_n - \epsilon_{j,\mathbf{k}}} \cdot \frac{1}{i\omega_i + i\omega_n - \epsilon_{l,\mathbf{k}+\mathbf{q}}}.\end{aligned} \tag{4.20}$$

Summing over the Matsubara frequencies we obtain [50, Chapter 14]

$$\Pi^0(\mathbf{q}, i\omega_i) = \sum_{jl\mathbf{k}} \frac{f(\epsilon_{j,\mathbf{k}}) - f(\epsilon_{l,\mathbf{k}+\mathbf{q}})}{i\omega_i - (\epsilon_{l,\mathbf{k}+\mathbf{q}} - \epsilon_{j,\mathbf{k}})}. \tag{4.21}$$

In a similar way as we did in Eq. (3.8) we analytically continue to the real axis using $i\omega_i \to \omega + i\gamma$

$$\Pi^0(\mathbf{q}, \omega) = \sum_{jl\mathbf{k}} \frac{f(\epsilon_{j,\mathbf{k}}) - f(\epsilon_{l,\mathbf{k}+\mathbf{q}})}{\omega - (\epsilon_{l,\mathbf{k}+\mathbf{q}} - \epsilon_{j,\mathbf{k}}) + i\gamma}. \tag{4.22}$$

The susceptibility can be calculated in terms of operators from Fig. 4.4 with [93]

$$\chi^{SL}(\omega_L) \propto \int \frac{d^2\mathbf{k}}{(2\pi)^2}\frac{d\omega}{2\pi} e^{i\omega 0^+} Tr\left\{\hat{G}^0(\mathbf{k}, \omega)\hat{d}^S(\mathbf{k})\hat{G}^0(\mathbf{k}, \omega - \omega_L)\hat{d}^L(\mathbf{k})\right\}. \tag{4.23}$$

Note that at this point the definition does not depend on the particular basis

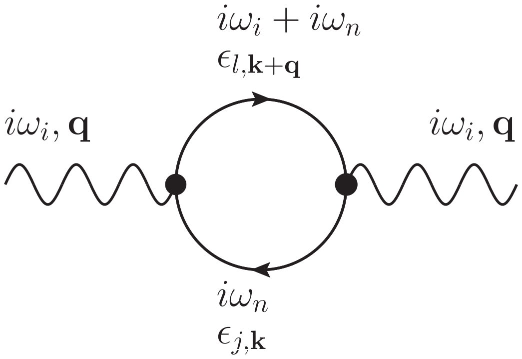

Figure 4.4: First order Feynman diagram for the dielectric response.

that we choose for the problem. To calculate the susceptibility we need to introduce a basis to describe the electronic states, the electron-phonon, and the electron-photon coupling matrix elements. The particular origin of the matrix elements is not important, these can be obtained from density functional theory calculations based on any basis set or semi-empirical models like tight binding or **k**.**p**. In the case of DFT calculations it is typical to describe the electrons on a discrete mesh of **k**-points. One can go back to the continuous dependence on **k**, however this is only relevant for cases where an analytic description of the matrix elements and eigenvalues is available. This is the case for **k**.**p** empirical models or the tight-binding description of materials with few bands.

With the discretization in reciprocal space and projecting the operators into a basis we obtain

$$\chi^{SL}(\omega_L) \propto \frac{1}{N_{\mathbf{k}}} \sum_{ij\mathbf{k}} \int \frac{d\omega}{2\pi} e^{i\omega 0^+} \left\{ G^0_{i\mathbf{k}}(\omega) \Lambda^S_{ij\mathbf{k}} G^0_{j\mathbf{k}}(\omega - \omega_L) \Lambda^L_{ji\mathbf{k}}. \right\} \tag{4.24}$$

The factor $e^{i\omega 0+}$ suggests a contour integration in ω in the upper half plane

$$\begin{aligned} \chi^{SL}(\omega_L) \propto \frac{1}{N_{\mathbf{k}}} \sum_{ij\mathbf{k}} \Bigg\{ & \left[f(\epsilon_{i\mathbf{k}}) \Lambda^S_{ij\mathbf{k}} G^0_{j\mathbf{k}}(\omega - \omega_L) \Lambda^L_{ji\mathbf{k}} \right]_{\omega = \epsilon_{i\mathbf{k}} + i\gamma/2} + \\ & \left[f(\epsilon_{j\mathbf{k}}) \Lambda^L_{ij\mathbf{k}} G^0_{i\mathbf{k}}(\omega) \Lambda^S_{ji\mathbf{k}} \right]_{\omega = \omega_L + \epsilon_{j\mathbf{k}} + i\gamma/2} \Bigg\} \end{aligned} \tag{4.25}$$

Substituting the form of the Green's function of equation (1.31) we obtain

$$\chi^{SL}(\omega_L) \propto \sum_{ij\mathbf{k}} \left\{ \frac{f(\epsilon_{i\mathbf{k}})(1-f(\epsilon_{j\mathbf{k}}))\Lambda^S_{ij\mathbf{k}}\Lambda^L_{ji\mathbf{k}}}{-\omega_L-(\epsilon_{j\mathbf{k}}-\epsilon_{i\mathbf{k}})+i\gamma} + \frac{f(\epsilon_{j\mathbf{k}})(1-f(\epsilon_{i\mathbf{k}}))\Lambda^S_{ij\mathbf{k}}\Lambda^L_{ji\mathbf{k}}}{\omega_L-(\epsilon_{i\mathbf{k}}-\epsilon_{j\mathbf{k}})+i\gamma} \right\}. \tag{4.26}$$

This is the most general form of the susceptibility and it can be applied to metals. In the case of a semiconductor where we can clearly define valence and conduction bands, this simplifies to

$$\chi^{SL}(\omega_L) \propto \sum_{cv\mathbf{k}} \left\{ \frac{\Lambda^S_{vc\mathbf{k}}\Lambda^L_{cv\mathbf{k}}}{\omega_L-(\epsilon_{c\mathbf{k}}-\epsilon_{v\mathbf{k}})+i\gamma} + \frac{\Lambda^S_{vc\mathbf{k}}\Lambda^L_{cv\mathbf{k}}}{-\omega_L-(\epsilon_{c\mathbf{k}}-\epsilon_{v\mathbf{k}})+i\gamma} \right\}. \tag{4.27}$$

We can again verify that the imaginary part of the susceptibility gives us the optical absorption using the following identity [50]

$$\lim_{\gamma\to 0^+} \frac{1}{x \pm i\gamma} = P\frac{1}{x} \mp i\pi\delta(x). \tag{4.28}$$

This allows us to write the imaginary part of the susceptibility in terms of

$$\text{Im}\{\chi(\omega_L)\} \propto \sum_{cv\mathbf{k}} \Lambda^S_{cv\mathbf{k}}\Lambda^L_{cv\mathbf{k}}\delta(\omega_L-\Delta\epsilon_{cv\mathbf{k}}), \tag{4.29}$$

with $\Delta\epsilon_{cv\mathbf{k}} = \epsilon_{c\mathbf{k}} - \epsilon_{v\mathbf{k}}$. Equation (4.29) indicates us that the absorption is always positive, which in turn means that for a system in equilibrium the radiation always looses energy to the system. If the particles have a finite lifetime, the delta function is broadened to a Lorentzian. If we consider the electron-light coupling matrix elements as a constant, the dielectric function is proportional to the joint-density of states (JDOS). The JDOS in turn corresponds to a histogram of the possible vertical transitions between valence and conduction bands energies.

4.4.1 The case of $MoTe_2$

Using Eq. (4.29) we can evaluate the optical absorption of $MoTe_2$ in the IP approximation. Understanding which electronic transitions contribute to it will help to interpret the Raman spectra [94] in Chapter 5. The calculations of the electronic band-structure were performed using the `pw.x` code from the `QE` [79] suite. The wave functions were obtained on a $60 \times 60 \times 1$ $\mathbf{k}$-grid in the Brillouin zone. We used a 90 Ry cutoff for the plane-wave basis set and the experimental lattice parameter of 3.52 Å [35]. The electron-light coupling matrix elements were calculated using the `yambo` code [55]. The results for single- and triple-layer $MoTe_2$ are shown in Fig. 4.5. Both in the case of single and triple-layer $MoTe_2$, the edge of the absorption is due to band-to-band transitions around K (red line). In the case of a 2D material with parabolic bands near the gap, the DOS looks like a step function. The same behavior occurs in the optical absorption spectra since the absorption is roughly proportional to the JDOS (See Eq.(4.29)). The valence bands are split due to spin-orbit coupling interaction by an energy of around 222 meV. This leads to a second plateau in the absorption spectrum (green lines). Finally at around 1.5 eV the bands near M and in the pocket between K and Γ start to contribute (blue line).

The results for IP absorption will be used in Chapter 5 to obtain the Raman susceptibility by finite differences upon atomic displacements. In Fig. 4.5 panel c) and d), we have demonstrated that the features in the absorption spectrum can be associated with electron-hole pair transitions at a certain energy. The connection between the absorption spectra and the band structure is sometimes cumbersome to establish. To clarify this connection, we will describe two additional representations.

In the case of the IP absorption, all the contributions add up since we sum the square of the matrix elements in Eq. (4.29) [1]. We can decompose the contri-

---

[1] This is not the case for the Raman susceptibilities where the intensities are proportional to the square of the sum of the contributions across the Brillouin zone as we will show in Chapter 5.

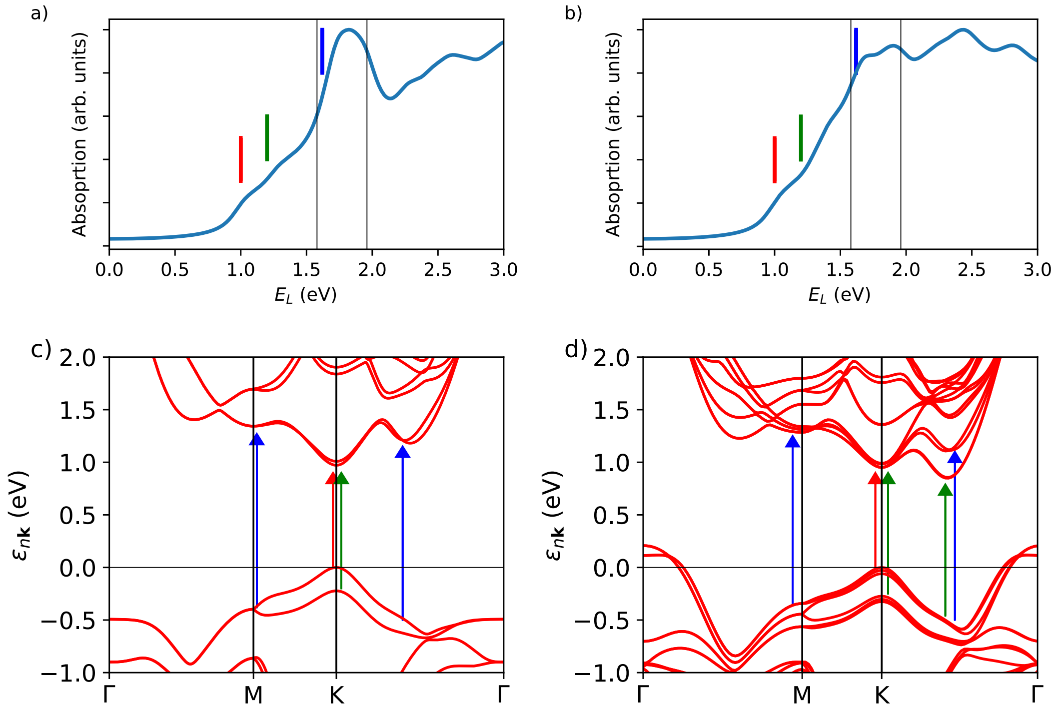

Figure 4.5: Independent-particle absorption for single- and triple-layer MoTe_2 in panel a) and b) respectively. The vertical lines at $E_L = 1.58$ and $E_L = 1.96$ eV represent the laser energies used in the experiments described in Chapter 5. A broadening of 0.1 eV is used. Electronic band structure of single- and triple-layer MoTe_2 in panel c) and d) respectively. The arrows represent the transitions contributing to the peaks in the optical absorption.

butions from the different **k** points using

$$\text{Im}\{\chi(\omega_L)\} \propto \sum_{\mathbf{k}} \text{Im}\{\chi_{\mathbf{k}}(\omega_L)\}. \tag{4.30}$$

This suggests a representation where the susceptibility is **k**-resolved in the Brillouin zone as a function of laser energy as shown in Fig. 4.6. Alternatively, we show in Fig. 4.7, as a color gradient, $\text{Im}\{\chi_{\mathbf{k}}(\omega_L)\}$ on a **k**-path along the high-symmetry lines in the Brillouin zone for single- and triple-layer MoTe_2. Also shown in Fig. 4.7) in light gray is a dispersion of the electron-hole transitions where energy differences between conduction and valence state energies is represented. The main contributions to $\text{Im}\{\chi(\omega)\}$ for laser energies between

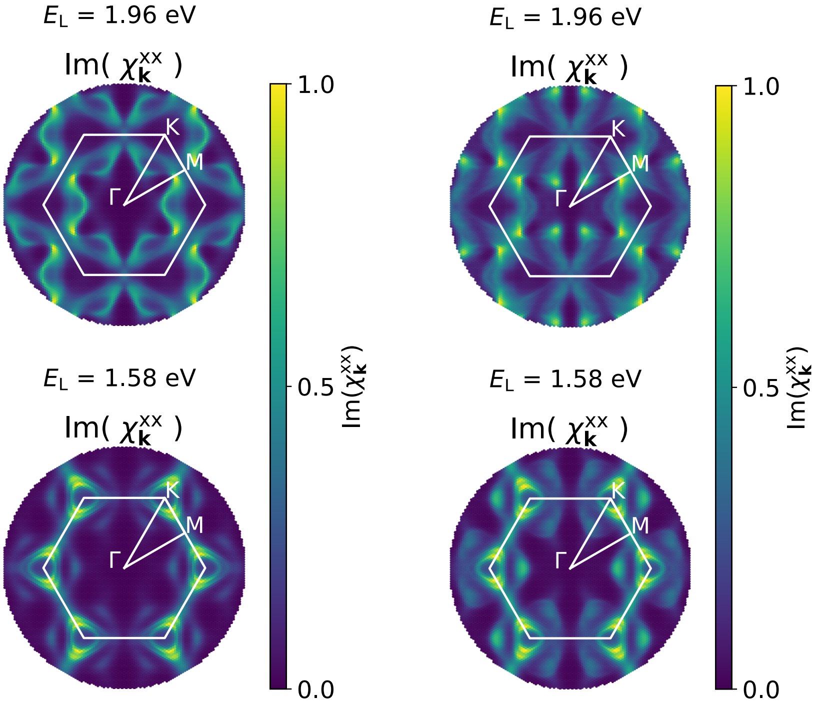

Figure 4.6: IP absorption Im($\chi_{\mathbf{k}}^{xx}$) for single- (left) and triple-layer MoTe$_2$ (right) resolved in the Brillouin zone at two different laser energies $E_L = 1.58$ eV and 1.96 eV. A broadening of 0.1 eV is used to simulate the electronic line width.

0.8 and 2 eV come from the lower bands in the transition representation in a region around K and between K and M.

These types of representations are particularly useful to understand which electronic transitions are contributing to the optical absorption. In combination with knowledge of the evolution of the bands with lattice vibrations (phonons), these representations will be helpful in understanding which bands and which regions in k-space contribute to the resonant Raman spectra of MoTe$_2$ in Chapter 5. In general, this representation may also be useful to understand how to tune the electronic properties as a function of external parameters in order to obtain the desired optical absorption spectra.

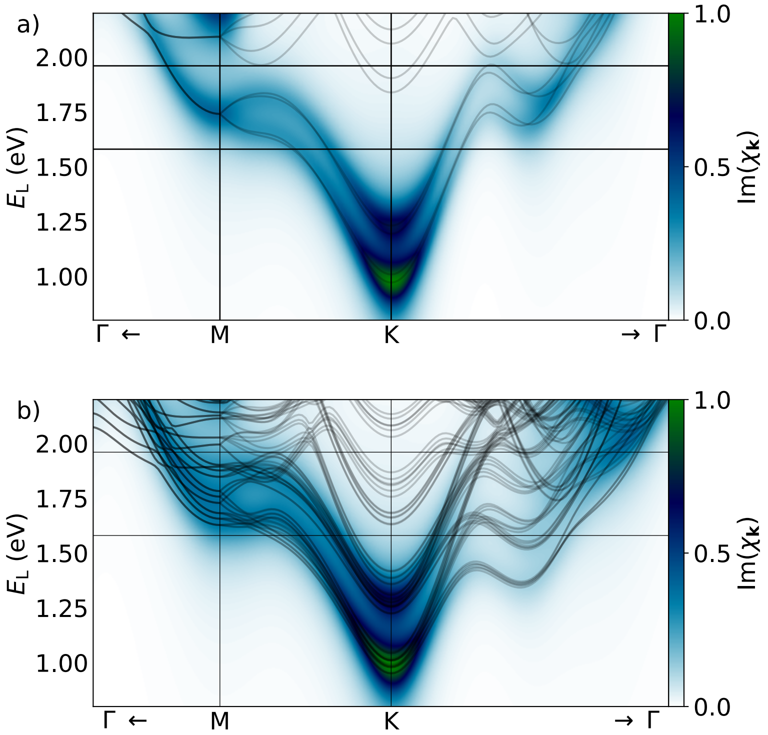

Figure 4.7: a) IP absorption Im($\chi_\mathbf{k}^{xx}$) represented in transition space along the high-symmetry points in the Brillouin zone for single- (panel a) and triple-layer MoTe$_2$ (panel b). We show only points close to M and K as there are no relevant transitions close to the Γ point for laser energies up to 2 eV.

4.5 Many-body effects in the optical absorption

Having calculated the independent-particle dielectric susceptibility we can consider the contribution of higher order terms i.e. different ways the electrons and holes interact. These terms appear when successively perturbing the electronic states with the different interactions in the material similarly to what was done in Chapter 1 and Chapter 3. A pictorial way to interpret this is to imagine the particles in the system moving from one point in space and time while interacting with all the other particles in all possible ways. This means that to calculate the probability of a physical process to happen we have to consider all the possible ways by which the process can happen. As a first step beyond the independent-particle approximation we can calculate the polarizability taking into account that the process represented in diagram in Fig. 4.4 can happen multiple times. This is the random phase approximation (RPA) introduced in Chapter 1. If the electron and hole in the diagrams of Fig. 1.5 interact with each other via the bare and screened Coulomb interaction as in Fig. 4.8 then they start to move together. This means that their propagation in the material is not independent. To account for this, one defines a propagator for the correlated movement of electrons and holes. Starting from Eq. (4.23) we can evaluate the trace

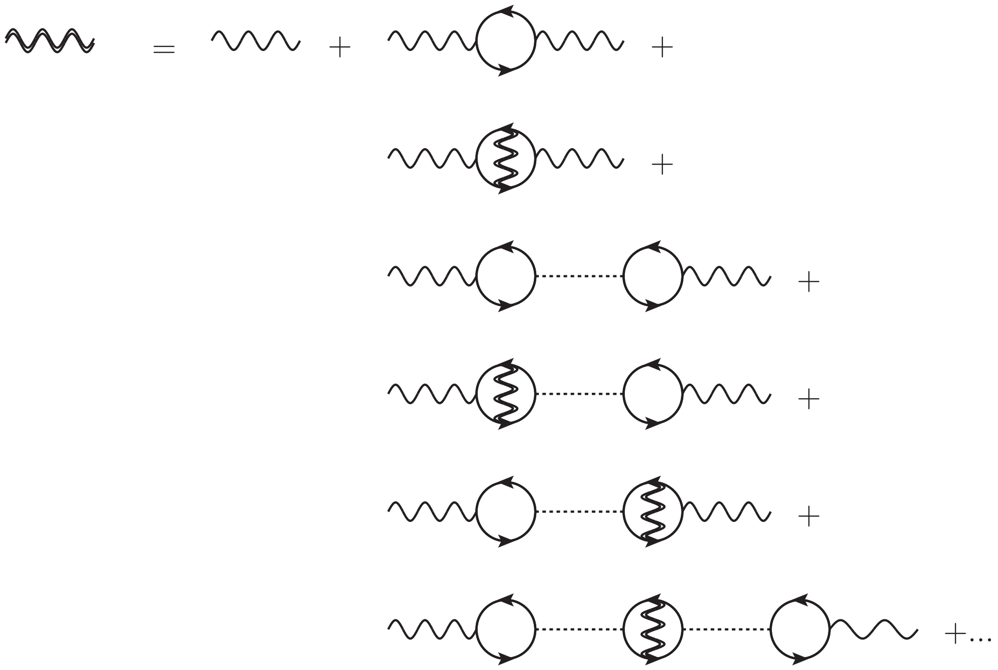

Figure 4.8: Dielectric susceptibility including Coulomb interaction between the electrons and the holes. There are more contributions of higher order not represented here.

$$\chi^{SL}(\omega_L) \propto \int \frac{d^2\mathbf{k}}{(2\pi)^2} \int \frac{d\omega}{2\pi} e^{i\omega 0^+} \left\{ \Lambda^S_{ij\mathbf{k}} \hat{G}^0_{j\mathbf{k}}(\omega) \Lambda^L_{ji\mathbf{k}} \hat{G}^0_{i\mathbf{k}}(\omega - \omega_L) \right\}, \tag{4.31}$$

and re-arrange the equation as

$$\chi^{SL}(\omega_L) \propto \int \frac{d^2\mathbf{k}}{(2\pi)^2} \left\{ \Lambda^S_{ij\mathbf{k}} \Lambda^L_{ji\mathbf{k}} \int \frac{d\omega}{2\pi} e^{i\omega 0^+} G^0_{j\mathbf{k}}(\omega) G^0_{i\mathbf{k}}(\omega - \omega_L) \right\}, \tag{4.32}$$

which, using

$$L^0_{ji\mathbf{k}}(\omega) = \int \frac{d\omega'}{2\pi} e^{i\omega' 0^+} G^0_{j\mathbf{k}}(\omega') G^0_{i\mathbf{k}}(\omega' - \omega), \tag{4.33}$$

can be re-written as

$$\chi^{SL}(\omega_L) \propto \int \frac{d^2\mathbf{k}}{(2\pi)^2} \sum_{\mathbf{k}} \left\{ \Lambda^S_{ij\mathbf{k}} \Lambda^L_{ji\mathbf{k}} \hat{L}^0_{ji\mathbf{k}}(\omega_L) \right\}. \tag{4.34}$$

With this we did not include any new physics in the description of the system. We did, however, define a new object, $L_0(\omega)$, that describes the collective movement of a non-interacting electron-hole pair. If the electron and the hole are not independent, i.e., if they are interacting with each other, this interaction should be taken into account when evaluating the propagator. In this case we define a new propagator $L(\omega)$. The dielectric function then is given by evaluating the diagram in Fig. 4.9. There, the propagator of the interacting electron-hole pair is described by the function $L(\omega)$. The dielectric function including excitonic effects can then be obtained by evaluating the diagram in Fig. 4.9. In the next section we will show how to calculate this new function using the Bethe-Salpeter equation (BSE).

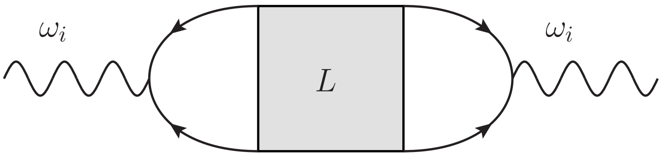

Figure 4.9: Diagram of the dielectric function including excitonic effects.

4.5.1 Bethe-Salpeter equation

The calculation of $L(\omega)$ corresponds to describing the movement of the interacting electron-hole pair. The interaction between them is due to the Coulomb force. It can be direct or mediated by a phonon due to electron-phonon interaction. Depending on how strong these two types of interaction are, it can be important to include them or not. The direct Coulomb interaction between an electron and a hole is stronger than the one mediated by the vibration of the nuclei, which dictates that it is more important to include the former than the later. As the computational methods advance, it will become feasible to include both interactions on the same level as shown in a recent publication [95]. Here, we will follow the standard schemes used in the literature so far and restrict ourselves to the study of the electron-hole interacting through the statically screened Coulomb force [96, 97]. This can be accomplished by summing over all the ladder diagrams of interaction between the electron and the hole in a Dyson equation, which leads us to the Bethe-Salpeter equation [96]

$$\hat{L}^0(\omega_L) = \hat{L}^0(\omega_L) + \hat{L}^0(\omega_L)\hat{K}\hat{L}(\omega_L), \tag{4.35}$$

where $\hat{K}$ is the BSE Kernel with the interactions that will be added in the Dyson equation for the two particle Green's functions. There is a great amount of literature with different derivations of the Bethe-Salpeter equation [98, 96]. Here we will show an approach [99] starting from the Hartree-Fock (HF) approximation and introducing the screening in the same way as done in the case of the GW approximation discussed in Chapter 1. To describe the correlated motion of electrons and holes, we introduce a basis set constructed as a weighted sum of individual electron-hole states

$$|s\rangle = \sum_{cv\mathbf{k}} A^s_{cv\mathbf{k}} \, |c\mathbf{k}\rangle \otimes |v\mathbf{k}\rangle \, , \tag{4.36}$$

where $A^S_{cv\mathbf{k}}$ are the coefficients of the new quasiparticles s written in terms of independent-particle electron and hole states. These particles are commonly called *excitons* as they are formed when an electron is excited to the conduction band and then interacts with the hole left behind. Considering again the many-body Hamiltonian of particles interacting through the Coulomb interaction from Eq. (1.35)

$$\hat{H} = \sum_{ij} h_{ij}\hat{c}_i^\dagger \hat{c}_j + \sum_{ij,nm} V_{ij,nm}\hat{c}_i^\dagger \hat{c}_j^\dagger \hat{c}_n \hat{c}_m, \tag{4.37}$$

where h_{ij} are the single particle Hamiltonian matrix elements, and $V_{ij,nm}$ are the Coulomb matrix elements. Calculating matrix elements of this new Hamiltonian, we get

$$\langle cv\mathbf{k}|\hat{H}|c'v'\mathbf{k}'\rangle = (\epsilon^{\mathrm{HF}}_{c\mathbf{k}} - \epsilon^{\mathrm{HF}}_{v\mathbf{k}})\delta_{cc'}\delta_{vv'}\delta_{\mathbf{k}\mathbf{k}'} - V_{v'c\mathbf{k},vc'\mathbf{k}'} + V_{v'c\mathbf{k},c'v\mathbf{k}'}, \tag{4.38}$$

where $V_{c'v,cv'}$ is the direct Coulomb interaction and $V_{v'c,c'v}$ is the exchange interaction. These two terms have close similarity with the two terms in Hartree-Fock self energy in Fig. 1.2. These can be also be written in terms of the functional derivative of the Hartree-Fock self-energy with respect to the Green's function [98, 100]

$$K(1,2,3,4) = \frac{\delta\Sigma^x(1,3)}{\delta G(2,4)}, \tag{4.39}$$

where each index indicated the coordinates of an electron in space, e.g., $1 = (x_1, t_1)$. We have discussed in Chapter 1 that the Hartree-Fock approximation does not yield good results in extended solids due to the lack of screening of the Coulomb interaction. We have also seen how to overcome this issue by including the screened Coulomb interaction in the RPA approximation in the same way we did in the GW approximation.

This leads to a modification of the direct interaction term $V_{c'v,cv'}$ by a screened one $W_{c'v,cv'}$ and the modification of the quasiparticle energies calculated with Hartree-Fock to the ones calculated with GW:

$$\langle cv\mathbf{k}|\hat{H}|c'v'\mathbf{k}'\rangle = (\epsilon^{\mathrm{GW}}_{c\mathbf{k}} - \epsilon^{\mathrm{GW}}_{v\mathbf{k}})\delta_{cc'}\delta_{vv'}\delta_{\mathbf{k}\mathbf{k}'} - W_{v'c\mathbf{k},vc'\mathbf{k}'} + V_{v'c\mathbf{k},c'v\mathbf{k}'} \tag{4.40}$$

Now that we have a form to the Hamiltonian, we can find the wave functions and energies of the new quasiparticle states by simply diagonalizing it:

$$\sum_{c'v'\mathbf{k}'} \langle cv\mathbf{k}|\hat{H}|c'v'\mathbf{k}'\rangle\, A^S_{c'v'\mathbf{k}} = E_S A^S_{cv\mathbf{k}} \tag{4.41}$$

Due to the size of the matrix (number of transitions time number of **k**-points), we need to be careful in choosing the diagonalization algorithm. In fact, in general, we are just interested in the first few states. The discussion of techniques to reduce the effective size of the Hamiltonian as well as to avoid the diagonalization of the full matrix will be the topic of discussion of the next section.

4.5.2 Diagonalization of the excitonic Hamiltonian

A technical problem arises here when dealing with Hamiltonians of large size. From Eq. (4.41) we see that the size of the Hamiltonian increases both with **k**-sampling as well as the number of bands included. This scaling of the Hamiltonian is quite critical, because the convergence of the optical spectrum is quite slow with the number of **k**-points. Several techniques have been employed to overcome this difficulty. On the one hand, it is possible to obtain the dielectric function using a Haydock iterative scheme [101, 102]. Although very efficient, this class of methods has the major drawback that they do not give direct access to the excitonic wave functions and energies, only to the spectral functions. Another method consists of sampling the quasiparticles on a finer **k**-mesh and in Eq. (4.40) using the values averaged over a set of neighboring **k**-points [103]. Such a technique does not increase the size of the Hamiltonian and leads to excitonic states in good agreement with calculations performed on larger **k**-grids. In the same spirit, one can calculate the excitonic Hamiltonian on a set of shifted grids and average the different obtained spectra [33]. All these different approaches lead to an improvement in the accuracy of the calculations at a smaller computational cost. However, they do not address the issue of obtaining the excitonic energies and wave functions of large systems. A first step to solve this problem is to efficiently parallelize the diagonalization of the excitonic Hamiltonian using the standard distributed linear algebra packages such as SCALAPACK [104]. Such distributions allow the diagonalization of the Hamiltonian of Eq. (4.41) for larger systems or including more valence and conduction states.

One major drawback of these algorithms is that they are designed to perform the diagonalization of the full Hamiltonian matrix. This is expensive in terms of memory and computing power. In addition, in most applications we are only interested in the excitons with lower energy, hence it is not required to obtain all the states. Here we propose and demonstrate an approach that relies on using iterative methods to calculate the excitonic wave functions and energies. We implemented this approach in the `yambo` code using the open-source library SLEPC [105]. This library allows one to use matrix-free methods for the calculation of eigenvalues and eigenvectors. In a matrix-free method, the diagonalization routine does not need to directly access the Hamiltonian. Instead, the input is another routine that calculates the product of the excitonic Hamiltonian with a vector. Using the SLEPC library makes it possible to adapt codes that currently use Haydock methods to calculate the excitonic absorption spectra to also obtain excitonic wave functions and energies. Additionally these methods can be combined with the interpolation schemes mentioned above, allowing the study of excitonic states on large extended systems. The excitonic states can, furthermore, serve as input for additional calculations. One of the applications that we envision for this implementation is to use these excitonic states to calculate the Raman intensities in a perturbative way as we will describe in the IP case in Chapter 6.

4.5.3 Optical absorption spectra with excitons: $MoTe_2$

Once we have obtained the excitonic states in Eq. (4.36), we can use them to calculate the optical absorption spectra. The dielectric susceptibility is obtained in terms of the excitonic states

$$\chi(\omega_L) \propto \sum_s \frac{\langle 0|\hat{H}_{\mathrm{e-L}}|s\rangle \langle s|\hat{H}_{\mathrm{e-L}}|0\rangle}{\omega_L - E_s + i\gamma} + \frac{\langle 0|\hat{H}_{\mathrm{e-L}}|s\rangle \langle s|\hat{H}_{\mathrm{e-L}}|0\rangle}{-\omega_L - E_s + i\gamma}, \tag{4.42}$$

where E_s are the excitonic energies and $|s\rangle$ the eigenstates obtained from Eq. (4.41) and γ is the excitonic line width.

The matrix elements of the coupling with the electric field can be obtained from

$$\begin{aligned} (\langle S| \otimes \langle 0|)\hat{H}_{\mathrm{e-L}}\,|s\rangle &= \sum_{cv\mathbf{k}} A^s_{cv\mathbf{k}}\,\langle 0|\hat{b}^S \hat{H}_{\mathrm{e-L}} \hat{c}^\dagger_{c\mathbf{k}} \hat{c}_{v\mathbf{k}}|0\rangle \qquad (4.43)\\ &= \sum_{cv\mathbf{k}} A^s_{cv\mathbf{k}} \Lambda^S_{cv\mathbf{k}} = \Gamma^S_s, \qquad (4.44) \end{aligned}$$

which, when inerted into Eq. (4.42), leads to

$$\chi(\omega_L) \propto \sum_s \frac{\Gamma^S_s \Gamma^{L*}_s}{\omega_L - E_s + i\gamma} + \frac{\Gamma^S_s \Gamma^{L*}_s}{-\omega_L - E_s + i\gamma}. \tag{4.45}$$

Using this equation as implemented in the `yambo` [55] code we evaluated the optical response including many-body effects of single- and triple layer MoTe$_2$. This is done including the GW correction in the form of a scissor shift and the BSE equation. The wave functions were obtained on a $36 \times 36 \times 1$ **k**-point sampling in the Brillouin zone. We used a 40 Ry cutoff for the plane-wave basis set and a Coulomb cutoff technique [106] to avoid spurious interactions between the periodic copies in the z-direction and a vacuum separation of 50 and 70 Bohr for single- and triple-layer, respectively. The results obtained using the Haydock method and the `slepc` library are shown in Figs. 4.10 and 4.11.

The first peak in both single- and triple-layer is labeled the A exciton [107]. The second peak is due to the spliting of the bands due to spin-orbit interaction as mentioned in the IP analysis in Section 4.4.1. The inter-layer interaction contributes additionally to the splitting of the excitonic states.

While it is possible to get a good description of the spectra using the Haydock method, it does not allow us to obtain the excitonic wave functions. This is, however, possible when using the `slepc` library. In it we choose to find the first N eigenstates of the full excitonic Hamiltonian. This means that we do not make any approximation in including less transitions in the Hamiltonian. Instead, we generate the full Hamiltonian but determine explicitly only a set of eigenstates.

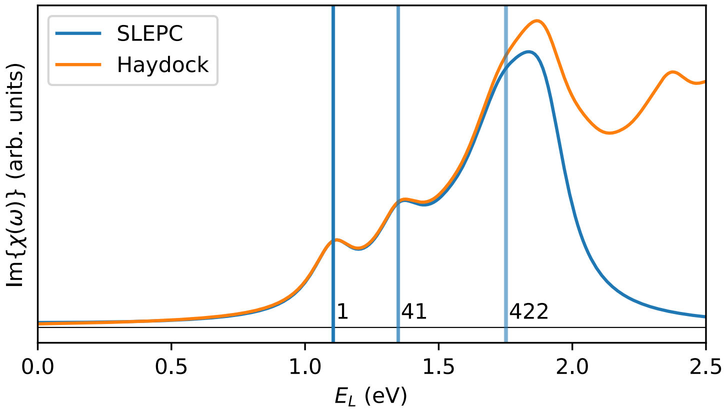

Figure 4.10: Optical absorption spectra of single-layer $MoTe_2$ using the BSE equation. In the SLEPC case the absorption spectrum was calculated using only the first few states. The vertical lines represent the energies and indices of the brightest excitons.

One of the important applications of determining the excitonic wave functions is to classify them according to their point group symmetry. This is not possible using the iterative Haydock method, instead we need to obtain explicitly the wave function either using the full diagonalization of the Hamiltonian or of a subspace using a library like the `slepc`. This was done in the case of single-layer hexagonal boron nitride [108]. This type of classification helps to better understand which excitons should be bright and under which conditions. This classification of the excitons can furthermore be used to interpret trends in the optical spectra of materials.

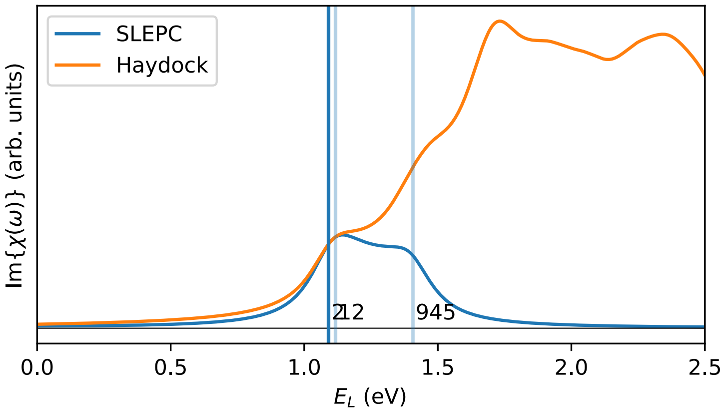

Figure 4.11: Optical absorption spectrum of triple-layer $MoTe_2$ using the BSE equation. In the SLEPC case the absorption spectrum was calculated using only the first few states. The vertical lines represent the energies and indices of the brightest excitons.

4.5.4 Representation of the excitonic states

The excitonic wave function depends on 6 coordinates where the first set of three coordinates represents the probability of finding a hole in one place given that the electron is in the position represented by the other three coordinates

$$|s\rangle = \sum_{cv\mathbf{k}} A^s_{cv\mathbf{k}} |c\mathbf{k}\rangle \otimes |v\mathbf{k}\rangle \tag{4.46}$$

$$\psi_s(\mathbf{r}_h, \mathbf{r}_e) = \sum_{cv\mathbf{k}} A^s_{cv\mathbf{k}} \psi_{v\mathbf{k}}(\mathbf{r}_h)\psi_{c\mathbf{k}}(\mathbf{r}_e). \tag{4.47}$$

There are different ways to represent this complicated function. We can represent the probability of finding an electron and a hole in the same point, which gives us information about where the excitons are formed or destroyed (called free-hole representation in the `yambo` code). Another way, the most used one, is to fix the position of the hole in one point and represent the probability density of the electron in all the other points in space.

We used our new implementation based on the SLEPC library to iteratively obtain the excitonic states of the BSE Hamiltonian in Eq. (4.41). In Fig. 4.12 we

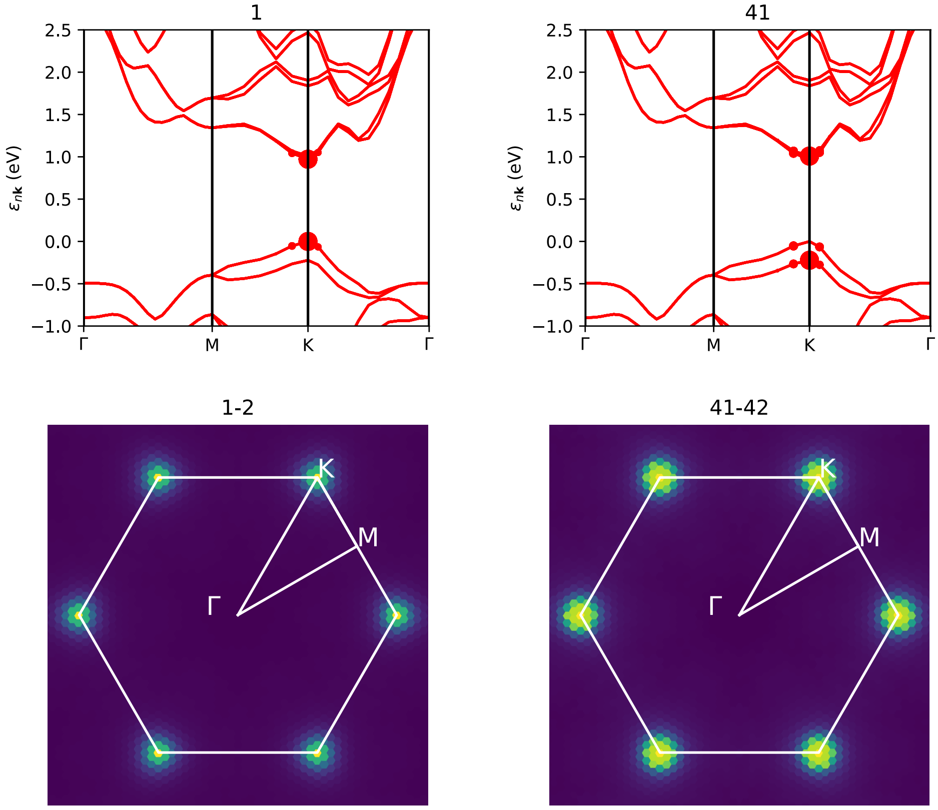

Figure 4.12: Electronic transitions contributing to the first (1-2) and second (41-42) brightest excitons for single-layer $MoTe_2$. In panel a) and b) we represent by a circle the Kohn-Sham states contributing to the excitonic state where the size of the circle is proportional to the weight of the electron-hole pair. In panels c) and d) we add the contributions of the different bands and represent their weight in the Brillouin zone.

show the transitions contributing to the first two bright excitons in single-layer $MoTe_2$ using the two different representations. In one case we add the contribution of all the transitions in the **k**-point and represent it in reciprocal space. This gives us information about which regions in the Brillouin zone are contributing to the excitonic state. In the second case we represent the weight of the contributions in the band-structure plotted along the high-symmetry line. In this case it becomes evident which transitions contribute are contributing to the excitonic state. For example, the first peak is due to transitions near the band-gap and the second peak due to the transitions between the second-higher valence band and the conduction band. The splitting between the higher and second-higher bands is due to the strong spin-orbit interaction in $MoTe_2$. The representation of these excitons in real space is shown in Fig. 4.13. Here we can see as expected that higher localization in reciprocal space corresponds to more delocalization in real space.

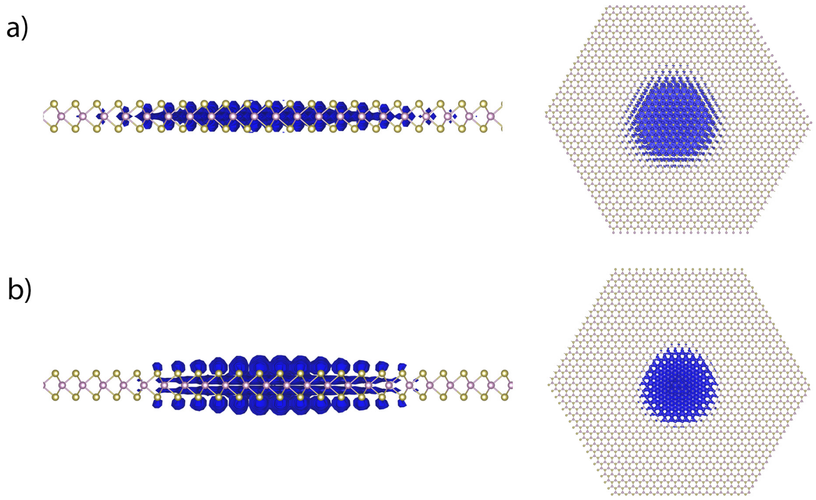

Figure 4.13: Real space excitonic wave functions of the first two brightest excitons in single-layer $MoTe_2$. The excitons with index 1-2 are shown in panel a) the 41-42 in panel b). These images are generated with the VESTA software.

We represent the transitions contributing to the formation of the excitons in triple-layer $MoTe_2$ in Fig. 4.14. In this case it is interesting to analyze how the electrons distribute in the different layers according to the position of the hole as shown in Fig. 4.15. In the representation shown here we fixed the hole in the central layer.

The representations shown in Figs 4.12 and 4.14 are done using the `yambopy` code. We plan their future implementation in the `phononwebsite`. This will allow for an easier and more educative analysis of the excitonic calculations.

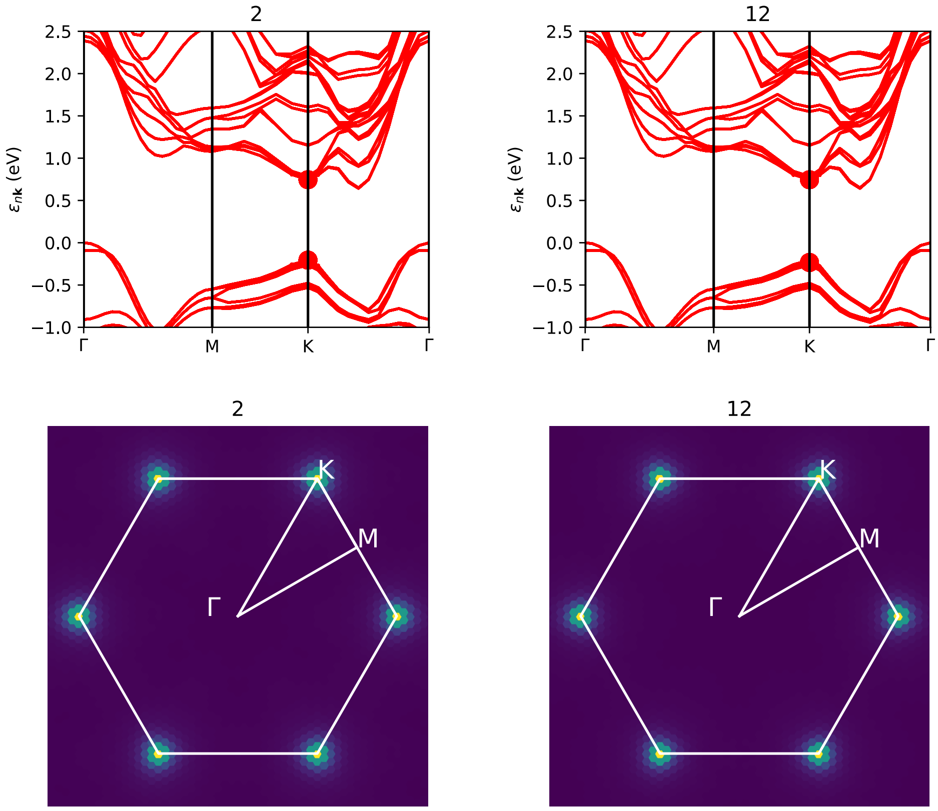

Figure 4.14: Electronic transitions contributing to the first (2) and second (12) brightest excitons for triple-layer $MoTe_2$. In panel a) and b) we represent with a circle the Kohn-Sham states contributing to the excitonic state where the size of the circle is proportional to the weight of the electron-hole pair. In panels c) and d) we add the contributions of the different bands and represent their weight in the Brillouin zone.

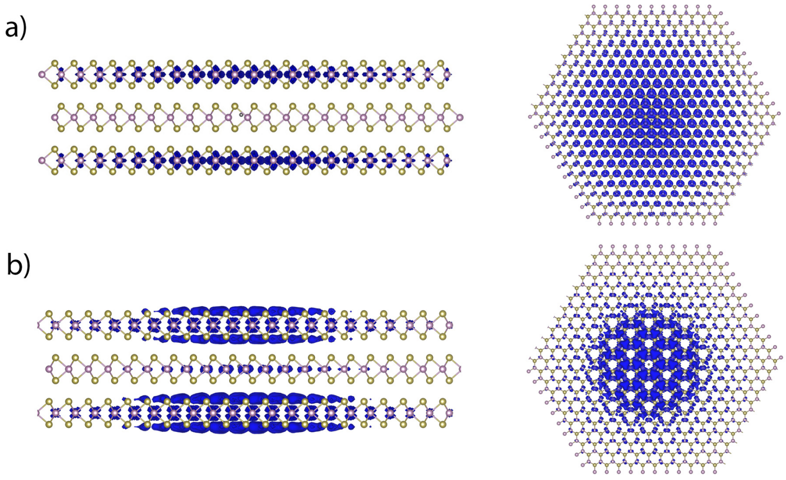

Figure 4.15: Real space excitonic wave functions of the first two excitons in triple-layer $MoTe_2$. The hole is fixed near the Mo atom in the central layer. The excitons with index 2 are shown in panel a) the 12 in panel b). These images are generated with the VESTA software.

4.5.5 Temperature dependent optical spectra: MoS_2

Apart from the inclusion of excitonic effects it is also possible to include the effect of temperature using the concepts introduced in Chapter 3. Here we show the results of a calculation of optical absorption of MoS_2 in the independent-particle approximation including the lifetimes due to electron-phonon scattering. The same principle applied here will be used to incorporate the effects of temperature in the Raman spectra in Chapter 6. Calculations including both the effect of temperature and the excitonic effects were demonstrated in the literature [109] but this topic is outside the scope of the current work.

To converge the calculation of the optical absorption spectra we interpolated the MoS_2 band structure using the method described in Section 3.3.1 on a grid of 240x240 **k**-points. The need for a fine sampling of the Brillouin zone is due to the low broadening of the electronic states near the absorption edge. In Fig. 4.16 we show the effect of the inclusion of the lifetimes of the electrons in the independent-particle absorption. There are two important effects in the optical spectrum due to temperature captured by this approach. The first ef-

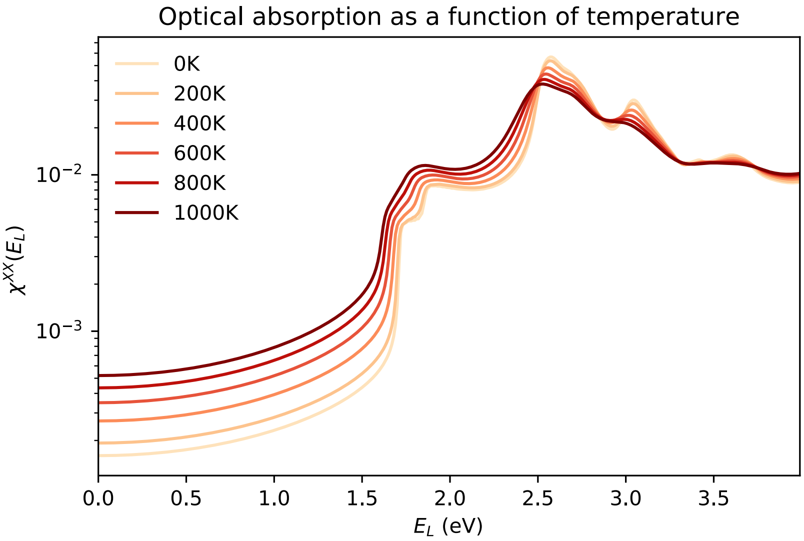

Figure 4.16: Temperature dependent optical absorption spectra of MoS_2.

fect is the band gap renormalization which shifts the absorption edge to lower energies as described in Chapter 3. Secondly there is a broadening of the peaks due to the increase of the quasi-particle linewidths.

5

Raman spectroscopy: Finite differences approach

5.1 Introduction

The Raman spectrum reveals information about excitations in the material. We start this chapter with a review of the Raman scattering amplitude from a classical perspective. We will define what is measured in a Raman experiment and describe a method to calculate it. One of the required quantities, the dielectric susceptibility, is calculated from first-principles using the methods described in Chapter 4. We apply this method to study one-phonon resonant Raman spectroscopy in single- and triple-layer $MoTe_2$ to compare with experimental results obtained by the group of Stéphane Berciaud at IPCMS/University of Strasbourg and other results in the literature [24, 25, 26].

In a recent experiment, a strong exciton-phonon coupling was reported for single-, double-, triple-layer, and bulk MoS_2 [18]. This experiment provided not only evidence of the symmetry-dependence of the exciton-phonon coupling but also about sharp features in the optical spectra namely the A, B excitons [110]. Our study of the dependance of the Raman intensities with laser energy was motivated by an earlier publication about the characterization of the phonon vibrational modes of $MoTe_2$ using Raman spectroscopy [24]. In it, the Raman spectrum of up to 10 layers was experimentally measured and described using a force constant model for the phonon frequencies and modes. This allowed the detailed study of the interlayer forces and determination of the frequencies of the Raman inactive phonon modes not directly measured in the experiment. Because single-layer $MoTe_2$ is a near-infrared direct optical band gap semiconductor (1.1 eV gap at room temperature), it is possible to probe the excitonic states with visible photon energies [107, 24]. Additionally the Davydov split modes appear prominently at visible (hence easily available) laser photon energies. The description of the Raman intensities was done using a *bond-polarizability* model [111]. In this model, the susceptibility of the material is empirically parameterized by the sum of the polarizabilities of the individual bonds. The results obtained for different multi-layers are reproduced in Fig. 5.1. This model, however, does not account for the dependence of the polarizability on the laser frequency and does not reproduce the intensities of the phonon modes at different laser energies (see supplementary material of Ref. [24]). This drawback is also common to the standard DFPT calculations of the Raman intensities where a static electric field is assumed [31, 32]. Up to now, most theoretical studies have been focused on this non-resonant regime, either using the bond-polarizability model or density functional perturbation

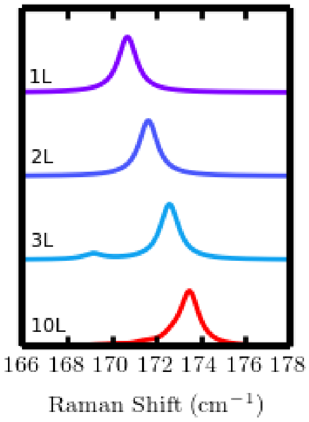

Figure 5.1: Raman spectra calculated using a bond-polarizability model. In this model a static electric field is considered. Figure taken from the supplementary material of Ref. [24].

theory [20, 21, 112].

It is well known from experiments that the Raman intensities have a strong dependence on the laser energy for certain phonon modes, as was shown for $MoSe_2$ [113, 114], MoS_2 [115], and WS_2 [116]. In $MoTe_2$ as well, the measurements show a strong dependence [117, 107, 24, 25, 26]. In the case of triple-layer $MoTe_2$, it was observed that the intensity ratio between the lowest- and highest-frequency modes belonging to the same A'_1 Davydov triplet significantly changes with laser photon energy [24, 25, 26].

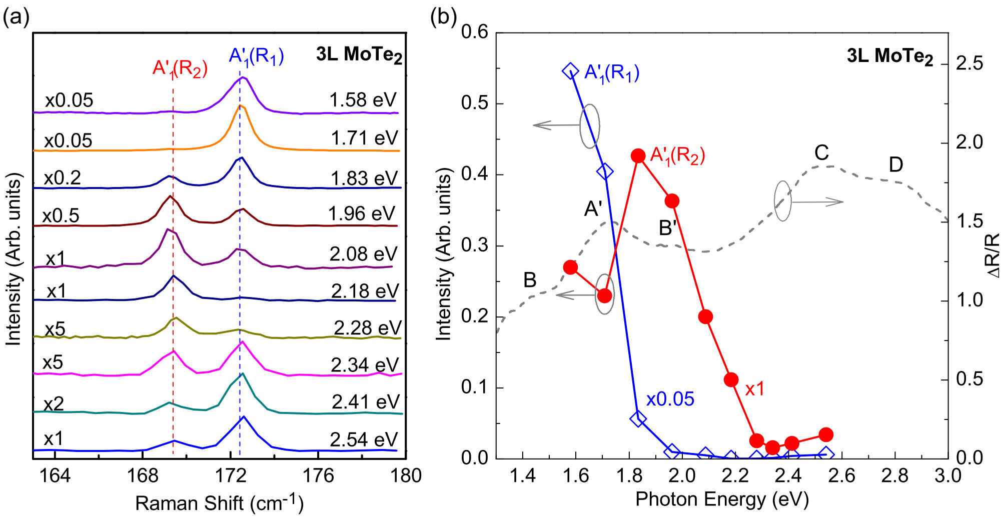

Figure 5.2: Raman spectra of Davydov doublets of the A'_1 modes in 3L $MoTe_2$ excited by ten laser excitation energies, where the Raman intensity is normalized to the A_3 mode in quartz at about 465 cm^{-1}. (b) The intensity of the $A'1$ (R_1) (blue open diamonds) and $A'1$ (R_2) (red solid circles) as a function of the excitation energy. The dashed gray line is the reflectance contrast spectrum $(\delta R/R)$ of 3L $MoTe_2$ in the visible range. Figure taken from Ref. [26].

In Fig. 5.2 we reproduce the main results of Ref. [26]. For laser energies up to approx. 1.8 eV the A'_1 mode with higher phonon frequency has a larger Raman intensity. This is in agreement with the results obtained in the non-resonant regime using the bond polarizability model reproduced in Fig. 5.1. However, for larger laser energies the A'_1 mode with lower frequency becomes dominant. This puts in evidence the limitations when comparing experimental Raman spectra measured in the resonant regime with models in the non-resonant regime.

We will present the use of a finite differences approach for the calculation of Raman intensities as a function of laser energy using the methods reported in Refs. [14, 30, 33]. In this framework, the Raman intensities are defined as the first order change of the dielectric susceptibility due to phonon vibrations (see Sec. 5.2.1).

5.2 Classical theory of light scattering

The theory of light scattering in solids can be introduced with concepts from classical electrodynamics [14]. Consider an electronic charge distribution evolving in time. Associated to this charge there is an electric polarization, **P**. Due to temperature or the action of external forces this charge will oscillate with a certain frequency ω_S. From Maxwell's equations, the energy of the radiation emitted per unit time, $W_S(\omega_S)$, by a dipole within a solid angle Ω is [14]

$$\frac{dW_S(\omega_S)}{d\Omega} = \frac{\omega_S^4}{(4\pi)^2\epsilon_0 c^3}|\mathbf{e}_S \cdot \mathbf{P}(\omega_S)|^2, \tag{5.1}$$

where $\mathbf{e}_S$ denotes the direction of the scattered light, ϵ_0 the permittivity of the vacuum and c is the speed of light. The external force driving the polarization is an external electromagnetic field with frequency ω_L. In that case the polarization is related to the incident electromagnetic field

$$\mathbf{P}(t) = \int \overline{\overline{\chi}}(t-t') \cdot \mathbf{e}_L E_L e^{i\omega_L t'} dt', \tag{5.2}$$

where E_L is the amplitude of the electromagnetic field, $\mathbf{e}_L$ the light polarization vector and, $\overline{\overline{\chi}}(\omega_L)$ is the dielectric susceptibility tensor of the material as defined in Chapter 4. Performing a Fourier transformation in time t to ω_S we obtain

$$\mathbf{P}(\omega_S) = \overline{\overline{\chi}}(\omega_S) \cdot \mathbf{e}_L E_L \delta(\omega_S - \omega_L). \tag{5.3}$$

Inserting Eq. (5.3) into Eq. (5.1) we obtain

$$\frac{dW_S(\omega_S)}{d\Omega} = \frac{\omega_S^4}{(4\pi)^2 \epsilon_0 c^3} |\mathbf{e}_S \cdot \overline{\overline{\chi}}(\omega_S) \cdot \mathbf{e}_L|^2 E_L^2. \tag{5.4}$$

The differential cross section can be obtained dividing by the incident energy per unit area $W_L = \epsilon_0 c E_L^2$

$$\frac{dW_S(\omega_S)}{d\Omega} \frac{1}{W_L} = \frac{d\sigma(\omega_S)}{d\Omega} = \frac{\omega_S^4}{(4\pi\epsilon_0)^2 c^4} |\mathbf{e}_S \cdot \overline{\overline{\chi}}(\omega_S) \cdot \mathbf{e}_L|^2, \tag{5.5}$$

The information about the excitations of the material is included in the dielectric response. At this point the scattered light will have the same frequency as the incident light. This is the definition of an elastic light scattering process. The description of elastic processes is, however, not enough to obtain information about lattice vibrations, and other excitations.

5.2.1 Inelastic light scattering

Considering again a monochromatic laser with frequency ω_L, the polarizability $\mathbf{P}$ oscillates with this frequency and is represented as a function of time in Fig. 5.3 a). This polarizability, like the total energy or any other macroscopic property, depends on the internal coordinates of the system (atomic positions, electronic states, etc.). These coordinates can change due to random thermal fluctuations or external forces, thus modifying the response function. If we consider a phonon vibrating with energy ω_μ and assume that the electrons relax much quicker than the phonons, the electronic energy levels will also oscillate with this phonon frequency. This causes the susceptibility (and consequently the polarization) to also oscillate with the phonon frequencies as shown in Fig. 5.3 b). The modulation of the polarizability with the energies

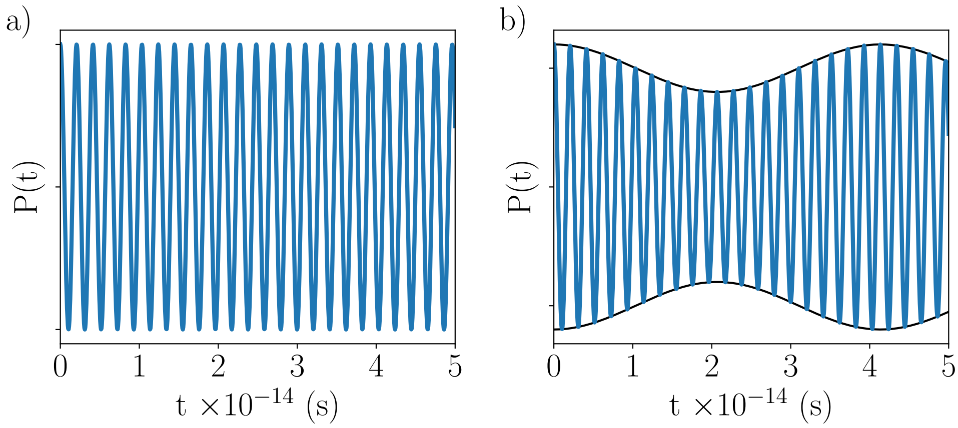

Figure 5.3: Panel a): polarizability of the system upon perturbation by a laser with energy 2 eV. In panel b) we consider that the susceptibility also oscillates as a function of time due to the phonon vibrations ω_μ with energy 0.1 eV (806.6 cm^{-1}). This leads to the polarization being modulated by the phonon frequencies.

of the elemental excitations leads to additional peaks in the Fourier transformation of the polarization shown in Fig. 5.4. These peaks mark the energies

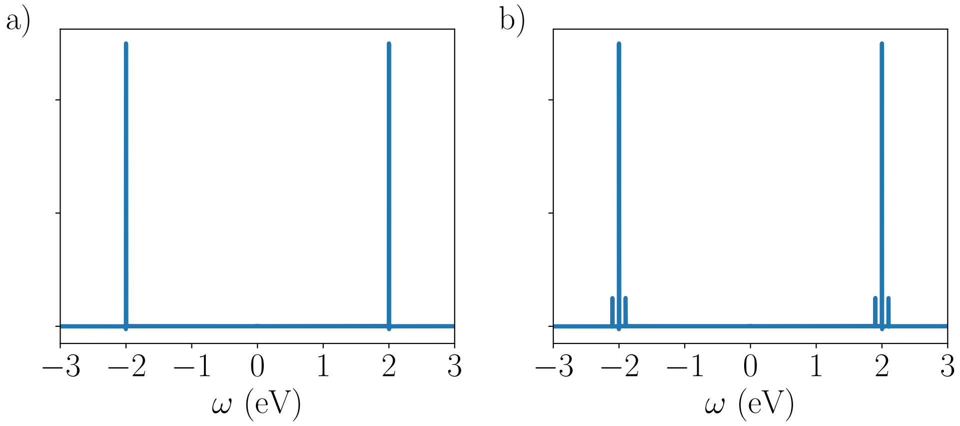

Figure 5.4: Fourier transformation of the polarizability as a function of time represented in Fig. 5.3. In panel a) we obtain a peak at the frequency of the laser light excitation. In panel b) we obtain, in addition to the main peak, two additional side peaks with frequency given by $\omega_L - \omega_\mu$ and $\omega_L + \omega_\mu$ related to emission and absorption of a phonon (these are called Stokes and anti-Stokes peaks respectively).

of the excitations, in this case a phonon, and their intensity is proportional to the strength of the coupling with the susceptibility. This coupling is related to the strength of the electron-phonon coupling. It is the vibrating polarization that creates the scattered light that reaches the detector with intensity given by Eq. (5.1). Most of this light has the same frequency as the incident light (elastic scattering) but a fraction of the scattered light experiences a shift in frequency due to the excitations (inelastic scattering). In a typical Raman spectrum, we are interested in the relative shift of these peaks with respect to the elastically scattered peak. A way to obtain these Raman shifts is to calculate the polariazability as a function of time letting the positions of the nuclei time evolve as outlined in Section 2.3.4. The Raman spectrum is then obtained by a Fourier transformation [118].

In our approach, we assume that electrons respond immediately to the phonon vibration. This is referred to as the *adiabatic limit*. This limit is valid as long as the following condition is fulfilled [14, 102]:

$$\omega_\mu \ll |\omega_L - (\epsilon_{c\mathbf{k}} - \epsilon_{v\mathbf{k}}) + i\gamma|, \tag{5.6}$$

where $\epsilon_{c\mathbf{k}}$ and $\epsilon_{v\mathbf{k}}$ are the energies of conduction and valence bands respectively and γ is the electronic broadening. As we will show later on, this approximation holds quite well even at laser energies close to resonance with the electronic states provided that the electronic broadening is large compared to the phonon frequencies.

We can define at each time a polarizability tensor, $\overline{\overline{\chi}}(\omega_L, \{Q\})$, that depends on the phonon displacements defined in Section 2.1, using an expansion similar to Eq. (2.1). Expanding in terms of the phonon displacements normalized according to

$$Q^\mu_{i\alpha}(\mathbf{q}) = \frac{1}{\sqrt{M_I}} \xi^\mu_{I\alpha}(\mathbf{q}), \tag{5.7}$$

we obtain

$$\begin{aligned}\overline{\overline{\chi}}(\omega_L,\{Q\}) = \overline{\overline{\chi}}(\omega_L,\{\mathbf{R}^0\}) +& \\ \frac{1}{2}\sum_{\mathbf{q}\mu}\frac{\partial\overline{\overline{\chi}}(\omega_L,\{\mathbf{R}^0\})}{\partial Q^{\mu}_{\mathbf{q}}}&\left[Q^{\mu}_{\mathbf{q}}e^{-i\omega_{\mu\mathbf{q}}t} + Q^{\mu *}_{\mathbf{q}}e^{i\omega_{\mu\mathbf{q}}t}\right] + \\ \frac{1}{4}\sum_{\mathbf{q}\nu\mu}\frac{\partial^2\overline{\overline{\chi}}(\omega_L,\{\mathbf{R}^0\})}{\partial Q^{\mu}_{\mathbf{q}}\partial Q^{\nu}_{\mathbf{q}}}&\Big[Q^{\mu}_{\mathbf{q}}Q^{\nu}_{\mathbf{q}}e^{-i(\omega_{\mu\mathbf{q}}+\omega_{\mu\mathbf{q}})t} + \\ &Q^{\mu}_{-\mathbf{q}}Q^{\nu *}_{-\mathbf{q}}e^{i(\omega_{\mu\mathbf{q}}-\omega_{\mu\mathbf{q}})t} + \\ &Q^{\mu *}_{\mathbf{q}}Q^{\nu}_{-\mathbf{q}}e^{i(\omega_{\mu\mathbf{q}}-\omega_{\nu\mathbf{q}})t} + \\ &Q^{*\mu}_{-\mathbf{q}}Q^{\nu}_{\mathbf{q}}e^{-i(\omega_{\nu\mathbf{q}}+\omega_{\nu\mathbf{q}})t}\Big].\end{aligned} \tag{5.8}$$

In a similar way as in section 2.1 where we defined forces and force constants to relate the change of the total energy to the displacements of the atoms, here we will relate the change of the susceptibility to the phonon displacements. The first term is just the dielectric susceptibility when all the atoms are in their equilibrium positions. The second and third terms are the first- and second-order Raman susceptibility tensors, respectively

$$\overline{\overline{\alpha}}^{(1)}_{\mu}(\omega_L) = \frac{\partial\overline{\overline{\chi}}(\omega_L,\{\mathbf{R}^0\})}{\partial Q^{\mu}_{\mathbf{q}=0}}, \qquad \text{One-phonon Raman tensor,} \tag{5.9}$$

$$\overline{\overline{\alpha}}^{(2)}_{\mu\nu\mathbf{q}}(\omega_L) = \frac{\partial^2\overline{\overline{\chi}}(\omega_L,\{\mathbf{R}^0\})}{\partial Q^{\mu}_{\mathbf{q}}\partial Q^{\nu}_{\mathbf{q}}}, \qquad \text{Two-phonon Raman tensor,} \tag{5.10}$$

where we simplified the one-phonon Raman tensor since only long-wavelength phonons ($\mathbf{q} \to 0$) couple with the light. This is due to the fact that the laser light has a long-wavelength when compared with the interatomic distances. These expressions relate the oscillations (or fluctuations) of the susceptibility to the vibration of the atomic nuclei. The magnitude of the change depends on the magnitude of the different components of the Raman tensor and on the thermodynamic average of the phonon displacements, i.e., how many of the phonon modes are excited (as discussed in 2.2).

Inserting Eq. (5.8) in Eq. (5.5) leads to a multitude of terms. Since we are interested in the first-order Raman processes we only keep the terms in $\overline{\overline{\boldsymbol{\alpha}}}_\mu^{(1)}(\omega_L)$

$$\frac{d\sigma_s(\omega)}{d\Omega} = \sum_\mu \frac{\omega^4}{(4\pi\epsilon_0)^2 c^4} |\mathbf{e}_S \cdot \overline{\overline{\boldsymbol{\alpha}}}_\mu^{(1)}(\omega_L) \cdot \mathbf{e}_L|^2 \left\langle Q^\mu Q^{\mu *} \right\rangle, \qquad \text{Stokes,} \tag{5.11}$$

$$\frac{d\sigma_a(\omega)}{d\Omega} = \sum_\mu \frac{\omega^4}{(4\pi\epsilon_0)^2 c^4} |\mathbf{e}_S \cdot \overline{\overline{\boldsymbol{\alpha}}}_\mu^{(1)}(\omega_L) \cdot \mathbf{e}_L|^2 \left\langle Q^{\mu *} Q^\mu \right\rangle, \qquad \text{anti-Stokes,} \tag{5.12}$$

where the first term gives the differential cross-section of the Stokes and the second that of the anti-Stokes Raman scattering process. In the classical case there is no distinction between the Stokes and anti-Stokes components as the expectation values of $\langle Q^{\mu *} Q^\mu \rangle$ and $\langle Q^\mu Q^{\mu *} \rangle$ are the same and given by Eq. (2.16). Additionally, in a purely classical description of Raman scattering, the Stokes and anti-Stokes components have the same intensities. This is not true according to experiments as shown in Fig. 5.5. To properly distinguish between these two components we have to quantize the phonons. This can still be done in a semi-classical way, by estimating the amplitudes of the vibrations of the phonon based on the total energy of the quantum harmonic oscillator which is given by $E = \hbar\omega_\mu[n(T, \omega_\mu) + 1/2]$. The amplitude is estimated from

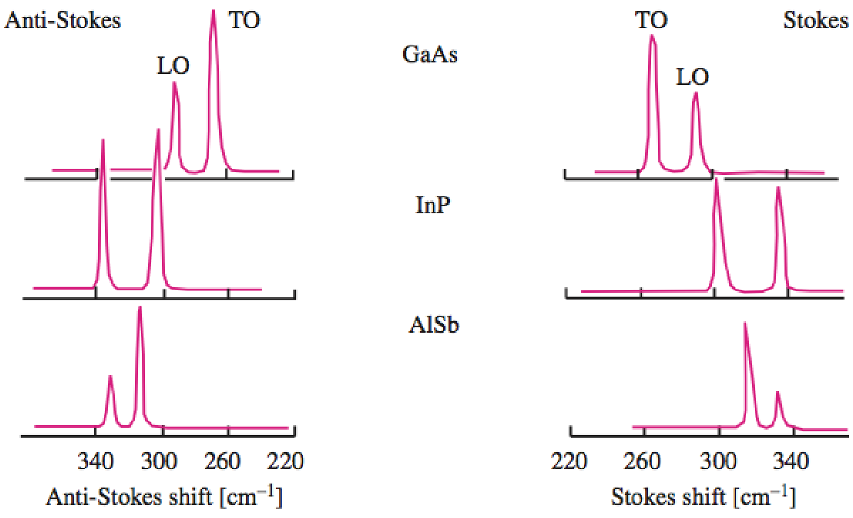

Figure 5.5: Stokes and anti-Stokes raman spectra of three zinc-blende-type semiconductors. Image reproduced from Ref. [30].

the potential energy at maximum enlongation

$$\langle Q_{\mathbf{q}}^{\mu *} Q_{\mathbf{q}}^{\mu} + Q_{\mathbf{q}}^{\mu *} Q_{\mathbf{q}}^{\mu} \rangle = \frac{\hbar}{\omega_\mu} \left[n(T,\omega_\mu) + \frac{1}{2} \right], \tag{5.13}$$

where $n(T,\omega) = (e^{\hbar\omega/k_B T} - 1)^{-1}$ is the Bose-Einstein distribution for the phonon states and k_B is the Boltzmann constant. At high temperature we recover the classical limit

$$\langle Q_{\mathbf{q}}^{\mu *} Q_{\mathbf{q}}^{\mu} + Q_{\mathbf{q}}^{\mu *} Q_{\mathbf{q}}^{\mu} \rangle = \frac{\hbar k_B T}{\omega_\mu}. \tag{5.14}$$

This is, however, still not enough to distinguish the Stokes and anti-Stokes components. To do so we need to introduce their expectation values using quantized phonons

$$\langle Q_{\mathbf{q}}^{\mu} Q_{\mathbf{q}}^{\mu *} \rangle = \langle n|\hat{a}|n+1\rangle \langle n+1|\hat{a}^\dagger|n\rangle = \frac{\hbar}{2\omega_\mu}[n(T,\omega)+1], \qquad \text{Stokes} \tag{5.15}$$

$$\langle Q_{\mathbf{q}}^{\mu *} Q_{\mathbf{q}}^{\mu} \rangle = \langle n|\hat{a}^\dagger|n-1\rangle \langle n-1|\hat{a}^\dagger|n\rangle = \frac{\hbar}{2\omega_\mu}[n(T,\omega)], \qquad \text{anti-Stokes} \tag{5.16}$$

where $\hat{a}^\dagger$ is the phonon creation operator and $\hat{a}$ the phonon annihilation operators introduced in Section 2.2. Equations (5.15) and (5.16) indicate a clearly different temperature dependence of the Stokes and anti-Stokes Raman scattering intensities.

Combining Eqs. (5.11) and (5.15) and taking the limit $\mathbf{q} \to 0$, we obtain for the differential cross-section of the Raman intensity

$$\frac{d\sigma_s(\omega_L)}{d\Omega} = \sum_\mu \frac{\omega_L^4}{(4\pi\epsilon_0)^2 c^4} |\mathbf{e}_S \cdot \overline{\overline{\alpha}}_\mu^{(1)}(\omega_L) \cdot \mathbf{e}_L|^2 \frac{\hbar}{2\omega_\mu}[n(T,\omega_\mu)+1]. \tag{5.17}$$

This equation will serve as the basis for the study of resonant Raman scattering in MoTe$_2$ in section 5.4. The calculation of the derivatives of the dielectric susceptibility is done by finite differences of the dielectric susceptibility obtained using the methods in Chapter 4. Alternatively, the differential cross section will be formulated in terms of MBPT in section 6.1.

As a final remark, the ratio between the Stokes and anti-Stokes cross-sections allows us to estimate the temperature of the sample using

$$\frac{d\sigma_s(\omega)}{d\Omega}[n(T,\omega)] = \frac{d\sigma_a(\omega)}{d\Omega}[n(T,\omega)+1]. \tag{5.18}$$

The temperature measured in this way is in general different from the environment temperature as the laser is transferring energy to the sample that is stored as vibrational energy of the nuclei and the electrons. Using Eq. (5.18) to estimate the temperature should give a more realistic value for the temperature of the system. This is important for the comparison between the experimental and the calculated spectrum when including temperature effects.

5.3 Selection rules and interference effects

Selection rules

The periodic crystals are classified according to their symmetries into space groups. The long-wavelength phonon modes (i.e. phonon modes with $\mathbf{q} \to 0$) can be classified according to the representation they have within that point group. Upon calculating the change of the susceptibility tensor (depending on the directions of the incoming electric field and the polarization) due to phonon modes belonging to a certain point group symmetry, some components of the Raman tensor vanish by symmetry. This fact can be studied systematically using group theory methods and selection rules can be obtained for the different phonon modes of a crystal. A complete table of the selection rules is shown in Ref. [119]. We reproduce here only the selection rules relevant to the systems under study[1] which belong to the D_{3h} point group.

---

[1] Both single- and triple-layer as well as odd multiple layers belong to the same point group. Even multiple layers and bulk belong to a different point group D_{3d} [22, 24].

Mode	A_1'	$E'(x)$	$E'(y)$
Raman tensor $\boldsymbol{\alpha}_\mu$	$\begin{bmatrix} a & & \\ & a & \\ & & b \end{bmatrix}$	$\begin{bmatrix} & d & \\ d & & \\ & & \end{bmatrix}$	$\begin{bmatrix} d & & \\ & -d & \\ & & \end{bmatrix}$

Table 5.1: Selection rules of the Raman tensor for the space group D_{3h}[15].

Interference effects

For the phonon modes that do not have zero Raman intensities due to selection rules, we would like to calculate the resonant Raman intensities. Furthermore, we would like to understand which bands and which **k** points are contributing to these intensities. For a detailed analysis, we proceed in a similar way as we did in Eq. (4.30) for the dielectric susceptibility. We write the Raman tensor from Eq. (5.9) as a sum over the Brillouin zone

$$\overline{\overline{\alpha}}(\omega) = \sum_{\mathbf{k}} \overline{\overline{\alpha}}_{\mathbf{k}}(\omega). \tag{5.19}$$

Contrary to the dielectric susceptibility, however, the Raman intensity (given by Eq. (5.17)) is the absolute square of the sum of $\overline{\overline{\alpha}}_{\mathbf{k}}(\omega)$

$$I \propto \left| \sum_{\mathbf{k}} \overline{\overline{\alpha}}_{\mathbf{k}} \right|^2 = \underbrace{\sum_{\mathbf{k}} \left| \overline{\overline{\alpha}}_{\mathbf{k}} \right|^2}_{\text{direct terms}} + \underbrace{\sum_{\substack{\mathbf{k},\mathbf{k}' \\ \mathbf{k}\neq\mathbf{k}'}} \left(\overline{\overline{\alpha}}_{\mathbf{k}}\right)^* \overline{\overline{\alpha}}_{\mathbf{k}'}.}_{\text{interference terms}} \tag{5.20}$$

The addition of complex numbers with a certain phase leads to constructive or destructive interference effects. If enough electronic transitions with a finite amplitude are in phase, we detect a large Raman intensity. If the contributions are out of phase, interference leads to a small or even zero Raman intensity. We will show that, in general, the biggest contribution comes from the interference terms in Eq. (5.20), with the direct terms being almost negligible. The interference between the different contributions can be related to the symmetry of the system which is reflected in the matrix elements that enter the computation of the Raman scattering.

5.4 Finite differences method applied to $MoTe_2$

In this section we demonstrate the application of the finite differences method to the calculation of the first-order Raman spectrum of single- and triple-layer $MoTe_2$. We have published these results in Ref. [35].

The accurate description of resonant Raman scattering is challenging due to the interplay between electronic correlation and electron-phonon coupling. Most *ab initio* methods available today assume static electromagnetic fields, which is not applicable in the resonant case where the dynamic dielectric response needs to be accounted for. Resonant Raman spectroscopy has also been studied using empirical models fitted from experiments to describe the electronic bands, phonon dispersion, and electron-phonon coupling [120]. These methods, even though successful to a certain extent, require previous knowledge about the material under investigation. More recently, a study of the double-resonant Raman process in $MoTe_2$ investigated the resonance surface in reciprocal space using calculations of the electronic structure and phonon dispersion [94]. In this analysis, the authors did not include the strength of the electron-phonon and electron-light coupling (and their phase), which leads only to a qualitative picture of the Raman intensities as we will show throughout this chapter.

We use an *ab initio* approach to calculate the first-order Raman susceptibility as a function of laser photon energy. We do so by calculating the directional derivative of the dielectric response function with respect to lattice displacements with finite differences [33, 34]. For this, we evaluate the dielectric susceptibility at the two displaced positions $R^{\pm}_{I\alpha} = R_{I\alpha} \pm \delta Q^{\mu}_{I\alpha}$ and divide by the amplitude of the two displacements. We will then use these results to discuss the main qualitative features on the independent-particle level and show that the inclusion of excitonic effects provides a reliable quantitative description of the Raman spectrum, in very good agreement with experimental results.

The key point of this analysis is then to use the concept of quantum interference to explain the observed behavior of the Raman intensity with laser energy in $MoTe_2$. Quantum interference was shown to be important in the

Raman intensities of graphene where an increase of the Raman intensity is observed when destructive interference terms are blocked by the Pauli principle through electron or hole doping [93, 121, 122, 123]. We show that selection rules manifest themselves at the level of quantum interference. Moreover, even when selection rules do not apply, quantum interference explains the observed behavior of the Raman intensity in triple-layer $MoTe_2$.

5.4.1 Experimental data

The experimental Raman spectra of single- and triple-layer $MoTe_2$ was measured by the group of Stéphane Berciaud at IPCMS/University of Strasbourg. Figure 5.6 shows micro-Raman spectra of single- and triple-layer $MoTe_2$. The number of $MoTe_2$ layers has been unambiguously identified as described in Ref. [24].

The raw spectra have been normalized by the integrated intensity of the T_{2g} Raman mode of silicon at $\approx$ 520 cm^{-1} for a qualitative comparison. The experimental details are described in Ref. [35] and will not be detailed here.

To quantitatively compare experimentally measured Raman intensities with the *ab initio* Raman intensities calculated according to Eq. (5.17), we have also taken optical interference effects into account and extracted the xx-component (incoming and scattered light are polarized in-plane) of the Raman susceptibility after carefully considering the polarization-dependent response of the setup.

In Figure. 5.6, we show the experimentally obtained Raman spectra of single- (panel (a)) and triple-layer (panel (b)) $MoTe_2$. The prominent A'_1 and E' modes are clearly visible. In single-layer $MoTe_2$, the A'_1 mode dominates the spectrum at laser energies of E_L=1.58 and 1.96 eV, while at E_L=2.33 eV the E' mode is dominant. Similarly, in triple-layer $MoTe_2$, the A'_1 and E' mode dominate the Raman spectrum at $E_L = 1.58$ eV and $E_L = 2.33$ eV, respectively. However, the A'_1 mode and the E' mode have comparable intensities at $E_L = 1.96$ eV.

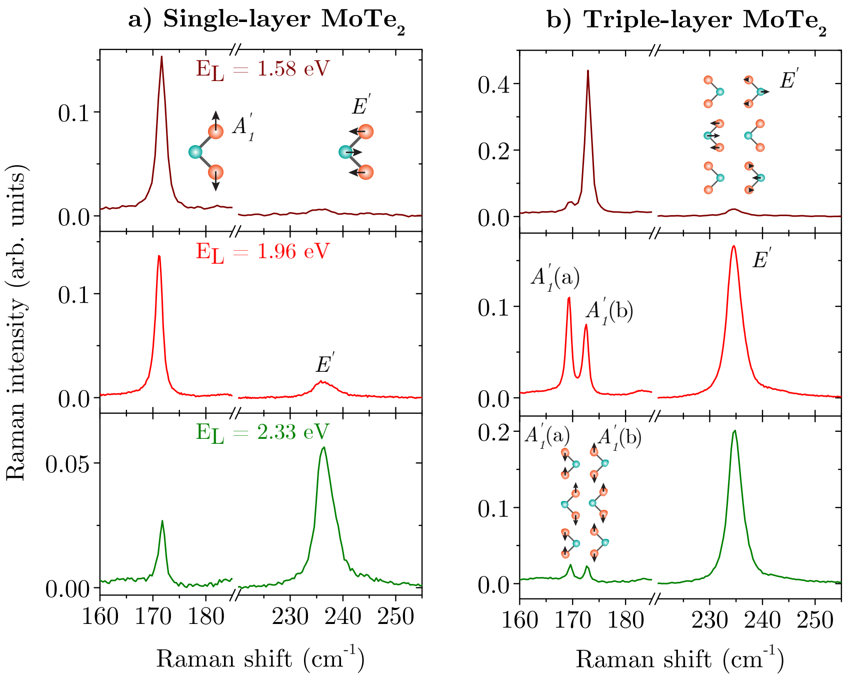

Figure 5.6: Micro-Raman spectra of single-layer (panel a) and triple-layer (panel b) MoTe$_2$ at three different laser energies in a backscattering geometry. All spectra have been normalized by the integrated intensity of the Raman mode from the underlying Si substrate at $\approx$ 520 cm^{-1}. The corresponding atomic displacements for the Raman-active modes are shown as insets in the upper panels. Figure taken from Ref. [35]. The representation of the Raman inactive phonon modes is available in Ref. [24].

5.4.2 Theoretical Raman spectrum of single-layer MoTe$_2$

In order to introduce the concept of quantum interference in a relatively easy way, we analyze the Raman spectrum for the A_1' and E' modes of single-layer MoTe$_2$. In all cases we will analyze the xx-component of the Raman susceptibility tensor, $\alpha^{xx}(\omega)$. The other components are related to the xx-component of α, as shown in Table 5.1.

The details of the calculations are specified in Section 4.5.3. Figure 5.7 a) shows the Raman susceptibility as a function of laser energy for both the IP (dashed lines) and BSE calculations (solid lines). Up to a laser energy of 2 eV the intensity of the A_1' mode is larger than that of the E' mode. At higher laser energy, the E' mode has a larger intensity than the A_1' mode, in good agreement with the experimental data reported here and in the literature [107, 24, 25]. The overall scale of the theoretical results (IP- and BSE-level) has been chosen to reflect that of the experimental results. This scale is the same for both the IP- and BSE-level calculations to allow for a comparison between the two. Since the overall scaling factor cancels when considering intensity ratios, the quantity that can be compared unambiguously between experiment and theory is the ratio of the intensities of the two phonon modes (A_1' and E'), as shown in Figure 5.7 b). The inclusion of many-body effects changes the relative intensities at the excitonic transition energies but does not change the general trend of the intensity as a function of laser energy.

As mentioned in Section 4.4.1 the main contributions to $\mathrm{Im}\{\chi(\omega)\}$ for laser energies between 0.8 and 2 eV come from the lower bands in transition space in a region around K and between K and M. It should be noted that only optically active transitions can contribute to the Raman susceptibility, but not all of them necessarily do so. For instance, near the band gap, the A_1' mode is active while the E' mode is silent, even though the same electronic transitions contribute and both modes are, in principle, allowed by lattice symmetry. This behavior can be understood in terms of angular momentum conservation analogously to the case of graphene [19, 123]. Near the band gap at K the band structure is rotationally symmetric and thus angular momentum is conserved. Both incoming and outgoing photons carry an angular momentum of $\pm\hbar$ while the E' phonon does as well. This implies that the final state has a total angular momentum of $\pm 2\hbar$ or 0, which violates angular momentum conservation and renders the E' mode silent. In contrast, the phonon corresponding to the A_1' mode does not carry angular momentum and hence the corresponding process is allowed.

This can also be understood from the point of view of quantum interference. For this purpose, we show the **k**-resolved Raman susceptibly as a function of ω in Fig. 5.8 in the full Brillouin zone and in Figure 5.9 b) along the high-symmetry lines. We color-encode the phase when the amplitude is larger

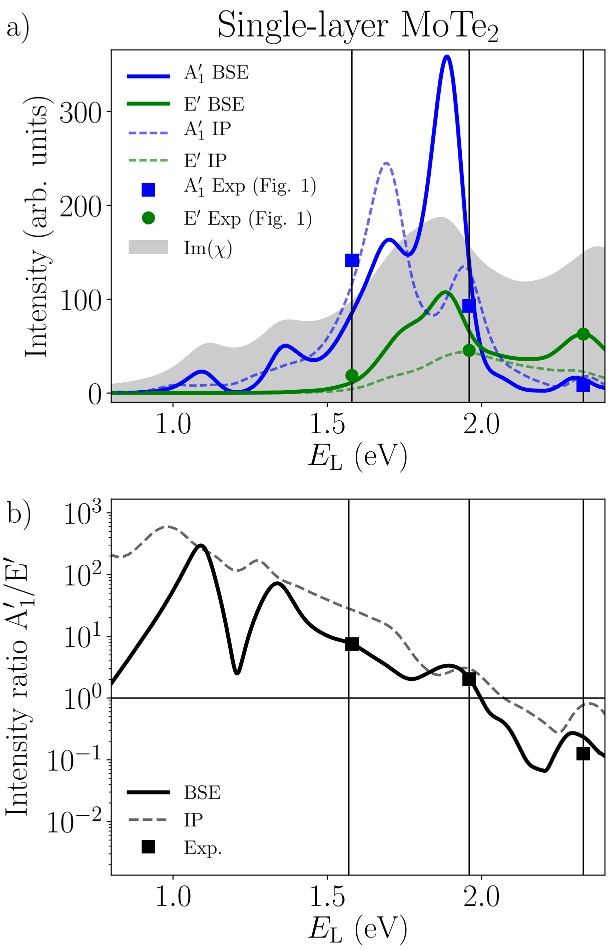

Figure 5.7: a) Calculated xx-component of the Raman susceptibility tensor squared ($|\alpha^{xx}|^2$) at the IP level (dashed line) and at the BSE level (solid lines) for single-layer MoTe$_2$ as a function of laser energy for the A'_1 and E' modes. The blue squares and green circles correspond to the same quantity (up to a normalization factor) extracted from the spectra in Figure 5.6 a) and b) using Eq. (5.17). The vertical lines at the position of the laser energies used in the experiment are guides to the eye. The BSE optical absorption is represented by the gray area. The optical gap is in good agreement with the experimental values reported in Refs. [107] and [24]. b) Ratio of the intensities of the A'_1 and E' modes calculated on the IP level (dashed line) and BSE level (solid line). The black squares represent the experimentally measured ratios. Figure taken from Ref. [35].

than 7% of the maximum amplitude at that laser energy. For the E' mode, the positive contribution from one side of the valley is added to the negative

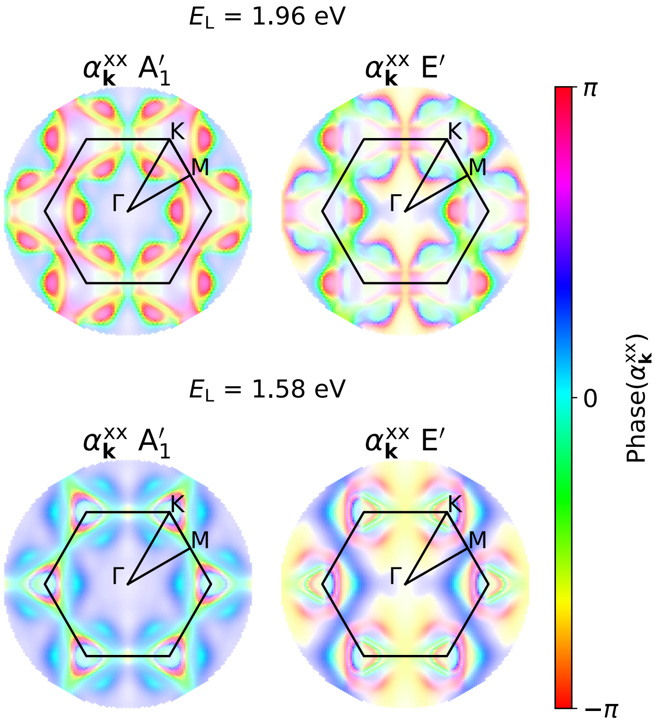

Figure 5.8: **k**-point-resolved contributions to the Raman susceptibility $\alpha_{\mathbf{k}}^{xx}(\omega)$ for single-layer MoTe$_2$ across the BZ for two different laser energies used in experiment. The E$'$ mode was chosen to be polarized in the y-direction. Figure taken from the supplementary information of Ref. [35].

contribution from the other side, which leads to an overall cancelation of the Raman intensity. By contrast, for the A' mode the contributions add up constructively. At higher laser energies, the full rotation symmetry gradually gets broken down to the 120° rotation symmetry of the lattice, an effect known as trigonal warping [124, 19, 123] of the electronic structure. Angular momentum is then only conserved up to integer multiples of $\pm 3\hbar$ and both the A_1' and E' modes become allowed.

In order to track down the origin of the phase of the Raman susceptibility, we take a closer look at the derivative of $\chi_{\mathbf{k}}(\omega)$ with respect to atomic displace-

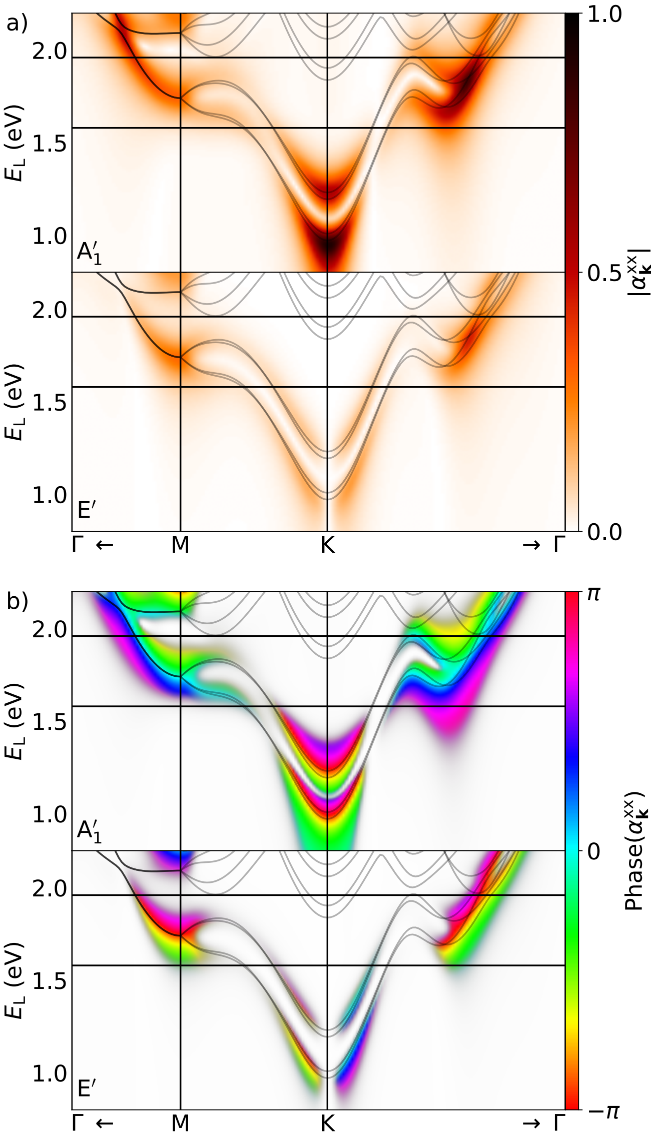

Figure 5.9: $\mathbf{k}$-point resolved contributions $\alpha_{\mathbf{k}}^{xx}(\omega)$ to the total Raman susceptibility for single-layer MoTe$_2$ along the high-symmetry lines. Panel (a) shows the absolute value, while panel (b) shows the phase of $\alpha_{\mathbf{k}}^{xx}(\omega)$. The phase is only shown if the absolute value if greater than 7% of the maximum value at that ω. Figure taken from Ref. [35].

ments [14, 34]

$$\frac{\partial \chi_{\mathbf{k}}^{SL}(\omega_L)}{\partial Q} \propto \left\{ \frac{\partial(\Delta\epsilon_{cv\mathbf{k}})}{\partial Q} \frac{(\Lambda_{vc\mathbf{k}}^{S}\Lambda_{cv\mathbf{k}}^{L})}{(\omega_L - \Delta\epsilon_{cv\mathbf{k}} + i\gamma)^2} + \right. \\ \left. \frac{\partial\left(\Lambda_{vc\mathbf{k}}^{S}\Lambda_{cv\mathbf{k}}^{L}\right)}{\partial Q} \frac{1}{\omega_L - \Delta\epsilon_{cv\mathbf{k}} + i\gamma} + (\omega_L \to -\omega_L) \right\}, \tag{5.21}$$

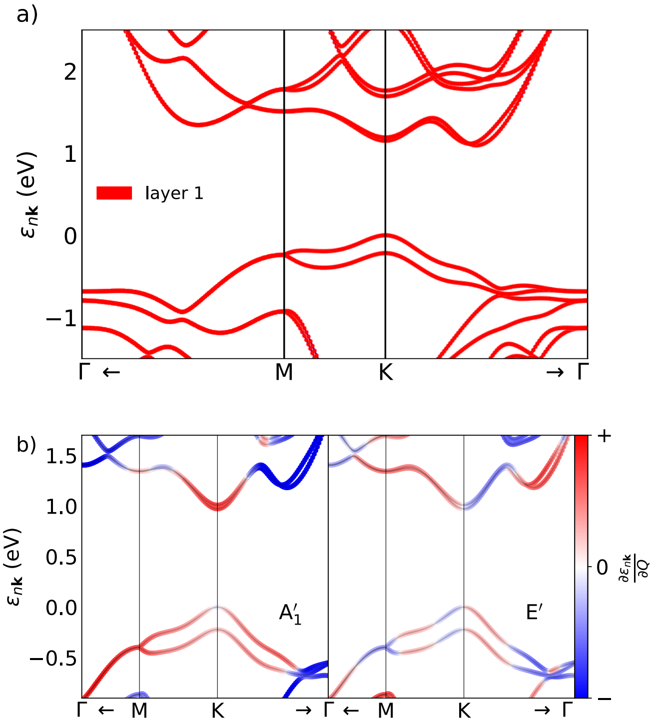

Figure 5.10: a) Band structures of single-layer $MoTe_2$ in the LDA approximation including spin-orbit coupling. b) Change of electronic bands with atomic displacements according to the A_1' and E' phonon modes.

where $\Delta\epsilon_{cv\mathbf{k}} = \epsilon_{c\mathbf{k}} - \epsilon_{v\mathbf{k}}$ and L and S denote the polarizations of the incoming and scattered light respectively. The first term involves the change of the electronic band energies, which is given by the diagonal (intra-band) electron-phonon coupling (EPC) matrix elements as we show in Eq. (C.2). The second term stems from the change of the electron-light coupling matrix elements upon atomic displacements and involves the off-diagonal EPC matrix elements as shown in Appendix C. The first term is double-resonant and corresponds to a process where an electron is excited to a conduction band, then scatters with a phonon within the same band, and finally decays to the valence band by emitting a photon. Since this term is double-resonant, we assume it to be dominant and we can directly relate the phase of the Raman susceptibility to the sign of the diagonal EPC matrix elements. We visualize these by plotting the change of the electronic band energies with respect to atomic displacements, which corresponds to the diagonal EPC matrix elements, as shown in Figure 5.10 b. From this plot we observe a direct correlation between the sign of the diagonal EPC and the phase of the Raman susceptibility in Figure 5.9 b. Therefore, we attribute constructive or destructive interference between regions of the BZ to differences in sign of the change of the electronic band energies.

5.4.3 Theoretical Raman spectrum of triple-layer MoTe$_2$

In the case of triple-layer MoTe$_2$, we focus our attention on the A_1'(a) and (b) modes, for which experiments reported here and in the literature [24, 25, 26] show a variation of the relative Raman intensity as a function of laser energy. Our calculations, both on the IP and BSE level, reproduce this observation very well, as shown in Figure 5.11 a) and b).

Common to both calculations is that the A_1'(a) phonon mode is dominant in intensity for laser energies up to 1.8 eV while at higher laser energies the A_1'(b) mode is dominant. However, only with the inclusion of excitonic effects (BSE) do we obtain the experimentally observed ratio. Contrary to the single-layer case, where the different intensities are related to different symmetries of the phonon modes, in the triple-layer case, the A_1'(a) and (b) modes belong to the same representation and hence symmetry based-arguments do not apply. However, we can still use the concept of quantum interference introduced previously to explain the intensity inversion.

We start by analyzing the behavior of the Raman susceptibility for laser energies near the band gap energy. There, the A_1'(b) mode has a large intensity while the A_1'(a) mode is practically silent. This can be understood from Figure 5.12 b), where we show the diagonal EPC matrix elements along the high-symmetry line in the BZ. For the A_1'(b) mode the lowest conduction and highest valence band states at K contribute with the same sign, while for the A_1'(a) mode they have opposite signs. This is a direct consequence of the band composition at K as shown in Fig. 5.12 b) and the way the layers vibrate (in-phase in the A_1'(b) mode and out-of-phase in the A_1'(a) mode) as shown in Fig. 5.6 b).

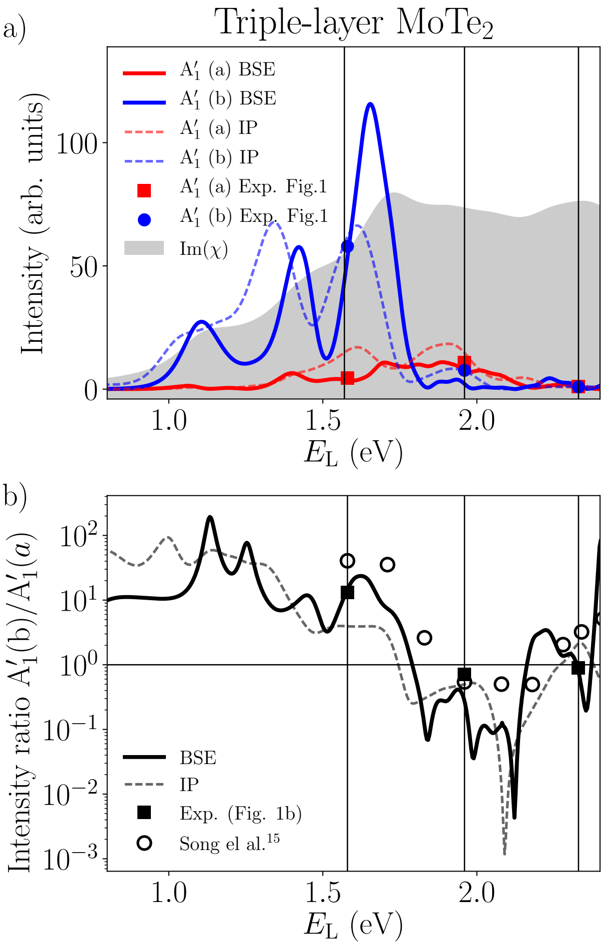

Figure 5.11: a) Calculated xx-component of the modulus square of Raman susceptibility tensor ($|\alpha^{xx}|^2$) at the IP level (dashed line) and at the BSE level (solid lines) for triple-layer MoTe$_2$ as a function of laser energy for the A_1'(a) and A_1'(b) modes. The blue squares and green circles correspond to the same quantity (up to a normalization factor) extracted from the spectra in Figure 5.6 a) and b using Eq. (5.17). The vertical lines are guides to the eye. The BSE optical absorption is represented by the gray area. The optical gap is in good agreement with the experimental values reported in Refs. [107] and [24]. b) Ratio of the intensities of the A_1'(b) and A_1'(a) modes calculated on the IP level (dashed line) and BSE level (solid line). The black squares represent the experimentally observed ratios. Figure taken from Ref. [35].

The Raman intensities at higher laser energies (between 1.58 and 1.96 eV) can also be understood from the point of view of quantum interference.

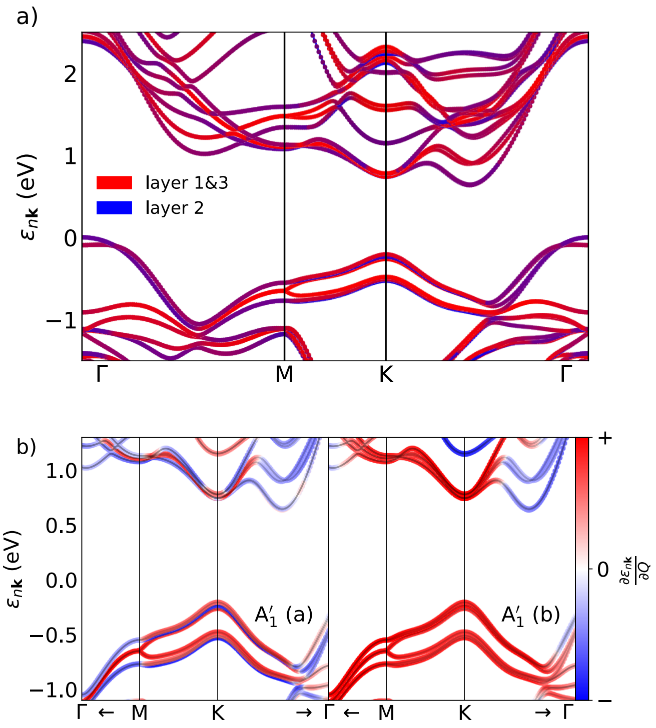

Figure 5.12: a) Band structure of triple-layer $MoTe_2$ in the LDA approximation including spin-orbit coupling. b) Change of the electronic bands with atomic displacements according to the A_1'(a) (left) and A_1'(b) modes (right).

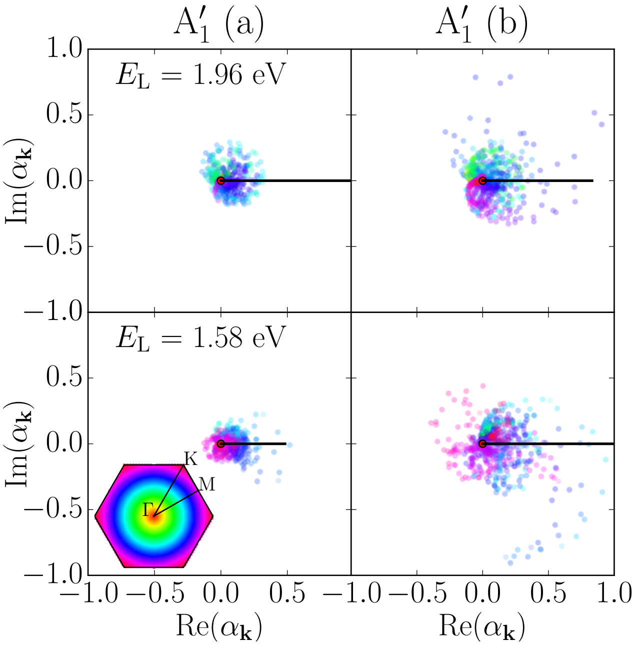

Figure 5.13: Argand plot of $\alpha_{\mathbf{k}}(\omega)$ for the A_1'(a) and (b) modes of triple-layer $MoTe_2$ for laser energies E_L=1.58 eV (bottom panel) and 1.96 eV (top panel). The colors represent the position of the point in the Brillouin zone (see inset).

For this, we represent the contributions from all **k**-points in the BZ as points in the complex plane (Argand plot) as shown in Fig. 5.13. By color-encoding the **k**-point location in the BZ, we can identify the regions which contribute constructively to the total Raman amplitude and those that are interfering destructively.

The overall phase of the different contributions has been fixed such that the total Raman susceptibility is real and positive (solid black line). At a laser energy of 1.58 eV, the contributions from the edge of the BZ, i.e., between K and M (purple dots), scatter concentrically around the origin and mostly cancel each other for both phonon modes. However, the regions between K and Γ and M and Γ (blue dots) are building the signal up.

Since these contributions have larger amplitude for the A_1'(b) mode than for the A_1'(a) mode, the former has a larger intensity at this laser energy. This becomes clear by looking at Figure 5.15, where we represent the absolute value

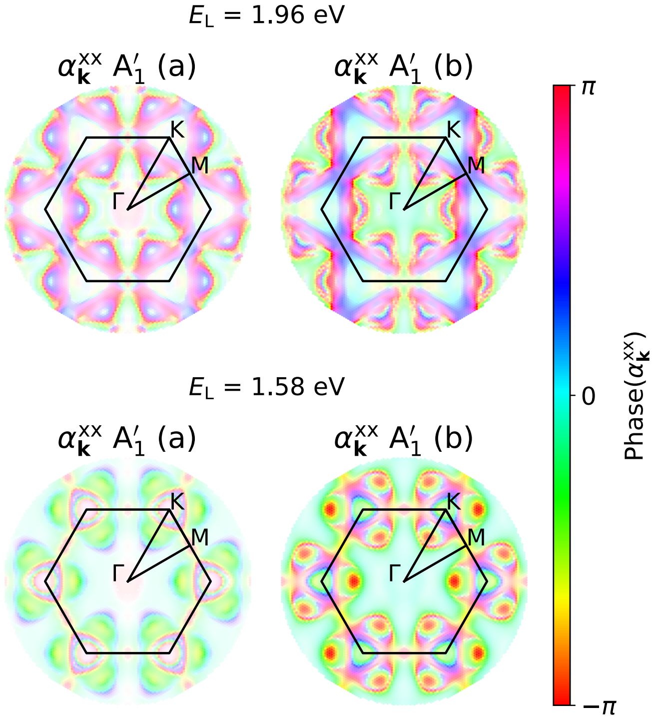

Figure 5.14: **k**-point-resolved contributions to the Raman susceptibility $\alpha_{\mathbf{k}}^{xx}(\omega)$ for triple-layer MoTe$_2$ across the BZ for two different laser energies used in experiment and two different phonon modes A_1' (a) on the left and A_1' (b) on the right. Figure taken from the supplementary information of Ref. [35].

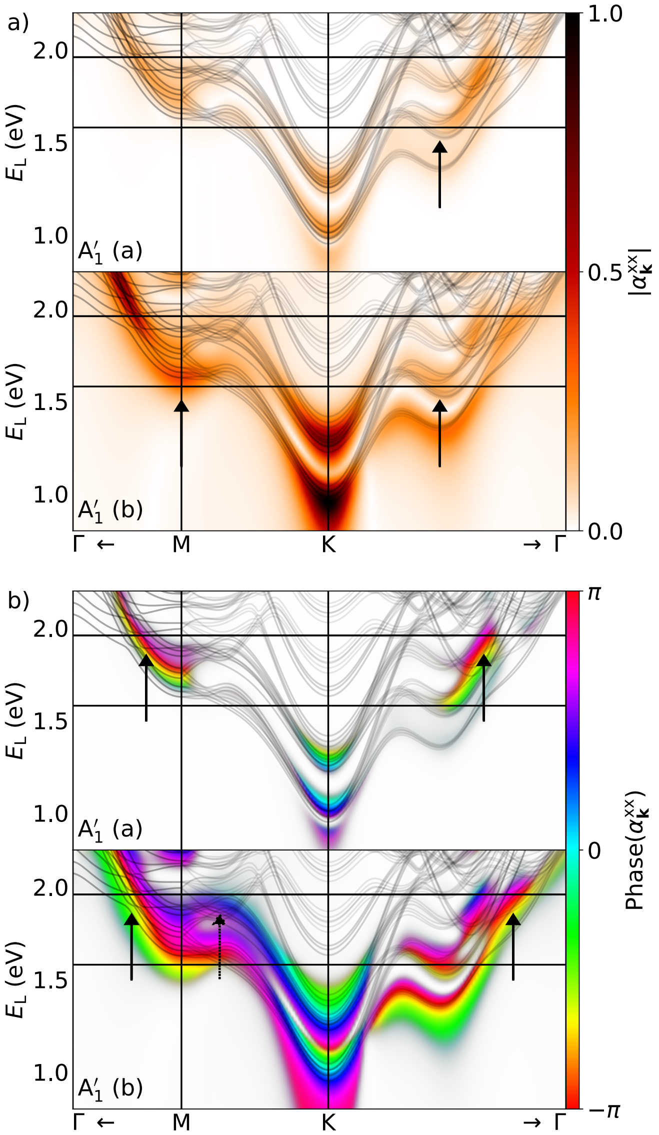

Figure 5.15: **k**-point resolved contributions $\alpha_\mathbf{k}^{\mathrm{xx}}(\omega)$ to the total Raman susceptibility for triple-layer $MoTe_2$ along the high-symmetry lines. Panel (a) shows the absolute value, while panel (b) shows the phase of $\alpha_\mathbf{k}^{\mathrm{xx}}(\omega)$. The phase is only shown if the absolute value if greater than 7% of the maximum value at that ω.

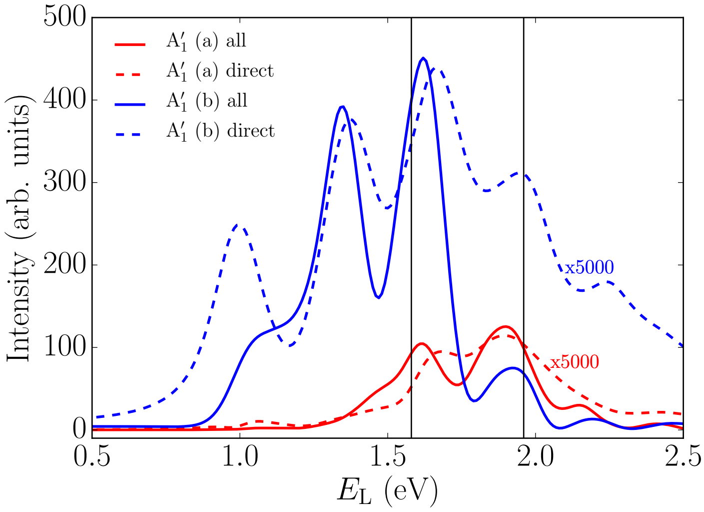

Figure 5.16: Relative contributions of the "direct" (dashed line) and "interference+direct" (solid line) terms to the total Raman susceptibility for triple-layer $MoTe_2$. The distinction between direct and interference terms is explained in Eq. (5.20). Figure taken from the supplementary information of Ref. [35].

of $\alpha_{\mathbf{k}}(\omega)$ along the high-symmetry line in panel (a) and its phase in panel (b). For a laser energy of 1.58 eV, there are resonant transitions between K and Γ and at M (see arrows in panel (a)). At these points the modulus of $\alpha_{\mathbf{k}}(\omega)$ is large and the phases are the same, which leads to constructive interference of the signal and an increase in the observed Raman intensity for both phonon modes.

At a laser energy of 1.96 eV, the situation is rather different. The $\alpha_{\mathbf{k}}(\omega)$ contributions from the region between K and M (purple dots in the Argand plot) no longer scatter concentrically around the origin and now destructively interfere with the contributions from the K-Γ and M-Γ regions (blue dots). We resolve which electronic transitions lead to these destructive interference effects by referring once more to Figure 5.15. The destructive contributions stem from transitions at M, which have a relative phase of $\pi/3$ (blue areas in Figure 5.15b) while the constructive ones have relative phases between $-\pi/2$ and $-\pi$ (green, yellow, and red areas).

In the case of the A_1'(a) mode, the amplitude of these destructive contributions is small and hence the resulting signal is higher than the one of the A_1'(b) mode, for which the destructive contributions have a sizable amplitude as shown in Fig. 5.16. From Figure 5.15 a) we can verify that both the amplitude of the $\alpha_{\mathbf{k}}(\omega)$ near the M point is higher for the A_1'(b) mode and that their phases are opposite to the ones from the contributions of the constructively interfering points (see dashed and solid arrows in panel (b)).

The reason for the small amplitudes in the K-M region for the A_1'(a) mode can be deduced from Figure 5.15 c). The diagonal EPC matrix elements for the A_1'(a) mode and the lowest conduction bands along the K-M direction have both positive and negative signs. Consequently, their contribution to $\alpha_{\mathbf{k}}(\omega)$ mostly cancels out, which leads to a small contribution to the Raman susceptibility. On the other hand, for the A_1'(b) mode, the different EPC matrix elements add up with the same sign and the **k**-points from this region give a larger contribution.

5.5 Conclusions

We described and demonstrated the use of an approach for the calculation of resonant Raman intensities based on finite differences of the dielectric susceptibility.

We obtained a qualitative agreement with the experimentally measured Raman intensities reported in the literature [24, 25, 26] of the A_1' Davydov triplet as a function of laser photon energy.

We started by analyzing the Raman intensities for the A_1' and E' phonon modes in the case of single-layer $\mathrm{MoTe_2}$. We then related the interference between the contributions from different **k**-points in the Brillouin zone to the symmetry of the phonon modes. We then used the same concepts to study the Raman intensities of the modes belonging to the same representation A_1'. There, we were able to explain the counter-intuitive experimentally measured dependence of the Raman intensities on laser energy in terms of interference effects. We additionally related the phase of the different contributions to the total Raman intensity to the sign of the change of the eigenvalues upon displacement according to the phonon mode which is in turn related to the electron-phonon matrix elements.

The simplicity of this method allows us to easily incorporate excitonic effects in the calculation of the Raman intensities by just calculating the dielectric susceptibility incorporating excitonic effects through the Bethe-Salpeter equation as described in Chapter 4.

There are, however, two drawbacks of using this method for the calculation of the Raman susceptibilities. The first one is that it relies on the adiabatic phonon approximation (see Eq. (5.6)). This approximation is not too dramatic when the phonon frequencies are small as is the case for TMDs (as we will show in the following chapters). The second drawback has to do with the computational effort required to evaluate the dielectric susceptibility for the different displacements. The displacements according to the phonon modes lead to a breaking of some of the lattice symmetries and to more **k**-points having to be treated explicitly. This is not very satisfactory, given that a large number of **k**-points is required to converge the dielectric response function and consequently also the Raman spectrum. This issue becomes more dramatic if we want to include the GW quasi-particle correction of eigenvalues and excitonic effects. In this case the GW and BSE calculations have to be performed for each of the different displacements which makes it impractical for large systems with a large number of phonon modes.

In addition to these issues, there is a growing interest in investigating Raman intensities of TMDs at different temperatures [125]. In practice, these studies allow us to monitor changes in the electronic and structural properties of a material for different operating temperatures, which is important for any practical device implementation. The theoretical simulation of the evolution of the Raman peaks can provide very useful and important data to interpret experiments and is as such highly desirable. It is, however, impossible to include the effects of temperature on the Raman spectra in a consistent way. Additionally, we are limited to the static phonon limit. Therefore, we will present in the following chapter an alternative approach based on perturbation theory.

6

Raman spectroscopy: Diagrammatic approach

6.1 Introduction

In this chapter we present an approach to calculate Raman spectra based on perturbation theory. In this case the one-phonon resonant Raman intensities are expressed as a sum over states of electron-phonon and electron-light coupling matrix elements. The matrix elements are calculated from first-principles and then used to obtain Raman spectra as a function of the incident laser energies. In this framework we can go beyond the adiabatic phonon approximation (see Eq. (5.6)) and include temperature effects. A summary of the different approaches and their advantages and drawbacks is shown in Table 6.1.

The theoretical foundations of this method were shown in the literature in previous works [15, 27, 28, 29, 30]. This method has been used to investigate the one- and two-phonon Raman spectrum of graphene relying on empirical models to calculate the coupling matrix elements [126, 93, 127, 128]. An implementation using quantities interpolated from first-principles was also demonstrated and applied to the study of the G peak [123].

In the preceding chapters we described how to calculate the coupling matrix elements from first-principle codes (see Chapters 3 and 4). Here we combine them in an in-house developed implementation to calculate the Raman intensities. This implementation is able to read these quantities from the different codes (`EPW`, `QE` + `yambo` and `abinit`) and use them to obtain Raman intensities as a post-processing step. This allows for the accurate comparison of the results obtained using different codes. Because it relies on first-principles calculations, the methods described here can also be promptly applied to different semiconductor systems. In practical terms, this implementation has the advantage that the electronic eigenvalues and eigenfunctions need to be calculated only once. The electron-phonon and electron-light matrix elements are calculated using these wave functions and the change of the self-consistent potential upon perturbation of the atoms (see Chapter 3). This allows for the calculations to be performed with much less computational resources than the finite differences method where the wave functions have to be calculated for each phonon displacement.

	Dynamic electric field	Dynamic phonons
DFPT [32]	no	no
Finite differences 5.4	yes	no
MBPT	yes	yes

Table 6.1: Limitations and advantages of the different available approaches to calculate Raman intensities.

The derivation of the expressions to evaluate the Raman susceptibility can be done in the framework of perturbation theory by considering a process involving one incoming photon, one outgoing photon and a phonon as shown in Sec. 6.1. We will first derive the expressions using the language of many-body perturbation theory (MBPT), then by taking analytic derivatives of the expression for the susceptibility. Finally we compare these expressions to the ones present in the literature. We then prove in Section 6.6, both theoretically and numerically, that these approaches reduce to the finite-differences method when the adiabatic phonon limit is considered.

The connection between the finite differences approach and the MBPT approach is in many aspects similar to the connection between the Allen-Heine-Cardona theory [129] for the band gap renormalization and the results derived from many-body perturbation theory [80].

The experimental observation of the temperature dependence of the Raman intensities was reported recently in the literature [125] and we will describe the approach to simulate this type of experiments in section 6.8. Within this framework we can include the effect of the band gap renormalization as a function of temperature using the concepts introduced in Chapter 3.

6.2 Raman scattering amplitude

The first-order Raman process involves two photons and one phonon interacting with the electrons. The Hamiltonian is

$$\hat{H} = \hat{H}_0 + \hat{H}_{en} + \hat{H}_{eL}, \tag{6.1}$$

where $\hat{H}_0$ is the Hamiltonian for non-interacting electrons, phonons and photons, $\hat{H}_{en}$ is the electron-phonon interaction treated in Chapter 3 and $\hat{H}_{eL}$ is the electron-light interaction treated in Chapter 4.

The Raman scattering cross section can be defined from a purely quantum mechanical perspective using Fermi's golden rule [15]. The cross section is then related to the transition probability from an initial state with the system in its ground state plus one incident photon with frequency ω_L to the final state where the crystal is again in the ground-state plus one phonon with frequency ω_μ and a photon with frequency $\omega_S = \omega_L - \omega_\mu$

$$\frac{1}{\tau} \propto \frac{d\sigma(\omega_S)}{d\Omega} \propto \sum_{LS\mu} |\overline{\overline{\alpha}}^{\mu}(\omega_L, \omega_\mu, \omega_S)|^2 \delta(\omega_S - \omega_L - \omega_\mu), \tag{6.2}$$

where $\overline{\overline{\alpha}}$ is the Raman tensor as defined before in Eq. (5.9). This definition is similar to Eq. (5.5). In this case, however, $\overline{\overline{\alpha}}^{\mu}(\omega, \omega_L)$ is evaluated from a perturbative calculation in terms of Feynman diagrams as opposed to finite differences of the dielectric susceptibility.

The formulation of the Raman tensor from a many-body perspective is not a closed issue. An alternative formulation of the scattering amplitude is developed and used in [130] and suggested in [126, Section C]. In this formulation the Raman scattering cross section is defined from a contribution to the imaginary part of the photon self-energy. This self-energy occurs due to the presence of electrons and phonons in the material and is represented in the diagram of Fig. 6.1. A technique to evaluate the imaginary part of Feynman diagrams is to use the *cutting rules* or *reduced graph expansion* as described in Ref. [50, Appendix N]. We did notice, however, that applying these rules does not seem to lead to a single contribution to the lifetime. Indeed there are multiple ways to “cut” the diagrams each of them giving a different contribution. Furthermore not all of these contributions lead to a photon and a phonon in the final state. In the case of [130] the energy transfer between initial and final state is imposed [130, Eq. 3.26] which corresponds to considering only a specific “cut” of the diagram leading to a photon and phonon in the final state. How to define the Raman scattering cross-section from an imaginary part of a self-energy should be the topic of further research but is beyond the scope of the current thesis.

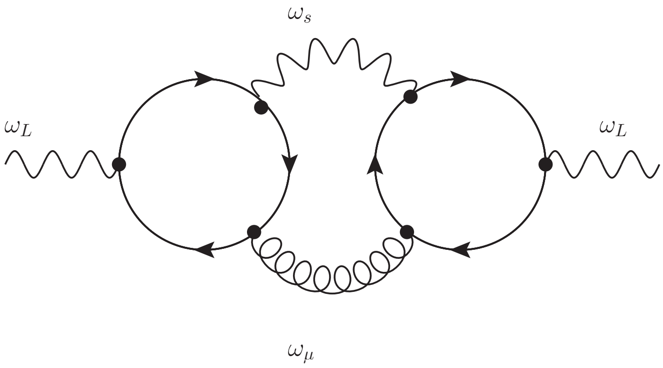

Figure 6.1: Feynman diagram of a process that appears in the expansion of the photon self-energy in a system with interacting electrons and phonons. The Raman scattering amplitude can be obtained by cutting the diagram across the lines ω_s and ω_μ as mentioned in [126, Section C].

Finally in Ref. [53] a formulation of the Raman scattering is provided in terms of a three-particle Green's function. In this formulation the excitonic effects are accounted for in the BSE formalism (discussed in chapter 4). In the introduction of their paper, they mention some of the problems in defining the Raman susceptibility in terms of a spectral function of the scattered light. One of such problems is how to perform analytic continuation of a quantity that depends on three imaginary frequencies (in the finite temperature formalism) to the real axis. A theory formulated in these terms enable us to calculate scattering processes with different particles in the final state, i. e. without forcing the energy conservation through a delta function and without the restriction to first order Raman scattering.

In the formalism presented here we will enforce the energy conservation, selecting the desired process as it is done in the literature [130, 53, 126, 15, 27, 28].

6.3 Feynman diagrams for Raman spectroscopy

The one-phonon Raman tensor is evaluated from the sum of the two Feynman diagrams in Fig. 6.2

$$\alpha^{LS\mu}(\omega_L,\omega_\mu,\omega_S) = M_1^{LS\mu}(\omega_L,\omega_\mu,\omega_S) + M_2^{LS\mu}(\omega_L,\omega_\mu,\omega_S). \tag{6.3}$$

Following the procedure in Refs. [126, 93, 19, 123] we translate the diagrams

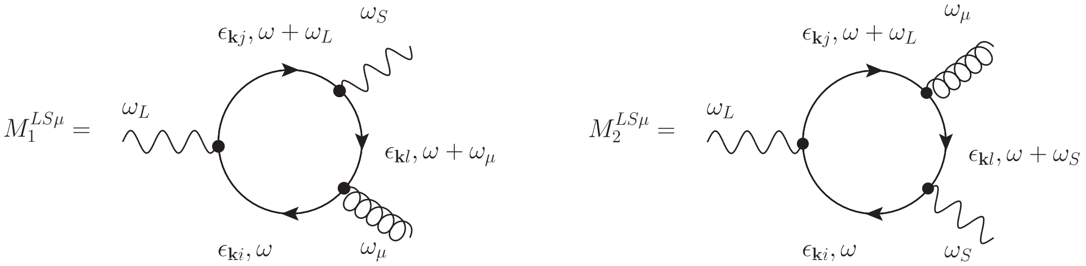

Figure 6.2: Feynman diagrams contributing to the Raman tensor.

into the following expressions

$$\begin{aligned} M_1^{LS\mu}(\omega_L,\omega_\mu,\omega_S) \propto \sum_{\mathbf{k}} \int \frac{d\omega}{2\pi} e^{i\omega 0^+} Tr\Big\{ & \hat{G}_{\mathbf{k}}(\omega)\hat{\Lambda}^S_{\mathbf{k}}\hat{G}_{\mathbf{k}}(\omega+\omega_S)\hat{g}^\mu_{\mathbf{k}} \\ & \hat{G}_{\mathbf{k}}(\omega+\omega_L)\hat{\Lambda}^L_{\mathbf{k}}\Big\}, \end{aligned} \tag{6.4}$$

$$\begin{aligned} M_2^{LS\mu}(\omega_L,\omega_\mu,\omega_S) \propto \sum_{\mathbf{k}} \int \frac{d\omega}{2\pi} e^{i\omega 0^+} Tr\Big\{ & \hat{G}_{\mathbf{k}}(\omega)\hat{g}^\mu\hat{G}_{\mathbf{k}}(\omega+\omega_\mu)\hat{\Lambda}^S \\ & \hat{G}_{\mathbf{k}}(\omega+\omega_L)\hat{\Lambda}^L\Big\}. \end{aligned} \tag{6.5}$$

To evaluate the trace, we expand the operators in a basis of electronic states

$$\begin{aligned} M_1^{LS\mu}(\omega_L,\omega_\mu,\omega_S) \propto \sum_{\mathbf{k}}\sum_{ijl} \int \frac{d\omega}{2\pi} e^{i\omega 0^+} \Big\{ & G_{i\mathbf{k}}(\omega)\Lambda^S_{il\mathbf{k}}G_{l\mathbf{k}}(\omega+\omega_S)g^\mu_{lj\mathbf{k}} \\ & G_{j\mathbf{k}}(\omega+\omega_L)\Lambda^L_{ji\mathbf{k}}\Big\}, \end{aligned} \tag{6.6}$$

$$\begin{aligned} M_2^{LS\mu}(\omega_L,\omega_\mu,\omega_S) \propto \sum_{\mathbf{k}}\sum_{ijl} \int \frac{d\omega}{2\pi} e^{i\omega 0^+} \Big\{ & G_{i\mathbf{k}}(\omega)g^\mu_{il\mathbf{k}}G_{l\mathbf{k}}(\omega+\omega_\mu)\Lambda^S_{lj\mathbf{k}} \\ & G_{j\mathbf{k}}(\omega+\omega_L)\Lambda^L_{ji\mathbf{k}}\Big\}, \end{aligned} \tag{6.7}$$

where L and S represent the set of quantum numbers (frequency and polarization) of the incoming and scattered light respectively and $G_{i\mathbf{k}}$ is given by Eq. (1.31). When performing the integration over frequency ω in the fermion loop we obtain for each of the two Feynman diagrams three expressions that correspond to the 6 Goldstone (time-ordered) diagrams [51]

$$
\begin{aligned}
M_1^{LS\mu}&(\omega_L, \omega_\mu, \omega_S) \propto \\
&\sum_{\mathbf{k}} \sum_{ijl\mathbf{k}} \Big\{ \big[f(\epsilon_{i\mathbf{k}}) \Lambda^S_{il\mathbf{k}} G_{l\mathbf{k}}(\omega + \omega_S) g^\mu_{lj\mathbf{k}} G_{j\mathbf{k}}(\omega + \omega_L) \Lambda^L_{ji\mathbf{k}}\big]_{\omega = \epsilon_{i\mathbf{k}} + i\gamma/2} + \\
&\qquad \big[f(\epsilon_{l\mathbf{k}}) g^\mu_{lj\mathbf{k}} G_{i\mathbf{k}}(\omega + \omega_L) \Lambda^L_{ji\mathbf{k}} G_{j\mathbf{k}}(\omega) \Lambda^S_{il\mathbf{k}}\big]_{\omega = \omega_S + \epsilon_{l\mathbf{k}} + i\gamma/2} + \\
&\qquad \big[f(\epsilon_{j\mathbf{k}}) \Lambda^L_{ji\mathbf{k}} G_{l\mathbf{k}}(\omega) \Lambda^S_{il\mathbf{k}} G_{i\mathbf{k}}(\omega + \omega_S) g^\mu_{lj\mathbf{k}}\big]_{\omega = \omega_L + \epsilon_{j\mathbf{k}} + i\gamma/2} \Big\},
\end{aligned}
\tag{6.8}
$$

$$
\begin{aligned}
M_2^{LS\mu}&(\omega_L, \omega_\mu, \omega_S) \propto \\
&\sum_{\mathbf{k}} \sum_{ijl} \Big\{ \big[f(\epsilon_{i\mathbf{k}}) g^\mu_{il\mathbf{k}} G_{l\mathbf{k}}(\omega + \omega_\mu) \Lambda^S_{lj\mathbf{k}} G_{j\mathbf{k}}(\omega + \omega_L) \Lambda^L_{ji\mathbf{k}}\big]_{\omega = \epsilon_{i\mathbf{k}} + i\gamma/2} + \\
&\qquad \big[f(\epsilon_{l\mathbf{k}}) \Lambda^S_{lj\mathbf{k}} G_{j\mathbf{k}}(\omega + \omega_L) \Lambda^L_{ji\mathbf{k}} G_{i\mathbf{k}}(\omega) g^\mu_{il\mathbf{k}}\big]_{\omega = -\omega_L + \epsilon_{l\mathbf{k}} + i\gamma/2} + \\
&\qquad \big[f(\epsilon_{j\mathbf{k}}) \Lambda^L_{ji\mathbf{k}} G_{i\mathbf{k}}(\omega) g^\mu_{il\mathbf{k}} G_{l\mathbf{k}}(\omega + \omega_\mu) \Lambda^S_{lj\mathbf{k}}\big]_{\omega = -\omega_S + \epsilon_{j\mathbf{k}} + i\gamma/2} \Big\} \quad .
\end{aligned}
\tag{6.9}
$$

After evaluating the poles of one of the Green's functions we obtain a two-particle propagator. We represent this propagator in matrix form as

$$
G_{ij\mathbf{k}}(\omega) = \frac{f(\epsilon_{i\mathbf{k}})}{\omega - (\epsilon_{i\mathbf{k}} - \epsilon_{j\mathbf{k}}) + i\gamma} + \frac{1 - f(\epsilon_{i\mathbf{k}})}{\omega - (\epsilon_{i\mathbf{k}} - \epsilon_{j\mathbf{k}})}
\tag{6.10}
$$

which should not be confused with the expression of the Green's function in Eq. (1.31)). Using this notation the matrix elements at any **k**-point can be evaluated using the expressions

$$
\begin{aligned}
M_1^{LS\mu}(\omega_L,\omega_\mu,\omega_S) \propto \sum_{\mathbf{k}}\sum_{ijl} \{ & f(\epsilon_{i\mathbf{k}})\Lambda^S_{il\mathbf{k}} g^\mu_{lj\mathbf{k}} \Lambda^L_{ji\mathbf{k}} G_{li\mathbf{k}}(\omega_S) G_{ji\mathbf{k}}(\omega_L) + \\
& f(\epsilon_{l\mathbf{k}}) g^\mu_{lj\mathbf{k}} \Lambda^L_{ji\mathbf{k}} \Lambda^S_{il\mathbf{k}} G_{jl\mathbf{k}}(\omega_\mu) G_{il\mathbf{k}}(-\omega_L+\omega_\mu) + \\
& f(\epsilon_{j\mathbf{k}}) \Lambda^L_{ji\mathbf{k}} \Lambda^S_{il\mathbf{k}} g^{lj\mathbf{k}} G_{ij\mathbf{k}}(-\omega_L) G_{lj\mathbf{k}}(\omega_S) \},
\end{aligned}
\tag{6.11}
$$

$$
\begin{aligned}
M_2^{LS\mu}(\omega_L,\omega_\mu,\omega_S) \propto \sum_{\mathbf{k}}\sum_{ijl} \{ & f(\epsilon_{i\mathbf{k}}) g^\mu_{il\mathbf{k}} \Lambda^S_{lj\mathbf{k}} \Lambda^L_{ji\mathbf{k}} G_{li\mathbf{k}}(\omega_\mu) G_{ji\mathbf{k}}(\omega_L) + \\
& f(\epsilon_{l\mathbf{k}}) \Lambda^S_{lj\mathbf{k}} \Lambda^L_{ji\mathbf{k}} g^{il\mathbf{k}} G_{jl\mathbf{k}}(\omega_L-\omega_\mu) G_{il\mathbf{k}}(-\omega_\mu) + \\
& f(\epsilon_{j\mathbf{k}}) \Lambda^L_{ji\mathbf{k}} g^\mu_{il\mathbf{k}} \Lambda^S_{lj\mathbf{k}} G_{ij\mathbf{k}}(-\omega_L) G_{lj\mathbf{k}}(-\omega_L+\omega_\mu) \}.
\end{aligned}
\tag{6.12}
$$

The resulting expressions here imply a triple sum over N bands which leads to a scaling with N^3. The Fermi occupations will however restrict the number of terms that are non-zero. For example it is immediately evident that the sum over the initial state i should be restricted to the valence bands leading to a $N_v \times N^2$ scaling, where N_v is the number of valence bands.

Because $G_{ij\mathbf{k}}(\omega)$ in Eq. (6.10) is composed of two terms and it appears twice in each of the 6 terms in Eqs. (6.11) and (6.12) this leads to a total of 24 terms. Some of these terms cancel exactly and hence the expressions should be simplified before the implementation in a computer code to avoid the numeric cancelation. The numeric cancelation is not exact due to floating point precision and leads to undesired numerical noise in the calculations. We will discuss how to obtain these simplified expressions in Section 6.6.

6.4 Virtual states

One important point of discussion and understanding of the Raman process has to do with virtual states and their meaning. We will outline here an example to clarify this concept.

A typical schematic representation of the Raman process is shown in Fig. 6.3. This representation only serves to show the type of perturbations that enter in the Raman process and its physical interpretation should not be taken too far. Firstly, this representation implies a certain time ordering of the processes. The total amplitude of the process, however, is calculated considering all possible time orderings for the different constituent processes (Eqs. (6.11) and (6.12)).

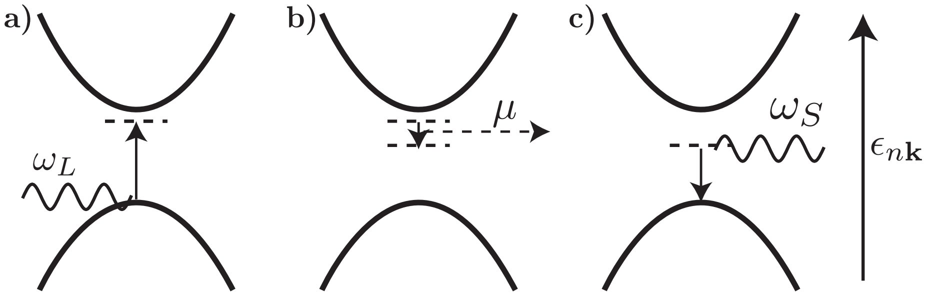

Figure 6.3: Pictorial representation of the steps involved in the Raman process. The physical interpretation of this pictorial representation should not be taken too far as in step b) the electron decays to an intermediate state that does not exist.

A common problem lies in the physical interpretation of the "virtual state" that appears when the electron seems to decay to a state below the gap. The virtual state is the name given to a transitory state of the system when going from an initial to a final state in higher orders of perturbation theory. In these cases, it seems that in between the initial and final states, that are eigenstates of the system, the particles can be in intermediate states that are not eigenstates of the system. This outcome stems from the typical expressions in perturbation theory although these are written exclusively in terms of real states of the system.

6.5 Practical implementation

To evaluate the Raman scattering cross section from first-principles, we need the electronic energies and phononic frequencies, the electron-phonon, and the electron-light coupling matrix elements. These should be obtained in the full Brillouin zone (FBZ) on a dense **k**-point grid. They can be calculated using different *ab initio* codes.

Currently we implemented interfaces with the `EPW` code, the `QE` suite and the `abinit` code. We use the `QE` suite to obtain the Kohn-Sham states and calculate the electron-phonon coupling matrix elements with DPFT. To obtain the electron-light coupling we use the `yambo` code. We had to modify the code to calculate the matrix elements for all the possible band combinations (by default it calculates only transitions between valence and conduction bands).

The `yambo` implementation allows us to include or not to include the non-local contributions due to the pseudo-potential in the calculation. The `EPW` code reads the Kohn-Sham states and derivative of the self-consistent potential upon atomic displacements from `QE`, calculates electron-phonon, and electron-light coupling matrix elements and allows one to interpolate them to a fine grid of q-points.[1]

To further verify the implementation, we used `abipy` to create a workflow using the `abinit` code to calculate the electron-light and electron-phonon coupling matrix elements. The electron-light matrix elements were stored in the `abinit` binary format. To read them in `Python` we modified the `optic` utility to convert it to the `netcdf` format which is then read by our `Python` classes. This interface can be improved by modifying the `abinit` code to write the matrix elements directly in `netcdf` format.

Since the matrix elements are gauge-dependent, the user must ensure that both electron-phonon and electron-light matrix elements were calculated consistently, i.e. using the same wave functions. To allow for maximum flexibility, our implementation abstracts these objects from their origin through the use of generic `Python` classes. For each of the quantities a new interface can be constructed that either reads the data from a file stored in disk, directly interfaces with the code or calculates the quantities using empirical models. This modu-

---

[1] We implemented two different interfaces. In one of them we store the electron eigenvalues, electron-phonon and electron-light coupling matrix elements in a binary file that is then read by the `Python` scripts. The other interface implemented by S. Reichardt reads the matrix elements in real-space Wannier representation which are then transformed to reciprocal space inside the python code allowing for more flexibility of changing the **k**-grids [123].

lar approach is the same one that we used in the `yambopy` package described in Appendix A.

6.5.0.1 Double grid technique

In order to improve the convergence of the final spectra with the number of **k**-points we implemented a double-grid technique. This approach relies on the fact that the matrix elements entering in Eqs. (6.11) and (6.12). are smoother as a function of **k** than the electronic $\epsilon_{n\mathbf{k}}$ eigenvalues. Additionally, it is computationally more expensive to evaluate the matrix elements than the eigenvalues. The convergence of the whole Raman scattering cross section can thus be improved by calculating only the eigenvalues on a finer mesh in a similar way as to what was shown for optical absorption at the BSE level [103, 102].

As an illustrative example let's consider the following expression contained in Eq. (6.11):

$$M_1^{LS\mu}(\omega_L,\omega_\mu,\omega_S) \supset \sum_{\mathbf{k}}\sum_{ijl} \Lambda^S_{il\mathbf{k}} g^\mu_{lj\mathbf{k}} \Lambda^L_{ji\mathbf{k}} G_{li\mathbf{k}}(\omega_S) G_{ji\mathbf{k}}(\omega_L) \tag{6.13}$$

If we define a grid of $\mathbf{k}'$-points with higher density than the **k**-grid, then Eq. (6.13) can be re-written as:

$$M_1^{LS\mu}(\omega_L,\omega_\mu,\omega_S) \supset \sum_{\mathbf{k}}\sum_{ijl} \Lambda^S_{il\mathbf{k}} g^\mu_{lj\mathbf{k}} \Lambda^L_{ji\mathbf{k}} \sum_{\mathbf{k}'\in\mathbf{k}^D} G_{li\mathbf{k}'}(\omega_S) G_{ji\mathbf{k}'}(\omega_L) \tag{6.14}$$

were $\mathbf{k}^D$ denotes a **k**-point grid denser than **k**. Which effectively corresponds to averaging the Green's function on the denser $\mathbf{k}'$ mesh.

6.5.0.2 Irreducible Brillouin zone

Another way to improve the speed of the calculation is to evaluate the Green's functions only on the irreducible Brillouin zone (IBZ). While this is in principle possible for the matrix elements as well, the implementation is more cumbersome so we left it for the future. The electron-light and electron-phonon coupling matrix elements transforms like a vector. A proper implementation accounting for the symmetries of the matrix elements in the full Brillouin (FBZ) should account for that. On the other hand the Green's functions are scalar quantities and they can be evaluated only once for each point in the IBZ and used to evaluate the expressions in Eqs. (6.11) and (6.12) on the FBZ. The implementation in this case is manageable and requires only the mapping of the k-points from the IBZ to the FBZ. In this case the Raman matrix elements are evaluated as

$$M_1^{LS\mu}(\omega_L,\omega_\mu,\omega_S) = \sum_{\mathbf{k}\in\mathbf{k}_{\text{IBZ}}} G_{li\mathbf{k}}(\omega_S)G_{ji\mathbf{k}}(\omega_L) \sum_{\mathbf{k}'\in\mathbf{k}^*} \sum_{ijl} \Lambda^S_{il\mathbf{k}'} g^\mu_{lj\mathbf{k}'} \Lambda^L_{ji\mathbf{k}'} \tag{6.15}$$

where $\mathbf{k}^*$ are the points that can be obtained from $\mathbf{k}$ using a symmetry transformation of the reciprocal lattice. Depending on the number of symmetries of the system, this can lead to a great speedup of the computation. The implementation of this functionality will be the topic of future developments in the implementation.

6.6 Static finite differences vs diagrammatic approach

In this section we show how the derivative of $\chi^{LS}(\omega_L)$ obtained using finite differences reduces to the expressions derived is Sec. 6.3 when setting the phonon frequency to zero (adiabatic phonon limit). We then proceed to obtain all the necessary quantities: the electronic states, electron-phonon and electron-light coupling matrix elements from different *ab initio* codes (`QE` + `yambo`, `abinit` and `EPW`) for a numerical comparison.

6.6.1 Analytical derivation

We will start with the expression of the susceptibility for a semi-conductor shown in Eq. (4.27). The derivative with respect to a generic atomic position $\mathbf{R}$

(represented by $\partial_{\mathbf{R}}$ for simplicity) leads to

$$\begin{aligned}\partial_{\mathbf{R}}\chi(\omega_L) \propto \sum_{vc\mathbf{k}} \Big[& \frac{\partial_{\mathbf{R}}(\Lambda^S_{vc\mathbf{k}})(\Lambda^L_{cv\mathbf{k}})}{(\omega_L - (\epsilon_{c\mathbf{k}} - \epsilon_{v\mathbf{k}}) + i\gamma)} + \frac{\partial_{\mathbf{R}}(\Lambda^S_{vc\mathbf{k}})(\Lambda^L_{cv\mathbf{k}})}{(-\omega_L - (\epsilon_{c\mathbf{k}} - \epsilon_{v\mathbf{k}}) + i\gamma)} + \\ & \frac{(\Lambda^S_{vc\mathbf{k}})\partial_{\mathbf{R}}(\Lambda^L_{cv\mathbf{k}})}{(\omega_L - (\epsilon_{c\mathbf{k}} - \epsilon_{v\mathbf{k}}) + i\gamma)} + \frac{(\Lambda^S_{vc\mathbf{k}})\partial_{\mathbf{R}}(\Lambda^L_{cv\mathbf{k}})}{(-\omega_L - (\epsilon_{c\mathbf{k}} - \epsilon_{v\mathbf{k}}) + i\gamma)} + \\ & \frac{(\Lambda^S_{vc\mathbf{k}})(\Lambda^L_{cv\mathbf{k}})}{(\omega_L - (\epsilon_{c\mathbf{k}} - \epsilon_{v\mathbf{k}}) + i\gamma)^2}(\partial_{\mathbf{R}}\epsilon_{c\mathbf{k}} - \partial_{\mathbf{R}}\epsilon_{v\mathbf{k}}) + \\ & \frac{(\Lambda^S_{vc\mathbf{k}})(\Lambda^L_{cv\mathbf{k}})}{(-\omega_L - (\epsilon_{c\mathbf{k}} - \epsilon_{v\mathbf{k}}) + i\gamma)^2}(\partial_{\mathbf{R}}\epsilon_{c\mathbf{k}} - \partial_{\mathbf{R}}\epsilon_{v\mathbf{k}}) \Big]\end{aligned} \tag{6.16}$$

The derivatives of the dipoles with displacements can be written in terms of sums of electron-phonon matrix elements. The full details of the derivation are shown in Appendix C. The final expression we obtain is

$$\begin{aligned}\partial_{\mathbf{R}}\chi(\omega_L) \propto & \sum_{\substack{vcc' \\ \mathbf{k}}} \frac{\Lambda_{vc'\mathbf{k}} g^{\mathbf{R}}_{c'c\mathbf{k}} \Lambda_{cv\mathbf{k}}}{R_{cv\mathbf{k}}(\omega_L) R_{c'v\mathbf{k}}(\omega_L)} + \sum_{\substack{vcv' \\ \mathbf{k}}} \frac{-g^{\mathbf{R}}_{vv'\mathbf{k}} \Lambda_{v'c\mathbf{k}} \Lambda_{cv\mathbf{k}}}{R_{cv\mathbf{k}}(\omega_L) R_{cv'\mathbf{k}}(\omega_L)} + \\ & \sum_{\substack{vcv' \\ \mathbf{k}}} \frac{\Lambda_{vv'\mathbf{k}} g^{\mathbf{R}}_{v'c\mathbf{k}} \Lambda_{cv\mathbf{k}}}{(\epsilon_{c\mathbf{k}} - \epsilon_{v'\mathbf{k}}) R_{cv\mathbf{k}}(\omega_L)} + \sum_{\substack{vcc' \\ \mathbf{k}}} \frac{-g^{\mathbf{R}}_{vc'\mathbf{k}} \Lambda_{c'c\mathbf{k}} \Lambda_{cv\mathbf{k}}}{(\epsilon_{c'\mathbf{k}} - \epsilon_{v\mathbf{k}}) R_{cv\mathbf{k}}(\omega_L)} + \\ & \sum_{\substack{vcc' \\ \mathbf{k}}} \frac{-\Lambda_{vc\mathbf{k}} \Lambda_{cc\mathbf{k}} g^{\mathbf{R}}_{c'v\mathbf{k}}}{(\epsilon_{c'\mathbf{k}} - \epsilon_{v\mathbf{k}}) R_{cv\mathbf{k}}(\omega_L)} + \sum_{\substack{vcv' \\ \mathbf{k}}} \frac{\Lambda_{vc\mathbf{k}} g^{\mathbf{R}}_{cv'\mathbf{k}} \Lambda_{v'v\mathbf{k}}}{(\epsilon_{c\mathbf{k}} - \epsilon_{v'\mathbf{k}}) R_{cv\mathbf{k}}(\omega_L)} + \\ & (\omega_L \to -\omega_L).\end{aligned} \tag{6.17}$$

with $R_{cv\mathbf{k}}(\omega_L) = [\omega_L - (\epsilon_{c\mathbf{k}} - \epsilon_{v\mathbf{k}}) + i\gamma]$. The symbol $\partial_{\mathbf{R}}$ corresponds to the derivative with respect to the displacement of an atom $R_{I\alpha}$. The Raman intensity of a certain phonon modes is given by

$$\alpha^{LS\mu}(\omega_L) = \sum_{I\alpha} \left| \frac{\partial\chi^{LS}(\omega_L)}{\partial R_{I\alpha}} Q^{\mu}_{I\alpha} \right|^2 . \tag{6.18}$$

These expressions are equivalent to the ones derived from the diagrammatic approach in Eqs. (6.11), (6.12) and (6.3) when setting $\omega_\mu = 0$. The expressions with explicit ω_μ are shown in Appendix C. Using these expressions has the advantage that we do not rely on the numeric cancelation of terms. This makes the calculation faster and more stable. In this case the scaling of the calculation is $(N_{\mathbf{k}} \times N_v \times N_c \times N)$.

These expressions are also equivalent to the ones derived by Yu and Cardona in Ref. [30]

$$\alpha^{LS\mu}(\omega_L) \propto \sum_{inn'} \Bigg\{ \frac{\langle\Psi_i|\hat{H}^L_{\mathrm{e-L}}|\Psi_n\rangle \langle\Psi_n|\hat{H}^\mu_{\mathrm{e-n}}|\Psi_{n'}\rangle \langle\Psi_{n'}|\hat{H}^S_{\mathrm{e-L}}|\Psi_i\rangle}{(\omega_L-(\epsilon_n-\epsilon_i))(\omega_L-\omega_\mu-(\epsilon_{n'}-\epsilon_i))} \tag{6.19}$$

$$\frac{\langle\Psi_i|\hat{H}^S_{\mathrm{e-L}}|\Psi_n\rangle \langle\Psi_n|\hat{H}^\mu_{\mathrm{e-n}}|\Psi_{n'}\rangle \langle\Psi_{n'}|\hat{H}^L_{\mathrm{e-L}}|\Psi_i\rangle}{(-\omega_L+\omega_\mu-(\epsilon_n-\epsilon_i))(-\omega_L-(\epsilon_{n'}-\epsilon_i))} \tag{6.20}$$

$$\frac{\langle\Psi_i|\hat{H}^L_{\mathrm{e-L}}|\Psi_n\rangle \langle\Psi_n|\hat{H}^S_{\mathrm{e-L}}|\Psi_{n'}\rangle \langle\Psi_{n'}|\hat{H}^\mu_{\mathrm{e-n}}|\Psi_i\rangle}{(\omega_L-(\epsilon_n-\epsilon_i))(\omega_\mu-(\epsilon_{n'}-\epsilon_i))} \tag{6.21}$$

$$\frac{\langle\Psi_i|\hat{H}^S_{\mathrm{e-L}}|\Psi_n\rangle \langle\Psi_n|\hat{H}^L_{\mathrm{e-L}}|\Psi_{n'}\rangle \langle\Psi_{n'}|\hat{H}^\mu_{\mathrm{e-n}}|\Psi_i\rangle}{(-\omega_L+\omega_\mu-(\epsilon_n-\epsilon_i))(\omega_\mu-(\epsilon_{n'}-\epsilon_i))} \tag{6.22}$$

$$\frac{\langle\Psi_i|\hat{H}^\mu_{\mathrm{e-n}}|\Psi_n\rangle \langle\Psi_n|\hat{H}^L_{\mathrm{e-L}}|\Psi_{n'}\rangle \langle\Psi_{n'}|\hat{H}^S_{\mathrm{e-L}}|\Psi_i\rangle}{(-\omega_\mu-(\epsilon_n-\epsilon_i))(\omega_L-\omega_\mu-(\epsilon_{n'}-\epsilon_i))} \tag{6.23}$$

$$\frac{\langle\Psi_i|\hat{H}^\mu_{\mathrm{e-n}}|\Psi_n\rangle \langle\Psi_n|\hat{H}^S_{\mathrm{e-L}}|\Psi_{n'}\rangle \langle\Psi_{n'}|\hat{H}^L_{\mathrm{e-L}}|\Psi_i\rangle}{(-\omega_\mu-(\epsilon_{n'}-\epsilon_i))(-\omega_L-(\epsilon_{n'}-\epsilon_i))} \Bigg\} \tag{6.24}$$

where in $\hat{H}^S_{\mathrm{e-L}}$ and $\hat{H}^\mu_{\mathrm{e-n}}$ the particular photon and phonon interacting are selected. Replacing the interaction terms $\hat{H}^L_{\mathrm{e-L}}$ with Eq. (4.19) and $\hat{H}^\mu_{\mathrm{e-n}}$ with Eq. (3.1) setting $\mathbf{q} \to 0$ leads to 12 expressions that are equivalent to (6.17) when $\omega_\mu = 0$ as shown in Ref. [131] and reproduced in Appendix C.

6.6.2 Numerical comparison: single-layer MoS$_2$

After proving analytically that the results obtained from the diagrammatic calculation are equivalent to the ones obtained from finite differences, we show that they are also numerically equivalent. We choose as test case for the comparison the Raman spectrum of MoS$_2$. In the comparison we will demonstrate that the interfaces between our implementation are working correctly and yield consistent results among the different codes (`QE` + `yambo`, `EPW` and `abinit`). We start by comparing the diagrammatic calculation of the Raman intensity using ingredients obtained from the different codes, obtaining remarkable agreement. When comparing the finite-differences calculations with the diagrammatic approach we note good agreement in the resonant regime but some discrepancy in the non-resonant regime.

6.6.2.1 `QE` + `yambo` vs `EPW`

The DFT ground-state calculations were performed with the `pw.x` code from the `QE` suite using LDA norm-conserving relativistic pseudo-potentials from the SSSP library [132]. The Brillouin zone was sampled with a 16x16x1 **k**-point mesh. We used a lattice parameter of 5.97 Bohr and a vacuum spacing of 50 Bohr between the adjacent layers. The phonon calculations were performed using the `ph.x` code. The relevant quantities for the finite differences method are the phonon displacements at $\mathbf{q} = \Gamma$ and the dielectric susceptibilities calculated at each displacement. To generate the different displaced cells we used an in-house developed `Python` code using the `yambopy` `Python` classes (see Appendix A). For the diagrammatic calculations, we need electron-phonon and the electron-light coupling matrix elements. These can be obtained using the `yambo` interface with `ph.x`, or using the interpolation implemented in the `EPW` [92] code. The later has the advantage that the matrix elements are projected onto a Wannier basis allowing for a fast interpolation to arbitrarily fine **k**-grids. The main drawback is that the interpolation needs first a Wannierization of the electronic band-structure which can be cumbersome and often requires human intervention. Additionally it can only be done for states well described by a localized Wannier basis which becomes difficult for higher energy states as they are more delocalized. We performed the Wannierization of the band-structure including spin-orbit coupling of MoS_2 for 26 bands (sp3 for S atoms and d for Mo). To obtain a reliable comparison between the two methods we included the same number of bands in both methods. We present the results of the comparison of the Raman intensities calculated with the two methods in Fig. 6.4.

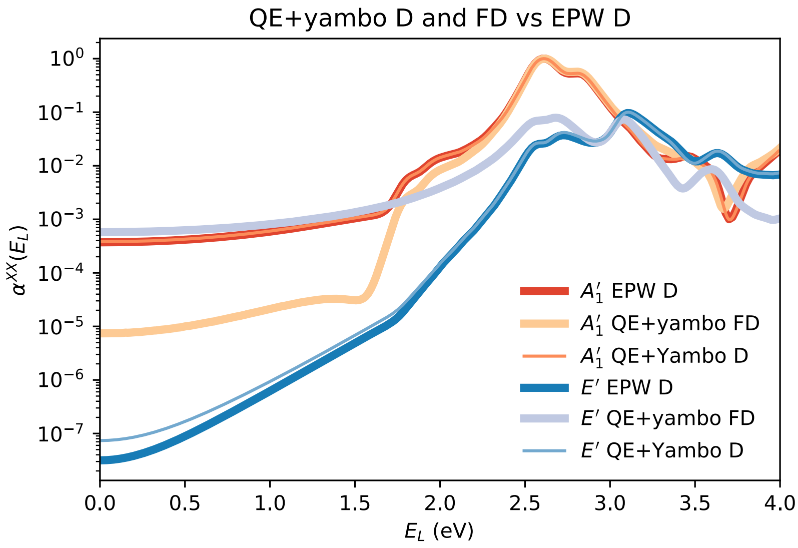

Figure 6.4: Comparison of the Raman intensity of single layer MoS_2 as a function of laser energy calculated using `QE` plus `yambo` and the `EPW` codes. The calculation is done including the effect of spin-orbit coupling.

The agreement between the diagrammatic calculation and the one obtained from the finite differences approach is good in the resonant regime as can be seen in Fig. 6.4. In the non-resonant case however, some discrepancies exist. The reason for this discrepancy might be due to the presence of an ionic static electric field in the finite differences case.

6.6.2.2 **`QE` + `yambo` vs `abinit`**

Here we compare numerically the results of the calculation using the `QE` + `yambo` and `abinit` codes. In this case we used the FHI LDA norm-conserving pseudopotentials without spin as those are available in both codes. The results are in remarkable good agreement as shown in Fig. 6.5. This shows consistency in the calculation of the electron-phonon matrix elements among the two different codes as previously shown in Ref. [133]. Additionally it shows agreement in the calculation of the electron-light coupling matrix elements between the `abinit` code and `yambo`.

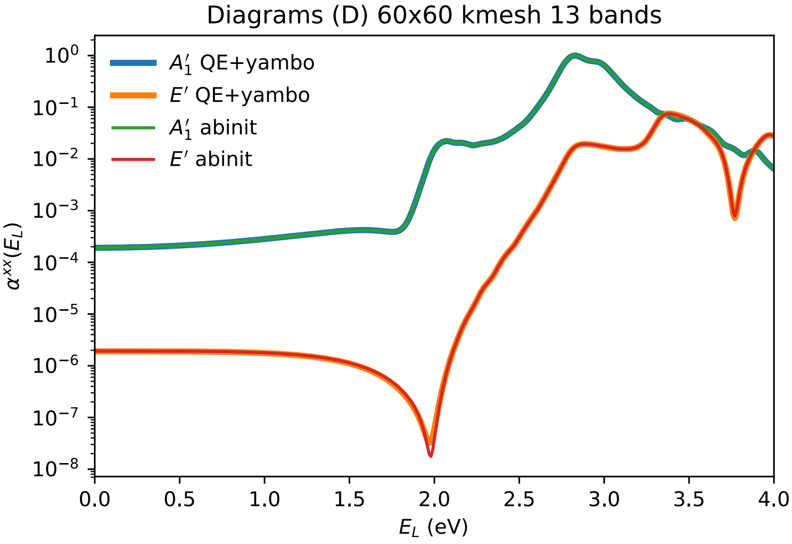

Figure 6.5: Comparison of the results for the Raman calculations using `QE` and the `yambo` codes and `abinit` using the diagrammatic approach. The calculation is done without spin-orbit coupling.

In Fig. 6.6 we compare the calculations performed with the two codes using the finite differences approach.

6.6.2.3 `abinit`

To further verify the implementation we calculated the Raman intensities with the finite differences and the diagrammatic approaches using the `abinit` code. We used FHI pseudopotentials without spin for the comparison. A grid of 60x60x1 **k**-points was used to sample the Brillouin zone. The calculations are performed using `abipy` which allows to quickly and easily perform the calculations for different materials. The results are shown in Fig. 6.7.

The agreement between the two approaches is quite good for the A_1' mode for energies beyond the gap. In the case of the E' mode some discrepancy exists even above the gap. This can be due to the inclusion of some static polarization in the case of finite differences. The origin and solution for the discrepancy should be the topic of further investigation.

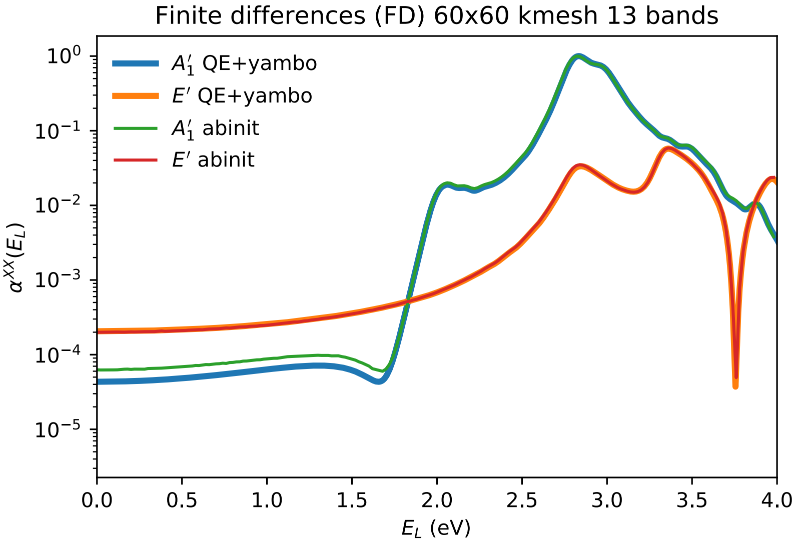

Figure 6.6: Comparison of the results for the Raman intensity as a function of laser energy for single-layer MoS_2. The calculations were done with the `QE` and the `yambo` codes and `abinit` using the finite differences approach. The calculation is done without the effect of spin-orbit coupling.

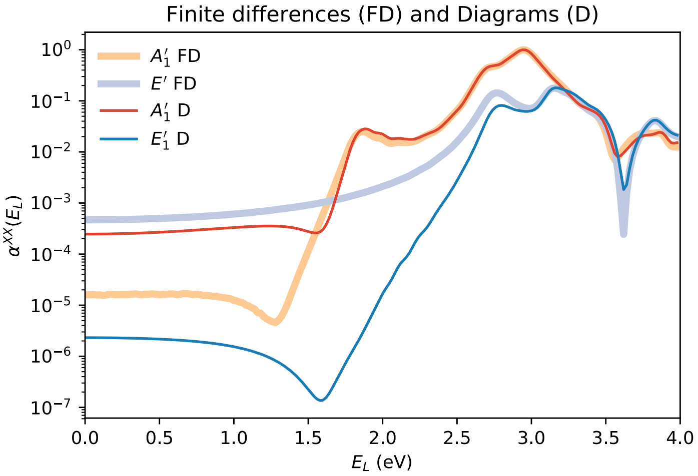

Figure 6.7: Comparison of the diagrammatic and finite differences approach for MoS_2.

6.7 Decomposition of the different contributions

Here will show how the different expressions from Eq. C.13 contribute to the Raman intensity in the case of single layer MoS_2. In this calculation we used the `EPW` interface

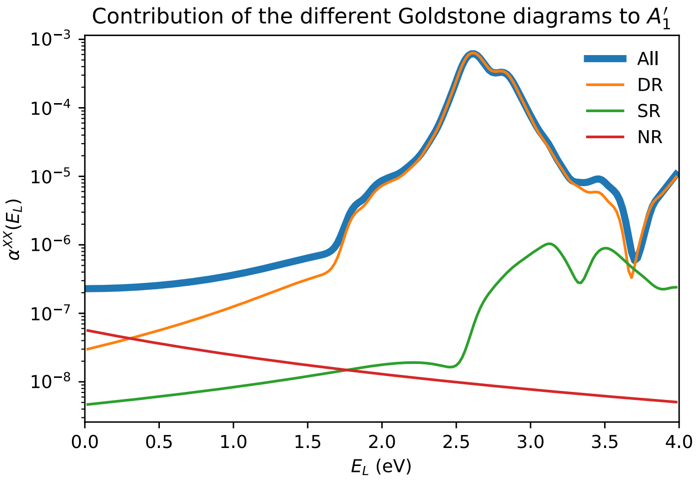

Figure 6.8: Decomposition of the different contributions to the Raman intensity of the A_1' mode of MoS_2. The calculation was performed using the `EPW` code on a 60x60 **k** grid.

The terms from Eq. C.13 can be separated into three different groups according to their denominators. These terms can be double, single or non-resonant according to whether the two, one or none of the denominators can become close to zero for a certain laser energy [123]. This analysis is instructive for two reasons. It was mentioned in the literature [30] that the double resonant term gives the largest contributions to the total Raman intensity in the case of the semiconductors. This approximation is also commonly used in the literature [18]. With our new approach we can verify this claim numerically using first-principles methods.

If this claim is verified, it can be used to obtain the Raman intensity faster by avoiding to sum over the terms that do not contribute significantly. The gain in speed might, however, not be worth the effort as the most costly part of the computation is the evaluation of the matrix elements and not the Raman intensities.

We summarize our results for decomposition of the different contributions in Fig. 6.8. We note that the double resonant term has the largest contribution almost over the entire energy range as normally assumed in the literature. In the case of graphene it was shown that all the different terms contribute to the final Raman intensity [123].

6.8 Temperature effects

Another important advantage of describing the Raman cross-section in a MBPT framework is to be able to include the effects of temperature in the Raman spectra.

In chapter 3 we showed how the energies and lifetimes of the electrons are affected by the presence of phonons in the system. The self-energy due to electron-phonon interaction is highly temperature dependent in contrast to the one due to electron-electron interaction. The main effect of temperature in the electrons is the broadening of the states and a renormalization of the band gap. As the temperature of the material increases, the nuclei oscillate with larger amplitude around their equilibrium positions (classical version in Eq. (2.16) or quantum mechanical version in Eq. (2.23)) which additionally leads to the thermal expansion which we did not account for in the calculations shown here. Lastly, the occupation of the scattered phonon modes also depends on the temperature (Eq. (5.17)), and as such, the scattering cross-section is also temperature dependent.

We use the calculations for MoS_2 to show how the inclusion of the electron self-energy due to electron-phonon interaction dresses the Green's function. To account for this self-energy would require to re-write the Green's functions as:

$$G_{n\mathbf{k}}(\omega) = G^0_{n\mathbf{k}}(\omega) + G^0_{n\mathbf{k}}(\omega)[\Sigma^{ep}_{n\mathbf{k}}(\omega)]G_{n\mathbf{k}}(\omega) \tag{6.25}$$

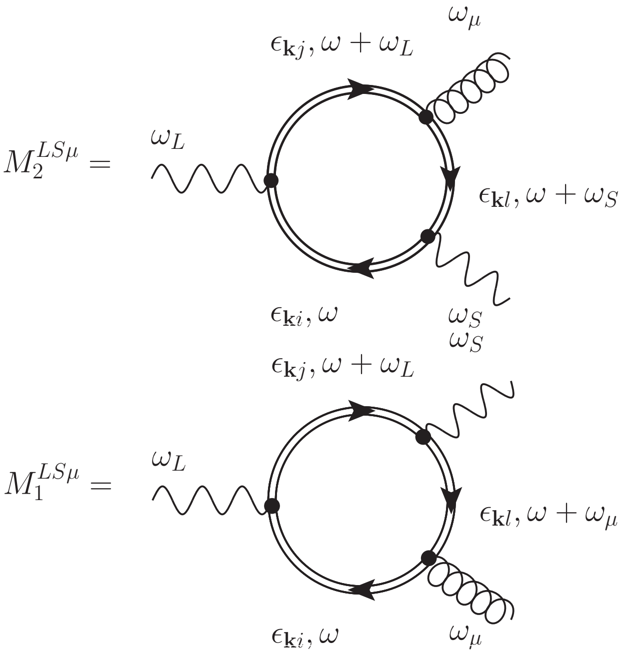

Figure 6.9: Diagrams for the Raman amplitude with the electrons circulating in the loop dressed by the electron-phonon self-energy.

In this case, the loop integrations in Eqs. (6.9) have to be done accounting for the poles of the new quasi-particle Green's functions.[1]. This method would, however, be very computationally demanding and impractical. One way to overcome this would be to create and diagonalize a full electron-phonon Hamiltonian [80] and use those states as the intermediate states of the system. This is however only important in systems where the electron-phonon coupling is strong enough to create electron-phonon bound states. Since in the case of most crystalline semi-conductors, the effect of electron-phonon coupling is not so strong, the effects can be included using the quasi-particle approximation. In this approximation, the Green's functions are re-written by shifting the eigenvalues due to the real part of the self-energy and an imaginary lifetime is added due to the imaginary part of the self-energy. The lifetimes of these quasiparticles depend on the temperature and will thus smear the Raman intensity peaks as shown in Fig. 6.10.

---

[1] A good introduction on the effect of a self-energy in the electron propagator is given in Ref. [50, Chapter 11].

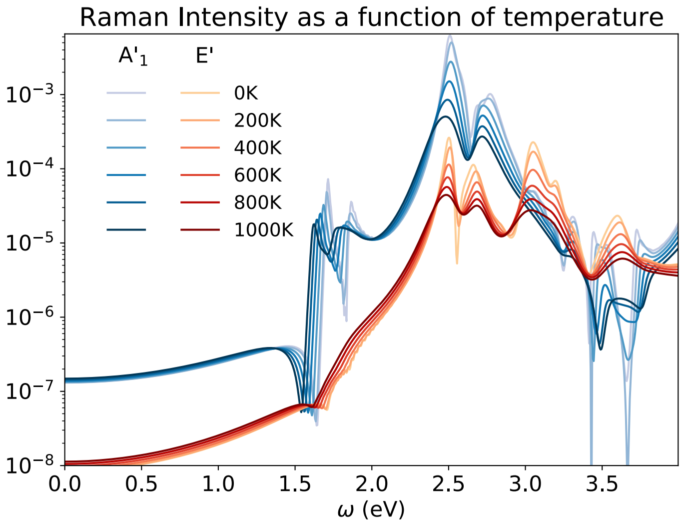

Figure 6.10: Temperature dependent Raman spectra of MoS_2. The electronic lifetimes were obtained using the methods described in Chapter 3 and used in a fine 240x240 **k**-mesh grid.

The physical picture is similar to what we observed in the case of temperature dependent optical absorption. The presence of the phonons in the system leads to the band-structure changing with the displacements of the phonons which leads to a smearing of the energies of the electrons.

6.9 Beyond the adiabatic approximation

An important advantage of this formulation is that it allows us to go beyond the static limit imposed in the case of the finite differences approach. This leads to a shift of the main resonance peak with respect to the static limit. This shift is positive in the case of Stokes Raman scattering (the one represented in Fig. 6.11) and negative in the case of anti-Stokes scattering. The value of the shift is equal to the phonon frequency with respect to *the static* case of the phonon mode considered.

We performed the calculation of the Raman intensities in the adiabatic

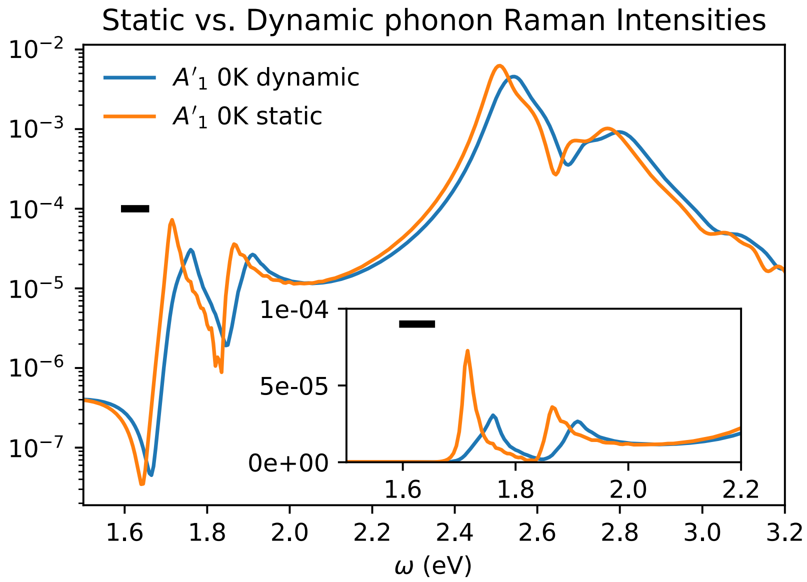

Figure 6.11: Comparison of static and dynamic calculation of the Raman intensities for MoS_2. The electronic broadening is the one calculated due to electron-phonon interaction at 0 K. The inset shows a zoom in near the optical gap in non-logarithmic scale.

phonon limit i.e. $\omega_\mu = 0$ and compared with the case where the phonon frequencies are included explicitly in the calculation. The results are shown in Fig. 6.11. The inclusion of phonon dynamical effects leads to a shift Raman spectra as a function of laser energy by an energy equal to the phonon frequency. Additionally it leads to a modification of the shape of the peaks. This is due to the change of the resonance conditions in the expressions in Eq. C.13.

6.10 Excitonic effects

In this section we outline the extension of the perturbative calculation described above to include excitonic effects. For that we follow the same approach outlined by Y. Gillet in his PhD thesis [131] for the derivation of the Raman susceptibility in the independent-particle approximation which we showed in Appendix C. In this case however we take the derivatives of the expression of the optical susceptibility including excitonic effects in Eq. (4.42)

$$\begin{aligned}\partial_{\mathbf{R}}\chi^{LS}(\omega_L) = &\sum_s \frac{\langle 0|\,\hat{H}_{\mathrm{e-L}}\partial_{\mathbf{R}}(|s\rangle)\,\langle s|\,\hat{H}_{\mathrm{e-L}}\,|0\rangle}{\omega_L - E_s + i\gamma} + \\ &\sum_s \frac{\langle 0|\hat{H}_{\mathrm{e-L}}|s\rangle\,\partial_{\mathbf{R}}(\langle s|)\hat{H}_{\mathrm{e-L}}\,|0\rangle}{\omega_L - E_s + i\gamma} + \\ &\sum_s \frac{\langle 0|\hat{H}_{\mathrm{e-L}}|s\rangle\,\langle s|\hat{H}_{\mathrm{e-L}}|0\rangle}{(\omega_L - E_s + i\gamma)^2}\partial_{\mathbf{R}}E_s + (\omega_L \to -\omega_L),\end{aligned} \tag{6.26}$$

were we do not write explicitly the photonic states for simplicity. These will set another index for the electron-light coupling matrix elements determining the polarization of the laser as we will show in Eq. (6.38).

To express the derivatives of the excitonic states we recall the excitonic Hamiltonian in Eq. (4.41)

$$\sum_{c'v'\mathbf{k}'} H^{BS}_{cv\mathbf{k},c'v'\mathbf{k}'}A^s_{c'v'\mathbf{k}'} = E_s\delta_{vv'}\delta_{cc'}\delta_{\mathbf{k}\mathbf{k}'}A^s_{cv\mathbf{k}}. \tag{6.27}$$

Taking derivatives with respect to the ionic positions, $\partial_{\mathbf{R}}$, yields

$$\begin{aligned}\sum_{c'v'\mathbf{k}'}\left(\partial_{\mathbf{R}}H^{BS}_{cv\mathbf{k},c'v'\mathbf{k}'} - \partial_{\mathbf{R}}E_s\delta_{vv'}\delta_{cc'}\delta_{\mathbf{k}\mathbf{k}'}\right)A^s_{c'v'\mathbf{k}'} = \\ \sum_{c'v'\mathbf{k}'}\left(E_s\delta_{vv'}\delta_{cc'}\delta_{\mathbf{k}\mathbf{k}'} - H^{BS}_{cv\mathbf{k},c'v'\mathbf{k}'}\right)\partial_{\mathbf{R}}A^s_{c'v'\mathbf{k}'}\end{aligned} \tag{6.28}$$

The excitonic states can be written as

$$|s\rangle = \sum_{cv\mathbf{k}} A^s_{cv\mathbf{k}}\,|c\mathbf{k}\rangle \otimes |v\mathbf{k}\rangle = \sum_{cv\mathbf{k}} A^s_{cv\mathbf{k}}\,|cv\mathbf{k}\rangle\,. \tag{6.29}$$

With this, we re-write Eq. (6.28) as

$$\left(\partial_{\mathbf{R}}\hat{H}^{BS} - \partial_{\mathbf{R}}E_s\right)|s\rangle = \left(E_s - \hat{H}^{BS}\right)\partial_{\mathbf{R}}\,|s\rangle\,, \tag{6.30}$$

The derivatives $\partial_{\mathbf{R}} |s\rangle$ are given by

$$\begin{aligned}\partial_{\mathbf{R}} |s\rangle = \frac{1}{E_S - \hat{H}} \sum_{s'} |s'\rangle \langle s'| \left(\partial_{\mathbf{R}} \hat{H}^{BS} - \partial_{\mathbf{R}} E_s\right) |s\rangle = \\ \sum_{s' \neq s} |s'\rangle \frac{\langle s' | \partial_{\mathbf{R}} \hat{H}^{BS} | s\rangle}{E_s - E_{s'}}\end{aligned} \tag{6.31}$$

where we have used

$$\partial_{\mathbf{R}} E_s = \langle s | \partial_{\mathbf{R}} \hat{H}^{BS} | s\rangle \tag{6.32}$$

which can be derived from the Hellman-Feynman theorem. The $\langle s | \partial_{\mathbf{R}} \hat{H} | s' \rangle$ term is the exciton-phonon coupling and can be calculated from

$$\begin{aligned}\Gamma^{\mathbf{R}}_{ss'} = \langle s | \partial_{\mathbf{R}} \hat{H} | s' \rangle = \sum_{cv\mathbf{k},c'v'\mathbf{k}'} \langle s | cv\mathbf{k} \rangle \, \partial_{\mathbf{R}} (\langle cv\mathbf{k} | \hat{H}^{BS} | c'v'\mathbf{k}' \rangle) \, \langle c'v'\mathbf{k}' | s' \rangle \\ \sum_{cv\mathbf{k},c'v'\mathbf{k}'} A^{s*}_{cv\mathbf{k}} A^{s'}_{c'v'\mathbf{k}'} \partial_{\mathbf{R}} H^{BS}_{cv\mathbf{k},c'v'\mathbf{k}'}\end{aligned} \tag{6.33}$$

The excitonic Hamiltonian was given in Eq. (4.40) in the basis of Kohn-Sham states. The derivatives $\partial_{\mathbf{R}} (\langle cv\mathbf{k} | \hat{H} | c'v'\mathbf{k}' \rangle)$ are calculated using the approach outlined in Ref. [134]. The derivative of the Bethe-Salpeter Hamiltonian is

$$\partial_{\mathbf{R}} H^{BS}_{cv\mathbf{k},c'v'\mathbf{k}'} = (\partial_{\mathbf{R}} \epsilon_{c\mathbf{k}} - \partial_{\mathbf{R}} \epsilon_{v\mathbf{k}}) \delta_{cc'} \delta_{vv'} \delta_{\mathbf{k}\mathbf{k}'} + \partial_{\mathbf{R}} K_{cv\mathbf{k},c'v'\mathbf{k}'}. \tag{6.34}$$

where $\partial_{\mathbf{R}} \epsilon_{n\mathbf{k}} = g^{\mathbf{R}}_{nn\mathbf{k}}$ are the diagonal electron-phonon matrix elements. To build the kernel of the BSE we assume $\frac{\delta W}{\delta G} \cong 0$ and hence $\partial_{\mathbf{R}} W \cong 0$ [134]

$$\begin{aligned}\partial_{\mathbf{R}} K_{cv\mathbf{k},c'v'\mathbf{k}'} = \sum_n P^{\mathbf{R}*}_{nc\mathbf{k}} K_{nv\mathbf{k},c'v'\mathbf{k}'} + P^{\mathbf{R}}_{nv\mathbf{k}} K_{cn\mathbf{k},c'v'\mathbf{k}'} + \\ P^{\mathbf{R}}_{nc'\mathbf{k}'} K_{cv\mathbf{k},nv'\mathbf{k}'} + P^{\mathbf{R}*}_{nv'\mathbf{k}'} K_{cv\mathbf{k},c'n\mathbf{k}'}.\end{aligned} \tag{6.35}$$

with

$$P^{\mathbf{R}}_{nn'\mathbf{k}} = \begin{cases} 0 & \text{if} \quad n = n' \\ \frac{g^{\mathbf{R}}_{nn'\mathbf{k}}}{\epsilon_{n'\mathbf{k}} - \epsilon_{n\mathbf{k}}} & \text{if} \quad n \neq n' \end{cases} \tag{6.36}$$

where $g^{\mathbf{R}}_{nn'\mathbf{k}}$ are the electron-phonon matrix elements corresponding to the displacement of one atom I in cartesian direction α. Inserting Eqs. (6.31), (6.32), and (6.33) in (6.26) leads to

$$\begin{aligned} \partial_{\mathbf{R}} \chi^{LS}(\omega_L) = & \sum_s \sum_{s' \neq s} \frac{\Lambda^S_{s'} \Gamma^{\mathbf{R}}_{s's} \Lambda^{L*}_s}{(\omega_L - E_s + i\gamma)(E_s - E_{s'})} + \\ & \sum_{ss' \neq s} \frac{\Lambda^S_s \Gamma^{\mathbf{R}}_{ss'} \Lambda^{L*}_{s'}}{(\omega_L - E_s + i\gamma)(E_{s'} - E_s)} + \\ & \sum_s \frac{\Lambda^S_s \Gamma^{\mathbf{R}}_{ss} \Lambda^{L*}_s}{(\omega_L - E_s + i\gamma)^2} + (\omega_L \to -\omega_L). \end{aligned} \tag{6.37}$$

where we have used that

$$(\langle 0| \otimes \langle L|) \hat{H}_{\text{e-L}} |s\rangle = \Lambda^L_s = \sum_{cv\mathbf{k}} A^s_{cv\mathbf{k}} \Lambda^L_{cv\mathbf{k}}. \tag{6.38}$$

$|L\rangle$ denotes a photonic state with quantum number L and $\Lambda^L_{cv\mathbf{k}}$ are the independent particle electron-light coupling matrix elements as defined in Eq. (4.16).

The expression from Eq. (6.37) gives the change of susceptibility upon atomic displacement which corresponds to the Raman tensor. Using that $\partial_{\mathbf{R}} = \frac{\partial}{\partial R_{I\alpha}}$ where I denotes an atom and α a cartesian direction, the Raman tensor for a certain phonon mode μ is given by

$$\alpha^{LS\mu}(\omega_L) = \sum_{I\alpha} \left| \frac{\partial \chi^{LS}(\omega_L)}{\partial R_{I\alpha}} Q^{\mu}_{I\alpha} \right|^2 \tag{6.39}$$

The practical implementation and comparison of this approach with the finite differences method will be the topic of further investigation. Additionally, the derivation of these expressions using a MBPT framework similar to what is outlined in [53] will allow to justify to which extent the static approximation holds.

6.11 Conclusions and Outlook

We have shown the derivation of the expressions and the practical implementation for the calculation of the Raman intensities using a perturbative approach. This has the advantage that it reduces to the finite differences in the static limit but allows to easily go beyond it including the effect of the phonon frequencies. The inclusion of the dynamical effects leads to a shift of the main scattering edge by an energy equal to the phonon frequency. This shift is known as Stokes or anti-stokes shift and it should be observed when measuring the Raman intensity as a function of the laser energy. This approach also has the advantage that only one calculation of the Kohn-Sham states is needed as opposed to the finite differences approach where at least one calculation per displacement is required.

In some materials, in particular 2D systems (due to their weak Coulomb screening), the electron-hole interaction leads to the formation of excitonic states. These effects were shown to play an important role in both the optical absorption spectra (see Chapter 4) and the Raman intensities in the case of $MoTe_2$ (see Chapter 5). We have outlined the mathematical expressions to extend the perturbative approach to include excitonic effects in Section 6.10. This approach will allow to avoid multiple calculations of the BSE for the different displacements.

7

Conclusions

The main goal of this work was to develop different computational approaches to simulate resonant Raman spectroscopy from first-principles methods. We have demonstrated the application of these methods to transition metal dichalcogenides, in particular MoS_2 and $MoTe_2$.

The calculation of Raman spectra involves the description of the electronic energy levels which we have done *ab initio* using density functional theory corrected with many-body perturbation theory using the GW approximation. It furthermore requires the knowledge of the lattice vibrations which we have studied using density functional perturbation theory.

Using a finite-difference approach based on *ab initio* methods, we have explained the experimentally observed dependence of the Raman intensities on the laser energy for single- and triple-layer $MoTe_2$ [24]. In the case of single-layer we observed that the different excitons couple differently with the A_1' and E' modes as observed in the case of MoS_2 [18]. This was understood in terms of symmetry of the bands near the optical gap or, equivalently, in terms of quantum interference effects. In the triple-layer case we have explained the experimentally observed [35] dependence of the Raman intensities of the Davydov triplet belonging to the A_1' representation. In this case, the symmetry argument does not hold as the modes belong to the same point group representation. We were, however, able to explain the effect in terms of quantum interference. This lead to the important conclusion that the Raman spectrum cannot be interpreted in the same way as the optical absorption spectrum. In the latter case, all the transitions contribute positively with more or less intensity. In the former, the contributions from different regions of the Brillouin zone can cancel each other leading to an unexpected behavior of the intensities. As such, the observed Raman intensities are a collective effect of the whole band structure. We also observed that in order to quantitatively reproduce the experimental ratios of the intensities between different modes, excitonic effects should be taken into account in $MoTe_2$ [35]. The qualitative picture, however, can already be understood on the independent-particle level. In practical terms, the finite-differences approach allows us to straightforwardly include many-body effects in the Raman intensities. However, it requires multiple computations of the full band structure and excitons upon atomic displacements. This rapidly becomes impractical for the application to a wide range of materials.

To overcome this we have proposed a method based on perturbation theory that requires only one computation of the band structure, the electron-light and electron-phonon matrix elements from first-principles. We compare the two approaches formally and show that the perturbative approach is more general in that it allows us to go beyond the adiabatic phonon limit. We reduce the perturbative approach to the static case to compare with the finite differences approach with good agreement in the resonant regime. Including the phonon dynamical effects correctly captures a shift of the resonance peak in the absorption edge with respect to the non-resonant case. This approach allows us to include the temperature effects in the Raman spectrum and we show calculations for the case of single-layer MoS_2. This method yields the same results as the finite differences approach but is much more computationally efficient which makes it more suitable for *high-throughput* applications. We also outlined an approach to calculate Raman intensities including excitonic effects by expressing the static derivatives of the dielectric susceptibility with excitons in terms of electron-phonon coupling matrix elements.

To visualize the intermediate results needed for the calculations of Raman spectra including excitonic effects we have developed two web based tools.

The `phononwebsite` [75] to visualize lattice vibrations. This tool allows the user to click on a point in the lattice dispersion and visualize the corresponding lattice vibration. We provide access to data from the `phonondb` database and some of our own calculations. The user can additionally visualize his own calculations from popular codes like `abinit`, `ph.x` from the `QE` suite and `phonopy`. We have created the `excitonwebsite` [135] to visualize optical absorption spectra including excitonic effects. There the user can click on a peak in the absorption spectrum of a given material and visualize the excitonic wave function in real space. We provide an interface with the `yambo` code so that users can visualize their own results.

Outlook

In the last years, with increasing computational power it has become possible to simulate the properties of materials from first-principles in a *high-throughput* way. In particular, a recent study was published on how to search for known materials that can be exfoliated to obtain 2D layers [136]. This means that currently, large sets of data are available with information on the electronic, vibrational and optical properties of these materials. The availability of this data allows one to predict its Raman spectra even without synthesizing the materials. This knowledge can provide very important information to experimentalists or companies trying to fabricate the materials.

The perturbative method outlined in this thesis allows to obtain the Raman spectra, starting from these databases, without much additional computation. The prompt availability of this data for the scientific community will constitute an important breakthrough and a future outcome of the work described in this document.

Another important aspect of obtaining the Raman spectra of different materials is to make it available to the community. For that, the knowledge and experience gathered in developing the interactive web based visualization tools will allow us to build a new tool to visualize and navigate the calculations

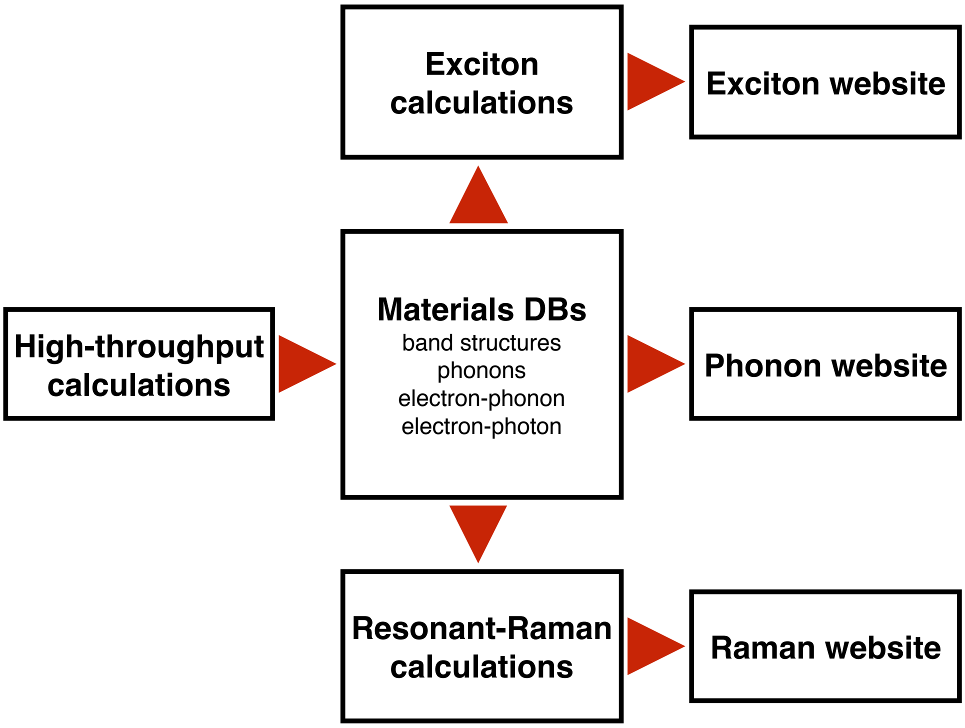

Figure 7.1: Representation of how the different developments discussed in this thesis can be used in a complete framework to predict and analyze Raman spectra calculated from first-principles.

of the Raman spectrum as a function of laser energy. This idea has been implemented to some degree in the WURM project [137]. However, the data available so far is limited to the non-resonant regime.

The basic quantities necessary to apply the perturbative method to obtain the Raman spectrum are the electronic energies and phonon frequencies, the electron-light, and the electron-phonon coupling matrix elements. These can be computed from existing databases, stored in compact formats and made available to the community. The development of such compact formats, although challenging, is possible using currently available approaches. Two possible ways to accomplish this are the use of semi-empirical parametrizations or the use of a Wannier basis [84]. These different quantities can then be combined to calculate different corrections to the quasi-particles and spectroscopic properties using many-body perturbative techniques. From these data bases, it will be easily possible to extract, e.g., the temperature dependent band structure (spectral function), optical absorption, and Raman spectra.

The work presented here is thus a first step towards making resonant Raman spectra available in a high-throughput manner.

Appendix A

`yambopy`

In order to simplify the workflow of `yambo` calculations and to run calculations more efficiently, we have created a new tool, `yambopy`. Similar to existing tools for the codes `abinit` [72] which is called `abipy` [138] and `QE` [79] which is called `aiida` [139].

A typical workflow of a many-body calculation (consider as an example a GW + BSE calculation) with the `yambo` [55] code involves multiple steps. First, it requires the calculation of the ground state properties using a DFT plane-wave basis code, e.g. `abinit` or `QE`. We developed `qepy` which is a tool to create input files and read the output of `QE` calculations distributed with `yambopy`.[1] Then it requires the translation of the wave functions and pseudo-potentials to the `netcdf` [140] format used by `yambo` (the `yambo` databases). The next step is to use `yambo` to calculate the dielectric screening in the independent-particle approximation (Eq. (1.38)). The dielectric screening is then convoluted with the Green's function to obtain the self-energy of the electrons due to the screened Coulomb interaction (Eq. (1.40)). The GW quasiparticle energies can then be used to build up the BSE Hamiltonian 4.5.1

---

[1] Different packages were made available to the community since we started the development of `qepy`. These packages also allow one to handle input-output from `QE` programs. One such packages is the already mentioned `aiida` [139]. As a long term goal we seek to make `yambopy` interoperable with different python packages handling the plane-wave code calculations like `abipy` in the case of `abinit` and `aiida` in the case of Quantum Espresso.

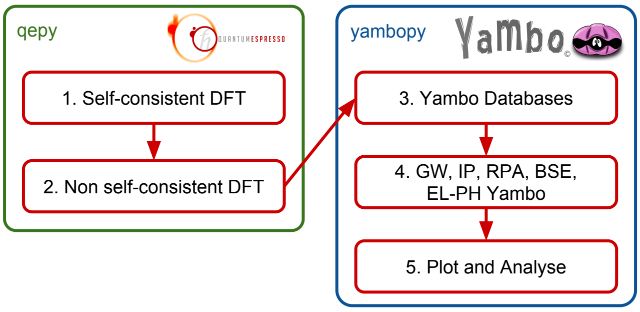

Figure A.1: The typical workflow of an MBPT calculation using the `yambo` [55] code.

(where also the dielectric screening is used). Once the calculation is done, we represent and analyze the results.

The difficulties in handling the many steps involved in the calculation are further aggravated by the fact that convergence tests are required at each step to ensure accurate results as exemplified in Fig. A.2.

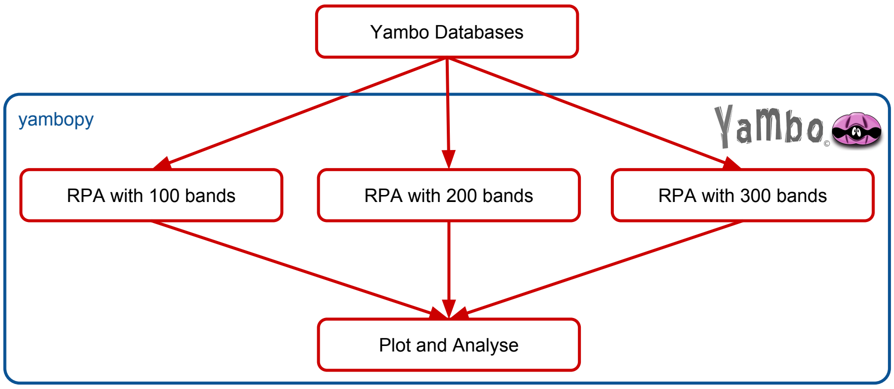

Figure A.2: Example of a workflow for the convergence of a RPA dielectric screening calculation (see Fig. 1.5).

In order to simplify these calculations we created `yambopy` [141]. `yambopy` is a set of classes and scripts written in `Python` that aim to provide a standard way to automatize and analyze many-body perturbation theory calculations made with the `yambo` code as well as to read, manipulate, and use the different basic quantities that enter the calculations. This idea has been implemented in similar programs like `ASE` [142], `abipy` [138], `aiida` [139], and `phonopy` [143] for other codes. Our goal was to apply the same concepts used in these packages to a new package using the `yambo` code. This will make many of the features of the `yambo` code not available in other codes acessible throught a python interface.

In the next section we will describe the modules available in `yambopy` and the main features. In the last section, we will outline a roadmap for further development.

A.1 Features

The two main building blocks of the `yambopy` scripts are the writing of the `yambo` input files and reading of the output. Since the `yambo` code generates the base input file for the desired runlevel, we implemented a class to read this file and store it in a `Python` class `YamboIn`. This allows to keep track of all the variables (important for reproducibility of the results) in the input file as well as to modify them from a `Python` script. To help in the convergence of calculations, the function `optimize` allows us to create a folder with a list of input files with variables changing according to a user pre-defined list. To submit jobs on different computer platforms we developed the `schedulerpy` package (also distributed with `yambopy`) that allows us to run commands in the `bash` shell or through commonly used job schedulers like `PBS` and `oar`.

The `yambo` code itself stores the intermediate and final results of the calculations in `netcdf`. `yambopy` provides a series of classes (for a complete list see the documentation [144]) to read the data in Python making it easier to manipulate and represent it using the `matplotlib` library. Having the possibility to read, plot, and change them allows for additional flexibility for the interpretation and analysis of the results. Some of the figures in this document were generated with tools we implemented in `yambopy` and made available in the standard distribution.

For quick access to some features from the command line, we provide the `yambopy` executable. This script is automatically installed with `yambopy` and is a platform to call some functionalities of `yambopy` directly from the command line (i.e., without needing to create a `Python` script). This script has now features to monitor the convergence of GW and BSE calculations executed with the `optimize` function and, to plot excitonic wave functions and the dielectric function among others.

To ensure the quality of the code and its usability by the community we rely on three platforms: open-source, documentation, and testing. A detailed documentation of the classes, features, and a tutorial are available in [144]. We keep a public `git` repository hosted on `github` [141] where the users can get the latest version of the code as well as contribute with patches and new features. We also created a series of tests that are executed at each modification of the code in the `github` repository using the Travis-CI platform [145]. This ensures the reliability of the code despite its continuous development.

A.2 Outlook

The `yambopy` package is usable as is although still under development. In the near future we seek to implement a series of additional features that will improve the usability of the code.

One of these developments is to allow the user to define and run "flows" like in the `fireworks` [146], `abipy`, or `aiida` codes. A "flow" consists of all the tasks necessary to obtain a simulation result. These tasks can be performed with the same or different codes. This allows us to write one `Python` script with all the steps of the calculation and the inter-dependencies of the multiple stages. Then it is possible to monitor the current status of the job and fix any problem that might occur at any stage of the calculation using a `Python` interface. Using this we can split the calculation into the maximum number of steps possible and optimize the parallelization for the different stages independently. For example, in a GW calculation, the screening for each q-point is independent, and in a practical calculation it is advantageous to submit more jobs of few CPUS simultaneously instead of one job with many CPUS. Once the "flow" is specified by the user in a `Python` script, the code will prepare the folder to run the calculations with the input files. Then using the `schedulerpy` it can run the different tasks according to the availability of computational resources.

For the practical implementation of this feature, one of the existing libraries (`fireworks`, `abipy`, or `aiida`) should be used as they already provide the python backend to submit the tasks to an HPC scheduler, keep track of the dependencies, and monitor their status. An effort in this direction is already underway with the `yambo aiida` plugin [147], the development of which is being done with our collaboration.

Another important feature is to automatically select the best parallelization possible for the different steps of the calculation. This can be done under the constraint of the number of computing nodes available (in similar style as to what is done with the `autoparal` function in `abinit`). Considering still the example of a GW calculation, the optimum parallelization for the dielectric screening might be different in number of cores/nodes for the calculation of the quasi-particle energies. The proper handling of this can be implemented using heuristics in a `Python` class. This will greatly facilitate the work for the users while improving the efficiency of the parallelization.

Appendix B

Electronic structure visualization tools

We have developed a set of online tools to visualize data from first- or second-principles calculations which we will describe here.

With the popularization of *ab initio* codes, it became easier to obtain electronic structure quantities from computational simulations. These quantities can be related to electronic states, phonon vibrations, or optical spectra (absorption, Raman, etc.) among others. The physical understanding and interpretation of the quantities and their relation to observables is not always easy to establish. Essential in this task is the use of tools to visualize the results. The currently available tools with this goal [148, 149, 150] mostly require a local installation of the software which binds the implementation to the platform where it is being used. Since different users might have different applications to visualize the data and different local system configurations, sharing the results in an efficient manner can become more difficult.

To overcome these two problems, we developed two web-based applications to facilitate the visualization and dissemination of results among scientists. The main goals of the project are fourfold:

- Allow one to easily visualize and interpret data from first principles calculations

- Share this data among scientists
- Provide an educational tool for students
- Allow for active participation of the community in contributing and modifying the website

We will describe the `phononwebsite` in section B.1 and the `excitonwebsite` in section B.2.

B.1 Phonon website

This project aims to provide a simple way to visualize the lattice vibrations of different materials.

With the popularization of *ab initio* codes the calculation of phonon modes for solids, molecules or nanostructures has become routine. In addition, with the exponential increase of computational power available, it became feasible to do these calculations for large sets of materials in a high-throughput fashion. Currently many repositories exist with electronic structure data openly available [151, 152, 153, 139] online. With this increasing amount of data, it becomes important to design new ways to visualize and navigate it. This has two important goals: at an educational level, it helps the students to link the concepts with the observable, at a research level it allows one to interpret the data and understand trends among different materials.

With these goals in mind we will present here an implementation of an interactive, web based tool to visualize lattice vibrations in solids and molecules.

This implementation differs from other currently available tools like `xcrysden` [148], `v-sim` [149] and `jmol` [150] in that it provides click-and-see interface between the phonon dispersion and the phonon vibrational modes, not previously available.

B.1.1 Visualization of lattice vibrations

In Chapter 2 we described in detail the theory of lattice vibrations. There we obtained an equation for the harmonic movement of the atoms (Eq. (2.8)). We also mentioned the two possible conventions to build up the dynamical matrix leading to two definitions of the vibrational modes up to a phase in (Eq. (2.11) and (2.12)). Special care should be taken to represent the vibrational modes depending on whether the code uses one or the other convention. To visualize the lattice vibrations of a certain phonon mode μ at a selected **q**-point we displace the atoms according to the formula:

$$Q^{\mu}_{I\alpha}(\mathbf{q}) = \frac{A}{\sqrt{M_I}} Re\left\{\xi^{\mu}_{I\alpha}(\mathbf{q}) e^{i\mathbf{q}\cdot R_{i\alpha}} e^{-i\omega t}\right\} \tag{B.1}$$

where A represents the amplitude and ω the frequency of the oscillation which can be changed by the user in the web interface. Different methods exist to calculate displacements of the atoms in the harmonic approximation as we mentioned in section 2.3. Many of these methods have implementations freely available online, one such example is `phonopy` that relies on the finite differences method briefly described in section 2.3.1. Another example is the density functional perturbation theory method also available in standard DFT codes like `abinit` [154] and `ph.x` [63].

B.1.2 Description and features

The webpage consists of three panels as shown in Fig. B.1: one panel shows the phonon dispersion of a given material (right), another panel shows the animation of the phonon mode at a given **q** point and phonon branch (center). The third panel is a control panel (left). The user can interact with the page by clicking on a certain **q**-point and phonon mode in the phonon dispersion in panel a) and visualize the pattern of vibration of the structure in panel b). This type of interface is the main novelty of this webpage.

The phonon data can have multiple proveniences. For that we designed a

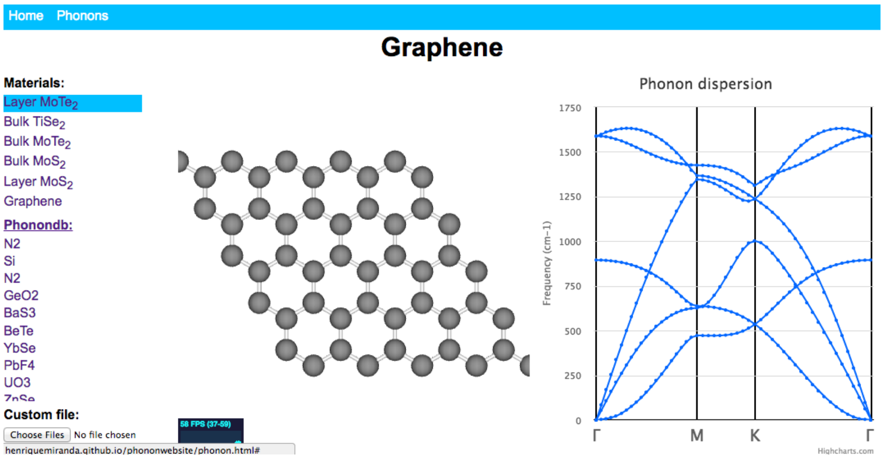

Figure B.1: Screenshot of the `phononwebsite` taken on 30/07/2017. `http://henriquemiranda.github.io/phononwebsite/`.

set of `Python` classes to convert the data from the `abinit` [72], `QE` [79] codes to an internal `.json` file that can be loaded onto the webpage. We have additionally implemented the option to load the phonopy `band.yaml` files directly onto the website. Furthermore, in collaboration with Atsushi Togo, the creator of `phonopy`, we provide access to phonon dispersion data from the `phonondb` [155] phonon database hosted at the Kyoto University and maintained by him.

To allow easier sharing, the user can either send the files with the phonon data or post it online. In the first case the files can then be loaded by the recipient user with the “Choose files” button. In the second case the user sending the data uploads the file online and sends the link `<link>` to the receiver with an HTML POST request indicating where the file was uploaded. The link instructs the website to download the file from the remote server and display it directly. To do this, the link of the page can be appended with one tag indicating the format of the file `?json=<link>` or `?yaml=<link>`.

To allow the use of the animations in different contexts, we implemented features to export the animations in `.gif` and `.mov` files. This is done using the open-source package `CCapture` [156].

In addition, we offer the possibility to generate supercells with a displacement according to a certain phonon mode. To do this the user can click on a point in the phonon dispersion, visualize the structure and then download a POSCAR file with a supercell. Further improvement of this feature is to choose a specific **q**-point and automatically choose the number of cell repetitions to build the cell commensurate with a phonon with this **q**-point.

B.1.3 Technologies used

One advantage of the application being web-based is that any change in the code is immediately distributed without the need of end user intervention. Additionally, this application can be used in virtually any computer or mobile device without the need for installation of any additional software apart from a webbrowser.

For the implementation of this software we used freely available open source libraries. To display the animation of the atomic structures with the phonon modes we used the `HTML5` canvas element to display `WebGL` objects.

To create and animate the atomic structures with the phonon modes we used the `Three.js` [157] `javascript` based API. This API is very complete and allows one to easily implement new features and representations of different quantities without much effort. The phonon dispersion graph is shown using the `Highcharts` [158] `javascript` library. This library also provides an extensive API for representing the data and interacting with it.

B.1.4 File formats

To represent the vibrational data, we created our own internal input `.json` format. The `.json` file is a text-based file that represents the internal data structures used in the `javascript` language. The format of the input file is specified in a static page in the phonon website [75] and serves as a reference for developers. To allow the output of different codes to be visualized with the phonon website we suggest two approaches to develop an interface. The first approach is to use an external script to create the input `.json` file that can be loaded with the “Choose Files” button. Using this method we implemented `Python` interfaces for the `abinit` [72] and `ph.x` codes [79]. These interfaces are available from the `github` repository [159] and the instructions of use are in the initial page [75].

Alternatively, a `javascript` function can be easily added to the code to parse the file to the internal `.json` format. This approach has advantages for the user, as no external scripts are required and the output file of the code can be loaded directly onto the website. Internally a function selects the parser according to the extension or header of the selected file and sends the file as plain-text input to the parsing function. Using this approach we developed an interface for the `phonopy` [62] code, which means that the `band.yaml` files can be loaded directly onto the page and they contain all the necessary information.

B.2 Exciton website

In a spirit very similar to the phonon website we developed a web tool to visualize excitons.

As discussed in Section 4.5.4 a large amount of information is generated from an exciton calculation. Different types of representations are possible, each putting in evidence different aspects of the results. One of such representations is the electron density when the hole is fixed in some position in the lattice. From it we obtain an idea of how localized the electrons are around the hole. In order to facilitate the visualization of this data we implemented a web-based tool, whose interface is described in Fig. B.2. The right panel shows the optical absorption spectrum of a given material. The different vertical lines mark excitonic states for which the wave function can be visualized. By clicking on one of the lines, the web-page displays the corresponding excitonic wave function for a given hole position. The isosurfaces of the electronic probability density can be adjusted in the control panel on the left side of the

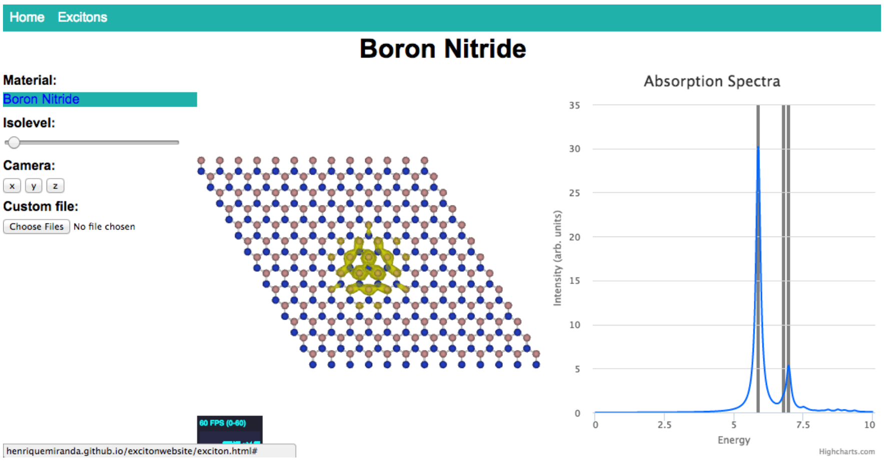

Figure B.2: Screenshot of the `excitonwebsite` taken on 30/07/2017. `http://henriquemiranda.github.io/excitonwebsite/`

web-page.

The technologies used for the visualization are the same as in the case of the phonon website (Sec. B.1). The data for visualization can be generated from any code that calculates the excitonic states from the BSE and stores the eigenvalues and eigenstates. Through the `yambopy` code we provide a `Python` interface to read and display the excitonic wave functions generated from the `yambo` code. The instructions of use and an example are made available on the front page of the website itself.

B.3 Conclusions and roadmap for future development

The `phononwebsite` and `excitonwebsite` offer didactic and interactive ways to visualize the results of *ab initio* calculations. They are both ready to use and were made available online. These tools are also completely open-source and hosted on `github` [160]. As such they can be easily “cloned” in a different location allowing it to be used in different websites and displaying data from different sources. As new features are implemented, they are automatically made available for the users.

In the future we aim to further expand the amount of data available, i.e. number of materials for which we show phonon dispersions and excitonic states. We also aim to improve their functionalities. For that we will describe some desired features with the aim to stimulate and orient their future development.

In the phonon website we will implement a feature to provide information about the direction of the momentum of the selected phonon. We want to allow the user to replicate the unit cells in the different directions according to non-diagonal supercells [161]. We plan to implement an interface able to read inter-atomic force constants and calculate the phonon frequencies and modes on the fly. This will allow the user to modify the path in reciprocal space and obtain immediately the new phonon dispersion. Additionally it will allow one to investigate how replicating the structure according to a certain supercell folds the phonon dispersion.

In the exciton website we aim to firstly introduce a larger set of calculations. This will imply the creation of a new database of excitonic calculations. Furthermore, we will introduce two additional different types of visualization: the excitonic wave function in reciprocal space and in the electron-hole dispersion as shown in Section 4.5.4. In the real space visualization we will allow the user to select among different positions of the hole in the structure and change the electronic density accordingly. We plan to improve the data format used to store the information of the excitonic density. Currently the data is being stored in text format which is not very efficient in terms of space and bandwidth required to transfer the data.

We believe that visualization of the results plays a very important role in understanding and interpreting the results from *ab initio* calculations. We will continue to develop and improve these tools based on feedback from the community.

Appendix C

Equivalence between the finite differences and dynamical approach

In this appendix we show the equivalence between the finite differences approach and both the diagrammatic one that we outlined in Section 6 and the expressions by Cardona [30]. This demonstration was previously shown by Y. Gillet in his PhD thesis [131]. To evaluate Eq. (6.16) we will re-write the derivatives of eigenvalues and wave functions in terms of the electron-phonon matrix elements. The derivative of the eigenvalues is directly obtained using the Hellman-Feynman theorem from Eq. (2.29)

$$\epsilon_{n\mathbf{k}} = \langle n\mathbf{k}|\hat{H}|n\mathbf{k}\rangle \,, \tag{C.1}$$

$$\partial_{\mathbf{R}}\epsilon_{n\mathbf{k}} = \left\langle n\mathbf{k} \,\middle|\, \partial_{\mathbf{R}}\hat{H} \,\middle|\, n\mathbf{k} \right\rangle . \tag{C.2}$$

The derivative of the dipole matrix elements (Eq. (4.16)) requires the knowledge of the derivative of the wave function

$$\partial_{\mathbf{R}}\Lambda_{cv\mathbf{k}} = \langle \mathbf{k}c|\, \hat{\mathbf{r}}\partial_{\mathbf{R}}(|\mathbf{k}v\rangle) + \partial_{\mathbf{R}}(\langle \mathbf{k}c|)\hat{\mathbf{r}}\,|\mathbf{k}v\rangle \,. \tag{C.3}$$

The derivative of the wave function can be obtained by taking derivatives of Eq. (1.14)

$$\begin{aligned} \partial_{\mathbf{R}} \hat{H} \left| n\mathbf{k} \right\rangle + \hat{H} \partial_{\mathbf{R}} \left| n\mathbf{k} \right\rangle &= \epsilon_{n\mathbf{k}} \partial_{\mathbf{R}} \left| n\mathbf{k} \right\rangle + \partial_{\mathbf{R}} \epsilon_{n\mathbf{k}} \left| n\mathbf{k} \right\rangle \Leftrightarrow \\ \left(\partial_{\mathbf{R}} \hat{H} - \partial_{\mathbf{R}} \epsilon_{n\mathbf{k}} \right) \left| n\mathbf{k} \right\rangle &= \left(\epsilon_{n\mathbf{k}} - \hat{H} \right) \partial_{\mathbf{R}} \left| n\mathbf{k} \right\rangle . \end{aligned} \tag{C.4}$$

Reshuffling the terms and inserting a completeness relation we obtain

$$\begin{aligned} \partial_{\mathbf{R}} \left| n\mathbf{k} \right\rangle &= \frac{1}{\epsilon_{n\mathbf{k}} - \hat{H}} \sum_{m} \left| m\mathbf{k} \right\rangle \left\langle m\mathbf{k} \right| \left(\partial_{\mathbf{R}} \hat{H} - \partial_{\mathbf{R}} \epsilon_{n\mathbf{k}} \right) \left| n\mathbf{k} \right\rangle \\ &= \sum_{m \neq n} \left| m\mathbf{k} \right\rangle \frac{\langle \mathbf{k}m | \partial_{\mathbf{R}} \hat{H} | \mathbf{k}n \rangle}{(\epsilon_{n\mathbf{k}} - \epsilon_{m\mathbf{k}})} + \langle \mathbf{k}n | \partial_{\mathbf{R}} \hat{H} | \mathbf{k}n \rangle - \partial_{\mathbf{R}} \epsilon_{n\mathbf{k}} \\ &= \sum_{m \neq n} \left| m\mathbf{k} \right\rangle \frac{g^{\mathbf{R}}_{nm\mathbf{k}}}{(\epsilon_{n\mathbf{k}} - \epsilon_{m\mathbf{k}})}, \end{aligned} \tag{C.5}$$

where in the last step we used again the result from the Hellman-Feynamn theorem in Eq. (C.2). Substituting the expression for the derivative of the wave function in Eq. (C.3) and using (4.16) leads to

$$\partial_{\mathbf{R}} \Lambda^{L}_{cv\mathbf{k}} = \sum_{\substack{n \neq v \\ \mathbf{k}}} \frac{\Lambda^{L}_{cn\mathbf{k}} g^{\mathbf{R}}_{nv\mathbf{k}}}{\epsilon_{v\mathbf{k}} - \epsilon_{n\mathbf{k}}} + \sum_{\substack{n \neq c \\ \mathbf{k}}} \frac{g^{\mathbf{R}}_{cn\mathbf{k}} \Lambda^{L}_{nv\mathbf{k}}}{\epsilon_{c\mathbf{k}} - \epsilon_{n\mathbf{k}}}. \tag{C.6}$$

Which when replacing by an explicit sum over conduction and valence bands leads to

$$\begin{aligned} \partial_{\mathbf{R}} \Lambda^{L}_{cv\mathbf{k}} = \sum_{\substack{v' \neq v \\ \mathbf{k}}} \frac{\Lambda^{L}_{cv'\mathbf{k}} g^{\mathbf{R}}_{v'v\mathbf{k}}}{\epsilon_{v\mathbf{k}} - \epsilon_{v'\mathbf{k}}} + \sum_{\substack{c' \\ \mathbf{k}}} \frac{\Lambda^{L}_{cc'\mathbf{k}} g^{\mathbf{R}}_{c'v\mathbf{k}}}{\epsilon_{v\mathbf{k}} - \epsilon_{c'\mathbf{k}}} + \\ \sum_{\substack{v' \\ \mathbf{k}}} \frac{g^{\mathbf{R}}_{cv'\mathbf{k}} \Lambda^{L}_{v'v\mathbf{k}}}{\epsilon_{c\mathbf{k}} - \epsilon_{v'\mathbf{k}}} + \sum_{\substack{c' \neq c \\ \mathbf{k}}} \frac{g^{\mathbf{R}}_{cc'\mathbf{k}} \Lambda^{L}_{c'v\mathbf{k}}}{\epsilon_{c\mathbf{k}} - \epsilon_{c'\mathbf{k}}}. \end{aligned} \tag{C.7}$$

Substituting in Eq. (6.16) leads to

$$
\begin{aligned}
\partial_{\mathbf{R}}\chi^{SL}(\omega_L) \propto &\sum_{\substack{vcv'\\ \mathbf{k}}} \frac{\Lambda^S_{vv'\mathbf{k}} g^{\mathbf{R}}_{v'c\mathbf{k}} \Lambda^L_{cv\mathbf{k}}}{(\epsilon_{c\mathbf{k}} - \epsilon_{v'\mathbf{k}}) R_{cv\mathbf{k}}(\omega_L)} + \sum_{\substack{vcc' \neq c\\ \mathbf{k}}} \frac{\Lambda^S_{vc'\mathbf{k}} g^{\mathbf{R}}_{c'c\mathbf{k}} \Lambda^L_{cv\mathbf{k}}}{(\epsilon_{c\mathbf{k}} - \epsilon_{c'\mathbf{k}}) R_{cv\mathbf{k}}(\omega_L)} + \\
&\sum_{\substack{vcv' \neq v\\ \mathbf{k}}} \frac{g^{\mathbf{R}}_{vv'\mathbf{k}} \Lambda^S_{v'c\mathbf{k}} \Lambda^L_{cv\mathbf{k}}}{(\epsilon_{v\mathbf{k}} - \epsilon_{v'\mathbf{k}}) R_{cv\mathbf{k}}(\omega_L)} + \sum_{\substack{vcc'\\ \mathbf{k}}} \frac{g^{\mathbf{R}}_{vc'\mathbf{k}} \Lambda^S_{c'c\mathbf{k}} \Lambda^L_{cv\mathbf{k}}}{(\epsilon_{v\mathbf{k}} - \epsilon_{c'\mathbf{k}}) R_{cv\mathbf{k}}(\omega_L)} + \\
&\sum_{\substack{vcv' \neq v\\ \mathbf{k}}} \frac{\Lambda^S_{vc\mathbf{k}} \Lambda^L_{cv'\mathbf{k}} g^{\mathbf{R}}_{v'v\mathbf{k}}}{(\epsilon_{v\mathbf{k}} - \epsilon_{v'\mathbf{k}}) R_{cv\mathbf{k}}(\omega_L)} + \sum_{\substack{vcc'\\ \mathbf{k}}} \frac{\Lambda^S_{vc\mathbf{k}} \Lambda^L_{cc\mathbf{k}} g^{\mathbf{R}}_{c'v\mathbf{k}}}{(\epsilon_{v\mathbf{k}} - \epsilon_{c'\mathbf{k}}) R_{cv\mathbf{k}}(\omega_L)} + \\
&\sum_{\substack{vcv'\\ \mathbf{k}}} \frac{\Lambda^S_{vc\mathbf{k}} g^{\mathbf{R}}_{cv'\mathbf{k}} \Lambda^L_{v'v\mathbf{k}}}{(\epsilon_{c\mathbf{k}} - \epsilon_{v'\mathbf{k}}) R_{cv\mathbf{k}}(\omega_L)} + \sum_{\substack{vcc' \neq c\\ \mathbf{k}}} \frac{\Lambda^S_{vc\mathbf{k}} g^{\mathbf{R}}_{cc'\mathbf{k}} \Lambda^L_{c'v\mathbf{k}}}{(\epsilon_{c\mathbf{k}} - \epsilon_{c'\mathbf{k}}) R_{cv\mathbf{k}}(\omega_L)} + \\
&\sum_{\substack{vc\\ \mathbf{k}}} \frac{\Lambda^S_{vc\mathbf{k}} g^{\mathbf{R}}_{cc\mathbf{k}} \Lambda^L_{cv\mathbf{k}}}{R_{cv\mathbf{k}}(\omega_L)^2} + \sum_{\substack{vc\\ \mathbf{k}}} \frac{-\Lambda^S_{vc\mathbf{k}} g^{\mathbf{R}}_{vv\mathbf{k}} \Lambda^L_{cv\mathbf{k}}}{R_{cv\mathbf{k}}(\omega_L)^2} + \\
&(\omega_L \rightarrow -\omega_L)
\end{aligned}
\tag{C.8}
$$

where we defined $R_{cv\mathbf{k}}(\omega_L) = [\omega_L - (\epsilon_{c\mathbf{k}} - \epsilon_{v\mathbf{k}}) + i\gamma]$. Combining the terms with $g_{c'c\mathbf{k}}$, $g_{cc'\mathbf{k}}$ and $g_{cc\mathbf{k}}$ leads to

$$
\sum_{\substack{vcc'\\ \mathbf{k}}} \frac{\Lambda^S_{vc'\mathbf{k}} g^{\mathbf{R}}_{c'c\mathbf{k}} \Lambda^L_{cv\mathbf{k}}}{[\omega_L - (\epsilon_{c\mathbf{k}} - \epsilon_{v\mathbf{k}}) + i\gamma][\omega_L - (\epsilon_{c'\mathbf{k}} - \epsilon_{v\mathbf{k}}) + i\gamma]}. \tag{C.9}
$$

And combining the terms with $g^{\mathbf{R}}_{v'v\mathbf{k}}$, $g^{\mathbf{R}}_{vv'\mathbf{k}}$ and $g_{vv\mathbf{k}}$ we get

$$
\sum_{\substack{vcc'\\ \mathbf{k}}} \frac{-g^{\mathbf{R}}_{vv'\mathbf{k}} \Lambda^S_{v'c\mathbf{k}} \Lambda^L_{cv\mathbf{k}}}{[\omega_L - (\epsilon_{c\mathbf{k}} - \epsilon_{v\mathbf{k}}) + i\gamma][\omega_L - (\epsilon_{c\mathbf{k}} - \epsilon_{v'\mathbf{k}}) + i\gamma]}. \tag{C.10}
$$

Combining Eqs. (C.8), (C.9) and (C.10) we finally obtain Eq. (6.17).

This expression, derived by taking finite differences of the dielectric susceptibility can be compared with the expressions found in the literature [30]

$$\begin{aligned}\alpha^{LS\mu}(\omega_L) \propto \sum_{inn'} \Bigg\{ & \frac{\langle\Psi_i|\hat{H}^{L}_{\mathrm{e-L}}|\Psi_n\rangle \langle\Psi_n|\hat{H}^{\mu}_{\mathrm{e-n}}|\Psi_{n'}\rangle \langle\Psi_{n'}|\hat{H}^{S}_{\mathrm{e-L}}|\Psi_i\rangle}{(\omega_L - (\epsilon_n - \epsilon_i))(\omega_L - \omega_\mu - (\epsilon_{n'} - \epsilon_i))} \\ & \frac{\langle\Psi_i|\hat{H}^{S}_{\mathrm{e-L}}|\Psi_n\rangle \langle\Psi_n|\hat{H}^{\mu}_{\mathrm{e-n}}|\Psi_{n'}\rangle \langle\Psi_{n'}|\hat{H}^{L}_{\mathrm{e-L}}|\Psi_i\rangle}{(-\omega_L + \omega_\mu - (\epsilon_n - \epsilon_i))(-\omega_L - (\epsilon_{n'} - \epsilon_i))} \\ & \frac{\langle\Psi_i|\hat{H}^{L}_{\mathrm{e-L}}|\Psi_n\rangle \langle\Psi_n|\hat{H}^{S}_{\mathrm{e-L}}|\Psi_{n'}\rangle \langle\Psi_{n'}|\hat{H}^{\mu}_{\mathrm{e-n}}|\Psi_i\rangle}{(\omega_L - (\epsilon_n - \epsilon_i))(\omega_\mu - (\epsilon_{n'} - \epsilon_i))} \\ & \frac{\langle\Psi_i|\hat{H}^{S}_{\mathrm{e-L}}|\Psi_n\rangle \langle\Psi_n|\hat{H}^{L}_{\mathrm{e-L}}|\Psi_{n'}\rangle \langle\Psi_{n'}|\hat{H}^{\mu}_{\mathrm{e-n}}|\Psi_i\rangle}{(-\omega_L + \omega_\mu - (\epsilon_n - \epsilon_i))(\omega_\mu - (\epsilon_{n'} - \epsilon_i))} \\ & \frac{\langle\Psi_i|\hat{H}^{\mu}_{\mathrm{e-n}}|\Psi_n\rangle \langle\Psi_n|\hat{H}^{L}_{\mathrm{e-L}}|\Psi_{n'}\rangle \langle\Psi_{n'}|\hat{H}^{S}_{\mathrm{e-L}}|\Psi_i\rangle}{(-\omega_\mu - (\epsilon_n - \epsilon_i))(\omega_L - \omega_\mu - (\epsilon_{n'} - \epsilon_i))} \\ & \frac{\langle\Psi_i|\hat{H}^{\mu}_{\mathrm{e-n}}|\Psi_n\rangle \langle\Psi_n|\hat{H}^{S}_{\mathrm{e-L}}|\Psi_{n'}\rangle \langle\Psi_{n'}|\hat{H}^{L}_{\mathrm{e-L}}|\Psi_i\rangle}{(-\omega_\mu - (\epsilon_{n'} - \epsilon_i))(-\omega_L - (\epsilon_{n'} - \epsilon_i))} \Bigg\}\end{aligned} \tag{C.11}$$

where in $\hat{H}^{S}_{\mathrm{e-L}}$ and $\hat{H}^{\mu}_{\mathrm{e-n}}$ the particular photon and phonon interacting are selected. This can be expanded in terms of electron-phonon and electron-light matrix elements using the Hamiltonians from Eq. (3.1) setting $\mathbf{q} \rightarrow 0$ and

Eq. (4.19) as [131]

$$
\begin{aligned}
\alpha^{LS\mu}(\omega_L) \propto \sum_{vcc'} \Bigg\{ & \frac{\Lambda^{L}_{vc} g^{\mu}_{cc'} \Lambda^{S}_{c'v}}{(\omega_L - (\epsilon_c - \epsilon_v))(\omega_L - \omega_\mu - (\epsilon_{c'} - \epsilon_v))} \\
& \frac{\Lambda^{S}_{vc} g^{\mu}_{cc'} \Lambda^{L}_{c'v}}{(-\omega_L + \omega_\mu - (\epsilon_c - \epsilon_v))(-\omega_L - (\epsilon_{c'} - \epsilon_v))} \\
& \frac{\Lambda^{L}_{vc} \Lambda^{S}_{cc'} g^{\mu}_{c'v}}{(\omega_L - (\epsilon_c - \epsilon_v))(\omega_\mu - (\epsilon_{c'} - \epsilon_v))} \\
& \frac{\Lambda^{S}_{vc} \Lambda^{L}_{cc'} g^{\mu}_{c'v}}{(-\omega_L + \omega_\mu - (\epsilon_c - \epsilon_v))(\omega_\mu - (\epsilon_{c'} - \epsilon_v))} \\
& \frac{g^{\mu}_{vc} \Lambda^{L}_{cc'} \Lambda^{S}_{c'v}}{(-\omega_\mu - (\epsilon_c - \epsilon_v))(\omega_L - \omega_\mu - (\epsilon_{c'} - \epsilon_v))} \\
& \frac{g^{\mu}_{vc} \Lambda^{S}_{cc'} \Lambda^{L}_{c'v}}{(-\omega_\mu - (\epsilon_{c'} - \epsilon_v))(-\omega_L - (\epsilon_{c'} - \epsilon_v))} \Bigg\} +
\end{aligned}
\tag{C.12}
$$

$$
\begin{aligned}
\sum_{vcv'} \Bigg\{ & \frac{-\Lambda^{L}_{v'c} g^{\mu}_{vv'} \Lambda^{S}_{cv}}{(\omega_L - (\epsilon_c - \epsilon_v))(\omega_L - \omega_\mu - (\epsilon_c - \epsilon_{v'}))} \\
& \frac{-\Lambda^{S}_{v'c} g^{\mu}_{vv'} \Lambda^{L}_{cv}}{(-\omega_L + \omega_\mu - (\epsilon_c - \epsilon_v))(-\omega_L - (\epsilon_c - \epsilon_{v'}))} \\
& \frac{-\Lambda^{L}_{v'c} \Lambda^{S}_{vv'} g^{\mu}_{cv}}{(\omega_L - (\epsilon_c - \epsilon_v))(\omega_\mu - (\epsilon_c - \epsilon_{v'}))} \\
& \frac{-\Lambda^{S}_{v'c} \Lambda^{L}_{vv'} g^{\mu}_{cv}}{(-\omega_L + \omega_\mu - (\epsilon_c - \epsilon_v))(\omega_\mu - (\epsilon_c - \epsilon_{v'}))} \\
& \frac{-g^{\mu}_{v'c} \Lambda^{L}_{vv'} \Lambda^{S}_{cv}}{(-\omega_\mu - (\epsilon_c - \epsilon_{v'}))(\omega_L - \omega_\mu - (\epsilon_c - \epsilon_v))} \\
& \frac{-g^{\mu}_{v'c} \Lambda^{S}_{vv'} \Lambda^{L}_{cv}}{(-\omega_\mu - (\epsilon_c - \epsilon_{v'}))(-\omega_L - (\epsilon_c - \epsilon_v))} \Bigg\}
\end{aligned}
\tag{C.13}
$$

These expressions are equivalent the ones reported in Eq. (6.17) when the phonon frequency is set to zero. These expressions avoid the numeric cancelation in Eqs. (6.11), (6.12) and (6.3), and reduce the scaling of the calculation as discussed in Section 6.6.

References

[1] K. S. Novoselov, A. K. Geim, S. V. Morozov, D. Jiang, Y. Zhang, S. V. Dubonos, I. V. Grigorieva, and A. A. Firsov. **Electric Field Effect in Atomically Thin Carbon Films**. *Science*, **306**(5696):666–669, 2004. 3

[2] K. S. Novoselov, A. K. Geim, S. V. Morozov, D. Jiang, M. I. Katsnelson, I. V. Grigorieva, S. V. Dubonos, and A. A. Firsov. **Two-Dimensional Gas of Massless Dirac Fermions in Graphene**. *Nature*, **438**(7065):197–200, 2005. 3

[3] M. R. Hilton and P. D. Fleischauer. **Applications of Solid Lubricant Films in Spacecraft**. *Surface and Coatings Technology*, **54**:435–441, 1992. 3

[4] Pulickel Ajayan, Philip Kim, and Kaustav Banerjee. **Two-Dimensional van Der Waals Materials**. *Physics Today*, 2016. 4

[5] B. Radisavljevic, A. Radenovic, J. Brivio, V. Giacometti, and A. Kis. **Single-Layer MoS2 Transistors**. *Nature Nanotechnology*, **6**(3):147–150, print March 2011. 4

[6] Hsinhan Tsai, Wanyi Nie, Jean-Christophe Blancon, Constantinos C. Stoumpos, Reza Asadpour, Boris Harutyunyan, Amanda J. Neukirch, Rafael Verduzco, Jared J. Crochet, Sergei Tretiak, Laurent Pedesseau, Jacky Even, Muhammad A. Alam, Gautam Gupta, Jun Lou, Pulickel M. Ajayan, Michael J.

BEDZYK, MERCOURI G. KANATZIDIS, AND ADITYA D. MOHITE. **High-Efficiency Two-Dimensional Ruddlesden–Popper Perovskite Solar Cells**. *Nature*, **536**(7616):312–316, 2016. 4

[7] QING HUA WANG, KOUROSH KALANTAR-ZADEH, ANDRAS KIS, JONATHAN N. COLEMAN, AND MICHAEL S. STRANO. **Electronics and Optoelectronics of Two-Dimensional Transition Metal Dichalcogenides**. *Nature Nanotechnology*, **7**(11):699–712, 2012. 4

[8] A. K. GEIM AND I. V. GRIGORIEVA. **Van Der Waals Heterostructures**. *Nature*, **499**(7459):419–425, 2013. 4

[9] K. S. NOVOSELOV, A. MISHCHENKO, A. CARVALHO, AND A. H. CASTRO NETO. **2D Materials and van Der Waals Heterostructures**. *Science*, **353**(6298):aac9439, 2016. 4

[10] RAFAEL ROLDÁN, ANDRÉS CASTELLANOS-GOMEZ, EMMANUELE CAPPELLUTI, AND FRANCISCO GUINEA. **Strain Engineering in Semiconducting Two-Dimensional Crystals**. *Journal of Physics: Condensed Matter*, **27**(31):313201, 2015. 4

[11] ANDREA C. FERRARI AND DENIS M. BASKO. **Raman Spectroscopy as a Versatile Tool for Studying the Properties of Graphene**. *Nature Nanotechnology*, **8**(4):235–246, 2013. 4

[12] C.V. RAMAN. **A New Radiation**. *Indian J. Phys*, **2**:387–398, 1928. 5

[13] ADOLF SMEKAL. **Zur Quantentheorie Der Dispersion**. *Naturwissenschaften*, **11**(43):873–875, 1923. 5

[14] MANUEL CARDONA AND GERNOT GÜNTHERODT. *Light Scattering in Solids II: Basic Concepts and Instrumentation*. Springer-Verlag, 1982. 5, 65, 98, 101, 113

[15] R. LOUDON. **Theory of the First-Order Raman Effect in Crystals**. *Proceedings of the Royal Society of London A: Mathematical, Physical and Engineering Sciences*, **275**(1361):218–232, 1963. 5, 6, 106, 125, 127, 129

[16] Eddwi H. Hasdeo, Ahmad R. T. Nugraha, Mildred S. Dresselhaus, and Riichiro Saito. **Breit-Wigner-Fano Line Shapes in Raman Spectra of Graphene**. *Physical Review B*, **90**(24):245140, 2014. 5

[17] H. Gretarsson, N. H. Sung, M. Höppner, B. J. Kim, B. Keimer, and M. Le Tacon. **Two-Magnon Raman Scattering and Pseudospin-Lattice Interactions in Sr2IrO4 and Sr3Ir2O7**. *Physical Review Letters*, **116**(13):136401, 2016. 5

[18] Bruno R. Carvalho, Leandro M. Malard, Juliana M. Alves, Cristiano Fantini, and Marcos A. Pimenta. **Symmetry-Dependent Exciton-Phonon Coupling in 2D and Bulk MoS2 Observed by Resonance Raman Scattering**. *Physical Review Letters*, **114**(13):136403, 2015. 5, 6, 95, 143, 155

[19] Sven Reichardt and Ludger Wirtz. *Raman Spectroscopy of Graphene*. World Scientific, 2016. Chap. 3, pp. 85-132. 5, 110, 112, 129

[20] Xin Luo, Yanyuan Zhao, Jun Zhang, Qihua Xiong, and Su Ying Quek. **Anomalous Frequency Trends in MoS2 Thin Films Attributed to Surface Effects**. *Physical Review B*, **88**(7):075320, 2013. 6, 97

[21] Xin Luo, Yanyuan Zhao, Jun Zhang, Minglin Toh, Christian Kloc, Qihua Xiong, and Su Ying Quek. **Effects of Lower Symmetry and Dimensionality on Raman Spectra in Two-Dimensional WSe2**. *Physical Review B*, **88**(19):195313, 2013. 6, 97

[22] Alejandro Molina-Sánchez, Kerstin Hummer, and Ludger Wirtz. **Vibrational and Optical Properties of MoS2: From Monolayer to Bulk**. *Surface Science Reports*, **70**(4):554–586, 2015. 6, 51, 105

[23] Nils Scheuschner, Roland Gillen, Matthias Staiger, and Janina Maultzsch. **Interlayer Resonant Raman Modes in Few-Layer MoS2**. *Physical Review B*, **91**(23):235409, 2015. 6

[24] Guillaume Froehlicher, Etienne Lorchat, François Fernique, Chaitanya Joshi, Alejandro Molina-Sánchez, Ludger Wirtz,

and Stéphane Berciaud. **Unified Description of the Optical Phonon Modes in N-Layer MoTe2**. *Nano Letters*, **15**(10):6481–6489, 2015. 6, 52, 95, 96, 97, 105, 108, 109, 110, 111, 115, 116, 122, 155

[25] M. Grzeszczyk, K. Gołasa, M. Zinkiewicz, K. Nogajewski, M. R. Molas, M. Potemski, A. Wysmołek, and A. Babiński. **Raman Scattering in Few-Layer MoTe2**. *2D Materials*, **3**(2):025010, 2016. 6, 95, 97, 110, 115, 122

[26] Q. J. Song, Q. H. Tan, X. Zhang, J. B. Wu, B. W. Sheng, Y. Wan, X. Q. Wang, L. Dai, and P. H. Tan. **Physical Origin of Davydov Splitting and Resonant Raman Spectroscopy of Davydov Components in Multilayer MoTe2**. *Physical Review B*, **93**(11):115409, 2016. 6, 95, 97, 115, 122

[27] Joseph L. Birman and Achintya K. Ganguly. **Theory of Enhanced Raman Scattering and Virtual Quasiparticles in Crystals**. *Physical Review Letters*, **17**(12):647–649, 1966. 6, 125, 129

[28] Achintya K. Ganguly and Joseph L. Birman. **Theory of Lattice Raman Scattering in Insulators**. *Physical Review*, **162**(3):806–816, 1967. 6, 125, 129

[29] Alberto Garcia Cristobal. **Efectos Resonantes de La Dispersion Raman En Semiconductores**. *Ph.D. Thesis*, 1996. 6, 125

[30] Peter YU and Manuel Cardona. *Fundamentals of Semiconductors: Physics and Materials Properties*. Springer Berlin Heidelberg, 2005. 6, 38, 65, 66, 98, 103, 125, 138, 143, 175, 178

[31] Michele Lazzeri and Francesco Mauri. **First-Principles Calculation of Vibrational Raman Spectra in Large Systems: Signature of Small Rings in Crystalline SiO2**. *Physical Review Letters*, **90**(3):036401, 2003. 6, 96

[32] M. Veithen, X. Gonze, and Ph. Ghosez. **Nonlinear Optical Susceptibilities, Raman Efficiencies, and Electro-Optic Tensors from First-**

Principles Density Functional Perturbation Theory. *Physical Review B*, **71**(12):125107, 2005. 6, 96, 126

[33] Yannick Gillet, Matteo Giantomassi, and Xavier Gonze. **First-Principles Study of Excitonic Effects in Raman Intensities**. *Physical Review B*, **88**(9):094305, 2013. 6, 83, 98, 107

[34] E. del Corro, A. Botello-Méndez, Y. Gillet, A. L. Elias, H. Terrones, S. Feng, C. Fantini, Daniel Rhodes, N. Pradhan, L. Balicas, X. Gonze, J.-C. Charlier, M. Terrones, and M. A. Pimenta. **Atypical Exciton–Phonon Interactions in WS2 and WSe2 Monolayers Revealed by Resonance Raman Spectroscopy**. *Nano Letters*, **16**(4):2363–2368, 2016. 6, 107, 113

[35] Henrique P. C. Miranda, Sven Reichardt, Guillaume Froehlicher, Alejandro Molina-Sánchez, Stéphane Berciaud, and Ludger Wirtz. **Quantum Interference Effects in Resonant Raman Spectroscopy of Single- and Triple-Layer MoTe2 from First-Principles**. *Nano Letters*, **17**(4):2381–2388, 2017. 7, 75, 107, 108, 109, 111, 112, 113, 116, 119, 121, 155, 156

[36] Richard M. Martin. *Electronic Structure: Basic Theory and Practical Methods*. Cambridge University Press, 2004. 11, 13, 14, 16, 17

[37] Richard M. Martin, Lucia Reining, and David M. Ceperley. *Interacting Electrons*. Cambridge University Press, 2016. 12, 13, 16, 22, 24, 25

[38] Lars Hedin. **New Method for Calculating the One-Particle Green's Function with Application to the Electron-Gas Problem**. *Physical Review*, **139**:A796–A823, 1965. 13

[39] Carlos Fiolhais, Fernando Nogueira, and Miguel A. L. Marques. *A Primer in Density Functional Theory*. Springer Science & Business Media, 2003. 13, 15

[40] P. Hohenberg and W. Kohn. **Inhomogeneous Electron Gas**. *Physical Review*, **136**:B864–B871, 1964. 13

[41] W. Kohn and L. J. Sham. **Self-Consistent Equations Including Exchange and Correlation Effects**. *Physical Review*, **140**:A1133–A1138, 1965. 13

[42] Sidney Yip. *Handbook of Materials Modeling*. Springer Science & Business Media, 2007. 13

[43] D. M. Ceperley and B. J. Alder. **Ground State of the Electron Gas by a Stochastic Method**. *Physical Review Letters*, **45**(7):566–569, 1980. 16

[44] John P. Perdew, Kieron Burke, and Matthias Ernzerhof. **Generalized Gradient Approximation Made Simple**. *Physical Review Letters*, **77**(18):3865–3868, 1996. 16

[45] Miguel A.L. Marques, Micael J.T. Oliveira, and Tobias Burnus. **Libxc: A Library of Exchange and Correlation Functionals for Density Functional Theory**. *Computer Physics Communications*, **183**(10):2272–2281, 2012. 16

[46] John C. Snyder, Matthias Rupp, Katja Hansen, Klaus-Robert Müller, and Kieron Burke. **Finding Density Functionals with Machine Learning**. *Physical Review Letters*, **108**(25):253002, 2012. 16

[47] JM Soler, Emilio Artacho, and JD Gale. **The SIESTA Method for Ab Initio Order- N Materials Simulation**. *Journal of Physics*, **2745**, 2002. 17

[48] Volker Blum, Ralf Gehrke, Felix Hanke, Paula Havu, Ville Havu, Xinguo Ren, Karsten Reuter, and Matthias Scheffler. **Ab Initio Molecular Simulations with Numeric Atom-Centered Orbitals**. *Computer Physics Communications*, **180**(11):2175–2196, 2009. 17

[49] Luigi Genovese, Alexey Neelov, Stefan Goedecker, Thierry Deutsch, Seyed Alireza Ghasemi, Alexander Willand,

Damien Caliste, Oded Zilberberg, Mark Rayson, Anders Bergman, and Reinhold Schneider. **Daubechies Wavelets as a Basis Set for Density Functional Pseudopotential Calculations**. *The Journal of Chemical Physics*, **129**(1):014109, 2008. 17

[50] Richard D. Mattuck. *A Guide to Feynman Diagrams in the Many-Body Problem*. Dover Publications, 2 edition, 1992. 18, 19, 20, 21, 22, 24, 27, 57, 72, 74, 128, 145

[51] Alexander L. Fetter and John Dirk Walecka. *Quantum Theory of Many-Particle Systems*. Courier Corporation, 2003. 18, 131

[52] Gerald D. Mahan. *Many-Particle Physics*. Springer Science & Business Media, 2000. 18, 37

[53] R. W. Saunders and W. Young. **Raman Scattering: One-Phonon Final States and Many-Body Effects**. *Journal of Physics C: Solid State Physics*, **13**(1):103, 1980. 21, 128, 129, 151

[54] Giovanni Onida, Lucia Reining, and Angel Rubio. **Electronic Excitations: Density-Functional versus Many-Body Green's-Function Approaches**. *Reviews of Modern Physics*, **74**(2):601–659, 2002. 22, 23

[55] Andrea Marini, Conor Hogan, Myrta Grüning, and Daniele Varsano. **Yambo: An Ab Initio Tool for Excited State Calculations**. *Computer Physics Communications*, **180**(8):1392–1403, 2009. 23, 24, 27, 28, 63, 70, 75, 85, 161, 162

[56] Xavier Gonze and Changyol Lee. **Dynamical Matrices, Born Effective Charges, Dielectric Permittivity Tensors, and Interatomic Force Constants from Density-Functional Perturbation Theory**. *Physical Review B*, **55**(16):10355–10368, 1997. 29, 39

[57] Peter Brüesch. *Phonons: Theory and Experiments I. Lattice Dynamics and Models of Interatomic Forces*. Springer-Verlag, 1982. 31, 33, 35, 36

[58] Ion Errea, Matteo Calandra, and Francesco Mauri. **First-Principles Theory of Anharmonicity and the Inverse Isotope Effect in Superconducting Palladium-Hydride Compounds**. *Physical Review Letters*, **111**(17):177002, 2013. 32

[59] Atsushi Togo, Laurent Chaput, and Isao Tanaka. **Distributions of Phonon Lifetimes in Brillouin Zones**. *Physical Review B*, **91**(9):094306, 2015. 32

[60] Feliciano Giustino. **Electron-Phonon Interactions from First Principles**. *Reviews of Modern Physics*, **89**(1):015003, 2017. 35, 41, 55

[61] O. Dubay and G. Kresse. **Accurate Density Functional Calculations for the Phonon Dispersion Relations of Graphite Layer and Carbon Nanotubes**. *Physical Review B*, **67**(3):035401, 2003. 38, 45, 47

[62] Atsushi Togo and Isao Tanaka. **First Principles Phonon Calculations in Materials Science**. *Scripta Materialia*, **108**:1–5, 2015. 39, 172

[63] Stefano Baroni, Stefano de Gironcoli, Andrea Dal Corso, and Paolo Giannozzi. **Phonons and Related Crystal Properties from Density-Functional Perturbation Theory**. *Reviews of Modern Physics*, **73**(2):515–562, 2001. 39, 169

[64] R. Car and M. Parrinello. **Unified Approach for Molecular Dynamics and Density-Functional Theory**. *Physical Review Letters*, **55**(22):2471–2474, 1985. 41

[65] O. Hellman, I. A. Abrikosov, and S. I. Simak. **Lattice Dynamics of Anharmonic Solids from First Principles**. *Physical Review B*, **84**(18):180301, 2011. 42

[66] R. A. Jishi, L. Venkataraman, M. S. Dresselhaus, and G. Dresselhaus. **Phonon Modes in Carbon Nanotubules**. *Chemical Physics Letters*, **209**:77–82, 1993. 43, 46

[67] Ludger Wirtz and Angel Rubio. **The Phonon Dispersion of Graphite Revisited**. *Solid State Communications*, **131**:141–152, 2004. 43, 44, 47

[68] Jing Li, Henrique Pereira Coutada Miranda, Yann-Michel Niquet, Luigi Genovese, Ivan Duchemin, Ludger Wirtz, and Christophe Delerue. **Phonon-Limited Carrier Mobility and Resistivity from Carbon Nanotubes to Graphene**. *Physical Review B*, **92**(7):075414, 2015. 43, 45, 47, 48, 58

[69] Cheol-Hwan Park, Nicola Bonini, Thibault Sohier, Georgy Samsonidze, Boris Kozinsky, Matteo Calandra, Francesco Mauri, and Nicola Marzari. **Electron–Phonon Interactions and the Intrinsic Electrical Resistivity of Graphene**. *Nano Letters*, **14**(3):1113–1119, 2014. 43, 47

[70] W. Kohn. **Image of the Fermi Surface in the Vibration Spectrum of a Metal**. *Physical Review Letters*, **2**(9):393–394, 1959. 43

[71] S. Piscanec, M. Lazzeri, Francesco Mauri, A. C. Ferrari, and J. Robertson. **Kohn Anomalies and Electron-Phonon Interactions in Graphite**. *Physical Review Letters*, **93**(18):185503, 2004. 43

[72] X. Gonze, J.-M. Beuken, R. Caracas, F. Detraux, M. Fuchs, G.-M. Rignanese, L. Sindic, M. Verstraete, G. Zerah, F. Jollet, M. Torrent, A. Roy, M. Mikami, Ph. Ghosez, J.-Y. Raty, and D.C. Allan. **First-Principles Computation of Material Properties: The ABINIT Software Project**. *Computational Materials Science*, **25**(3):478–492, 2002. 43, 70, 161, 170, 172

[73] J. L. Mañes. **Symmetry-Based Approach to Electron-Phonon Interactions in Graphene**. *Physical Review B*, **76**(4):045430, 2007. 45, 46

[74] Thibault Sohier, Matteo Calandra, Cheol-Hwan Park, Nicola Bonini, Nicola Marzari, and Francesco Mauri.

Phonon-Limited Resistivity of Graphene by First-Principles Calculations: Electron-Phonon Interactions, Strain-Induced Gauge Field, and Boltzmann Equation. *Physical Review B*, **90**(12):125414, 2014. 46

[75] HENRIQUE MIRANDA. **Phonon Website**, 2016. 48, 50, 51, 157, 171, 172

[76] ROBERT S. MULLIKEN. **Report on Notation for the Spectra of Polyatomic Molecules**. *The Journal of Chemical Physics*, **23**(11):1997–2011, 1955. 51

[77] A. MOLINA-SÁNCHEZ AND L. WIRTZ. **Phonons in Single-Layer and Few-Layer MoS2 and WS2**. *Physical Review B*, **84**(15):155413, 2011. 51

[78] A. DAVYDOV. *Theory of Molecular Excitons*. Springer, 2013. 52

[79] PAOLO GIANNOZZI, STEFANO BARONI, NICOLA BONINI, MATTEO CALANDRA, ROBERTO CAR, CARLO CAVAZZONI, DAVIDE CERESOLI, GUIDO L CHIAROTTI, MATTEO COCOCCIONI, ISMAILA DABO, ANDREA DAL CORSO, STEFANO DE GIRONCOLI, STEFANO FABRIS, GUIDO FRATESI, RALPH GEBAUER, UWE GERSTMANN, CHRISTOS GOUGOUSSIS, ANTON KOKALJ, MICHELE LAZZERI, LAYLA MARTIN-SAMOS, NICOLA MARZARI, FRANCESCO MAURI, RICCARDO MAZZARELLO, STEFANO PAOLINI, ALFREDO PASQUARELLO, LORENZO PAULATTO, CARLO SBRACCIA, SANDRO SCANDOLO, GABRIELE SCLAUZERO, ARI P SEITSONEN, ALEXANDER SMOGUNOV, PAOLO UMARI, AND RENATA M WENTZCOVITCH. **QUANTUM ESPRESSO: A Modular and Open-Source Software Project for Quantum Simulations of Materials.** *Journal of physics. Condensed matter : an Institute of Physics journal*, **21**(39):395502, 2009. 55, 59, 70, 75, 161, 170, 172

[80] ELENA CANNUCCIA AND ANDREA MARINI. **Ab-Initio Study of the Effects Induced by the Electron-Phonon Scattering in Carbon Based Nanostructures**. 2013. 55, 57, 127, 145

[81] H. Y. FAN. **Temperature Dependence of the Energy Gap in Semiconductors**. *Physical Review*, **82**(6):900–905, 1951. 56

[82] S. Poncé, Y. Gillet, J. Laflamme Janssen, A. Marini, M. Verstraete, and X. Gonze. **Temperature Dependence of the Electronic Structure of Semiconductors and Insulators**. *The Journal of Chemical Physics*, **143**(10):102813, 2015. 57

[83] N. V. Podberezskaya, S. A. Magarill, N. V. Pervukhina, and S. V. Borisov. **Crystal Chemistry of Dichalcogenides MX2**. *Journal of Structural Chemistry*, **42**(4):654–681, 2001. 59

[84] Nicola Marzari and David Vanderbilt. **Maximally Localized Generalized Wannier Functions for Composite Energy Bands**. *Physical Review B*, **56**(20):12847–12865, 1997. 61, 158

[85] Robert van Leeuwen. **First-Principles Approach to the Electron-Phonon Interaction**. *Physical Review B*, **69**(11):115110, 2004. 64

[86] H. Bilz, D. Strauch, and R. K. Wehner. *Light and Matter Id / Licht Und Materie Id: Infrared and Raman Spectra of Non-Metals*. Springer Science & Business Media, 2012. 65, 68, 69

[87] Peter Hertel. *Lectures on Theoretical Physics, Linear Response Theory*. 2012. 66, 67

[88] John David Jackson. *Classical Electrodynamics*. Wiley, 1975. 67

[89] Herbert B. Callen and Theodore A. Welton. **Irreversibility and Generalized Noise**. *Physical Review*, **83**(1):34–40, 1951. 68

[90] Morten Førre and Aleksander Skjerlie Simonsen. **Generalized Velocity-Gauge Form of the Light-Matter Interaction Hamiltonian beyond the Dipole Approximation**. *Physical Review A*, **93**(1):013423, 2016. 69

[91] R. Del Sole and Raffaello Girlanda. **Optical Properties of Semiconductors within the Independent-Quasiparticle Approximation**. *Physical Review B*, **48**(16):11789–11795, 1993. 69, 70

[92] S. Poncé, E. R. Margine, C. Verdi, and F. Giustino. **EPW: Electron–phonon Coupling, Transport and Superconducting Properties Using Maximally Localized Wannier Functions**. *Computer Physics Communications*, **209**:116–133, 2016. 70, 139

[93] D. M. Basko. **Calculation of the Raman G Peak Intensity in Monolayer Graphene: Role of Ward Identities**. *New Journal of Physics*, **11**(9):095011, 2009. 72, 108, 125, 129

[94] Huaihong Guo, Teng Yang, Mahito Yamamoto, Lin Zhou, Ryo Ishikawa, Keiji Ueno, Kazuhito Tsukagoshi, Zhidong Zhang, Mildred S. Dresselhaus, and Riichiro Saito. **Double Resonance Raman Modes in Monolayer and Few-Layer MoTe2**. *Physical Review B*, **91**(20):205415, 2015. 75, 107

[95] Gabriel Antonius and Steven G. Louie. **Theory of the Exciton-Phonon Coupling**. *arXiv 1705.04245 [cond-mat]*, 2017. 81

[96] Michael Rohlfing and Steven G. Louie. **Electron-Hole Excitations and Optical Spectra from First Principles**. *Physical Review B*, **62**(8):4927–4944, 2000. 81

[97] Andrea Marini. **Ab Initio Finite-Temperature Excitons**. *Physical Review Letters*, **101**(10):106405, 2008. 81

[98] G. Strinati. **Application of the Green's Functions Method to the Study of the Optical Properties of Semiconductors**. *La Rivista del Nuovo Cimento (1978-1999)*, **11**(12):1–86, 1988. 81, 82

[99] Thorsten Deilmann, Matthias Drüppel, and Michael Rohlfing. **Three-Particle Correlation from a Many-Body Perspective: Trions in a Carbon Nanotube**. *Physical Review Letters*, **116**(19):196804, 2016. 81

[100] Gianluca Stefanucci and Robert van Leeuwen. *Nonequilibrium Many-Body Theory of Quantum Systems: A Modern Introduction*. Cambridge University Press, 2013. 82

[101] Myrta Grüning, Andrea Marini, and Xavier Gonze. **Exciton-Plasmon States in Nanoscale Materials: Breakdown of the Tamm-Dancoff Approximation**. *Nano Letters*, **9**(8):2820–2824, 2009. 83

[102] Yannick Gillet, Matteo Giantomassi, and Xavier Gonze. **Efficient On-the-Fly Interpolation Technique for Bethe–Salpeter Calculations of Optical Spectra**. *Computer Physics Communications*, **203**:83–93, 2016. 83, 101, 135

[103] David Kammerlander, Silvana Botti, Miguel A. L Marques, Andrea Marini, and Claudio Attaccalite. **Speeding up the Solution of the Bethe-Salpeter Equation by a Double-Grid Method and Wannier Interpolation**. *Physical Review B*, **86**(12):125203, 2012. 83, 135

[104] **ScaLAPACK**. 84

[105] Vicente Hernandez, Jose E. Roman, and Vicente Vidal. **SLEPc: A Scalable and Flexible Toolkit for the Solution of Eigenvalue Problems**. *ACM Trans. Math. Softw.*, **31**(3):351–362, 2005. 84

[106] Carlo A. Rozzi, Daniele Varsano, Andrea Marini, Eberhard K. U. Gross, and Angel Rubio. **Exact Coulomb Cutoff Technique for Supercell Calculations**. *Physical Review B*, **73**(20):205119, 2006. 85

[107] Claudia Ruppert, Ozgur Burak Aslan, and Tony F. Heinz. **Optical Properties and Band Gap of Single- and Few-Layer MoTe2 Crystals**. *Nano Letters*, **14**(11):6231–6236, 2014. 85, 96, 97, 110, 111, 116

[108] Thomas Galvani, Fulvio Paleari, Henrique P. C. Miranda, Alejandro Molina-Sánchez, Ludger Wirtz, Sylvain Latil, Hakim Amara, and François Ducastelle. **Excitons in Boron Nitride Single Layer**. *Physical Review B*, **94**(12):125303, 2016. 86

[109] Alejandro Molina-Sánchez, Maurizia Palummo, Andrea Marini, and Ludger Wirtz. **Temperature-Dependent Excitonic Effects in the Optical Properties of Single-Layer MoS2**. *Physical Review B*, **93**(15):155435, 2016. 92

[110] Alejandro Molina-Sánchez, Davide Sangalli, Kerstin Hummer, Andrea Marini, and Ludger Wirtz. **Effect of Spin-Orbit Interaction on the Optical Spectra of Single-Layer, Double-Layer, and Bulk MoS2**. *Physical Review B*, **88**(4):045412, 2013. 95

[111] Ludger Wirtz, Michele Lazzeri, Francesco Mauri, and Angel Rubio. **Raman Spectra of BN Nanotubes: Ab Initio and Bond-Polarizability Model Calculations**. *Physical Review B*, **71**(24):241402, 2005. 96

[112] P. Umari, Alfredo Pasquarello, and Andrea Dal Corso. **Raman Scattering Intensities in Alpha-Quartz: A First-Principles Investigation**. *Physical Review B*, **63**(9):094305, 2001. 97

[113] P. Soubelet, A. E. Bruchhausen, A. Fainstein, K. Nogajewski, and C. Faugeras. **Resonance Effects in the Raman Scattering of Monolayer and Few-Layer MoSe2**. *Physical Review B*, **93**(15):155407, 2016. 97

[114] Kangwon Kim, Jae-Ung Lee, Dahyun Nam, and Hyeonsik Cheong. **Davydov Splitting and Excitonic Resonance Effects in Raman Spectra of Few-Layer MoSe2**. *ACS Nano*, **10**(8):8113–8120, 2016. 97

[115] Jae-Ung Lee, Jaesung Park, Young-Woo Son, and Hyeonsik Cheong. **Anomalous Excitonic Resonance Raman Effects in Few-Layered MoS2**. **7**(7):3229–3236, 2015. 97

[116] Matthias Staiger, Roland Gillen, Nils Scheuschner, Oliver Ochedowski, Felix Kampmann, Marika Schleberger, Christian Thomsen, and Janina Maultzsch. **Splitting of Monolayer Out-of-Plane A1′ Raman Mode in Few-Layer WS2**. *Physical Review B*, **91**(19):195419, 2015. 97

[117] Mahito Yamamoto, Sheng Tsung Wang, Meiyan Ni, Yen-Fu Lin, Song-Lin Li, Shinya Aikawa, Wen-Bin Jian, Keiji Ueno,

Katsunori Wakabayashi, and Kazuhito Tsukagoshi. **Strong Enhancement of Raman Scattering from a Bulk-Inactive Vibrational Mode in Few-Layer MoTe2**. *ACS Nano*, **8**(4):3895–3903, 2014. 97

[118] Sean A. Fischer, Tyler W. Ueltschi, Patrick Z. El-Khoury, Amanda L. Mifflin, Wayne P. Hess, Hong-Fei Wang, Christopher J. Cramer, and Niranjan Govind. **Infrared and Raman Spectroscopy from Ab Initio Molecular Dynamics and Static Normal Mode Analysis: The C–H Region of DMSO as a Case Study**. *The Journal of Physical Chemistry B*, **120**(8):1429–1436, 2016. 101

[119] R. Loudon. **The Raman Effect in Crystals**. *Advances in Physics*, **13**(52):423–482, 1964. 105

[120] A. Cantarero, C. Trallero-Giner, and M. Cardona. **Excitons in One-Phonon Resonant Raman Scattering: Deformation-Potential Interaction**. *Physical Review B*, **39**(12):8388–8397, 1989. 107

[121] Martin Kalbac, Alfonso Reina-Cecco, Hootan Farhat, Jing Kong, Ladislav Kavan, and Mildred S. Dresselhaus. **The Influence of Strong Electron and Hole Doping on the Raman Intensity of Chemical Vapor-Deposition Graphene**. *ACS Nano*, **4**(10):6055–6063, 2010. 108

[122] Chi-Fan Chen, Cheol-Hwan Park, Bryan W. Boudouris, Jason Horng, Baisong Geng, Caglar Girit, Alex Zettl, Michael F. Crommie, Rachel A. Segalman, Steven G. Louie, and Feng Wang. **Controlling Inelastic Light Scattering Quantum Pathways in Graphene**. *Nature*, **471**(7340):617–620, 2011. 108

[123] Sven Reichardt and Ludger Wirtz. **Ab Initio Calculation of the G Peak Intensity of Graphene: Laser-Energy and Fermi-Energy Dependence and Importance of Quantum Interference Effects**. *Physical Review B*, **95**(19):195422, 2017. 108, 110, 112, 125, 129, 134, 143, 144

[124] R. Saito, G. Dresselhaus, and M. S. Dresselhaus. **Trigonal Warping Effect of Carbon Nanotubes**. *Physical Review B*, **61**(4):2981–2990, 2000. 112

[125] Katarzyna Gołasa, Magda Grzeszczyk, Maciej R. Molas, Małgorzata Zinkiewicz, Łukasz Bala, Karol Nogajewski, Marek Potemski, Andrzej Wysmołek, and Adam Babiński. **Resonant Quenching of Raman Scattering Due to Out-of-Plane A1g/A'1 Modes in Few-Layer MoTe2**. *Nanophotonics*, **0**(0), 2017. 123, 127

[126] D. M. Basko. **Theory of Resonant Multiphonon Raman Scattering in Graphene**. *Physical Review B*, **78**(12):125418, 2008. 125, 128, 129

[127] Pedro Venezuela, Michele Lazzeri, and Francesco Mauri. **Theory of Double-Resonant Raman Spectra in Graphene: Intensity and Line Shape of Defect-Induced and Two-Phonon Bands**. *Physical Review B*, **84**(3):035433, 2011. 125

[128] Kwanpyo Kim, Sinisa Coh, Liang Z. Tan, William Regan, Jong Min Yuk, Eric Chatterjee, M. F. Crommie, Marvin L. Cohen, Steven G. Louie, and A. Zettl. **Raman Spectroscopy Study of Rotated Double-Layer Graphene: Misorientation-Angle Dependence of Electronic Structure**. *Physical Review Letters*, **108**(24):246103, 2012. 125

[129] P. B. Allen and M. Cardona. **Temperature Dependence of the Direct Gap of Si and Ge**. *Physical Review B*, **27**(8):4760–4769, 1983. 127

[130] R. K. Wehner and R. Klein. **Scattering of Light by Entropy Fluctuations in Dielectric Crystals**. *Physica*, **62**(2):161–197, 1972. 128, 129

[131] Yannick Gillet. **Ab Initio Study of Raman and Optical Spectra of Crystalline Materials and Their Temperature Dependence**, 2017. 138, 147, 175, 179

[132] **Standard Solid State Pseudopotentials (SSSP)**. 139

[133] S. Poncé, G. Antonius, P. Boulanger, E. Cannuccia, A. Marini, M. Côté, and X. Gonze. **Verification of First-Principles Codes: Comparison of Total Energies, Phonon Frequencies, Electron–phonon Coupling and Zero-Point Motion Correction to the Gap between ABINIT and QE/Yambo**. *Computational Materials Science*, **83**:341–348, 2014. 140

[134] Sohrab Ismail-Beigi and Steven G. Louie. **Excited-State Forces within a First-Principles Green's Function Formalism**. *Physical Review Letters*, **90**(7):076401, 2003. 149

[135] Henrique Miranda. **Exciton Website**, 2017. 157

[136] Nicolas Mounet, Marco Gibertini, Philippe Schwaller, Andrius Merkys, Ivano E. Castelli, Andrea Cepellotti, Giovanni Pizzi, and Nicola Marzari. **Novel Two-Dimensional Materials from High-Throughput Computational Exfoliation of Experimentally Known Compounds**. 2016. 157

[137] Razvan Caracas and Ema Bobocioiu. **WURM - Home**. *The WURM project – a freely available web-based repository of computed physical data for minerals*, **96**:437–444, 2011. 158

[138] **Abipy: Open-Source Library for Analyzing the Results Produced by ABINIT**, 2017. 161, 163

[139] Giovanni Pizzi, Andrea Cepellotti, Riccardo Sabatini, Nicola Marzari, and Boris Kozinsky. **AiiDA: Automated Interactive Infrastructure and Database for Computational Science**. *Computational Materials Science*, **111**:218–230, 2016. 161, 163, 168

[140] Russ Rew, Glenn Davis, Steve Emmerson, Cathy Cormack, John Caron, Robert Pincus, Ed Hartnett, Dennis Heimbigner, Lynton Appel, and Ward Fisher. **Unidata NetCDF**. 1989. 161

[141] Henrique Miranda. **Yambopy on Github**, 2017. 162, 164

[142] Ask Hjorth Larsen, Jens Jørgen Mortensen, Jakob Blomqvist, Ivano E. Castelli, Rune Christensen, Marcin Dułak, Jesper Friis, Michael N. Groves, Bjørk Hammer, Cory Hargus, Eric D. Hermes, Paul C. Jennings, Peter Bjerre Jensen, James Kermode, John R. Kitchin, Esben Leonhard Kolsbjerg, Joseph Kubal, Kristen Kaasbjerg, Steen Lysgaard, Jón Bergmann Maronsson, Tristan Maxson, Thomas Olsen, Lars Pastewka, Andrew Peterson, Carsten Rostgaard, Jakob Schiøtz, Ole Schütt, Mikkel Strange, Kristian S. Thygesen, Tejs Vegge, Lasse Vilhelmsen, Michael Walter, Zhenhua Zeng, and Karsten W. Jacobsen. **The Atomic Simulation Environment—a Python Library for Working with Atoms**. *Journal of Physics: Condensed Matter*, **29**(27):273002, 2017. 163

[143] Laurent Chaput, Atsushi Togo, Isao Tanaka, and Gilles Hug. **Phonon-Phonon Interactions in Transition Metals**. *Physical Review B*, **84**(9):094302, 2011. 163

[144] Henrique Miranda, Alejandro Molina-Sanchez, Alexandre Morlet, and Fulvio Paleari. **Yambopy Documentation: Read the Docs**, 2017. 163, 164

[145] **Travis CI - Test and Deploy Your Code with Confidence**. 164

[146] Anubhav Jain, Shyue Ping Ong, Wei Chen, Bharat Medasani, Xiaohui Qu, Michael Kocher, Miriam Brafman, Guido Petretto, Gian-Marco Rignanese, Geoffroy Hautier, Daniel Gunter, and Kristin A. Persson. **FireWorks: A Dynamic Workflow System Designed for High-Throughput Applications**. *Concurrency and Computation: Practice and Experience*, **27**(17):5037–5059, 2015. 164

[147] **AiiDA – Plugins**. 165

[148] Anton Kokalj. **Computer Graphics and Graphical User Interfaces as Tools in Simulations of Matter at the Atomic Scale**. *Computational Materials Science*, **28**(2):155–168, 2003. 167, 168

[149] William Humphrey, Andrew Dalke, and Klaus Schulten. **VMD: Visual Molecular Dynamics**. *Journal of Molecular Graphics*, **14**(1):33–38, 1996. 167, 168

[150] R. M. Hanson. **Jmol – a Paradigm Shift in Crystallographic Visualization**. *Journal of Applied Crystallography*, **43**(5):1250–1260, 2010. 167, 168

[151] Anubhav Jain, Shyue Ping Ong, Geoffroy Hautier, Wei Chen, William Davidson Richards, Stephen Dacek, Shreyas Cholia, Dan Gunter, David Skinner, Gerbrand Ceder, and Kristin A. Persson. **Commentary: The Materials Project: A Materials Genome Approach to Accelerating Materials Innovation**. *APL Materials*, **1**(1):011002, 2013. 168

[152] Stefano Curtarolo, Wahyu Setyawan, Gus L. W. Hart, Michal Jahnatek, Roman V. Chepulskii, Richard H. Taylor, Shidong Wang, Junkai Xue, Kesong Yang, Ohad Levy, Michael J. Mehl, Harold T. Stokes, Denis O. Demchenko, and Dane Morgan. **AFLOW: An Automatic Framework for High-Throughput Materials Discovery**. *Computational Materials Science*, **58**:218–226, 2012. 168

[153] **Novel Materials Discovery Laboratory (Nomad)**, 2017. 168

[154] Xavier Gonze. **First-Principles Responses of Solids to Atomic Displacements and Homogeneous Electric Fields: Implementation of a Conjugate-Gradient Algorithm**. *Physical Review B*, **55**(16):10337–10354, 1997. 169

[155] Togo Atsushi. **Phonon Database at Kyoto University**, 2017. 170

[156] Jaume Sanchez. **Ccapture.Js: A Library to Capture Canvas-Based Animations at a Fixed Framerate**, 2017. 170

[157] Mr.doob. **Three.Js: JavaScript 3D Library**. 2017. 171

[158] **Highcharts**, 2017. 171

[159] Henrique Miranda. **Phononwebsite on Github**, 2017. 172

[160] **Github**, 2017. 173

[161] Jonathan H. Lloyd-Williams and Bartomeu Monserrat. **Lattice Dynamics and Electron-Phonon Coupling Calculations Using Nondiagonal Supercells**. *Physical Review B*, **92**(18):184301, 2015. 174